

Beetaloo Basin Shale Long-term Competency after Decommissioning

Elaheh Arjomand, Jeremie Dautriat, James Kear and
Cameron Huddleston-Holmes

October 2024

Citation

Elaheh Arjomand, Jeremie Dautriat, James Kear, and Cameron Huddlestone-Holmes (2024). Beetaloo Basin Shale Long-term Competency after Decommissioning. CSIRO report number EP2024-3095. CSIRO, Canberra.

Copyright

© Commonwealth Scientific and Industrial Research Organisation 2024. To the extent permitted by law, all rights are reserved and no part of this publication covered by copyright may be reproduced or copied in any form or by any means except with the written permission of CSIRO.

Important disclaimer

CSIRO advises that the information contained in this publication comprises general statements based on scientific research. The reader is advised and needs to be aware that such information may be incomplete or unable to be used in any specific situation. No reliance or actions must therefore be made on that information without seeking prior expert professional, scientific and technical advice. To the extent permitted by law, CSIRO (including its employees and consultants) excludes all liability to any person for any consequences, including but not limited to all losses, damages, costs, expenses and any other compensation, arising directly or indirectly from using this publication (in part or in whole) and any information or material contained in it.

CSIRO is committed to providing web accessible content wherever possible. If you are having difficulties with accessing this document, please contact csiroenquiries@csiro.au.

Contents

Abbreviations	1
Executive summary	3
Preface	6
Chapter 1	8
1.1 Introduction	9
1.1.1 Creep mechanism	16
1.1.2 Shale barrier validation using logging techniques, with the aim of qualifying a formed barrier.....	18
1.2 Techniques and approaches to stimulate and activate shale in decommissioned wells	21
1.3 Theoretical and experimental lab investigations.....	22
1.3.1 Effect of water content on shale mechanical properties.....	26
1.3.2 Effect of loading rate on shale mechanical properties	27
1.3.3 Effect of elevated temperature on the shale creep process	28
1.3.4 Effect on the shale creep process of incorporating chemicals into the annular fluid	31
1.4 Creep modelling.....	39
1.4.1 Analytical (rheological) modelling.....	39
1.4.2 Numerical simulations	45
1.4.3 Discussion of shale creep modelling	48
1.5 Evaluation and selection of chemical fluids.....	48
1.6 Conclusion	49
Chapter 2	51
2.1 Introduction.....	52
2.2 Shale chemoporomechanical characterisation	52
2.2.1 Clay mineralogy classifications	54
2.3 Beetaloo sub-basin shale mineralogy studies.....	56
2.3.1 Velkerri Formation	56
2.3.2 Kyalla Formation	56
2.3.3 Acquisition of core samples from Shenandoah-1A.....	57
2.4 Determination of mineralogy by XRD and XRF	57
2.5 Commissioning the MicroRX rig	60
2.6 Measuring chemoporoeelastic properties.....	61
2.6.1 Sample preparation	61
2.6.2 Governing equations.....	62
2.6.3 Experimental procedures.....	63
2.7 Experimental results and discussion	68
2.7.1 Measuring the chemoporoeelastic properties of samples obtained from the Velkerri formation (depth 2316.3–2511 m)	69
2.7.2 Measuring the chemoporoeelastic properties of samples obtained from the Kyalla Formation (depth 1500 m)	71
2.8 Discussions.....	74
2.8.1 Chemomechanical properties	74
2.9 Conclusion	76
Chapter 3	78

3.1.	Introduction	79
3.2.	Downscaled laboratory experiments	80
3.2.1.	Received core collection	80
3.2.2.	Sample preparation and collection	83
3.2.3.	Geomechanical testing equipment	87
3.2.4.	Geomechanical testing procedures	88
3.3.	Predicting creep behaviour using empirical and analytical models	91
3.3.1.	Empirical creep models.....	91
3.3.2.	Analytical models	92
3.3.3.	Measuring goodness of fit	95
3.4.	Results	96
3.4.1.	STXL test on dry sample 3991	96
3.4.2.	MSTXL creep test on dry sample 3992.....	98
3.4.3.	MSTXL creep tests on synthetic-brine saturated sample 3933.....	106
3.4.4.	MSTXL creep test on Na ₂ SiO ₃ -saturated sample 3994	115
3.5.	Discussion	125
3.6.	Conclusion	128
Chapter 4	130	
4.1	Introduction	132
4.2	Developing a leakage rate simulator	132
4.2.1	Potential leakage pathways	132
4.2.2	Methodology.....	133
4.3	Incorporating the creep behaviour of Beetaloo Sub-basin shale properties into the leakage simulator	141
4.4	Summary and conclusion	144
Chapter 5	145	
5.1	Introduction	146
5.2	Integrity failures of plugged and decommissioned wells	147
5.2.1	Methane emission measurements	148
5.3	Environmental contamination and adverse impacts	150
5.3.1	Air contamination	150
5.3.2	Soil contamination	150
5.3.3	Water contamination.....	151
5.4	Time-dependent barrier material retrogression and deterioration	151
5.4.1	Cement deterioration	152
5.4.2	Casing deterioration	153
5.5	Formation as barrier deterioration	153
5.6	Defining ‘long-term’	154
5.7	Summary and conclusion	154
References	155	
	Appendix I: Map of petroleum wells in the Northern Territory	166
	Appendix II: Creeping formation criteria.....	167
	Appendix III: Report on diffraction, mineralogy and geochemistry characterisation	168
	Appendix IV: Measuring exchangeable cations using NH ₄ ⁺ guidelines.....	181
	Appendix V: Calculating osmotic pressure	182

List of figures

<i>Figure 1: Section milling procedures involve removing a portion of the well casing to enable cement placement during plugging and decommissioning (van Oort, Thombare, Aldin & Lucas, 2022)</i>	9
<i>Figure 2: Shale formation fills up the annular space due to the creep phenomenon (van Oort et al., 2020)</i>	10
<i>Figure 3: Beetaloo Sub-basin boundaries are depicted by dashed lines (Crombez et al., 2022)</i>	11
<i>Figure 4: Stratigraphy of the Roper Group consisting of two sub-groups, Maiwok and Collara (Burgess, 2010)</i>	12
<i>Figure 5: Schematic north–south cross-section of the Beetaloo Sub-basin (Hall et al., 2020)</i>	13
<i>Figure 6: Completion schematic of the Shenandoah-1A well, illustrating the penetrated geological formations and their respective depths</i>	15
<i>Figure 7: The three stages of creep</i>	18
<i>Figure 8: Roadmap to verify the suitability of a shale formation as a barrier during decommissioning (Fedorova, 2021)</i>	20
<i>Figure 9: Stimulation techniques to activate shale and form a barrier in decommissioned wells: (a) pressure drop technique, (b) increasing temperature and (c) combining the incorporation of chemical solution along with increasing temperature. (Kristiansen et al., 2018)</i>	21
<i>Figure 10: (a) Evolution of creep strain with time when subjected to different stresses; (b) stable creep when subjected to σ_1 and unstable creep when subjected to σ_2 and σ_3 ($\sigma_1 < \sigma_2 < \sigma_3$) (Zhou et al., 2022)</i>	22
<i>Figure 11: (a) Pressure-pulse decay test setup; (b) top view of cylindrical shale sample with concentric casing (Thombare et al., 2020; Enayatpour et al., 2019)</i>	23
<i>Figure 12: Axisymmetric plane-strain problem setup, illustrating the relationship between radial displacement and strain in a borehole subjected to far-field stress and mud pressure, used for analysing borehole creep with various creep models. (Liu et al., 2011)</i>	39
<i>Figure 13: Maxwell creep model with spring and dashpot (Liu et al., 2011)</i>	41
<i>Figure 14: Kelvin creep model (Gupta & Mishra, 2017)</i>	42
<i>Figure 15: The four-element Burgers model (Li & Ghassemi, 2012)</i>	43
<i>Figure 16: Bingham visco-plastic model (Augustesen et al., 2004)</i>	44
<i>Figure 17: Schematic of the layered structures of key clay minerals: (a) kaolinite (1:1 structure), (b) smectite (2:1 structure) and (c) illite (2:1 structure) with less swelling, highlighting their different layer arrangements and interaction with water (Martín et al., 2022)</i>	54
<i>Figure 18: Core trays from Shenandoah-1A well in the Beetaloo Basin, stored in NTGS core library</i>	57
<i>Figure 19: Components of the MicroRX apparatus</i>	61
<i>Figure 20: A cross-section of the cylindrical specimen subjected to three modes of loading (Yan et al., 2014)</i>	64
<i>Figure 21: (a) Axial displacement vs time throughout the whole experiment at 32°C for a sample obtained from a depth of 2511 m; (b), (c) and (d) plots of axial displacements as a function of time throughout different stages of the mechanical and osmotic loading, along with the prior and posterior results</i>	70
<i>Figure 22: (a) Axial displacement vs time throughout the whole experiment at 32°C for a sample obtained from a depth of 2316 m; (b), (c) and (d) plots of axial displacements as a function of time throughout different stages of the mechanical and osmotic loading, along with the prior and posterior results</i>	71
<i>Figure 23: (a) Axial displacement vs time throughout the whole experiment at 32°C for a sample obtained from the depth of 1590 m; (b), (c) and (d) plots of axial displacements as a function of time throughout different stages of the mechanical and osmotic loading, along with the prior and posterior results</i>	73
<i>Figure 24: (a) Creep stages versus time; (b) creep rate variations as a function of time</i>	79
<i>Figure 25: Axial and longitudinal XRCT 2D slices obtained on core section Shenandoah-1A (depth 1591.42–1591.53 m)</i>	82
<i>Figure 26: Axial and longitudinal XRCT 2D slices obtained on core section Shenandoah-1A (depth 1592.23–1592.37 m)</i>	82
<i>Figure 27: Axial and longitudinal XRCT 2D slices obtained on core section Shenandoah-1A (depth 2512.40–2512.54 m)</i>	82
<i>Figure 28: Axial and longitudinal XRCT 2D slices obtained on core section Shenandoah-1A (depth 2513.25–2513.42 m)</i>	83
<i>Figure 29: Axial and longitudinal XRCT 2D slices obtained on core section Jamison-1 (depth 1025.75–1025.85 m)</i>	83
<i>Figure 30: Axial and longitudinal XRCT 2D slices (a) and a picture of sample 3991 before STXL testing (b)</i>	85
<i>Figure 32: Axial and longitudinal XRCT 2D slices (a) and a picture of sample 3993 before brine saturation and creep MSTXL testing (b)</i>	86
<i>Figure 31: Axial and longitudinal XRCT 2D slices (a) and a picture of sample 3992 before dry creep MSTXL testing (b)</i>	86

Figure 33: Axial and longitudinal XRCT 2D slices (a) and a picture of sample 3994 before sodium silicate solution saturation and creep MSTXL testing (b).....	87
Figure 34: Schematic of ATC installation and its cross-section	87
Figure 35: Schematic of the Kelvin–Voigt fractional-order derivative model	92
Figure 36: Schematic of the standard linear model	94
Figure 37: Schematic of the Burgers model	94
Figure 38: Stress–strain curves inferred from an STXL test on a dry sample (sample 3991).	96
Figure 39: Longitudinal XRCT 2D slices (a) and a picture of sample 3991 after the dry STXL test (b).....	97
Figure 40: Stress path employed for MSTXL creep test.....	98
Figure 41: (a) Axial, radial and volumetric strains obtained from the MSTXL creep test; (b) stress–strain relationship for sample 3992.....	99
Figure 42: (a) Differential stress–strain behaviour over time obtained from performing MSTXL creep tests; (b) differential stress–strain (including elastic and creep strain) behaviour over time for each stage	100
Figure 43: Evolution of total axial, elastic, and creep strain across each stage over time for sample 3992	101
Figure 44: Magnitudes of creep strain vs elastic strain, as well as the creep strain rate over time, for each stage of testing sample 3992.....	102
Figure 45: Comparative analysis of the fitted creep models and corresponding standard errors across multiple stages of the MSTXL creep test	106
Figure 47: Stress vs axial total strain measured during the MSTXL creep test on sample 3993	107
Figure 46: Stress path employed for the MSTXL creep test on sample 3993	107
Figure 48: (a) Differential stress–strain behaviour over time obtained from performing a MSTXL creep test on sample 3993 saturated with synthetic brine; (b) analysing differential stress–strain behaviour (including elastic and creep strain) over time for each stage.....	108
Figure 50: The magnitudes of creep strain (dark red), elastic strain (green) and creep strain rate (red) over time during each stage for sample 3993.....	109
Figure 49: The evolution of total axial, elastic and creep strain over time during each of the four stages for sample 3993	109
Figure 51: Comparative analysis of fitted creep models and corresponding standard errors across	114
multiple stages of the triaxial creep test on sample 3993	114
Figure 52: Stress path employed to investigate the response of sample 3994 saturated with Na_2SiO_3 to the MSTXL creep test	115
Figure 53: Stress–strain response of sample 3994, saturated with Na_2SiO_3 solution, to the MSTXL creep test	116
Figure 54: (a) Differential stress–strain behaviour over time in the MSTXL creep test on sample 3944; (b) analysing the differential stress–strain (including elastic and creep strain) behaviour over time for each stage	117
Figure 55: The evolution of total axial, elastic, and creep strain over time for each stage of testing sample 3994.....	118
Figure 56: The magnitudes of creep strain, elastic strain and creep strain rate over time for each stage of testing sample 3994.....	119
Figure 57: Comparisons of fitted creep models and their corresponding standard errors across multiple stages of the triaxial creep test on sample 3994.....	123
Figure 58: Comparing the stress–strain response of the shale samples to MSTXL creep tests under three conditions: dry and after saturation with the synthetic brine or Na_2SiO_3 solution	125
Figure 59: (a) Comparison of the axial strain and creep strain magnitudes of the three shale samples under MSTXL creep tests; the conditions are dry and after saturation with synthetic brine or Na_2SiO_3 solution	126
Figure 60: Conceptual leakage pathways (numbered 1–7) through degraded well barriers	132
Figure 61: An arbitrary well schematics used in the case study	139
Figure 63: The input parameters required for calculating leakage rate through the cement bulk, and the associated results	140
Figure 62: Potential leakage pathways at the marked portion of a plugged and decommissioned well	140
Figure 64: Potential leakage pathways at the interface of the casing and the rock formation (annulus).....	141
Figure 65: (a) The input parameters and (b) the associated results to calculate the formation creep strain and the corresponding leakage rate evolution	143
Figure 66: Schematic of a plugged well and its leakage pathways (P1–P7) (Nichol & Kariyawasam, 2000)	147
Figure 67: A visual representation of petroleum well sites in the Northern Territory	166
Figure 68: XRD pattern of micronised bulk, Ca-saturated Shenandoah-1A depth 2316.3 m sample (Co $\text{K}\alpha$ radiation) .	172
Figure 69: XRD pattern of the $<0.2 \mu\text{m}$ Ca-saturated fraction of Shenandoah-1A depth 2316.3 m sample (Co $\text{K}\alpha$ radiation)	172

Figure 70: XRD pattern of the 0.2 to 2 μm Ca-saturated fraction of Shenandoah-1A depth 2316.3 m sample (Co K α radiation)	173
Figure 72: XRD pattern of the <0.2 μm Ca-saturated fraction of Shenandoah-1A depth 2511 m sample (Co K α radiation)	174
Figure 73: XRD pattern of the 0.2 to 2 μm Ca-saturated fraction of Shenandoah-1A depth 2511 m sample (Co K α radiation)	175
Figure 74: XRD pattern of micronised bulk, Ca-saturated Kyalla 1591.5 m sample (Co K α radiation)	179
Figure 75: XRD pattern of the <0.2 μm Ca-saturated fraction of Kyalla 1591.5 m sample (Co K α radiation)	179
Figure 76: XRD pattern of the 0.2 to 2 μm Ca-saturated fraction of Kyalla 1591.5 m sample (Co K α radiation)	180

List of tables

Table 1: Shenandoah-1A well, the formation tops, their associated TVDRT* and true thickness measurements	16
Table 2: Mineralogy of Marcellus shale obtained from XRD studies (Gupta et al., 2017)	25
Table 3: Mineralogy and the mechanical properties of the four tested samples (Li & Ghassemi, 2012)	26
Table 4: Water content assessments of Campos Basin shale samples after 2 hours of air drying and after 2 and 4 weeks of immersion in oil, highlighting the redistribution of free, bound and crystalline water within the shale (Santos et al., 1996).....	27
Table 5: Mineralogical composition of Green River oil shale (Voltolini, 2020)	28
Table 6: Mineralogy and mechanical properties of Pierre shale and North Sea shales (field shales) (Bauer et al., 2019; Xie et al., 2020)	29
Table 7: Lark–Horda shale (North Sea) mineralogy (Enayatpour et al., 2019)	31
Table 8: Pore fluid compositions used in triaxial tests on Lark–Horda shale to evaluate the effects of sodium silicate and lithium silicate on shale creep and barrier development (Enayatpour et al., 2019)	32
Table 9: Summary of the experimental parameters of various studies mentioned in this literature review	34
Table 10: The mechanical components of the analytical model and their associated responses (Paraskevopoulou & Diederichs, 2013)	40
Table 11: Summary of the analytical models and their associated strain-vs-time and stress-vs-time behaviour (Paraskevopoulou & Diederichs, 2013; Augustesen et al., 2004)	45
Table 12: Clay mineral and their associated properties (Kim et al., 2020; Ahmed et al., 2019)	55
Table 13: Quantitative XRD analysis results (%wt) of the bulk, micronised and Ca-saturated samples.....	59
Table 14: Quantitative XRD analysis results (%wt) of <0.2 μm fractions of the samples (relative concentrations)	59
Table 15: Quantitative XRD analysis results (%wt) of 0.2 to 2 μm fractions of the samples (relative concentrations)....	59
Table 16: Chemical composition of samples as measured by XRF	60
Table 17: Exchangeable cations and CEC at pH 8.5 (oven-dried 60°C basis)	68
Table 18: Results for tests on materials derived from each core	72
Table 19: Core sections of Jamison-1 and Shenandoah-1A drill holes received from the NTGS library	80
Table 20: Measured chemical composition of brine equilibrated with shale powder	84
Table 21: Samples available for geomechanical and creep testing	84
Table 22: Mechanical properties of a sample of the Kyalla Formation as inferred from a dry STXL test at 82°C	97
Table 23: Fitted parameters from empirical models of dry shale	103
Table 24: Fitted parameters of empirical laws models for the shale sample saturated with the synthetic brine	111
Table 25: Fitted parameters of empirical law models for shale saturated with Na_2SiO_3 solution	124
Table 26: Summary of average published methane emission rates released from unplugged and plugged wells in the USA (Kang et al., 2014)	149
Table 27: Creeping formation criteria retrieved from NOROK-D10*	167
Table 28: Quantitative XRD analysis results (wt.%) of the bulk, micronised and Ca-saturated samples (relative concentrations).....	169
Table 29: Quantitative XRD analysis results (wt.%) of <0.2 μm fractions of the samples (relative concentrations)	170
Table 30: Quantitative XRD analysis results (wt.%) of 0.2 to 2 μm fractions of the samples (relative concentrations).	170
Table 31: <0.2 μm and 0.2–2 μm particle size fractions (wt.%) of the samples.....	170
Table 32: XRF results of bulk samples.....	171
Table 33: Exchangeable cations and CEC at pH 8.5 (oven-dried 60°C basis)	171
Table 34: Quantitative XRD analysis results (wt.%) of the bulk, micronised and Ca-saturated, <0.2 μm and 0.2 to 2 μm fractions of the sample (relative concentrations)	177
Table 35: <0.2 μm and 0.2 to 2 μm particle size fractions (wt.%) of the sample	177
Table 36: XRF results of the bulk sample	178
Table 37: Exchangeable cations and CEC at pH 8.5 (oven-dried 60°C basis)	178

Abbreviations

Abbreviation	Definition
ATCs	Autonomous triaxial cells
BPD	Barrels per day
Ca	Calcium
CIBP	Cast iron bridge plug
CEC	Cation exchange capacity
CBLs	Cement bond logs
CBL-VDL	Cement bond log–variable density log
FTIR	Fourier-transform infrared spectroscopy
Fm	Formation
H	Hydrogen
HCl	Hydrochloric acid
ICDD	International Centre for Diffraction Data
K	Potassium
KCl	Potassium chloride
Li	Lithium
LVDT	Linear variable differential transducer
mEq	Milliequivalent
Mg	Magnesium
MSTXL	Multi-stage triaxial
Na	Sodium
NaCl	Sodium chloride
NH ₄	ammonium
P&N	Plugged and abandoned
PQL	Practical quantification limit
STXL	Single-stage triaxial
SSA	Specific surface area
SST	Total sum of squares
Sst	Sandstone
stderr	Standard error of the residuals
TGA	Thermogravimetric analyser
TOC	Total organic carbon
TVDRT	True Vertical Depth referenced to Rotary Table
UCS	Unconfined/ Uniaxial compressive strength
WBE	Well barrier elements

XRCT	X-ray computed tomography
XRD	X-ray diffraction
XRF	X-ray fluorescence
XRPD	X-ray powder diffraction

Executive summary

The enhancement of natural shale barriers through creep mechanisms is intended to potentially complement the cement plugging and other decommissioning procedures outlined in the Northern Territory code of practice that are intended to prevent the movement of formation fluids in decommissioned petroleum wells. This report explores the potential for augmenting zonal isolation in decommissioned wells in the Beetaloo Sub-basin by leveraging the inherent capability of shale formations to creep, which could serve as an extra measure for preventing fugitive emissions and enhancing overall well integrity.

The study begins with a state-of-the-art review of creep mechanisms in chapter 1, emphasising the importance of shale mineralogy in promoting creep deformation. The review highlights that shale serves as a highly effective barrier material with an established track record in trapping formation fluids and acting as a barrier for oil and gas reservoirs for millions of years. The findings also suggest that mineralogy is a deterministic factor in the overall behaviour of shale and its creep deformation characteristics. Additionally, the report explores various stimulation techniques to enhance creep deformations in shales, providing a natural barrier and achieving complete zonal isolation.

In chapter 2, X-ray diffraction (XRD), X-ray fluorescence (XRF) and cation exchange capacity (CEC) studies were conducted to determine the mineral phases, composition and petrophysical properties of samples from the Velkerri and Kyalla formations, obtained from the Shenandoah-1A well in the Beetaloo Sub-basin. The results revealed that both the Velkerri and Kyalla formations are high in quartz content, contributing to their brittle behavior. Due to this high quartz content, stimulation techniques could play a critical role in enhancing creep and promoting long-term sealing capabilities, making these formations more suitable as barriers in decommissioned wells.

Additionally, CEC was measured for different cations, including calcium (Ca), magnesium (Mg), sodium (Na), potassium (K) and total CEC using ammonium (NH_4^+). CEC is an important parameter that indicates the shale's ability to exchange cations with surrounding fluids, influencing its reactivity. While higher CEC values suggest a greater potential for interaction with chemical solutions, these interactions may enhance creep deformation, depending on specific conditions. These include the type of chemical solution (e.g. brine, sodium silicate), shale mineralogy (particularly the type and content of clay minerals), temperature, pressure conditions and the duration of exposure. The fluid's pH and ionic strength also play a role, as more reactive fluids may alter the mineral structure of the shale. In some cases, these combined factors promote creep mechanisms, potentially contributing to the formation of effective natural barriers in decommissioned wells.

Chapter 3 explores the complex relationship between the time-dependent behaviour of shales and factors such as the magnitude and duration of applied stress, the chemistry of the surrounding environment, and the geomechanical properties of the shale, particularly in the context of decommissioning wells. It also examines how incorporating chemical solutions can induce creep deformation to establish barriers.

Focusing on the samples acquired from the Kyalla Formation from the Shenandoah-1A well, the study involved both experimental testing and subsequent data analyses to examine the creep behaviour and obtain constitutive parameters of creep models. Core samples from the Kyalla

Formation were subjected to geomechanical tests, including a single-stage triaxial (STXL) compression test and multi-stage triaxial (MSTXL) creep tests, under dry conditions as well as after saturation with a synthetic brine solution and a Na_2SiO_3 solution. These tests were conducted under in-situ temperature conditions (82°C).

The results showed that dry samples exhibited greater stiffness and brittleness, while samples treated (pre-saturated) with chemical solutions became more ductile, with decreased Young's modulus and enhanced creep deformation. This indicates that chemical solutions can significantly soften shale, making it more flexible and deformable, which is beneficial for inducing creep deformation and establishing effective barriers during well decommissioning. Chemical solutions reduce friction between shale grains and facilitate smoother sliding which facilitates deformation. Clay–fluid interactions lead to shale hydration, double-layer repulsion, mineral dissolution, mineral distortion, and rearrangement at both the grain and molecular levels.

To predict the long-term viscoelastic characteristics of shale gas reservoirs, the experimental data were fitted to various empirical creep models (parabolic, logarithmic, hyperbolic and crack-damage) and analytical or rheological models (Kelvin–Voigt, standard linear and Burgers). The parabolic and hyperbolic models demonstrated the best performance in capturing the creep deformation behaviours of the samples tested using the constitutive parameters obtained from curve fittings.

It is important to mention that the results presented in chapters 2 and 3 are constrained by the limited number of samples tested, which may impact the extent to which these findings can be generalised. The limited number of samples may not fully represent the behaviour of shale reservoirs in the Beetaloo Sub-basin. To address this limitation, similar experiments should be conducted on a greater number of core samples to examine the variability in shale properties and their impact on creep behaviour across the substantial thicknesses of the Velkerri and Kyalla shales, which extend over several hundred metres.

A leakage calculator was developed (chapter 4) to evaluate the potential risks and magnitudes of hydrocarbon fluid escape through potential leakage pathways from decommissioned wells. It considers potential pathways created along micro-annuli at the cement sheath interfaces with the casing and the formation, as well as within the cement sheath due to degradation and mechanical failure. This leakage calculator also integrates the empirical model that best fits the experimental outcomes to predict long-term shale creep behaviour. Specifically, the parabolic (power-law) model was incorporated to assess whether the annulus gap between the casing and shale formation would gradually close over time due to shale creep or remain open. This predictive capability is crucial for decision-making in well integrity studies, providing valuable insights into the long-term behaviour of shale and its interaction with the surrounding environment.

Understanding the adverse effects of contaminations on air, soil and groundwater is crucial. Additionally, the ageing and deterioration of well components over time are critical considerations. Chapter 5 explains the potential mechanisms for degradation of cement and casing due to exposure to downhole conditions and formation fluids. The efficacy of newly formed shale barriers may change based on variations in in-situ stress, highlighting the dynamic nature of well infrastructure.

Finally, the report addresses the complexities of ensuring long-term well integrity in chapter 5. Engineering challenges emerge in quantifying the maximum allowable leakage rate, necessitating

innovative solutions and a comprehensive understanding of the dynamic interplay between well components and the surrounding geological environment.

Preface

Decommissioned petroleum wells

Petroleum wells at the end of their serviceable life are subjected to decommissioning. This critical phase involves permanently sealing (cement plugging) the well and dismantling all surface infrastructure. The main objective of decommissioning is to ensure the permanent safety and environmental protection of the well site. This is achieved by securely sealing the well to prevent any future leakage of hydrocarbons or other substances to the surrounding environment. The choices and actions taken during these preceding stages play a crucial role in determining the long-term integrity of decommissioned wells. Proper decommissioning not only protects environmental and human health but also ensures regulatory compliance, thereby fostering the sustainable and responsible management of petroleum resources.

The development of natural shale barriers through creep mechanisms aims to provide an additional layer of protection that could supplement cement plugging and other decommissioning procedures outlined in the Northern Territory code of practice. These measures are designed to prevent the movement of formation fluids in decommissioned wells.

This report explores the potential for improving zonal isolation in decommissioned wells within the Beetaloo Sub-basin by leveraging the natural tendency of shale formations to creep, either naturally or through stimulation techniques. This capability could provide an extra barrier against fugitive emissions and enhance the overall integrity of the wells. This project aims to determine and characterize the creep behavior in the targeted formations in Beetaloo Sub-basin (Velkerri and Kyalla formations) while also exploring stimulation techniques through experiments on shale samples from the Shenandoah-1A well. It examines how changes in fluid chemistry can influence the shale's response, with the goal of artificially inducing creep behavior.

Creep behaviour of rocks

Creep is a time-dependent, inelastic deformation behaviour of rocks that can occur under saturated, sub-saturated or dry conditions. Unlike swelling, which is induced by the presence of water, creep occurs as a result of being subjected to constant mechanical stresses. This deformation mechanism involves mineral distortion, particle sliding and compression, and the shifting and redistribution of molecular bonds under continuous stress. In the context of maintaining the integrity of decommissioned petroleum wells, understanding creep is crucial as it can lead to the creation of natural barriers that seal gaps and voids around the wellbore, thereby enhancing the long-term integrity of these wells. By studying the creep tendencies of specific shale formations, such as the Velkerri and Kyalla formations in the Beetaloo Sub-basin, we can better predict their ability to act as an additional barrier, enhancing well integrity after decommissioning and contributing to environmental protection.

Shale as a well barrier

Recent studies suggest that shale formations can serve as natural barriers, improving the integrity of decommissioned wells. The natural creep deformation of these shales can fill up the annular spaces behind the casing, creating a low-permeability barrier that further limits fluid movement and enhances well integrity. Shales with high clay content and low levels of cementation materials (e.g. quartz and carbonates) are particularly prone to forming effective annular barriers that prevent fluid

migration and seal the wellbore. This makes the study of shale mineralogy and petrophysical properties essential for understanding their sealing potential. By analysing the mineralogical composition, particularly the presence of different clay minerals and cementation materials, we can better predict the behaviour of these formations. Chapter 2 assesses the shale mineralogy and petrophysical properties to provide a detailed understanding of the composition and behaviour of these formations.

Artificial stimulation of creep

Creep can be artificially stimulated through changes in applied stress, temperature and fluid chemistry. This study considers exposure to engineered fluids as a potential method for stimulating creep. Chapter 3 examines the creep behaviour of shale samples from the Beetaloo Sub-basin (sourced from the Shenandoah-1A well) through single- and multi-stage triaxial creep tests. Additionally, it explores the effects of chemical fluid saturation on these samples to evaluate the potential for inducing creep deformation through stimulation.

Geological setting of the Beetaloo Sub-basin

The Mesoproterozoic Velkerri and Kyalla formations within the Beetaloo Sub-basin encompass some of the oldest shale reservoirs in the world. They are targeted for unconventional gas exploration due to their appropriate lithologies, high organic carbon content and significant reservoir thickness. In this study the samples were selected for these two formations from Shenandoah-1A well.

Shenandoah-1A well

The Shenandoah-1 well, drilled in 2007 by PetroHunter Energy, reached a total depth of 1550 m and encountered hydrocarbon shows in the Hayfield Sandstone and the upper Kyalla Shale. In 2009, Falcon Oil & Gas deepened the well to 2714 m as Shenandoah-1A, observing several gas zones in the lower Kyalla Shale, Moroak Sandstone and Velkerri Shale. These gas zones comprise:

- gas shows in the lower Kyalla at a depth of 1500–1718 m
- a Moroak conventional gas play from 1717 to 2060 m, with the upper 88 m representing high permeability
- intermittent gas shows in the Moroak Sandstone to 2200 m
- a mid-Velkerri gas shale play from 2400 to 2558 m.

Chapter 1

Literature review of current scientific knowledge on shale creep behaviour

1.1 Introduction

The primary goals of cement plugging and well decommissioning operations are to prevent leakage of sub-surface fluids to the surface, avoid mixing of hydrocarbon and other fluids among different geological formations, limit pressure breakdown of shallow formations and prevent contamination of water-bearing zones (Liversidge et al., 2006; Huddleston-Holmes et al., 2017). However, a perceived risk exists if the integrity of the plugged and decommissioned wells is compromised, either at an individual or multiple-well barrier, leading to the creation of leakage pathways. At this point, a decommissioned well may turn into connectivity pathways for formation fluids, posing a potential risk to the environment (Ford et al., 2017). Such unintended vertical hydrocarbon movement could subsequently lead to contamination of overlying groundwater aquifers and the surrounding environment, potentially causing negative effects for groundwater users and subsurface microbial communities (Ford et al., 2017).

Plugging and decommissioning hydrocarbon exploration and production wells can be complex. It entails re-establishing natural barriers to the vertical movement of fluids along the well bore. Activities typically include the installation of cement plugs, confirming and where necessary re-establishing barriers behind casing and can extend to section milling (Lucas et al., 2018; van Oort et al., 2022a) (Figure 1), removal of casing strings to allow placement of formation to formation cement plugs (Huddleston-Holmes et al., 2017). It can be very costly to plug, decommission and establish barriers behind a casing as the processes are time-consuming and require specialised equipment,

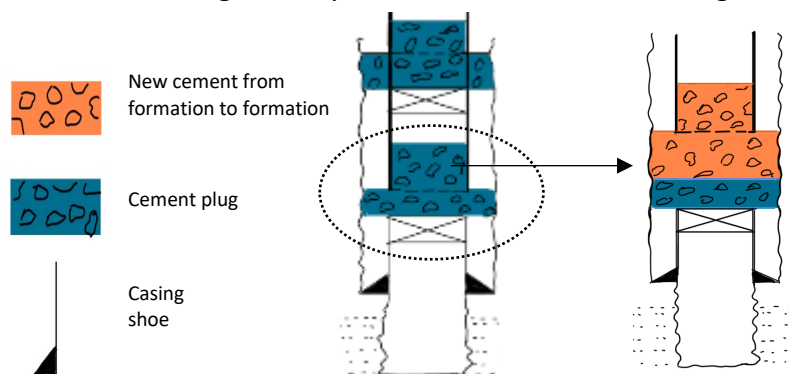


Figure 1: Section milling procedures involve removing a portion of the well casing to enable cement placement during plugging and decommissioning (van Oort, Thombare, Aldin & Lucas, 2022)

including a full drill rig (van Oort et al., 2020).

Recent studies, including field observations by van Oort et al. (2020), have demonstrated an alternative process in which specific geological formations, including mobile salt and shales, tend to creep into any uncemented annular space and form a permanent natural barrier against hydrocarbon fluid movements (Figure 2), consequently reducing the risk of contaminants entering the surrounding environment. The integrity of the newly formed barrier can be seen on sonic and ultrasonic bond logs and verified by performing pressure tests (van Oort et al., 2020). This method could potentially be considered a complementary approach, providing an additional layer of barrier integrity alongside the mandatory requirements outlined in the Northern Territory code of practice for plugging and decommissioning (Northern Territory Government., 2019).

Shale has traditionally served as a natural barrier to hydrocarbon migration, effectively trapping oil and gas in reservoirs for millions of years. Recently, there has been growing interest in using shale as a well barrier. Shale can be more effective than cement due to its low permeability and the healing properties of its clay minerals. Shale's ability to form effective well barriers is attributed to its creep behaviour, whereby the rock matrix gradually adjusts to stress over time through processes such as grain rotation, grain sliding and cracking. This deformation enables shales to encase the pipe and close the annulus, providing a robust seal. However, the effectiveness of shale as a barrier varies significantly, as different shales exhibit this behaviour to various extents (Dahi Taleghani & Santos, 2023; Kristiansen et al., 2021).

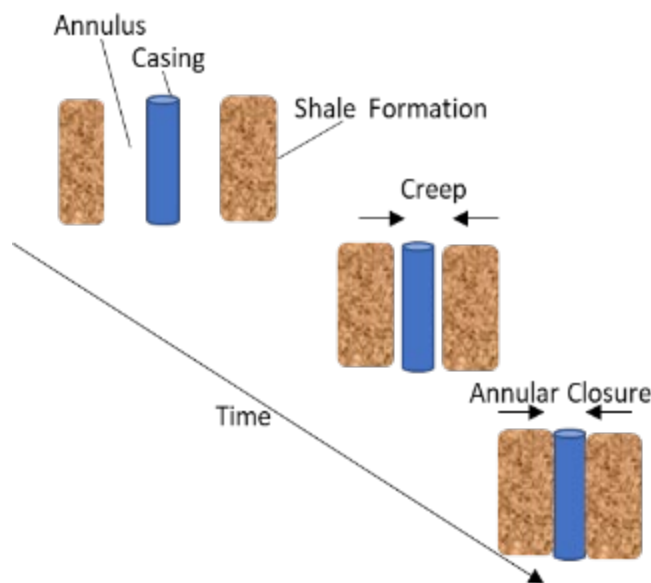


Figure 2: Shale formation fills up the annular space due to the creep phenomenon (van Oort et al., 2020)

This project focuses on enhancing understanding of how decommissioned wells in the Beetaloo Sub-basin maintain their long-term integrity, which is a critical concern for Northern Territory community groups, government regulators and industry stakeholders. The primary objective is to evaluate the self-sealing capability (creep behaviour) of shales within the Beetaloo Sub-basin, using samples acquired from the Shenandoah-1A well.

The Beetaloo Sub-basin, part of the larger Proterozoic McArthur Basin, is located approximately 500 km south-east of Darwin, as illustrated in Figure 3 (Landon, 2005). It is well-known for its substantial shale gas resources, primarily within the Mesoproterozoic Roper Group, considered a key area for shale gas exploration in Australia. Appendix I shows a map of petroleum wells in the Northern Territory.

Figure 4 illustrates the stratigraphy of the Roper Group, comprising the upper Maiwok and lower Collara subgroups (Gorter & Grey, 2012). The Maiwok subgroup comprises five formations: Kyalla Formation, Moroak Sandstone, Velkerri Formation, Bessie Creek Sandstone and Corcoran Formation. Two ungrouped, subsurface siliciclastic successions consisting of the informally named Jamison Sandstone and Hayfield Mudstone unconformably overlie the Kyalla Formation, Moroak Sandstone and Velkerri Formation variously and form the top of the McArthur Basin succession in the Beetaloo Sub-basin (Yang et al., 2018).

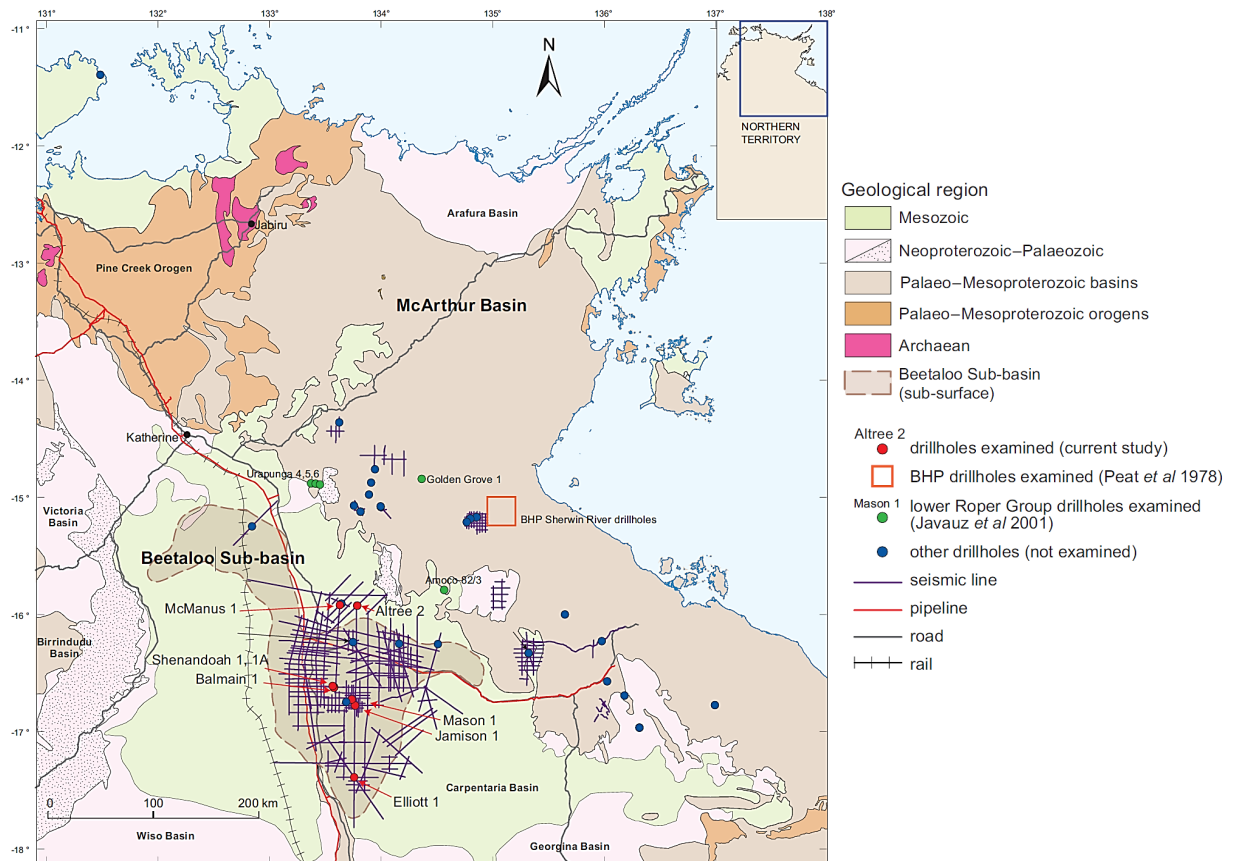


Figure 3: Beetaloo Sub-basin boundaries are depicted by dashed lines (Crombez et al., 2022)

In the Urupunga region, to the north of the Beetaloo Sub-basin, three different formations are recognised:

- the Sherwin Formation between Moroak Sandstone and the Kyalla Formation
- Bukalorkmi Sandstone, overlying the Kyalla and Chambers River formations, which caps the succession
- the undated Chambers River Formation, which may correlate with the ungrouped units at the top of the Beetaloo Sub-basin succession rather than being part of the Roper Group (Munson, 2016).

Roper group	Maiwok subgroup	Kyalla Fm
		Moroak Sst
		Velkerri Fm
		Bessie Creek Sst
		Corcoran Fm
		Hodgson Sst
	Collara subgroup	Jalboi Fm
		Arnold Sst
		Crawford Fm
		Mainoru Fm
		Limmen Sst
		Mantungula Fm

Figure 4: Stratigraphy of the Roper Group consisting of two sub-groups, Maiwok and Collara (Burgess, 2010)

Five different unconventional play types have been characterised within the Beetaloo Sub-basin:

- dry gas hosted in the Velkerri Formation shales
- liquids-rich gas hosted in the Velkerri Formation shales
- liquids-rich gas hosted in the Kyalla Formation shales
- the hybrid Kyalla Formation play (including tight sands adjacent to the organic-rich shale intervals)
- tight gas, condensate and potentially volatile oil within the Hayfield Sandstone member of the Hayfield Mudstone (Huddlestone-Holmes et al., 2020).

The Velkerri and Kyalla formations within this Mesoproterozoic sub-basin contain the world’s oldest shale plays (Faiz et al., 2024), which are rich in organic matter and have been identified as significant sources of hydrocarbons, showing considerable prospectivity in the Proterozoic sandstone reservoirs (H. Li et al., 2023). Figure 5 illustrates the stratigraphy of the north–south cross-sections of the Beetaloo sub-basin.

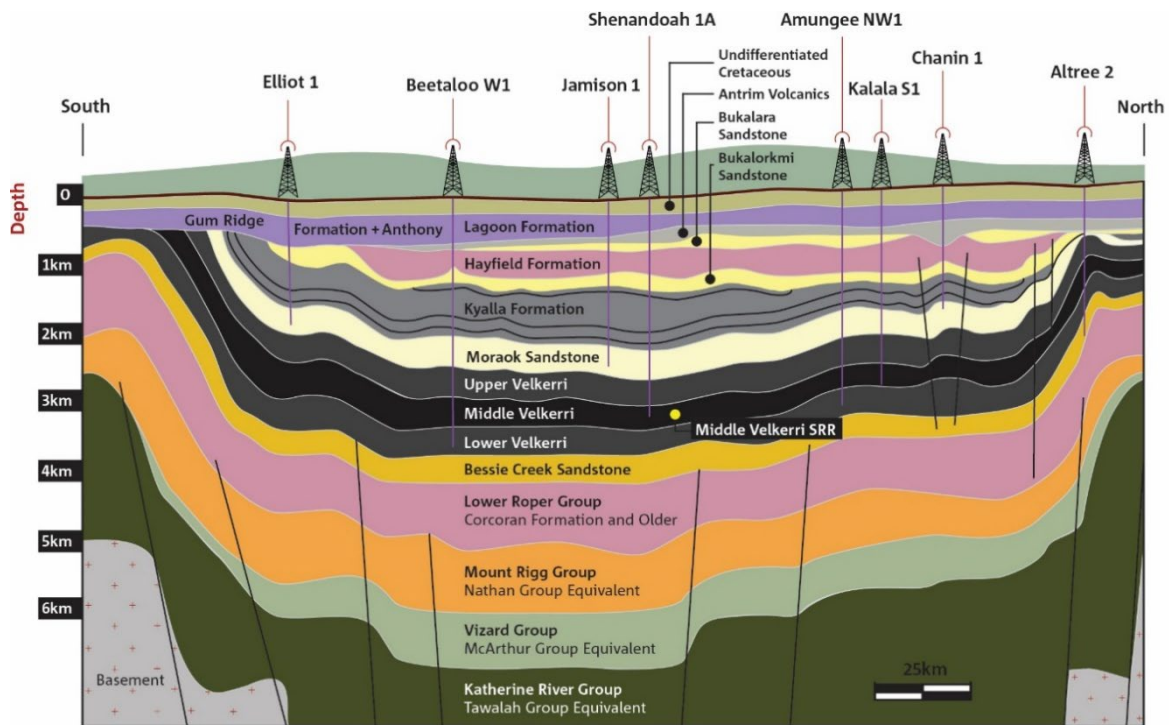


Figure 5: Schematic north–south cross-section of the Beetaloo Sub-basin (Hall et al., 2020)

Shenandoah-1A wellbore characteristics and downhole conditions

Shenandoah-1 is a key gas exploration well located in the Beetaloo Sub-basin that was drilled by Sweetpea Petroleum in September 2007. In 2009 it was deepened to 2714 m and re-entered as Shenandoah-1A by Falcon Oil & Gas Australia, involving additional testing and stimulation to assess its potential for gas production. The well is situated within Exploration Permit EP98 and was drilled to explore the gas potential of the Velkerri and Kyalla formations.

A schematic of Shenandoah-1A’s completion is illustrated in Figure 6. Originally drilled by PetroHunter Energy to a total depth of 1550 m, Shenandoah-1 encountered hydrocarbon shows in the Hayfield Sandstone at a depth of 780 m. This zone, along with substantial oil pay zones in the upper Kyalla Shale at depths of 943–1020 m, is considered highly prospective. Approximately 40 m of the upper Kyalla Shale is regarded as an oil pay zone following subsequent stimulation. The well’s location was chosen to penetrate the formations at their deepest points in the centre of the basin. Additionally, oil shows have been recorded in both the Hayfield Sandstone and the Upper Kyalla Formation (Silverman & Ahlbrandt, 2011).

After Falcon Oil & Gas deepened the well as Shenandoah-1A, several gas zones were observed in the lower Kyalla Shale, Moroak Sandstone and Velkerri Shale. These gas zones comprise:

- gas shows in the lower Kyalla at a depth of 1500–1718 m
- a Moroak conventional gas play from 1717 to 2060 m, with the upper 88 m representing high permeability

- intermittent gas shows in the Moroak sandstone to 2200 m
- a mid-Velkerri gas shale play, from 2400 to 2558 m (Silverman & Ahlbrandt, 2011).

Shenandoah-1A was plugged and abandoned (P&A) on 7 November 2011. Each tested interval was isolated with a cast iron bridge plug (CIBP). On top of the shallowest CIBP, a 15 m long cement plug was installed, followed by another 15 m long surface cement plug.

Figure 6 illustrates the plug and decommissioned status of Shenandoah-1A, showing the stratigraphic layers drilled through and the casing design used. The diagram displays key geological formations, starting from Tindall Limestone (Tindall LS), Antrim Volcanics, Bukalara, Hayfield, Jamison, Kyalla, Moroak, and Velkerri, as well as the total depth (TD) reached at 2701 meters Measured Depth Relative to Tool (MDRT). TD stands for Total Depth, which marks the final depth reached during drilling. MDRT stands for Measured Depth Relative to Tool, indicating the actual depth along the well path as measured by the tool.

Table 1 provides detailed information on the formation tops encountered in the Shenandoah-1A well, along with their corresponding True Vertical Depth referenced to Rotary Table (TVDRT) and true thickness measurements. The table highlights the significant zones of interest, such as the Lower Kyalla Formation and various Velkerri shale beds, which are critical for evaluating gas and oil potential within the Beetaloo Sub-basin (Geological & Report, n.d.).

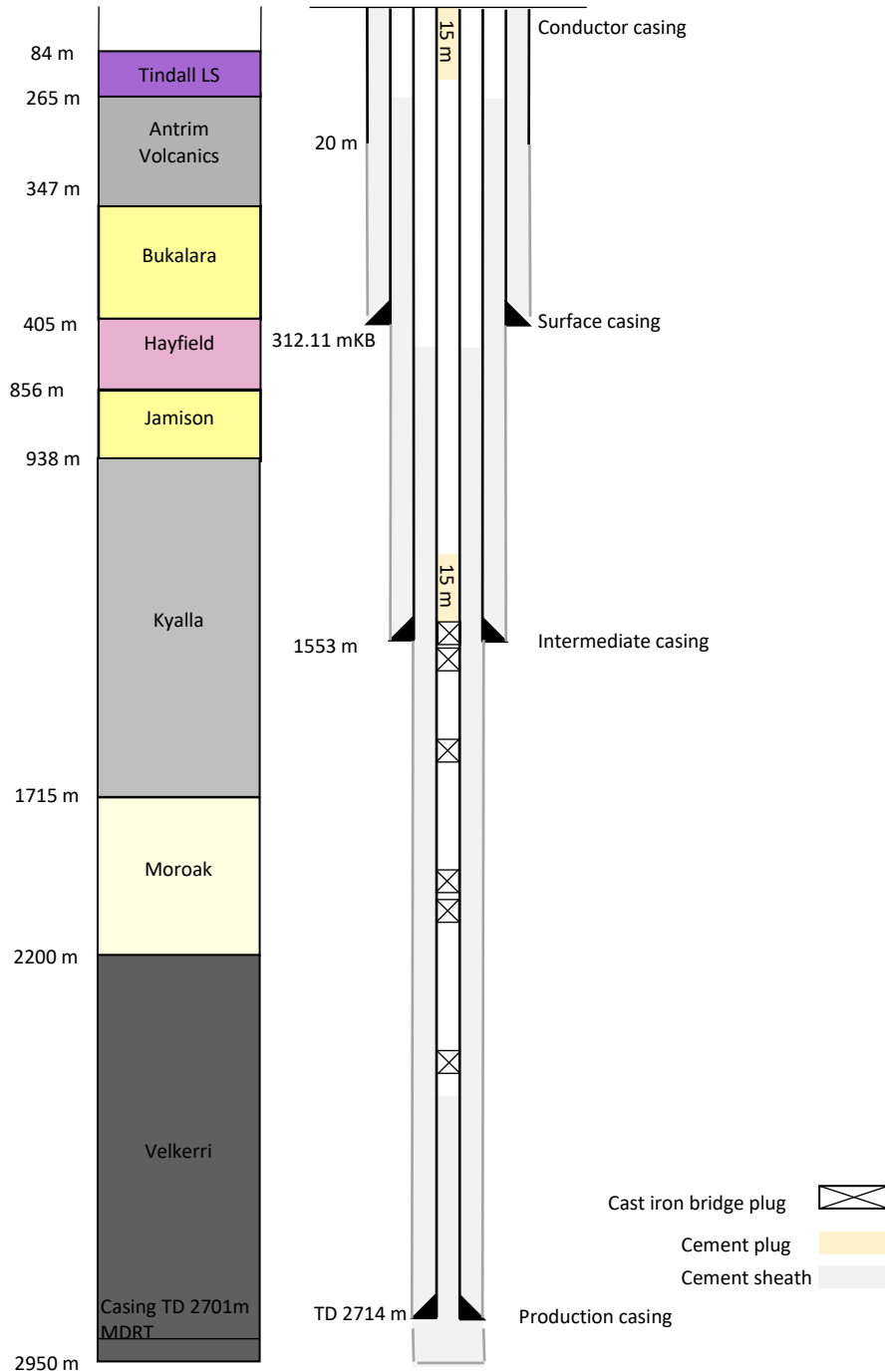


Figure 6: Completion schematic of the Shenandoah-1A well, illustrating the penetrated geological formations and their respective depths

Table 1: Shenandoah-1A well, the formation tops, their associated TVDRT* and true thickness measurements

Formation tops	TVDRT* (m)	True thickness (m)
Lower Kyalla Formation	1488.4	227.9
Moroak Sandstone	1716.3	482.9
Upper Velkerri Formation	2199.2	514.4
Velkerri 'A' Bed	2399.1	51.0
Lower Velkerri 'A' Bed	2450.1	N/A
Velkerri 'B' Bed	2469.1	33.0
Lower Velkerri 'B' Bed	2502.1	N/A
Velkerri 'C' Bed	Absent	N/A
Lower Velkerri Formation	2557.1	156.5 ⁺
Bessie Creek Sandstone	Not penetrated	
Total depth	2713.6	

⁺ Thickness is at least 156.5 m, but the full thickness might not be completely determined within the scope of the given data

* TVDRT stands for true vertical depth relative to rotary table

1.1.1 Creep mechanism

Shales, sometimes called mudstones, largely consist of silicate or aluminosilicates – including quartz, feldspars and clay minerals – as well as carbonates such as calcite, dolomite and other minor accessory minerals such as pyrite. The clay content in the shale matrix is important in terms of its reactivity with water-based fluids. For example, shales with high smectite content react more to water than those with higher illite content (Boul et al., 2017).

Creep in shales is effectively a time-dependent and viscoelasto-plastic behaviour deformation mechanism due to mineral distortion under stress. In addition, creep can occur in saturated and dry rocks in which strain occurs due to imposed long-term stresses and viscoelastic behaviour in the solid matrix to the point where failure eventually occurs (Cerasi et al., 2017). The creep process is similar to the swelling of a material; however, swelling happens only in the presence of water, while creep can occur with or without water. The strain rate and magnitudes depend on the material properties, the surrounding temperature, exposure time and the applied pressure.

Fracture closure in a shale reservoir can also be attributed to viscous flow or creep, which depends on the elastic, plastic and viscous properties of the shale. Elastic closure happens once the reservoir is depleted, and the net effective minimum horizontal stress rapidly increases; however, strains in the elastic stage are usually small and not enough to seal the wellbore annulus. These early stages of fracture closure are controlled by the elastic property of the shale formation, with creep playing a major role in the later stages of fracture closure (Li & Ghassemi, 2012).

The creep rate depends on several factors, including rearrangement of the shale microfabric, the sliding and compression of particles, delayed water movements (which transfer and aggregate shale

macro-pores), readjusting of molecular bonds, the flow of adsorbed water in double layers of clay particles, and viscous adjustment of the clay structure (Feng et al., 2016).

The Norwegian Shelf's Competitive Position (NORSOK) (Poole, 2021) standards have recognised shales as acceptable well barriers for decommissioning activities (van Oort et al., 2020). The acceptance criteria for using shale as a well barrier are detailed in Table 27 (Appendix II). This table outlines the functional requirements and performance characteristics that shale must meet, such as low permeability and self-sealing properties through creep, ensuring long-term integrity and sealing capability of the wellbore. Shale barriers are verified using industry-standard methods such as pressure testing and bond logging, similar to cement barriers.

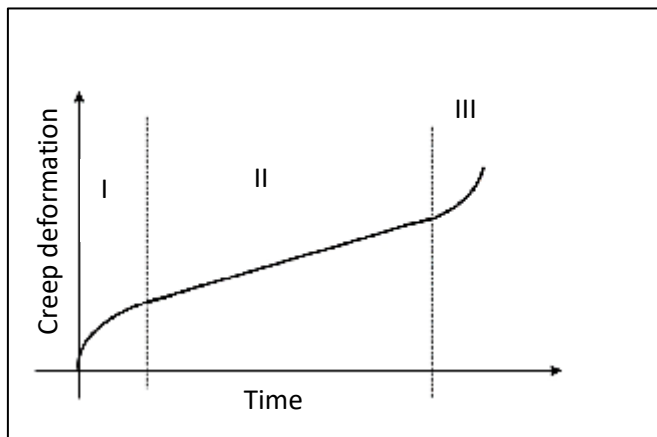
Furthermore, the UK Oil and Gas Guidelines for well decommissioning (OEUK, 2022) also acknowledge the use of natural barriers, including shales. These guidelines emphasise the importance of ensuring that barriers provide a long-term seal to prevent any uncontrolled release of hydrocarbons. The guidelines detail the procedures for verifying the integrity of these barriers, including monitoring and testing protocols to confirm their effectiveness over time.

It is worth noting that NORSOK standards, developed by the Norwegian petroleum industry, ensure safe and efficient operations in the oil and gas sector. These standards are globally recognised for their stringent requirements. Acceptance by NORSOK indicates that shale meets high industry standards for well barriers, providing assurance of its low permeability, ductility, chemical resistance, and bonding capability to steel, which are crucial for maintaining long-term well integrity. This endorsement signifies the effectiveness and reliability of shales in providing zonal isolation and preventing the movement of formation fluids. In other words, shales that are suitable for using creep to fill the annular space of a well and act as an effective well barrier, as illustrated in Figure 2, should possess the following characteristics: low strength and high ductility (evident by low values of Young's modulus, cohesion, friction and dilation angle), high clay content (particularly smectite), minimal quartz and carbonate cementation, moderately high porosity and low compressional wave velocity (Kristiansen et al., 2018).

However, there might be potential risks associated with using shales as barriers in oil and gas wells, including (van Oort et al., 2022):

- creep deformation leading to casing ovalisation and adversely affecting casing connections
- if stimulations were performed by pressure shock (see section 1.2), a small amount of solids or gels from the mud may remain in the annulus due to the thixotropic properties of the mud
- implementing pressure shock or dropping the pressure as a stimulation technique may cause well-control issues (Kristiansen et al., 2021).

Creep deformation can be divided into three stages (Figure 7) (Ozan et al., 2018):



- I: Primary/transient creep
- II: Secondary/steady state creep
- III: Tertiary/accelerating creep

Figure 7: The three stages of creep

- a) primary/transient creep – this stage initially includes large deformations at an accelerated creep rate before levelling out to a relatively constant creep rate
- b) secondary/steady-state creep – this is the strain-hardening phase, the slowest creep rate in which deformation increases at a slow and constant rate; deformation within this phase is irreversible and classified as plastic deformation
- c) tertiary/accelerating creep – in the third stage, the deformations increase exponentially, and unstable cracks propagate, resulting in material failure (Fredagsvik, 2017).

1.1.2 Shale barrier validation using logging techniques, with the aim of qualifying a formed barrier

Determining the state of the bond between the wellbore components is an important step in the decommissioning stage of oil and gas wells. The integrity of the interfaces between the barrier elements (i.e. cement plugs, cement sheath or shale as the barrier with the casing) is critical to providing complete isolation in a decommissioned well.

Impermeable shales, which may be considered barriers due to their creep, can be identified by gamma-ray logs, electrical logs and cuttings description logs. For shale to act as an annular barrier it should cover an adequate length and depth of the well, and the rock deformation mechanisms must meet all the aforementioned criteria (section 1.1) (Austbø, 2016). Logging technologies – including cement bond logs (CBLs), ultrasonic imaging logs and pressure testing – are typically employed to investigate the condition of the bond and verify the state of the barriers (Zhang et al., 2019).

According to NORSOK regulations, verification of shale acting as an annular barrier should be performed by bond logs as follows (Lavery et al., 2019):

- Two independent logging measurements/tools should be employed to provide azimuthal data.
- Staff with competent skills and knowledge in interpreting logging data should verify and document the data.
- Prior to logging operations, the log response criteria should be determined.
- A minimum contact length of 50 m with 360° of qualified bonding should be established between the shale interval and the wellbore.

Fedorova (2021) designed a roadmap/algorithm (Figure 8) as a protocol to assess the suitability of a shale formation as a barrier. According to this roadmap, two independent logging runs should be carried out regardless of the cause of creep occurrence within the shale formation (whether it happened naturally or via stimulation). The first is to run a cement bond log–variable density log (CBL-VDL) and evaluate the obtained CBL amplitude and bond index, followed by a second independent bond logging (e.g. an ultrasonic logging tool). It is important that the outcomes of these independent logs complement each other and be consistent. The length of the created barrier should meet the criteria defined by the local regulations. If the bond logging is convincing, and pressure testing hasn't yet been performed on the target shale formation, supplementary pressure testing is required. Thus, the barrier can be verified only if the results of the previous tests are positive.

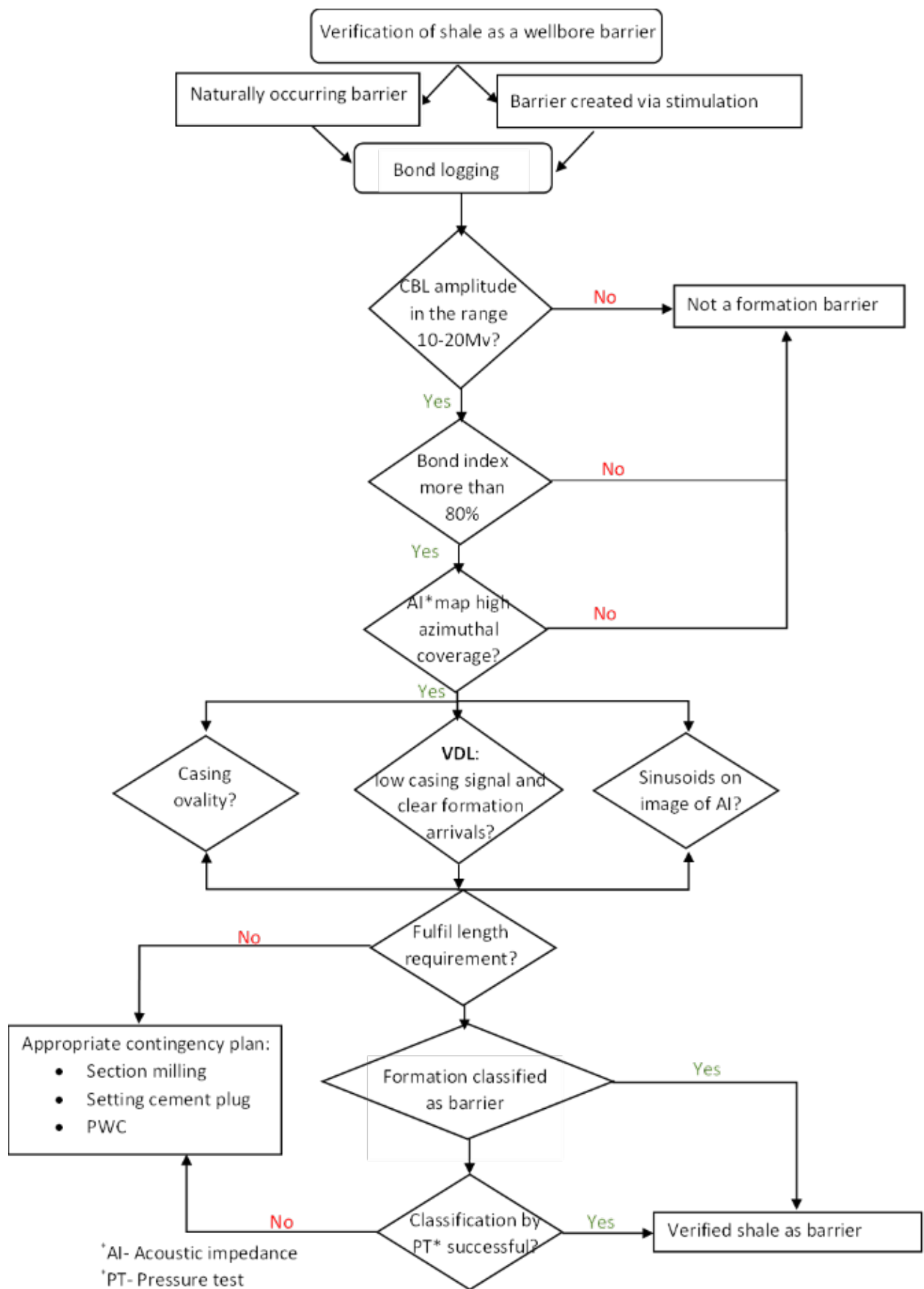


Figure 8: Roadmap to verify the suitability of a shale formation as a barrier during decommissioning (Fedorova, 2021)

1.2 Techniques and approaches to stimulate and activate shale in decommissioned wells

Stimulation and activation of shale formations that haven't yet contacted the casing can be created via the following techniques (Kristiansen et al., 2018):

- decreasing the annulus pressure rapidly (Figure 9a)
- increasing the shale temperature (Figure 9b)
- changing the chemistry of the annular fluid either as a standalone practice or in combination with increasing the shale rock temperature (Figure 9c).

Dropping the pressure or 'pressure shock' (van Oort et al., 2022) can be carried out by perforating

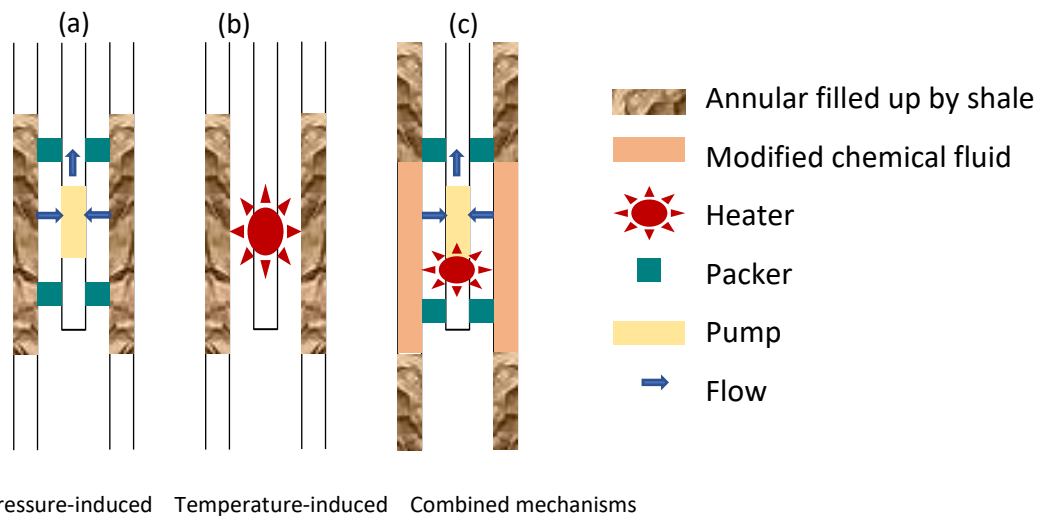


Figure 9: Stimulation techniques to activate shale and form a barrier in decommissioned wells: (a) pressure drop technique, (b) increasing temperature and (c) combining the incorporation of chemical solution along with increasing temperature. (Kristiansen et al., 2018)

the casing at spots where no annular cement is present. Then the shale formation is subjected to a pressure drop either by lowering the hydrostatic head or using a pump along with isolation packers (van Oort et al., 2022). Increasing the shale temperature also leads to an increase in creep deformation. Thermal stimulation of the shale can be done by employing a downhole heater.

However, activating the shale by increasing the temperature or decreasing the pressure (by reducing the hydrostatic head in the wellbore) can raise more practical challenges. For example, in the field, heating a long shale section through the casing might be challenging. Reducing the wellbore pressure, particularly when no barrier exists, may cause wellbore control issues (van Oort et al., 2020). Since rock formation temperature and pore pressure collectively determine the stress state in porous media, any imposed thermal stress will impact the stress distribution in the vicinity of the wellbore and could potentially cause borehole instability (Yan et al., 2014). In particular, during the injection of high-temperature fluid, thermal diffusion imposes pore pressure variations and reduces formation strength. In addition, thermal diffusion in shales takes place more rapidly than does hydraulic diffusion; this means that pore pressure variations and subsequent stress redistributions may occur very quickly (Chen et al., 2003). Thus, increasing the downhole temperature to more than 200°C requires thorough investigation to evaluate the imposed

compressive strength on the casing in addition to potential damage to the rock formation (van Oort et al., 2022).

Another approach to activating the shale is to incorporate chemicals into the annular fluid, which can be done as a standalone method or accompanied by increasing temperature. A combination of methods is used when it is difficult to stimulate the shale by one method alone (Kristiansen et al., 2018). The effectiveness is a matter of controversy. Kristiansen et al. (2018) studied different fields in which various implementations of chemical loading were made by changing the chemistry of the annular fluids using water-based fluids. They concluded that this method is less successful compared with thermal stimulation and pressure shock loading. However, van Oort et al. (2020) noted that by combining temperature increases and changing the chemistry of the annular fluid, they succeeded in greatly increasing the rate of creep deformation. The details of both studies, including the shale mineralogy, experiment type, chemicals and outcomes, are discussed in following sections.

1.3 Theoretical and experimental lab investigations

The magnitude of shale creep depends on, but is not limited to, the shale's mineralogy, temperature, pressure and environmental chemistry. The mineralogy of a shale formation, specifically its clay content, determines whether the formation can act as a barrier (if so, the clay content needs to be greater than 40%). The magnitude of creep is also influenced by the amounts of smectite (which acts as a bonding agent), quartz, illite, kaolinite and chlorite. Smectitic clays usually swell more, are less stiff and show more ductility than other clay minerals. Creep accelerates as the applied stress and temperature increase. It is therefore important to identify the original stress and pore pressure state in situ, the imposed differential stresses from drilling to abandonment, and the yield stress and failure stress of the formation. The closer the stress state is to failure; the more creep will be observed.

Creep tests on samples are useful for characterising the creep rate, determining different creep stages and identifying the threshold stress for various creep behaviours. The shape of the creep

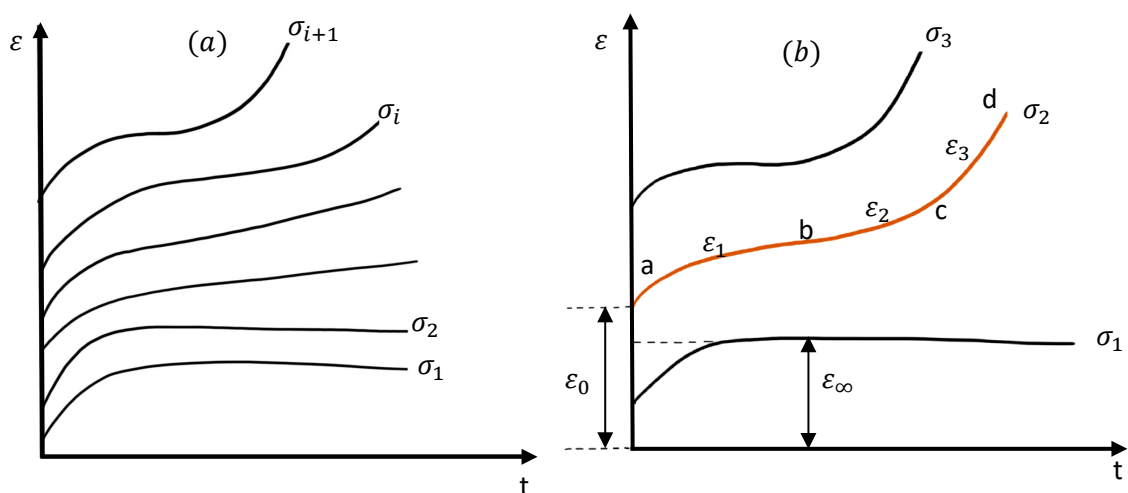


Figure 10: (a) Evolution of creep strain with time when subjected to different stresses; (b) stable creep when subjected to σ_1 and unstable creep when subjected to σ_2 and σ_3 ($\sigma_1 < \sigma_2 < \sigma_3$) (Zhou et al., 2022)

curve alters with increasing loading stresses. Figure 10a illustrates a shale sample subjected to different loading stresses where $\sigma_1 < \sigma_2 < \dots < \sigma_{i+1}$. Figure 10b illustrates the relationship between stress levels and creep strain over time, showcasing three representative creep curves where $\sigma_1 < \sigma_2 < \sigma_3$. At the lower stress level (σ_1), the creep strain initially increases but eventually stabilises, indicating a state of stable creep. As stress levels rise to σ_2 and σ_3 , the creep strain does not stabilise and continues to grow, leading to unstable creep and potential rock failure. This transition from stable to unstable creep behaviour is critical for understanding the material's response under different stress conditions. It highlights how increasing stress can accelerate deformation, which is essential for accurately predicting long-term material performance under varying conditions. The curve for σ_2 provides a comprehensive view of both stable and unstable creep phases, offering key insights into the complete creep behaviour of the material (Zhou et al., 2021).

The mechanical properties of shale rocks, including their compressive strength and elastic moduli, are controlled by the mineralogical composition of the shale and its porosity, water content, pressure and temperature. Shales are typically transversely isotropic materials, so their strength and elastic properties differ when loaded parallel to, normal to or at angles to their bedding planes (Rybacki et al., 2015).

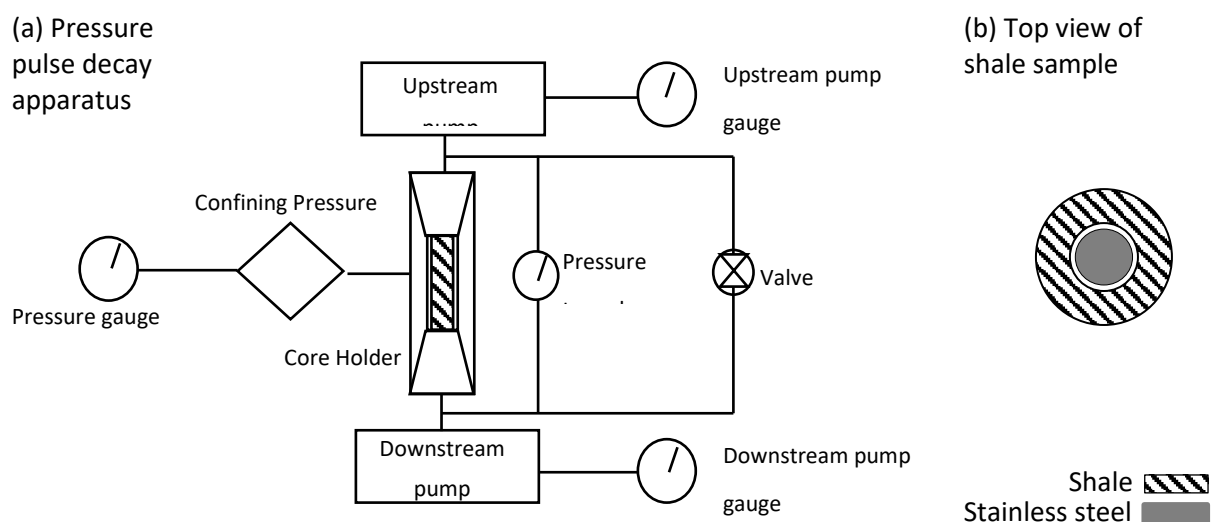


Figure 11: (a) Pressure-pulse decay test setup; (b) top view of cylindrical shale sample with concentric casing (Thombare et al., 2020; Enayatpour et al., 2019)

To characterise a given shale's behaviour, and confirm its ability to act as a barrier, experiments such as creep tests, pressure-pulse decay tests and pressure-breakthrough/leak-off tests are useful. For example, a pressure-pulse decay experiment can characterise the permeability of the annular shale barrier. It can determine whether the shale specimen forms an effective barrier or if the annulus remains open or is only partially closed.

The experimental setup (Figure 11a) consists of two upstream and downstream fluid pumps connected to a core holder containing a hollow cylindrical sample of shale. To simulate the borehole steel casing, a stainless steel rod is mounted at the centre of the sample, creating an initial annular gap between the shale and the rod (Figure 11b) (Thombare et al., 2020). A pressure pulse (a sudden

increase in pressure) is periodically imposed at the top of the shale sample (the upstream side), and the pressure response on the downstream side is simultaneously monitored.

An immediate downstream pressure response indicates that fluid has flowed freely down the annular gap between the shale and the rod (i.e. pressure communication is unconstrained), meaning that the annular gap is open. On the other hand, a delayed response to the pressure change – fluid diffuses and pressure reaches an equilibrium on the downstream side – indicates that creep of the shale has fully (or partially) closed the annular gap. Sometimes, when restoring pressure on the upstream and downstream sides to its original value, an accelerated creep rate can also be observed, and this indicates that the creep rate of the shale being tested might be capable of being enhanced via variation of the annular fluid pressure (Thombare et al., 2020; Enayatpour et al., 2019).

To determine different shale characteristics and failure modes, Holt et al. (2019) performed a series of experiments on consolidated, undrained triaxial hollow samples of shale. They investigated the development of the barrier and its associated sealing capabilities. Their triaxial tests demonstrated that the shales showed both normal consolidation (ductile behaviour) and over-consolidation (brittle behaviour). These experiments allowed them to see how, as pore pressure increased, failure initiated through various failure modes.

They found that, in normally consolidated shales, there was ductility and distributed failure at the time of failure. In contrast, they found that pore pressure was reduced in over-consolidated shales, resulting in more localised failure (Holt et al., 2019). In addition, after heating samples to 110°C, porosity was determined via water loss tests. Clay content was calculated from XRD analyses prior to geomechanical testing. Their observations on four soft shales showed that the shale samples with the best potential sealing capabilities had higher porosity, higher clay content, lower uniaxial compressive strength (UCS), lower friction angle and lower P-wave velocity (Holt et al., 2019).

In this report, the inclusion of various examples of testing on different shales from across the globe is crucial for understanding the diverse behaviours exhibited by shale under different conditions. Shales, being highly heterogeneous sedimentary rocks, can exhibit significantly varied mechanical properties depending on their mineral composition and clay content, and the geological conditions under which they were formed. By comparing the creep behaviour of shales with different properties, such as those with varying clay content or organic matter, we can gain valuable insight into how these factors influence the rock's response to stress over time.

Gupta et al. (2017) performed uniaxial and triaxial compression tests (complying with ASTM standard D7012) on Marcellus shales with very low clay content (Table 2). Shale samples were extracted from an outcrop of the Marcellus formation near Allentown, Pennsylvania, USA. Their aim was to determine the yielding point of the shale through creep tests. Cylindrical samples, 105 mm long and 53 mm in diameter, were subjected to triaxial creep testing up to 80% of their strength and under different confining pressures until tertiary creep commenced. Specimens were wrapped in plastic during transport to avoid moisture movement and alteration of their microstructure. Due to the high amount of calcite and quartz and the low amount of clay, the samples showed brittle behaviour with high compressive strength.

Table 2: Mineralogy of Marcellus shale obtained from XRD studies (Gupta et al., 2017)

Shale	Calcite %	Illite %	Quartz %	Pyrites %	Clay %
Marcellus	75.14	12.94	8.74	3.18	*

*Not provided in the paper.

Uniaxial and triaxial compression tests led to the following observations:

- the response of parallel specimens was stiffer than perpendicular ones
- the magnitudes of the yield stress, failure stress and residual strength increased as confining pressure increased
- the dilation angle (described by equation (4), in section 1.3.3) for all specimens reduced as confining pressure increased.

The outcomes of the triaxial creep tests on parallel specimens illustrate the important role of confining pressure and axial strain rate, with the time taken to reach the tertiary creep stage increasing as the confining pressure and axial stress increased. Some of their triaxial creep tests on perpendicular specimens could not be finished because of pre-existing damage within the samples; this highlights the importance of proper preservation of the samples and checking for existing damage or fractures before testing.

Performing multi-stage creep tests at various differential stresses and confining pressures has also been suggested by Li and Ghassemi (2012). To acquire creep parameters at different stress-state conditions, they employed a stepwise loading path on Barnett, Haynesville and Marcellus shales. They showed that creep strain can be described by a power-law function of time. As shown in Table 3, the shale samples were remarkably different in terms of clay and carbonate content. All the samples were drilled perpendicular to their bedding plane and kept under room conditions. The experiments (uniaxial and MSTXL creep tests) were run under dry and drained conditions at room temperature.

According to the outcomes, Young's modulus (E), which generally correlates with shale mineralogy and clay content, is a strong factor in the viscoelastic behaviour of the samples. As can be seen in Table 3, Barnett has a higher Young's modulus and lower clay content than Haynesville. The MSTXL tests (with both shales subjected to the same loading path; a confining pressure of 16 MPa and a deviator stress of 63 MPa) showed that the stiffer shale (Barnett) had less creep. Creep strains of 0.04 and 0.01 were achieved for Haynesville and Barnett, respectively.

Table 3: Mineralogy and the mechanical properties of the four tested samples (Li & Ghassemi, 2012)

Shale	QFP %	Carbonate %	Clay %	Others %	E (GPa)
Marcellus	28	9	40	24	*
Barnett	60	10	25	5	27.8
Haynesville (sample 21)	25	23	33	18	14.5
Haynesville (sample 22)	25	23	33	18	17.6

QFP = quartz, feldspar, plagioclase and pyrite component

*Not provided in the paper.

The rest of the outcomes demonstrated that:

- shales with less clay content and more cement were stiffer and had higher elastic moduli
- the creep rate in second phase 2 (steady-steady state) increased linearly with deviator stress
- applying higher confining pressures leads to a larger creep strain under the same deviator stress.

1.3.1. Effect of water content on shale mechanical properties

Clay-rich sedimentary rocks, including shales, have low permeability because pore spaces in the rock are very narrow (diameter in the range of nanometres). The interaction between water molecules and mineral surfaces in clays, together with the presence of these narrow pores, make these types of rock extremely water-sensitive (Holt & Kolstø, 2017). In other words, the propensity for shale to deform and accommodate water molecules as free water, bound water and crystalline water controls the shale's reactivity with water.

Bound water is defined electrochemically as water within a clay matrix or near a pore surface bound within an electrical double layer (Wang et al., 2020), and plays a major role in the static and mechanical properties of shales (Horsrud et al., 1998). In comparison, free water is present within the shale pore space and among the grains, and has a lesser impact on how shale interacts with different fluids (Lal, 1999). Crystalline water/crystal water is present inside or among clay crystals; variations in crystalline water impose variations in clay structure and can be a sign of structural damage within a shale (Lavery et al., 2019; Fedorova, 2021).

Santos (1997) presented a method of determining shale water content using a thermogravimetric analyser (TGA). The TGA determines free water, bound water and crystalline water by accurately measuring the weight loss of a specimen as a function of time and temperature (up to 800°C). The key benefit of the TGA is that weight loss can be measured at different locations in a sample as it only requires 20–80 g of sample (powdered shale is preferable).

At first, the sample is kept at room temperature (22°C) for 16 h so that it doesn't lose any weight. Then the temperature is increased at a rate of 2°C/min up to 110°C and kept constant for 3 h, allowing free water to escape the sample. The same procedure is repeated until the temperature reaches 250°C and it is kept there for another 3 h, allowing bound water to escape. Finally, the rate of temperature increase is reduced to 0.1°C/min until a final temperature of 800°C is reached, when

crystalline water escapes (although at this high temperature some gases may also be released). For instance, for shales containing calcite, at temperatures of 700–750°C CO₂ may also escape (Santos, 1997).

Santos et al. (1996) conducted laboratory experiments using a TGA to assess the impact of water content on the Campos Basin shale (offshore from Brazil), measuring shale reactivity as the key parameter. It is worth mentioning that TGA requires well-preserved samples. This particular shale was selected due to its mineralogy: a high amount of calcite (>50%) and a low amount of illite/smectite (<10%), typical of low-reactivity shale. Three samples were acquired from a preserved core to assess the water redistribution via immersion tests. The samples were air-dried for 2 h, with one sample being immersed in deionised water; the other two samples were immersed in mineral oil for different durations to prevent drying out and to facilitate water redistribution. Table 4 shows the results of the tests at different periods.

Table 4: Water content assessments of Campos Basin shale samples after 2 hours of air drying and after 2 and 4 weeks of immersion in oil, highlighting the redistribution of free, bound and crystalline water within the shale (Santos et al., 1996)

Description	Free water	Bound water	Crystalline water
Original water content	7.08	0.81	17.88
After 2 h of drying in air	4.21	1.01	18.5
After 2 weeks of immersion in oil	6.70	2.16	18.25
After 4 weeks of immersion in oil	6.11	1.21	18.15

As shown in Table 4, water redistribution in the samples immersed in oil was observed even after a short period, with free water being lost. This loss of free water also leads to changes in bound water. However, the crystalline water remains relatively unchanged throughout the experiment. Water content significantly impacts the behaviour of shale, especially in shales with high clay mineral content. An increase in water content can reduce strength and stiffness due to capillary and osmotic suction, resulting in more swelling and greater deformations (Vergara & Triantafyllidis, 2016).

1.3.2. Effect of loading rate on shale mechanical properties

Mahanta et al. (2018) estimated the effect of strain rates during loading of dry Jhiri shale samples, as well as their geomechanical properties, including UCS, tensile strength (σ_t), Young's modulus (E), failure strain (ϵ_f), mode I and mode II fracture toughness (K_{IC} and K_{IIC}), and brittleness index (B_1 and B_2). The samples were obtained from the Damoh district in Madhya Pradesh, India. The obtained stress–strain behaviour under four different strain rates (varying from 1.7×10^{-2} to $7.9 \times 10^{-5} \text{ s}^{-1}$) showed that all the aforementioned mechanical parameters, excluding failure strain, exhibited an apparent increase with higher strain rates. This response of the shale was attributed to stress redistribution during grain fracturing.

Uniaxial compression tests with a range of strain rates on Longmaxi shale specimens were performed by He et al. (2022). The shale samples were sourced from the fossil-rich Longmaxi Formation, which is part of the Silurian group located in Chongqing, China. The Longmaxi Shale

Formation is distributed extensively across almost all regions of the Sichuan Basin, with the exception of the north-west, covering parts of eastern Sichuan Province and Chongqing. They considered different bedding orientations to investigate the effect of strain rate on the anisotropic mechanical behaviour of the shale.

The unconfined compression tests were performed under three different strain rates: 10^{-2} s^{-1} (considered a static loading rate), $5 \times 10^{-4} \text{ s}^{-1}$ (a critical rate between the static and intermediate loading rates) and 10^{-3} and 10^{-2} s^{-1} (dynamic loading rates). UCS and E with different bedding orientations were found to be rate-dependent: as the strain rate increased, the shale's anisotropic strength and elastic modulus usually increased. Increased strain rate also changed the failure mode from pure shearing failure (under a low strain rate) to a combination of tensile cracks and shearing failure (under a high strain rate).

In the context of onshore petroleum wells, the near-wellbore shale material will experience a rapid change in stress (analogous to high loading or unloading rates) during drilling, and potentially during decommissioning operations. However, after decommissioning is finalised, any subsequent stress changes will be much slower. Therefore, the impact of these loading rates during the decommissioned stage is an influential factor in the creep behaviour of shales adjacent to decommissioned wells.

1.3.3. Effect of elevated temperature on the shale creep process

The creep rate of shales with large amounts of organic matter appears sensitive to temperature changes. Voltolini (2020) conducted in-situ synchrotron X-ray micro-computed tomography studies on organic-rich Green River oil shale in Colorado. The equipment included a mini-triaxial that operates at high pressure and temperatures. The employed materials were resistant to high temperatures and had low X-ray attenuation. The temperature was managed by two thermocouples installed near the surface of the sample. The objective was to assess the brittle-to-ductile transition while the sample was undergoing an increase in temperature.

Table 5: Mineralogical composition of Green River oil shale (Voltolini, 2020)

Minerals				Clay content		Carbonates	
Quartz %	Pyrite %	Albite %	Analcime %	Illite %	Others %	Calcite %	Dolomite%
20.5	0.4	13.5	7.9	9.2	1.3	1.2	46

Consequently, the confining pressures were gradually increased to stimulate fracture closure until indications of brittle behaviour were detected. Table 5 shows the shale mineralogy obtained by X-ray powder diffraction (XRPD).

The results showed that the creep rate, especially for organic-rich shales, is very sensitive to temperature. For example, by increasing the temperature to 75°C , the creep rate was accelerated and a fracture aperture closing rate of $13 \mu\text{m/h}$ was observed (Voltolini, 2020).

Chu and Chang (1980) also conducted an experimental study to investigate the impact of elevated temperature on the strength and creep rate of oil shales. Their uniaxial compression tests and creep

compression tests were performed on cylindrical samples while increasing the test temperature from 24°C to 204°C. Their results showed that increasing temperature while testing oil shales caused a strength reduction within the shale matrix, leading to a highly increased creep strain rate. The high sensitivity of creep rate in oil shales can be attributed to the kerogen (organic matter) content of these shales, which becomes less viscous at increased temperatures.

Equations (1) and (2) were obtained from regression analyses of the compressive strength experiments under elevated temperatures (Chu & Chang, 1980):

$$\sigma_u = ae^{-bT} \quad (1)$$

$$E = ce^{-dT} \quad (2)$$

where σ_u , E and T represent the ultimate strength, the moduli of elasticity and temperature, respectively; and a , b , c and d are the kerogen-dependent coefficients of oil shale grade.

Equations (1) and (2) show that the mechanical properties of the shale depend strongly on kerogen content and temperature.

In low permeability shales, increasing the temperature leads to increased pore pressure in the heated areas (and consequently reduced effective stress) due to the higher thermal expansion coefficient of pore fluid compared with the thermal expansion coefficient of the rock matrix. Triaxial compression experiments were performed by Bauer et al. (2019; Xie et al., 2020) on core plugs of Pierre shale (widespread in the US states of North and South Dakota, Nebraska, eastern Wyoming, eastern Montana, eastern Colorado, north-western Kansas and extreme western Minnesota (Abel & Donald Gentry, 1975) and some other shales (obtained from different fields in the North Sea) under varying temperatures (from 100–400°C). Table 6 summarises the mineralogy and mechanical properties of these shales. The tests were performed using an innovative setup that heats the wall of a 10-cm-outside diameter (OD) hollow cylinder representing the borehole (similar to technique described in Figure 9b).

Table 6: Mineralogy and mechanical properties of Pierre shale and North Sea shales (field shales) (Bauer et al., 2019; Xie et al., 2020)

Shale	Depth (km)	Total clay content %	Smectite content %	Quartz %	TOC %	E (GPa)
Pierre shale	outcrop	47.9	5	26.6	1.1	1.0
Field shales	1.4	85.2	67	5.3	3.3	0.13 0.53

TOC = total organic carbon content
 E = Young's modulus

This setup provided the capability of measuring temperature and pore pressure at different radii inside the specimen. Triaxial tests were performed while the temperature was increased from 100°C to 400°C. The results indicated that increasing the temperature inside a borehole leads to heat diffusion and an increase in pore pressure in the vicinity of the borehole. Furthermore, pore pressure increases in low-permeability rock, including shale, may result in shear or tensile failure. In

addition, the impact of Young's modulus (E) can be explained through these two different mechanisms acting against each other. Firstly, according to Hooke's law, a higher Young's modulus leads to smaller rock deformation for the same stress change. Secondly, the thermal stress (σ_t) is higher when the E is higher (equation (3)):

$$\sigma_t = E \alpha \Delta T \quad (3)$$

where α and ΔT represent coefficients of thermal expansion and temperature change, respectively.

The results showed that below or above a specific temperature (200°C according to test results on the second sample from the North Sea), one of the mechanisms dominates over the other. Therefore, controlled heating could potentially stimulate large plastic deformation in the surrounding shale, which could result in borehole closure. Table 6 summarises the important observations of this study.

The outcomes of hydrostatic and deviatoric triaxial creep tests performed by Ghassemi et al. (2012) (Ghassemi & Suarez-Rivera, 2012) on Haynesville shale (USA) are in consistent with the aforementioned study. They tested the creep rate under four different temperatures (24°C, 40°C, 60°C and 140°C) and showed that at 140°C the creep rate accelerated massively in a way that failure occurred after a short steady-state creep period.

In shales, heat diffusion occurs more rapidly than hydraulic diffusion. Therefore, increasing temperature results in increasing pore pressure and, consequently, a decrease in effective stress on the shale. Reduction in effective stress near the wellbore could potentially result in plastic shear deformation (Bauer et al., 2017). However, the plastic deformation required to close an annulus around the well casing (generally a few cm) is dependent on the rock dilatancy angle (ψ), defined as the ratio of plastic volumetric strain to plastic shear strain (equation (4)):

$$\psi = \arcsin \frac{\Delta \varepsilon_v^p}{\Delta \varepsilon_v^p - 2\Delta \varepsilon_1^p} \quad (4)$$

where $\Delta \varepsilon_v^p$ is the plastic volumetric strain increment and $\Delta \varepsilon_1^p$ is the plastic strain increment (Zhao et al., 2022).

Rock dilatancy generally describes the volume increase or expansion rate after rock failure. The dilatancy angle regulates the plastic volume changes (Zhao et al., 2022): a more dilatative rock (a rock with a higher dilatancy angle) exhibits a larger volume increase compared with rocks with smaller dilatancy angles.

Khosravi and Ghassemi (2017) reported a significant increase in the creep rate of Mancos shale due to elevated temperatures. They conducted multi-stage creep tests on Mancos shale, an important Cretaceous shale formation in western USA rich in organic material with a porosity of 6–8% and a clay content of approximately 20–25% (Torsæter et al., 2012). Their samples were cored both perpendicular and parallel to the bedding plane. They found that the sample cored parallel to the bedding plane exhibited higher stiffness and a lower creep strain rate compared with the sample cored perpendicular to the bedding plane when subjected to elevated temperatures.

However, further examinations have shown that accelerating creep by increasing temperature may damage the shale formation due to the creation of diskings cracks within the sample. Initiation and propagation of the diskings cracks may potentially compromise the integrity of the barrier. There is

also the likelihood that, after disconnecting the heat source, the damage (cracks) may self-heal naturally with time (van Oort et al., 2022).

1.3.4. Effect on the shale creep process of incorporating chemicals into the annular fluid

Chemical activation might be more straightforward in field applications than procedures entailing increasing the temperature or reducing the pressure. Chemical solutions can be circulated through the annular space by perforating casings with a workstring and packer arrangement (Figure 9) (Carpenter, 2021).

Enayatpour et al. (2019) proposed that, by using chemical solutions to accelerate creep and form a barrier in Lark–Horda shale, the stiffness of the shale formation near the wellbore might be reduced. Lark–Horda shale is a fine-grained, clay-rich formation located in the North Sea. Cylindrical shale samples with a diameter of 3.81 cm, a length of 7.62 cm and an internal borehole diameter of 1.44 cm were placed in a core holder. A solid steel cylindrical rod (representing the casing) with a diameter of 1.22 cm was mounted inside the borehole running through the centre of the cylindrical shale sample, leaving an annular gap of approximately 0.11 cm between the steel rod and the shale rock sample (the same set-up as depicted in Figure 11). The mineralogy of the Lark–Horda shale is demonstrated in Table 7.

Table 7: Lark–Horda shale (North Sea) mineralogy (Enayatpour et al., 2019)

Non-clay mineralogy					Clay content					
Quartz %	Pyrite %	Carbonates (calcite and dolomite) %	Trace minerals %			Smectite %	Illite/ smectite %	Illite/mica %	Kaolinite %	Chlorite %
			K-feldspar	Plagioclase	Apatite					
19–21	5–9	1–2	1			3–4	9–12	37–40	18–21	1

A core holder was placed between two end platens that are connected to upstream and downstream reservoirs and loaded in a triaxial load frame through which confining pressure and axial pressure can be applied. The annular fluids and pressure in both the reservoirs and the load cell are managed by an arrangement of pumps, displacement vessels and pressure transducer (Figure 11a). After the targeted stress condition and temperature are attained, the annular fluid containing either sodium silicate solution or lithium silicate solution (Table 8) displaces the base fluid.

The outcomes of laboratory strain measurements and pressure-pulse decay tests on Lark–Horda shale have shown that alteration of the annular fluid chemistry can massively affect the shale creep rate (and therefore barrier development) through incorporating sodium and lithium silicate fluids. The complete barrier creation time for filling the annular gap (creep strain) for the base test took 18.2 days, whereas by incorporating first sodium silicate and second lithium silicate into the test

fluid, the number of days to close the annular space was reduced to 5.1 and 2.9 days, respectively. In fact, the effect of such chemical solutions was larger than the effect of raising the temperature. Elevating the temperature to 85°C reduced the annular closure time to 11.5 days, which is less than 18.2 days (base test under 54°C) but still longer than tests in which chemicals were incorporated.

Table 8: Pore fluid compositions used in triaxial tests on Lark–Horda shale to evaluate the effects of sodium silicate and lithium silicate on shale creep and barrier development (Enayatpour et al., 2019)

Pore fluid composition	
Base fluid	Sodium hydroxide test with highly alkaline (pH = 12) 2M NaOH fluid (50.28 mg/l NaCl, 17.48 mg/l MgCl ₂ .6H ₂ O, 7.81 mg/l CaCl ₂ .2H ₂ O, and 0.35 mg/l K ₂ SO ₄)
Sodium silicate fluid	10% v/v sodium silicate fluid
Lithium silicate fluid	10% v/v lithium silicate fluid

This impact can be attributed to the high alkalinity of sodium and lithium silicate fluids (Table 8), which weakens the shale and results in shale dispersion and cation exchange in the clays, leading to improved intermolecular hydration forces and double-layer repulsion between the clay particles (Gawal et al., 2021). However, from a wellbore stability point of view, weakening the shale formation might be problematic.

Studies have shown that a key reason behind causing wellbore instability is that the strength of the shale is reduced by being subjected to drilling fluids, which causes shale swelling due to hydration and dispersion. Especially in cases where the shale is hard and brittle (rich in illite), creating microfractures during well operations makes the rock more susceptible to hydration and dispersion, leading to incidents including fragmentation of cuttings, wellbore collapse, and the pipe sticking at deep intervals (Li et al., 2022; Carney, 1986).

It is worth noting that incorporating sodium and lithium silicate solutions into the drilling fluids has been studied in terms of their impact on wellbore instability during the drilling phase (Li et al., 2021; Li et al., 2022). Sodium silicate is classified as a shale inhibitor that acts as a pore-plugging material which mitigates shale hydration. Generally, inorganic silicates, including sodium silicate and lithium silicate, create a protective film on the shale surface, blocking the shale pores and hindering pressure transmission (Y. Li et al., 2021, 2022).

Gawal et al. (2021) have also assessed incorporating chemicals to stimulate creep. They argue that the Lark–Horda shale used by Van Oort et al. (2022) (van Oort et al., 2020) is a weak shale with a Young’s modulus of 827.4 MPa and a clay content of around 70%; therefore, it would be straightforward to promote shale creep.

They proposed altering the mechanical properties of strong and brittle shale (such as Pierre shale I having a high amount of quartz and a low amount of clay) by removing the cementitious materials in the shale (quartz, calcite and dolomite) using acid treatments. Removal was achieved by chemical leaching of carbonates using hydrochloric acid (HCl). To assess the effect of modifying shale formations by chemical leaching, the mechanical properties of the specimens were compared before and after leaching. The results showed that by removing 4–5% cementitious materials (in

this case, mostly dolomite) from the shale matrix, the strength of the shale was reduced by 43% compared with shale exposed only to sodium chloride (NaCl) solution.

Table 9 provides a summary of the experimental parameters used in various studies mentioned in this literature review.

Table 9: Summary of the experimental parameters of various studies mentioned in this literature review

Shale	Specimen shape and size	Bedding angle	Experiment type	Depth (km)	Porosity	Permeability (nD)	Non-clay mineralogy content (wt%)		Clay content (wt.%)	TOC %	Experimental properties					Outcome	Reference
											Temperature (°C)	Loading rate (1/s)	Confining pressure (MPa)	Test duration (h)	Sample preservation		
Longmaxi shale	Cylinder L = 100 mm D = 50 mm	Different bedding angle from 0° to 90°	UCS	*	*	*	Quartz: 55.5 Other minerals: 72.9	*	3–8	*	*	10 ⁻⁴ 5 × 10 ⁻⁴ 10 ⁻³ 10 ⁻²	0	*	*	<ul style="list-style-type: none"> CS and <i>E</i> are loading rate and bedding plane dependent Strain rate increase can decrease the impact of bedding structures/orientation on the mechanical behaviour and alter the failure mode 	He et al. (2022)
Colony Pilot Mine to the north of Grand Valley, Colorado	Cylinder L ≈ 46.8 mm D = 23.4 mm	*	Triaxial heating compression tests	*	*	*	*	*	*	*	23.9°C 37.8°C 121°C	*	Constant stress ratio of 0.45	90	*	<ul style="list-style-type: none"> The secondary creep strain rate increases as temperature increases The strain rate increases from 3.33 × 10⁻⁸ 1/min at 23.9°C to 16.7 × 10⁻⁸ 1/min at 121.11°C (almost 5 times) 	Ch & Chang (1980)
Shale #1 Shale #2 Shale #3	Cylindrical *	*	Un-drained heating triaxial	1.6 1.9 2.1	0.24 0.214 0.205	*	Quartz: 48 25 26	48 47 43	*	*	Step-wise increase from	*	7 11 6	*	*	<ul style="list-style-type: none"> Increasing the temperature may lead to rock failure due to thermally induced 	Bauer et al. (2017)

Shale #4			compression tests	2.4	0.161		32 41	23			65°C to 120°C		10 20 20			pore pressure increase and subsequently reduction of effective stress	
Lark-Horda shale	Hollow cylinder OD = 38.1 mm ID = 12.7 mm L = 76.2 mm	*	Pressure-pulse decay	1.41	*	3.5	Quartz : 19–21 Pyrite: 5–9 Carbonates (calcite and dolomite): 1–2 Trace minerals: (Plagioclase, apatite and K-feldspar) 1	Total clay: 70–73 Smectite: 3–4 Illite/smectite: 9–12 Illite/ mica: 37–40 Kaolinite: 18–21 Chlorite: 1	*	*	54°C	*	11	437 h/ 18.2 days 122.4 h/ 5.1 days & 69.6 h/ 2.9 days	*	<ul style="list-style-type: none"> Increasing temperature in moderate degrees (which is site-dependent) may result in large plastic deformation (creep) to fill up the annulus space The incorporation of sodium and lithium silicate into the annular fluid during pressure pulse decay expedites creep rate significantly 	(Enayatpour et al., 2019; van Oort et al., 2020)

Marcellus	Cylinder L ≈105.38 mm D = 52.98 mm	Parallel and perpendicular to the bedding for triaxial tests	Uniaxial, triaxial compression and triaxial creep tests	*	*	*	Quartz: 8.74	*	*	*	Room conditions	5.96×10 ⁻⁸ 4×10 ⁻⁸ 1.66×10 ⁻⁸ 7×10 ⁻⁹ 1.23×10 ⁻⁸ 9×10 ⁻⁸	3.45 6.89 10.34 13.79 6.89 10.34	58.49 243.56 145.12 210 158.9 65.45	Specimens were kept in plastic sheets during transportation	<ul style="list-style-type: none"> • The response of the parallel specimens is stiffer than the perpendicular ones • The magnitude of the yield stress, failure stress and residual strength increases as confining pressure increases • Dilatation angle for all the specimens reduces as confining pressure increases • The time taken to reach the tertiary creep stage increases as confining pressure increases 	Gupta & Mishra (2017)
Marcellus Barnett Haynesville	Cylinder L ≈ 50.8 mm D = 25.4 mm	Perpendicular to the bedding	Uniaxial and MSTXL creep tests	1.8 1.7 3.8	*	*	28 60 25	40 25 33	*	*	Room humidity conditions	* 19 16 5 16 0 0	148 * * 70 (three stages) 120 *	*	<ul style="list-style-type: none"> • Barnett has higher Young's modulus and less amount of clay content compared with Haynesville. Comparing the outcomes of MSTXL (both shales subjected to the same loading path) has shown that the 	Li & Ghassemi (2012)	

													160	90 (three stages)	*	<p>stiffer shale (Barnett) crept less. Creep strain of 0.04 and 0.01 achieved for Haynesville and Barnett, respectively</p> <ul style="list-style-type: none"> • By employing the higher confining pressure, a larger creep strain can be achieved in a given time when subjected to the same deviator stress • Creep rate in phase 2 (pseudo-steady state) increases linearly with deviator stress increases 	
Pierre shale	Hollow cylinder OD = 100 mm ID = 12.7 L = *	*	Borehole heating tests	Outcrop	0.2	30	Quartz 26.6	Clay content 47.9 ▪Smectite 5	1.1	*	Varying temperatures from 100°C to 400°C	*	Initial confining pressure was set at 14 MPa and then was increased stepwise to 17 MPa. Lastly, de-	*	*	<ul style="list-style-type: none"> • Larger borehole-wall displacement was observed for the sample with lower Young's modulus (softer rock) within the temperature range 200–350°C 	(Mahanta et al. (2018); He et al. (2022))

Two shale samples obtained from the North Sea				1.4	0.397	300 90–120	Quartz 5.3	Clay content 85.2 ▪Smectite 67	3.3	*		creased to 14 MPa		<ul style="list-style-type: none"> Below or above a specific temperature (200°C according to test results on the second sample from the North Sea), controlled heating could potentially be used to stimulate large plastic deformations in the surrounding shale, which can result in borehole closure 	
---	--	--	--	-----	-------	---------------	---------------	---	-----	---	--	----------------------	--	--	--

*Not provided in paper
CS = Compressive strength
E = Young's modulus
TOC = Total organic carbon
OD = Outside Diameter
ID = Inside Diameter

1.4 Creep modelling

1.4.1. Analytical (rheological) modelling

Generally, the creep strain rate ($\dot{\epsilon}^c$) is assumed to depend on time t , stress σ and temperature T , as shown in equation (5):

$$\dot{\epsilon}^c = f(t, \sigma, T) \quad (5)$$

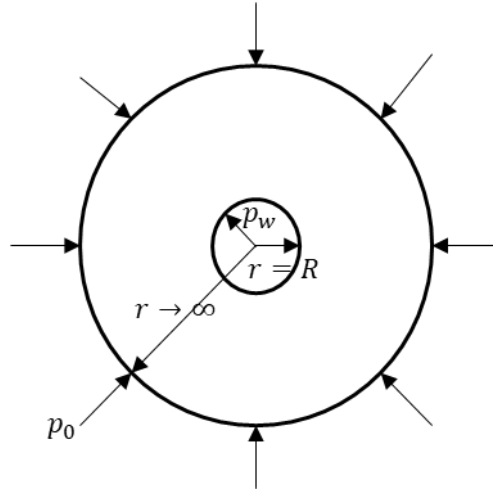


Figure 12: Axisymmetric plane-strain problem setup, illustrating the relationship between radial displacement and strain in a borehole subjected to far-field stress and mud pressure, used for analysing borehole creep with various creep models. (Liu et al., 2011)

Different creep models can be derived based on the form of function f in equation (5) (X. Liu et al., 2011). An axisymmetric plane-strain problem is defined to achieve an analytical (or semi-analytical) solution for creep modelling (Figure 12). The far-field stress and mud pressure are represented by p_0 and p_w , respectively. As can be seen in Figure 12, p_w is applied to the wellbore wall. The radial and tangential stress are represented by σ_r and σ_θ .

Boundary conditions are applied as follows:

$$\text{I. } \sigma_r = p_w \quad r = R \quad (6)$$

$$\text{II. } \sigma_r = p_0 \quad r \rightarrow \infty \quad (7)$$

At the initial time, $t = 0$, it is assumed that no creep strain has occurred:

$$\epsilon_r^c = \epsilon_\theta^c = 0. \quad (8)$$

The rock is assumed elastic, and Lamé's formulation gives stress and radial displacement around the wellbore:

$$\sigma_r = p_0 \left(1 - \frac{R^2}{r^2} \right) + p_w \frac{R^2}{r^2} \quad (9)$$

$$\sigma_\theta = p_0 \left(1 + \frac{R^2}{r^2} \right) - p_w \frac{R^2}{r^2} \quad (10)$$

$$u = \frac{R^2}{2Gr} (p_o - p_w), \quad (11)$$

where G and u represent shear modulus and radial displacement, respectively.

1.3.4.1. Baker's Norton model

Baker's Norton creep model (Barker et al., 1994) connects the creep strain rate to stress and temperature as:

$$\dot{\epsilon} = A e^{-(B/T)} \sigma^n \quad (12)$$

where T is the temperature in kelvin, A is the viscosity constant in 1/psi.sec, B is a temperature exponent, n is a stress exponent and σ is stress.

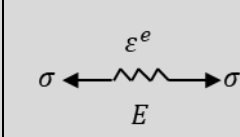
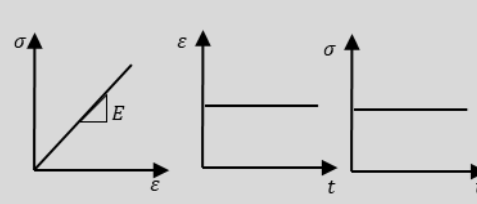
Barker et al. (2011) derived a closed-form equation to achieve a solution to the wellbore closure rate with the assumption that the rock is inelastic and incompressible during creep events (which may not be plausible assumptions). According to their model, the final radius of the wellbore can be computed as:

$$R = R_o \exp \left(-\frac{(\sqrt{3})^{(n+1)}}{4n-2} \right) A e^{-\frac{B}{T}} (p_o - p_w)^n \Delta t \quad (13)$$

According to the investigations of Willson et al. (2002), Baker's Norton model may overestimate deformations for salt (the n parameter for salt formations is chosen between 3.5 and 6,) because the stresses don't relax. This is an important consideration when evaluating casing loading, as the time at contact (the onset of casing loading) would be inaccurately predicted using the closed-form solution of equation (9) (X. Liu et al., 2011).

Analytical/rheological models for shales comprised of mechanical components coupled in series or in parallel have been employed to simulate elasticity (springs) and viscosity (dashpots) as shown in Table 10 (Paraskevopoulou & Diederichs, 2013). The most common viscoelastic models include the Kelvin model (Gupta & Mishra, 2017), the Maxwell model (X. Liu et al., 2011) and the Burgers model (Li & Ghassemi, 2012). The Bingham model (Augustesen et al., 2004) is later introduced as a viscoplastic model.

Table 10: The mechanical components of the analytical model and their associated responses (Paraskevopoulou & Diederichs, 2013)

Component	Mechanical analogue	Behaviour response
Spring		

Dashpot		
Slider (plastic)		

1.3.4.2. Maxwell viscoelastic creep model

The Maxwell model comprises a spring element and a Newtonian dashpot in a series connection (Figure 13). The elastic (ε^e) and creep strain rate ($\dot{\varepsilon}^c$) are as defined in equation (14):

$$\begin{cases} \varepsilon^e = \frac{\sigma}{E} \\ \dot{\varepsilon}^c = \frac{\sigma}{\eta} \end{cases} \quad (14)$$

where E is the elastic modulus of the spring and η is the viscosity of the dashpot.

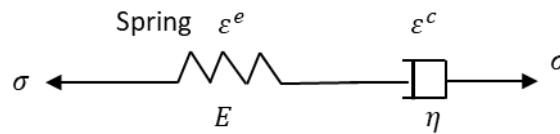


Figure 13: Maxwell creep model with spring and dashpot (Liu et al., 2011)

The Maxwell constitutive equation is as follows (Liu et al., 2011):

$$\dot{\varepsilon} = \frac{\dot{\sigma}}{E} + \frac{\sigma}{\eta} \quad (15)$$

The derivation, along with the meaning of the Laplace transform of equation (15), are fully explained by Liu et al. (2011). The viscoelastic displacement solution can be written as:

$$u(t) = (1 + \nu)(p_0 - p_w) \frac{R^2}{r} \left(\frac{1}{E} + \frac{t}{\eta} \right) \quad (16)$$

where t and ν represent time and Poisson's ratio, respectively.

At time $t = 0$, before creep instigation, viscoelastic displacement of the rock formation around a wellbore is equal to the elastic displacement of the rock, which yields:

$$u(0) = (1 + \nu)(p_0 - p_w) \frac{R^2}{rE} \quad (17)$$

According to equation (12), if $t \rightarrow \infty$ then $u \rightarrow \infty$, which implies that in the Maxwell model creep increases without limit as a function of time. So, differentiating creep rate with respect to time will give:

$$\dot{u}(t) = \frac{(1 + \nu)R^2}{\eta r} (p_0 - p_w) \quad (18)$$

The creep rate in equation (18) is known as the steady-state creep and is independent of time.

1.3.4.3. Kelvin viscoelastic model

The elastic strain and the creep strain are described as:

$$\begin{cases} \varepsilon^e = \frac{\sigma}{E} \\ \dot{\varepsilon}^c = \frac{\sigma}{\eta} \end{cases} \quad (19)$$

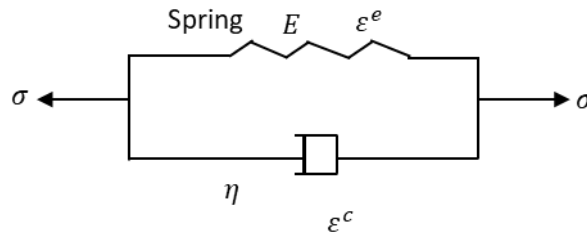


Figure 14: Kelvin creep model (Gupta & Mishra, 2017)

The constitutive equation of the Kelvin model (Gupta & Mishra, 2017) comprised of a spring and a dashpot connect in parallel, as shown in Figure 14, can be defined using equation (20):

$$\sigma = E\varepsilon + \eta\dot{\varepsilon} \quad (20)$$

The viscoelastic displacement solution can be written as:

$$u(t) = \frac{(1 + \nu)}{E} (p_0 - p_w) \frac{R^2}{r} \left(1 - e^{-\frac{E}{\eta}t} \right) \quad (21)$$

$$u(t) = \frac{(1 + \nu)}{E} (p_0 - p_w) \frac{R^2}{r} \left(1 - e^{-\frac{E}{\eta}t} \right) \quad (22)$$

When $t = 0$, equation (21) becomes:

$$u(0) = 0, \quad (23)$$

which indicates that no displacement occurs within the rock formation around a wellbore at time zero.

When $t \rightarrow \infty$, then $u(\infty)$ becomes:

$$u(\infty) = (1 + \nu)(p_0 - p_w) \frac{R^2}{rE} = \frac{R^2}{2Gr} (p_0 - p_w) \quad (24)$$

which equals the elastic deformations (i.e. the maximum displacements achievable from the Kelvin creep model are the elastic displacement during the primary stage of the creep process).

1.3.4.4. Burgers model

The Burgers model (Li & Ghassemi, 2012) can be used to model multi-stage creep by incorporating four elements: a Maxwell unit and a Kelvin unit (a spring and dashpot) connected in series, as shown in Figure 15 (Paraskevopoulou & Diederichs, 2013).

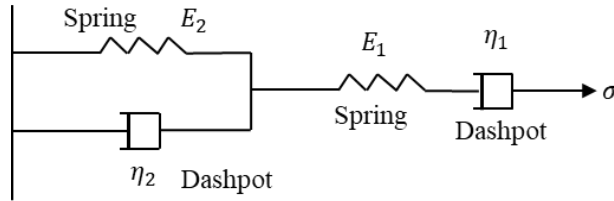


Figure 15: The four-element Burgers model (Li & Ghassemi, 2012)

The one-dimensional constitutive equations in a uniaxial stress state for the generalised Voigt–Kelvin model and the Burgers model are described by equations (25) and (26) as follows (Li & Ghassemi, 2012):

$$\varepsilon_{h-k} = \frac{\sigma}{E_h} + \frac{\sigma}{E_k} \left(1 - \exp\left(-\frac{E_k}{\eta} t\right) \right) \quad (25)$$

$$\varepsilon_{m-k} = \frac{\sigma}{E_m} + \frac{\sigma}{E_k} \left(1 - \exp\left(-\frac{E_k}{\eta_k} t\right) \right) + \frac{\sigma}{\eta_m} t \quad (26)$$

where σ is the axial stress, ε is the axial strain, E is the viscoelastic modulus, η is the viscosity coefficient, and the subscripts h , k and m represent the components of the Hookean, Kelvin and Maxwell units, respectively.

1.3.4.5. Bingham model

The Bingham model (Augustesen et al., 2004) comprises three elements (two groups of components) in which a spring in series is connected to a dashpot and a slider in parallel connection (Figure 16). The time-independent group contains a spring (elastic behaviour, E), and the time-dependent group contains the dashpot with a viscosity coefficient (η) and the slider with yield stress (σ_y) connected in parallel, simulating the visco-plastic response.

The slider acts only when the applied stress exceeds the yield stress. Therefore, prior to reaching this point, the model performs similarly to the Maxwell model in describing the secondary stage of creep. However, the applied stress is replaced by $\sigma - \sigma_y$ and strain is simulated as a constant. Equation (27) describes the constitutive equation of the Bingham model:

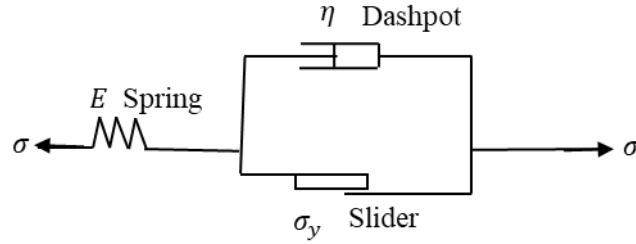


Figure 16: Bingham visco-plastic model (Augustesen et al., 2004)

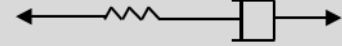
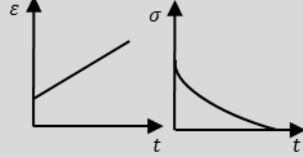
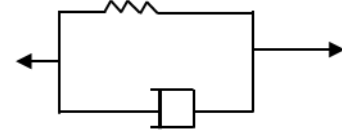
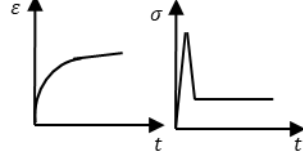
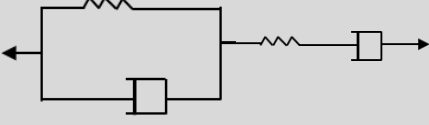
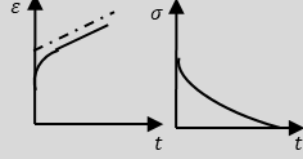
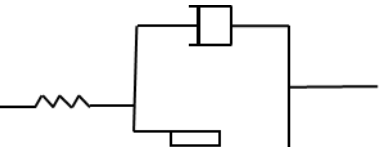
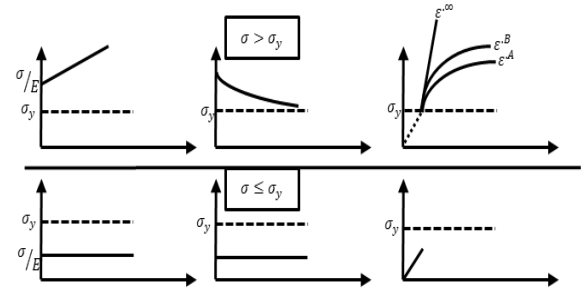
$$\dot{\epsilon} = \left\{ \begin{array}{l} \dot{\epsilon}^e + \dot{\epsilon}^{vp} = \frac{\dot{\sigma}}{E} + \frac{(\sigma - \sigma_y)}{\eta} \quad \text{for } \sigma > \sigma_y \\ \dot{\epsilon}^e = \frac{\dot{\sigma}}{E} \quad \text{for } \sigma \leq \sigma_y \end{array} \right\} \quad (27)$$

where $\dot{\epsilon}$ represents total strain rate, and $\dot{\epsilon}^e$ and $\dot{\epsilon}^{vp}$ represent strain rates in the elastic and visco-plastic elements, respectively.

Table 11 summaries the above four models, along with their associated stress–strain and stress–time relationships.

- The Kelvin model is employed to simulate the instantaneous elastic behaviour during the first stage of creep in rocks when subjected to a constant load. In other words, the Kelvin model captures the time-dependent softening stage of creep until equilibrium is reached.
- The Maxwell viscoelastic model is used to model the secondary state of creep, which is the state prior to rock failure. The Maxwell model simulates indefinite deformation under a constant load.
- The Burgers model is composed of both Kelvin and Maxwell elements. It therefore captures both the primary stage (strain increasing while strain rate decreasing) and secondary stage of creep (where the displacement increases linearly with time).
- For the Bingham model, the constitutive equation assumes that the material response is elastic before reaching a threshold stress (σ_y), after which the material is subjected to a constant stress of $\sigma - \sigma_y$, which results in a constant plastic strain (ϵ^{vp}) and the material does not harden.

Table 11: Summary of the analytical models and their associated strain-vs-time and stress-vs-time behaviour (Paraskevopoulou & Diederichs, 2013; Augustesen et al., 2004)

Model	Spring + dashpot analogue	Strain–time; stress–time
Maxell (secondary stage)		
Kelvin (primary)		
Burgers (primary + secondary)		
Bingham (secondary + plastic strain)		

1.4.2. Numerical simulations

The conventional linear analytical models, including the Maxwell model and the Kelvin model, are all well-recognised viscoelastic models that amalgamate one or two elastic Hookean springs with a Newtonian viscous dashpot, either in series or in parallel. The quantity and configuration of springs and dashpots can be altered based on the creep responses of different rocks. However, increases in the number of springs or dashpots can lead to a heavy regression process and some negative fitting parameters that are not physically interpretable (Shi, 2022).

A more exact solution can be found by using finite element discretisation in a numerical model and can be based on either a finite element model in the space domain or finite difference discretisation in the time domain. Employing numerical models, including finite element methods, provides the advantage of being able to incorporate different nonlinear constitutive models (visco-plastic), different complex geometries and boundary conditions, and in-situ stress conditions (Gray et al., 2009).

Fjær et al. (2016) used finite element simulations to study how geomechanical characteristics affected the way in which shale forms a barrier in abandoned wells and concluded that plastic deformations are essential to barrier creation. They used a visco-plastic model in which stress relaxation was incorporated by assuming that displacements can be decomposed into elastic and plastic deformations. They represented creep as a time-dependent plastic shear deformation at the grain contacts, under the assumption that that plastic deformations do not alter the forces or moments acting on the system. If that total displacements between the two elements are constant, creep causes an increase in the plastic component, while elastic displacements and associated stresses are reduced. The final result is a time-dependent reduction in the forces acting between the discrete elements. The plastic deformation $\Delta\varepsilon_p$ in a period Δt can be computed as:

$$\tau' = \tau - M\Delta\varepsilon_p \quad (28)$$

where τ is shear stress at the contact between the two contact elements and reduces to τ' after a time Δt , and M is the modulus. The creep strain in a period Δt will be:

$$\Delta\varepsilon_p = V_0 e^{-(\beta/T)} \left(\frac{\tau}{\tau_m}\right)^n \Delta t \quad (29)$$

where V_0 , β , τ_m and n are constants and T is the temperature.

The interaction between the rock formation and the steel casing was defined through a constitutive contact law. They assumed that originally the materials were bonded. Creep was then created by inserting a time-dependent plastic shear displacement, suggesting that plastic strains were caused through distortions of grains, not volume variations. Their simulations showed that the annular space quickly reduced at the beginning although, due to arching effects, the closure rate started to rapidly decrease, which decreased the driving force for gap closure.

Elevated temperatures may expedite the gap closure process, but the long-term impact requires more investigation.

It is worth mentioning that because shale creep imposes an uneven load on the casing, ovalisation and collapse of the casing may occur.

Firme et al. (2014) ran finite element simulations to compare the performance of three power-law models – Norton's power law (PL), the double mechanism creep law (DM) and the multi-mechanism deformation creep law (MD) – to see how compatible they were with experimental data.

The creep deformation in the PL model was simulated as a function of stress, temperature and time, as shown in equation (30):

$$\varepsilon(t) = A\sigma_{eq}^n t^m T^v \quad (30)$$

where σ_{eq} is the equivalent multiaxial stress (or the deviatoric stress), t is time and T the temperature. The empirical parameters are A , n , m and ν , which are, respectively, the power-law multiplier and the stress, time and temperature exponents.

The DM model was implemented as an Abaqus subroutine to simulate the visco-plastic behaviour of creep in the steady-state step, based on equation (31):

$$\dot{\varepsilon} = \dot{\varepsilon}_0 \exp\left(\frac{Q}{RT_0} - \frac{Q}{RT}\right) \left(\frac{\sigma_{eq}}{\sigma_0}\right)^n \quad (31)$$

where $\dot{\varepsilon}$, T_0 and σ_0 are, respectively, the creep rate, temperature and stress at the experimental point where the transition of the governing mechanism is observed, Q is the thermal activation energy and R is the universal gas constant (8.314 J/mol·K). Other parameters have the same physical meaning as described in the PL model.

The MD model can simulate, in the steady-state creep stage, transient and steady-state creep according to the three micromechanical creep mechanisms:

$$\dot{\varepsilon}_s = A_1 \exp\left(\frac{-Q_1}{RT}\right) \left(\frac{\sigma_{eq}}{G}\right)^{n_1} + A_2 \exp\left(\frac{-Q_2}{RT}\right) \left(\frac{\sigma_{eq}}{G}\right)^{n_2} + H \left| \sigma_{eq} - \sigma_0 \right| \left[\begin{array}{l} B_1 \exp\left(\frac{-Q_1}{RT}\right) \\ B_2 \exp\left(\frac{-Q_2}{RT}\right) \end{array} \right] \times \sinh\left[\frac{q(\sigma_{eq} - \sigma_0)}{G}\right] \quad (32)$$

Orlic and Buijze (2014) and Orlic et al. (2019) employed numerical modelling to estimate creep deformations and duration. They assumed that the casing section over the part of a formation consisting of rock salt was absent, so that a sealant barrier was created by the creep of rock salt. Salt creep was modelled as steady-state creep together with linear and nonlinear (power-law) creep components. In the steady-state step, creep deformations in rock salt occur due to two mechanisms: nonlinear creep or dislocation creep, and linear creep, while the brine is present at the grain boundaries. The two-component creep law for steady-step creep is:

$$\dot{\varepsilon}_{vert} = A_1 \exp\left(\frac{-Q_1}{RT}\right) \left(\frac{\Delta\sigma}{\alpha}\right)^{n_1} + A_2 \exp\left(\frac{-Q_2}{RT}\right) \left(\frac{\Delta\sigma}{\alpha}\right)^{n_2} \quad (33)$$

where $\dot{\varepsilon}_{vert}$ is the vertical strain (1/s), $\Delta\sigma = \sigma_{vert} - \sigma_{hor}$ is the differential stress (Pa), A_1 and A_2 are the creep strain rate coefficients (1/s), Q_1 and Q_2 are the activation energies (J/mol), R is the gas constant (8.314 J/mol.K), T is the ambient temperature (K), α is the reference stress (Pa), and n_1 and n_2 are the exponents for the nonlinear creep ($n_1 > 1$) and linear creep ($n_2 = 1$) in each branch, respectively.

The linear creep rate factor (A_2) and the Newtonian viscosity used in the Maxwell viscoelastic model (μ) are inversely proportional (i.e. $\mu = 1/A_2$).

Their numerical simulations demonstrated that in-situ temperature, differential stress and rock salt properties are major factors in determining creep rate and wellbore closure duration. In the deeper section of the reservoir, where temperatures and differential stresses are higher, the creep rate is quicker, and so the wellbore closure time is shorter. Thus, based on the targeted depth, the closure time can vary from a few weeks to a few years.

It is fair to say that there is no model that can simulate the response of all types of shale formations to any downhole (Santos et al., 1996). Nonetheless, there are similarities between models describing salt creep and shale creep that might usefully simulate the formation of a shale barrier. For instance, the rate of creep strain depends on various factors, including temperature, differential stress, confining pressure, grain size and the presence of inclusions of free water or gas bubbles. Moreover, the evolution of creep strain in a salt formation is identical to that in a shale formation. In a salt formation, creep occurs in three stages: primary, secondary and tertiary. In the tertiary stage, due to the creation of microfractures, there is dilation and an increase in volume until the rock undergoes failure (Wang & Samuel, 2016).

1.4.3. Discussion of shale creep modelling

The constitutive material relationships in the above rheological models (comprising springs, dashpots and sliders) are assumed to be linear. However, the response of shale rock is not linear. The Kelvin model predicts primary creep and the Maxwell model secondary creep. The Burgers model can simulate both stages since it comprises Kelvin and Maxwell models connected in series. The Bingham model assumes that, after reaching the yield stress, plastic creep strain will remain constant, which is not a realistic assumption considering that creep strain rate accelerates in the tertiary stage. In addition, the constitutive relationships in the rheological models are defined in one-dimensional space, so that materials are only subjected to uniaxial compression stress (Augustesen et al., 2004).

It is also worth mentioning that, when considering creep phenomena during decommissioning, there are multiple sources of nonlinearity in borehole closure, including material nonlinearity, geometric nonlinearity and boundary conditions. Performing a numerical simulation makes it possible to incorporate nonlinear constitutive material relationships, complex geometries, and nonlinear and changing boundary conditions. For instance, during a simulation boundary condition can change when the shale fills up the annular space and contacts the casing. In a finite element analysis, discontinuous contact will constrain how the pressure is transmitted from the shale to the casing (the constraints only apply when the two materials come into contact). The other important factor that might be considered in a numerical simulation is the state of the stress and initial conditions prior to creep instigation. It needs to be kept in mind, however, that numerically simulating the nonlinear behaviour of a shale formation can be computationally expensive, compared with linear models (Mazon, 2022).

1.5 Evaluation and selection of chemical fluids

Ozan et al. (2018) proposed that smectite content, total organic carbon (TOC) and clay content are the most important material properties affecting creep behaviour. The chemical activity of the clays also controls creep behaviour, as the most active clay types (smectite > illite > kaolinite) tend to show the highest time-dependent response.

In a study by Ewy (2014), the term 'water activity' refers to the relative humidity or vapor pressure exerted by water in a solution, which influences the swelling and shrinkage behaviour of shales. Ewy

examined how nine different shale samples responded to suction and direct brine contact. The study found that shale samples typically swell when exposed to brine, even if the water activity of the brine is lower than the inherent water activity of the shale. This means that shale can absorb water from brine despite the brine having a lower moisture content than the shale itself, leading to swelling. Swelling in shales and claystone occurs within the water-bound pore space, and the swelling magnitude directly relates to the increase in water content. Due to ionic diffusion, shale pore water (free water) comes into equilibrium with the solutes of the exposed brine. Because of osmotic effects, higher concentrations of NaCl lead to less swelling and less increase in water content compared with lower NaCl concentrations, which can be attributed to osmotic effects between shale pore water and the clay interlayer space. According to this study, potassium, sodium and calcium (in order of effectiveness) prevent swelling.

Studies investigating the effect of pore fluid chemistry on Lark–Horda shale (section 1.3.4) showed that incorporating sodium silicate and lithium silicate may expedite the creep process (van Oort et al., 2020). Further studies have also shown the efficiency of potassium chloride (KCl) solution in accelerating the creep process (van Oort et al., 2022). However, using KCl may be controversial due to its demonstrated role as an effective inhibitor of clay swelling. The efficiency of KCl is attributed to the effect of high KCl concentrations on hydration stresses and the total effective stress. Lark–Horda shale shows high sensitivity to KCl due to its high amount of smectite, making it more susceptible to creep (van Oort, 2003). Thus, the sensitivity of other shales to specific chemical changes aimed at increasing creep deformation and filling the annular space needs to be examined case by case.

1.6 Conclusion

This report provides a state-of-the-art review of ways to natural shale barriers could be created in decommissioned wells via creep phenomena. The literature review has collected published information on creep mechanisms and identified the factors that are important in promoting creep deformation in boreholes, including shale mineralogy and theoretical and experimental research in relation to creep mechanism in shales.

As part of a system in conjunction with well barriers including the cement plugs, the natural shale around a borehole can contribute to forming an effective seal. In the long term, natural shale might outperform cement, as demonstrated by shale’s ability to trap oil and gas in reservoirs for millions of years. The occurrence of shale forming such natural barriers has been recorded by sonic and ultrasonic well logs in the fields. On this basis, perhaps overburden and reservoir shales may have already undergone creep and sealed the annular space within decommissioned wells, creating a permanent and impervious barrier to the movement of fluids deep in the formation and protecting surface aquifers.

However, if we wish to deliberately achieve complete zonal isolation of a borehole by stimulating the creep within a shale formation, we need to understand the creep mechanisms, the mineralogy of the specific shale and the response of the shale formation to variations of downhole conditions.

The mineralogy of a shale is a strong indicator of its propensity to creep and close annular spaces. Shales with a high amount of clay (i.e. with comparatively high smectite content and low amounts of quartz and carbonate cementation) are suitable candidates for undergoing creep.

This review has also explored well-recognised analytical (rheological) models and numerical models which, along with their detailed components, are able to predict creep under downhole conditions. The suitability of each model has been found to depend on the properties of the rock concerned. The geometry, boundary conditions, and in-situ stress conditions must be validated by comparing model predictions with experimental data to ensure the models accurately reflect the real-world behavior of the rock.

In this study, we have identified the Velkerri and Kyalla formations in the Beetaloo Sub-basin as target formations. Their mineralogy and susceptibility to creep require further investigation. Previous studies have shown that the Velkerri Formation, due to its high quartz content, exhibits very brittle behavior. As a result, it may not serve as an effective self-sealing barrier, particularly in the short term, without the use of stimulation techniques to enhance its creep properties. However, published studies indicate that the Kyalla Formation, due to its high clay content, might be able to act as a competent barrier in decommissioned wells, either naturally or through application of stimulation techniques.

Chapter 2

Evaluation of the Beetaloo Sub-basin shale mineralogy and chemoporomechanical properties

2.1. Introduction

Shales are generally layered sedimentary rocks composed of fine-grained minerals. The clay mineral content is typically the most important factor influencing a shale's sealing ability. However, other constituents, such as quartz, feldspar, calcite, and organic components, also play vital roles in determining the shale's response to downhole conditions (Ilgen et al., 2017).

Understanding the chemoporoelastic properties of shales is crucial for various geological and engineering applications. This chapter examines the intricate characteristics of shales, focusing on their specific surface area (SSA) and cation exchange capacity (CEC), which are fundamental indicators of their reactivity and interaction with fluids. The mineralogical composition of shales, determined through XRD and XRF analyses, provides essential insights into the types and quantities of minerals present, influencing the rock's mechanical and chemical behaviour.

Additionally, the chapter explores methods for measuring chemoporoelastic properties, drawing on advanced research methodologies to provide a comprehensive understanding of shale behaviour under varying environmental conditions. These analyses not only elucidate the inherent properties of shales but also contribute to optimising their exploitation and management in various industrial contexts.

2.2. Shale chemoporomechanical characterisation

The geomechanical, physical and petrophysical properties of shales are mostly associated with their nanoscale features and thus the SSA and CEC. These physicochemical properties, associated with petrophysical features, cannot be obtained from standard well logs (Josh et al., 2015).

SSA is a material property of solids that indicates the total surface area per unit mass; in other words, it defines the SSA of grains on the microscale. The electrical properties of clays and shales show a complex frequency response to water content, surface area, charge density, pore fluid salinity and microstructure (Josh et al., 2015). Clay minerals have high SSA areas in mudrocks, increasing progressively in magnitude from kaolinite (lowest) to illite to smectite (highest).

CEC is an important petrophysical parameter of a rock–fluid system. It controls how clay minerals affect reservoir properties such as porosity and permeability, and indicates how shale exchanges cations with an adjacent solution (Derkowski et al., 2015). CEC can also be described as the dispersibility of a shale as it undergoes reversible chemical reactions (Derkowski et al., 2015) and as the quantity of the available cations to be exchanged at a given pH – the number of negatively charged sites on the surface of the shale that can adhere to cations with positive charges (which pertains to the clay mineral layer charge) (Bunger et al., 2014). CEC is typically measured as milliequivalents (mEq) per 100 g of rock and indicates the sum of all the exchangeable soil cations that can be adsorbed at a specific pH (i.e. the number of negative charges and the capacity of the material to grasp cations) (Osman & Suter, 2000).

In general, SSA and CEC depend on the size distribution of fine grains and their shapes and texture, clay interlayers and the atomic structure of the clay minerals within them (i.e. the clay type and quantity). The surface area of a shale is predominantly due to kerogen and clay minerals and is influenced by factors such as kerogen type, thermal maturity, clay mineral content and type, overburden depth and moisture content. These determining factors are ultimately related to the geological formation and depositional environment of the shale (Cao et al., 2015).

There is a strong relationship between the mechanical properties of a clay-bearing shale and its chemistry. The ion exchange that occurs during the interaction of a shale with fluids leads to alterations in its behaviour so that it begins to act as a semi-permeable membrane. Ion exchange can affect hydraulic and osmotic flows and thus impact the stresses and pore pressure conditions around a wellbore. For instance, ion exchange can cause shale shrinkage or swelling depending on the chemistry of the fluid (Josh et al., 2015).

Shales are classified as leaky or nonideal osmotic membranes. The pressure difference (ΔP) between the pore fluid pressure inside the shale and the pressure outside the shale can be computed (Ewy, 2015) using equation (34):

$$\Delta P = \sigma \left(\frac{RT}{V} \right) \ln \left(\frac{a_{ws}}{a_{wf}} \right) \quad (34)$$

where R is the gas constant, T is the absolute temperature, V is the partial molar volume of water, a_{ws} and a_{wf} are the shale's water activity and fluid water activity in contact with the shale, and σ is the 'membrane efficiency'.

Membrane efficiency varies between 0 (indicating a non-selective shale) to 1 (indicating an ideal semi-permeable membrane). Thus, a membrane efficiency of less than 1 means ion transport is occurring to some degree (Ewy, 2015).

Ewy (2014) analysed the swelling/shrinkage of nine different preserved shale samples, each representative of a specific geological condition and in-situ stress, subjected to total suction. The outcomes of this study showed that shale typically swells when subjected to brine, even though the water activity of the brine might be less than the water activity of the shale. Swelling in shales and claystone occurs within the water-bound pore space, and the swelling magnitude directly relates to the increase in water content. Due to ion diffusion, shale pore water (free water) comes into equilibrium with the solutes of the exposed brine. Because of osmotic effects, a higher concentration of NaCl leads to less swelling and a lower increase in water content compared with lower NaCl concentrations, and this can be attributed to the osmotic relationships between shale pore water and the clay interlayer space. According to this same study, potassium, sodium and calcium (in this order, from most effective to least effective) prevent shale swelling (Ewy, 2014).

Ewy et al. (2008) evaluated variations in the confined compressive strength of four types of shales due to brine exposure. The main difference in the mineralogy of the shales was that two shale samples (shale 2 and shale 4) were low in kaolinite, while two samples (1 and 3) were high in kaolinite. The high CEC for shales 2 and 4 was attributed to the high amount of kaolinite. Shales 1 and 3 had more clay than the other two types. The results showed that exposure to 19% KCl strengthened the shales substantially, while exposure to 23% NaCl only slightly increased the shale matrix. On the other

hand, exposure to 14% NaCl and 22% CaCl₂ led to a slight decrease in the confined strength of the shales. Shales with higher porosity were weakened more than shales with higher compressive strength and lower porosity. The highest efficiency of KCl is due to the diffusion of potassium ions into the shale, which stabilises the clay and prevents swelling.

2.2.1. Clay mineralogy classifications

The main groups of clays are kaolinite, smectite, illite, halloysite, vermiculite and chlorite. The first

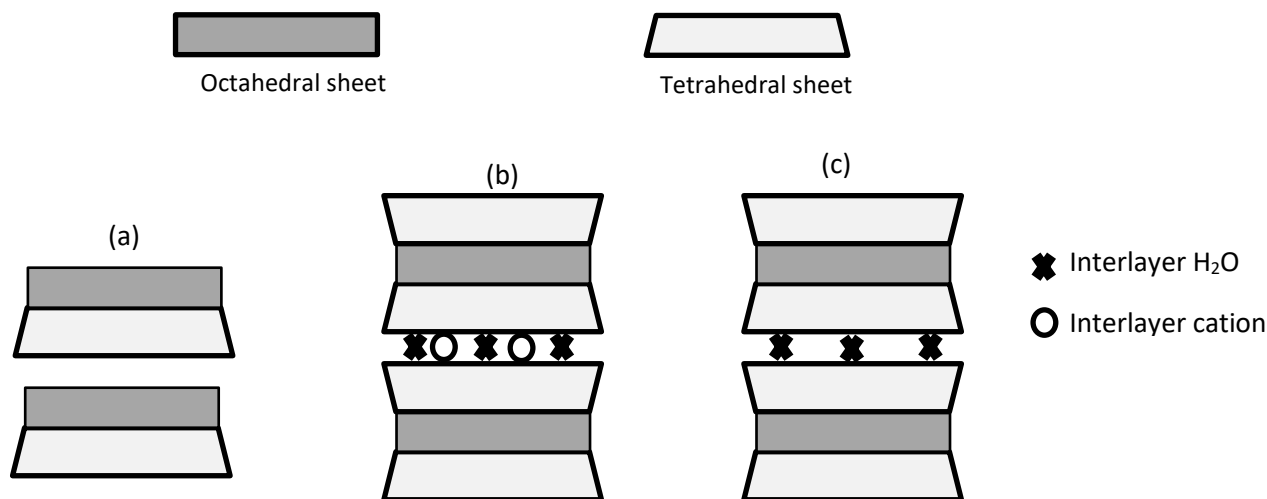


Figure 17: Schematic of the layered structures of key clay minerals: (a) kaolinite (1:1 structure), (b) smectite (2:1 structure) and (c) illite (2:1 structure) with less swelling, highlighting their different layer arrangements and interaction with water (Martín et al., 2022)

three are the most important in terms of drilling (Al-Arfaj et al., 2014). The response of each clay type to interaction with water depends on its crystal structure and the surface chemistry of clay and water. In addition to clays, shales have some amount of quartz and other minerals, which also affect the response of the shales to water exposure (Spagnoli et al., 2009). Figure 17 shows the sheet-like (layered) structure of clay minerals made up of two basic components: a tetrahedral silicon sheet (T) and an octahedral alumina sheet (O) (Qin et al., 2019). Most natural clays can be grouped as having a 1:1 structure (T-O), a 2:1 structure (T-O-T) or mixed layers (interstratified). The smectite group can also have a three-layered structure (T-O-T) (Qin et al., 2019).

The two-sheet structure of kaolinite comprises one silica tetrahedral sheet and one alumina octahedral sheet (Figure 17a). Na-smectite structure consists of a three-sheet composition: one alumina octahedral sheet located between two silica tetrahedral sheets (Figure 17b). The structure of illite is also composed of three layers: one octahedral sheet between two silica tetrahedral sheets (Figure 17c) (Spagnoli et al., 2009; Martín et al., 2022).

The most important minerals of the smectite group are montmorillonite, beidellite, nontronite, saponite and hectorite. Smectite clays carry variable net negative charge balanced by sodium (Na), calcium (Ca), magnesium (Mg) and/or hydrogen (H). The most distinctive feature of smectite clays is possession of exchangeable cations. The most common exchangeable ions are Ca, Mg, Na and H, but small amounts of exchangeable potassium (K) and lithium (Li) occur in some smectites.

Smectite clays are most developed, and also most stable, in surface and shallow subsurface environments. At depths (2000–4000 m), smectite clays undergo modifications and illite–smectite mixed layers (interstratified) form. At greater depths (more than 4000 m), the mixed layers change to illite through adsorption of K in interlayer positions or change to chlorite if Mg is plentiful (Odom, 1984).

Owing to the swelling potential of clay minerals with a 2:1 structure, swelling is generally seen in smectites, while kaolinite has the least swelling tendency due to its 1:1 structure (Ahmed et al., 2019a). In other words, the water absorption capacity of clay minerals is the determining factor. The hydration swelling sequence of clay minerals is montmorillonite > illite > kaolinite > chlorite (J. Lin, 2022).

Clay minerals are divided into four main groups (Karpiński & Szkodo, 2015):

- kaolinite – a 1:1 highly stable structure and a non-swelling clay with a comparatively small surface area and low adsorptive capacity; shales with a substantial amount of kaolinite are brittle (Gholami et al., 2018)
- smectites – a 2:1 structure that leads to swelling upon wetting and shrinking upon drying; they have a large surface area and relatively high adsorptive capacity
- illite – with a 2:1 structure, illite is a micaceous clay mineral that appears broadly in soils and sediments; its structure is similar to the smectites, with a lesser adsorptive and swelling/shrinking capacity and properties transitional between kaolinite and smectites
- chlorites – a 2:1 structure that doesn't exhibit significant hydration/swelling; however, the presence of chlorite can alter a shale's overall behaviour.

In addition, mixed-layer clay minerals are formed from several of these four basic groups. Table 12 summarises the clay mineral types and their associated properties (Ahmed et al., 2019b; Kim et al., 2020).

Table 12: Clay mineral and their associated properties (Kim et al., 2020; Ahmed et al., 2019)

Clay mineral	Layer arrangement	Cation exchange capacity (mEq/100 g)	Average surface area (m ² /g)	Density (g/cm ³)	Surface charge
Smectite	2:1	60–100	700	2–2.7	Negative
Illite	2:1	20–40	100	2.6–2.9	Negative
Chlorite	2:1	10–30	100	2.6–2.8	Positive
Kaolinite	1:1	3–15	20	2.5–2.7	Negative

2.3. Beetaloo sub-basin shale mineralogy studies

2.3.1. Velkerri Formation

The Velkerri Formation (Figure 5) is the oldest confirmed petroleum source rock in the Beetaloo Sub-basin. It has been mapped using seismic, gamma ray and resistivity logs and stretches over hundreds of kilometres (Gorter & Grey, 2012). The Velkerri dry gas play is the most materially and technically mature hydrocarbon resource in the Beetaloo Sub-basin (Côté et al., 2018).

Algazlan et al. (2019) performed an extensive set of petrophysical characterisations, including mineralogy, using samples from the Middle Velkerri Formation. The samples were characterised by a high quartz content of 52.6%, which significantly contributes to its brittleness. Other significant minerals detected included clay minerals such as illite-muscovite (15.7%) and illite-smectite (7.4%). Additionally, the detected phases include clinocllore (2.0%), albite (8.0%) and pyrite (9.5%).

2.3.2. Kyalla Formation

The Mesoproterozoic Kyalla Formation is subdivided into three primary source rock reservoirs, known informally by Origin Energy as 'upper Kyalla', 'middle Kyalla' and 'lower Kyalla' (Altmann et al., 2018; Baruch et al., 2018). Kyalla Formation has the largest clay content, while middle Velkerri has a higher amount of quartz and some carbonate-rich shales (Ruble et al., 2019). XRD investigations performed by Ruble et al. (2019)(Ruble et al., 2019) using samples obtained from 13 wells within the Mesoproterozoic Roper Group showed that in the Kyalla Formation clays are the most plentiful minerals in the samples, with the total clay content averaging about 54%. The dominant clay types are illite/mica, while quartz particles are the main non-clay type.

Another study carried out by Baruch et al. (2018) showed that the mineral composition of the Kyalla formation shales obtained from XRD analyses comprises 50–70% wt (on average) clays, and locally up to 80% wt, including illite, interstratified illite-smectite (I/S), mica, kaolinite and chlorite. Other constituents are quartz (40% wt average) and minor to trace amounts of feldspar, pyrite, siderite, calcite and dolomite. However, Altmann et al. (2018) dispute the high amount of clay (>65% wt) published by XRD analyses, saying it is misleading due to the inability of XRD to distinguish between muscovite/biotite and illite. Fourier-transform infrared spectroscopy (FTIR) data showed that almost half the traditional XRD illite/mica peak comprises muscovite/biotite (Hunziker et al., 1986).

The mineral composition of a rock is the most important factor determining whether its response will be brittle or ductile. The brittleness index (BI) quantifies the brittleness of a rock mass. Many different formulas for the brittleness index have been presented in the literature, and each uses a different approach and reflects different brittleness characteristics (D. Zhang et al., 2016). Equation (35) sets out one formula to quantify the brittleness index, with higher values representing more brittle rocks (Ruble et al., 2019):

$$BI = \frac{W(\text{QFM}) + W(\text{Carb})}{W(\text{total})} \approx \frac{W(\text{QFM}) + W(\text{Calcite}) + W(\text{Dolomite})}{W(\text{total})} \quad (35)$$

where $W(\text{QFM})$ represents the weights of quartz, feldspar and mica; $W(\text{Carb})$ is the weight of carbonate minerals, including dolomite, calcite and others; and $W(\text{total})$ is the total weight of minerals (D. Zhang et al., 2016).

Generally, a rock is brittle if it contains a high amount of quartz or carbonate; in contrast, rocks with a higher amount of clays are more ductile (Yasin et al., 2017).

2.3.3. Acquisition of core samples from Shenandoah-1A

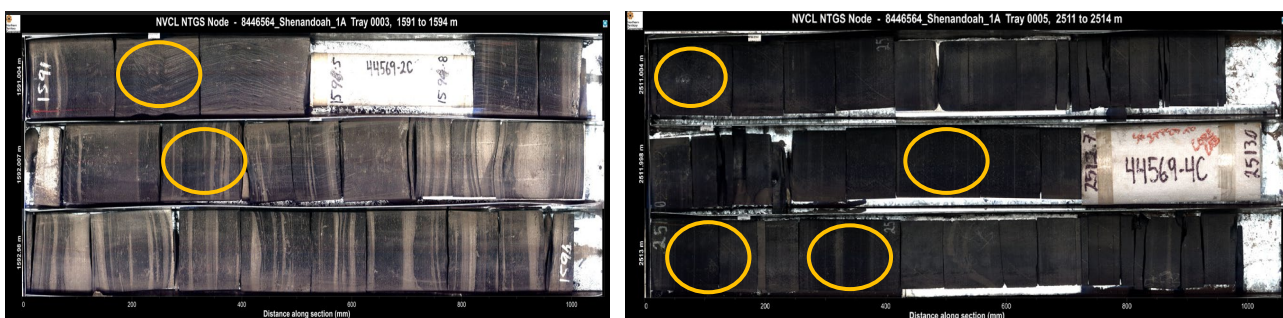


Figure 18: Core trays from Shenandoah-1A well in the Beetaloo Basin, stored in NTGS core library

In this study, samples were acquired from the Velkerri and Kyalla formations in the well Shenandoah-1A, specifically to determine whether their mineral compositions conformed to or diverged from previously published data. Figure 18 shows Hylogger images of the two core trays, and the samples (circled) were acquired from the Northern Territory Geological Survey (NTGS) core library. The samples were obtained from a depth of approximately 1590 m (Kyalla Formation) and 2316 m and 2511 m (Velkerri Formation). Notably, these samples were not preserved in oil but were exposed to air. This method of handling is particularly important to note because exposure to air can lead to oxidation of certain minerals.

The mineral composition of the samples (section 2.2) was determined through XRD, as well as by XRF (section 2.3). The chemomechanical properties were measured using the MicroRX apparatus (sections 2.6.1 and 2.6.2).

2.4. Determination of mineralogy by XRD and XRF

XRD is broadly employed as an analysis method for determining the quality and quantity of different minerals within geological specimens (Nayak & Singh, 2007; Zhou et al., 2018). Powder X-ray diffraction (XRD) was applied in this study to determine the mineralogical composition of shale samples obtained from Shenandoah-1A from a depth of 2300–2500 m and from 1500 m. A beam of X-rays was pointed at the powder samples, and the diffracted X-rays were detected at different angles. Each crystalline component generates a specific pattern that can be readily identified and

differentiated from the patterns of other components. Each pattern is a qualitative indicator of a specific mineral in terms of its crystal structure and lattice parameters (Holder & Schaak, 2019).

Quantitative XRD analysis results are given in Tables 13, 14 and 15. Clay minerals identified in the sample are smectite, kaolinite, interstratified illite–smectite, chlorite and mica. Other phases identified in the sample are quartz, pyrite, plagioclase feldspar (albite), hematite, anatase, marcasite, fluorapatite, siderite, calcite and dolomite.

Table 13 provides the quantitative XRD analysis results for bulk, micronized, and Ca-saturated samples from the Shenandoah-1A well at various depths in the Velkerri and Kyalla formations. The Velkerri Formation samples show high quartz content (46-47%) and significant amounts of mica (26-39%), with minor quantities of smectite, pyrite, and feldspar. The Kyalla Formation sample, taken at a depth of 1591.53 m, has a higher quartz content (53%) along with substantial interstratified illite–smectite (13%) and chlorite (10%).

Table 14 presents the XRD analysis results of the <0.2 μm fractions, focusing on the relative concentrations of minerals in the finer particles. The Velkerri Formation samples exhibit a higher concentration of mica (42-71%) and interstratified illite–smectite (23-48%), with less quartz (5-10%). The Kyalla Formation sample shows a higher concentration of interstratified illite–smectite (55%) and some chlorite (8%), confirming a higher clay content compared to the Velkerri samples.

Table 15 details the XRD results for the 0.2 to 2 μm fractions. The Velkerri Formation samples continue to show high quartz content (48-51%) and considerable amounts of mica (26-35%), with small amounts of smectite, kaolinite, and pyrite. The Kyalla Formation, however, demonstrates a lower quartz content (23%) but a higher concentration of interstratified illite–smectite (30%) and chlorite (19%), further reinforcing its clay-rich nature.

Together, these tables provide a comprehensive mineralogical analysis of the Velkerri and Kyalla formations at various grain sizes. The Velkerri Formation is dominated by quartz and mica, indicating brittle behavior, while the Kyalla Formation, with its higher clay content (especially in smaller fractions), shows greater potential for self-sealing through creep processes.

However, it is important to note that these samples were obtained from specific depths and may not fully represent the entire mineralogical composition of the Velkerri and Kyalla formations, which are hundreds of meters thick. The mineral content can vary significantly with depth, meaning that the findings from these particular samples might not capture the full variability of the formations.

Additionally, quartz-rich layers in shale cores tend to be more stable and resistant to degradation over time compared to clay-rich layers. Quartz, being a hard and chemically stable mineral, resists weathering and alteration, so it is often well-preserved in core samples. In contrast, clay minerals, especially smectites and other expandable clays, are more prone to degradation, swelling, or alteration when exposed to environmental factors such as humidity, temperature fluctuations, or changes in pore fluids. This disparity in preservation should be considered when evaluating the mineralogical data, as the clay-rich layers may have experienced some degree of degradation over time, affecting the overall interpretation of the samples' composition.

Table 13: Quantitative XRD analysis results (%wt) of the bulk, micronised and Ca-saturated samples

Minerals	Shenandoah-1A depth 2316.3 m (Velkerri Formation)	Shenandoah-1A depth 2511 m (Velkerri Formation)	Shenandoah-1A depth 1591.53 m (Kyalla Formation)
Smectite	<1	<1	
Kaolinite	1	1	
Interstratified illite– smectite	13	<1	13
Mica	26	39	19
Quartz	47	46	53
Pyrite	2	3	
Plagioclase feldspar	9	7	4
Hematite	<1	<1	
Anatase	1	<1	
Marcasite	1		
Fluorapatite	1		
Siderite		<1	
Calcite		1	
Dolomite		3	1
Chlorite			10

Table 14: Quantitative XRD analysis results (%wt) of <0.2 µm fractions of the samples (relative concentrations)

Minerals	Shenandoah-1A depth 2316.3 m (Velkerri Formation)	Shenandoah-1A depth 2511 m (Velkerri Formation)	Shenandoah-1A depth 1591.53 m (Kyalla Formation)
Smectite			
Kaolinite	<1	<1	
Interstratified illite– smectite	48	23	55
Mica	42	71	34
Quartz	10	5	3
Pyrite			
Plagioclase feldspar			
Chlorite			8

Table 15: Quantitative XRD analysis results (%wt) of 0.2 to 2 µm fractions of the samples (relative concentrations)

Minerals	Shenandoah-1A depth 2316.3 m (Velkerri Formation)	Shenandoah-1A depth 2511 m (Velkerri Formation)	Shenandoah-1A depth 1591.53 m (Kyalla Formation)
Smectite	<1	<1	
Kaolinite	1	1	
Interstratified illite– smectite	18	7	30
Mica	26	35	27
Quartz	48	51	23
Pyrite	<1	1	

Plagioclase feldspar	5	4	1
Hematite	<1	<1	
Anatase	<1	<1	
Siderite		<1	
Chlorite			19

Interstratified illite–smectite plays a major role in the samples’ chemomechanical responses. Illite and smectite both contain aluminosilicate layers that interchange with each other to form interlayers (Stixrude & Peacor, 2002). Interstratified illite–smectite clays emerge when layers of illite (a non-swelling clay) interchange with those of smectite (a swelling clay). The main difference between illite and smectite is attributed to the non-hydrated, interlayer cations (especially K⁺) in illite’s well-delineated positions (Garg & Skibsted, 2016).

XRF is another analytical technique that was applied to identify the mineralogy of the shales. XRF quantifies the characteristic X-rays emitted by components in a sample, which can be used to determine and measure its chemical composition. Table 16 lists the chemical composition of the samples from different depths of Shenandoah-1A well.

Table 16: Chemical composition of samples as measured by XRF

	SiO ₂ (%)	TiO ₂ (%)	Al ₂ O ₃ (%)	Fe ₂ O ₃ (%)	MnO (%)	MgO (%)	CaO (%)	Na ₂ O (%)	K ₂ O (%)	P ₂ O ₅ (%)	SO ₃ (%)	SUM (%)
Shenandoah-1A depth 2316.3 m	69.7	0.54	12.4	3.9	0.01	1.0	0.8	1.1	2.7	0.5	0.2	92.8
Shenandoah-1A depth 2511 m	65.6	0.49	12.0	4.3	0.05	1.4	1.7	0.8	2.8	0.4	0.2	89.62
Shenandoah-1A depth 1500 m	69.0	0.7	14.0	6.0	0.1	1.9	0.4	0.2	2.8	0.1	0.1	95.3

The details of the XRD patterns and XRF examinations, and the methodologies employed, are described in Appendices III and IV.

2.5. Commissioning the MicroRX rig

In this project, the chemoporoelastic parameters of the shale samples were determined by performing millimetre-scale experiments using a special apparatus, MicroRX, developed by CSIRO in 2014 (Bunger et al., 2014).

Figure 19 depicts the MicroRX components. The recommissioning procedures involved the following measures:

- upgrading the peristaltic pump to produce less residual heat (and less effect on internal temperatures)
- installing a linear variable differential transducer (LVDT) and signal conditioner to measure sample displacement to within microns

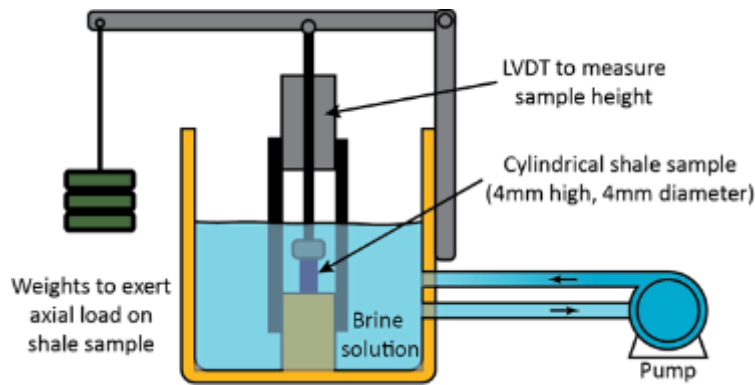


Figure 19: Components of the MicroRX apparatus

- installing an osmolarity sensor to monitor fluid salt concentrations
- installing external and internal temperature sensors to monitor noise sources that could affect the signal
- installing a data acquisition unit to integrate and digitise sensor outputs
- developing software applications to consolidate all data streams into a single user interface for monitoring and logging
- modifying the existing graphical user interface, developed by Bungler (2009) and Bungler et al. (2014)(Bungler, 2010; Bungler et al., 2014), based on the LVDT calibrations and the new format.

2.6. Measuring chemoporoelastic properties

2.6.1. Sample preparation

The water content of shale decreases when it is exposed to air, unless the relative humidity of the air is equal to or greater than the shale's native water activity. Native water activity is defined as the propensity of free water to escape pore spaces within shales when shales are preserved in their inherent condition (Ewy et al., 2008). Maintaining the water content in shale is important because loss of water can create shrinkage cracks and damage samples (Ewy, 2015).

Shale samples from different depths have, under zero stress, negative pore pressure. The capillary tension acts as an effective confining stress (a pseudo-cohesion) to keep the shale intact. When a shale sample under zero stress is exposed to air or brine, the capillary tension is released and the amount of interlayer water in the clay increases markedly, which results in swelling (Ewy, 2015). Swelling reduces the shale strength. However, swelling due to exposure to brine can be lessened if the shale is subjected to sufficient stress prior to this exposure, and even a low stress of 5 MPa will minimise swelling to less than 1% (Ewy, 2015). Accordingly, Ewy (2015) recommends that exposure to air prior to testing should be minimised and that a shale sample under zero stress should not contact water or brine. Ewy also lists the following guidelines to ensure sample preservation prior to testing:

- To prevent water evaporation and to minimise water transfer between the surrounding air and the shale, samples should be kept covered in sealed airtight containers under hydrocarbon.
- Samples should be kept in sealed airtight containers with a minimal volume of air.
- Samples should be kept in a desiccator or under managed relative humidity.
- Samples under zero stress should not be exposed to brine as it causes swelling.
- During cutting and trimming, samples should be kept wet using hydrocarbon.

In this study, we had no control over how the samples were preserved before arrival. However, after receiving them the pieces were stored in Shell Ondina 68 process oil. Cylindrical specimens, 4.47 mm in diameter and 4–5 mm long, were prepared using a hand-held, high-speed rotary drill press.

2.6.2. Governing equations

The constitutive equations relating to stress and strain can be divided into the deviatoric part (pure elastic) and the volumetric part (describes interactions between the solid matrix, the saturating fluid and the solute) (Sarout & Detournay, 2011):

$$\begin{pmatrix} \varepsilon \\ \xi \\ \theta \end{pmatrix} = \bar{C} \begin{pmatrix} \sigma \\ p_h \\ p_c \end{pmatrix} \quad (36)$$

where \bar{C} is the drained elastic volumetric compliance, ε represents the volumetric strain, ξ and θ represent, respectively, the Biot fluid content and relative ionic content to the mean stress σ , and p_h and p_c are the hydraulic pore pressure and the osmotic pore pressure, respectively.

Thus,

$$\bar{C} = \begin{pmatrix} C_d & bC_d & -\alpha bC_d \\ C_d & \frac{bC_d}{B} & -\beta \frac{bC_d}{B} \\ -\alpha bC_d & -\beta \frac{bC_d}{B} & -\gamma \end{pmatrix} \quad (37)$$

where B represents Skempton's coefficient, C_d represents the drained elastic compliance, and b , β and γ are Biot's constant, the chemohydraulic coupling coefficient and the chemical coupling coefficient, respectively.

The osmotic pressure can be computed based on Van't Hoff's law as $p_c = R_g T c_s$, where c_s is the molar salt concentration, R_g is the gas constant (8.31 J/mol K) and T is the absolute temperature:

$$2G\bar{\varepsilon} = \bar{\sigma} - \frac{3\nu}{1+\nu} \sigma \bar{I} + \frac{1-2\nu}{1+\nu} b\bar{I}(p_h - \alpha p_c), \quad (38)$$

where \bar{I} is the second rank identity tensor and G is the elastic shear modulus.

The linear momentum balance, considering zero body forces, can be defined by equation (39):

$$\nabla \cdot \bar{\sigma} = 0 - F^* \quad (39)$$

The strain–displacement relationship is given, for displacement vector u , by

$$\bar{\varepsilon} = \frac{1}{2} (\nabla \bar{u} + {}^T \nabla \bar{u}) \quad (40)$$

The mass balance equations for the fluid and ionic phases are defined in equations (41) and (42):

$$\nabla \cdot \bar{q} = -\dot{\xi} \quad (41)$$

$$\nabla \cdot \bar{w} = -\dot{\theta} \quad (42)$$

Coupled transport equations are described by equations (43) and (44):

$$\bar{q} = -\kappa \nabla p_h + \kappa \mathcal{R} \nabla p_c \quad (43)$$

$$\bar{w} = \mathcal{R} \kappa \nabla p_h - \frac{D_c}{N} \nabla p_c \quad (44)$$

where $N = RgT/vs$, vs signifies the molar volume of the salt ($vs = 0.03$ L/mol for NaCl), D_c is the effective ionic diffusivity, κ is the fluid mobility coefficient and \mathcal{R} is the reflection coefficient.

Hydraulic diffusivity is defined as follows:

$$D_h = \frac{\kappa}{S_s}, \quad S_s = b \left[\frac{\eta}{G} + \left(\frac{1}{B} - b \right) C_d \right], \quad \eta = \frac{b(1-2\nu)}{2(1-\nu)} \quad \text{and} \quad G = \frac{E}{2(1+\nu)} \quad (45)$$

2.6.3. Experimental procedures

1. The MicroRX rig is maintained at a temperature of 32°C in the apparatus oven.
2. The sample is submerged in an initial bath filled with brine (3.5% salinity: reverse osmosis water and NaCl).
3. Immediately after the second step, a hanger (0.016 kg) and one dead weight (0.1 kg) are applied as an initial mechanical/axial load, and the system is allowed to reach equilibrium.
4. An additional mechanical load (five more dead weights, each weighing 0.1 kg) is applied to the specimens through dead weights hanging from the end of the lever arm, and the system is then allowed to stabilise and reach equilibrium (the mechanical loading stage).
5. Finally, the sample is subjected to osmotic loading (radial) of 3–4 MPa (the osmotic pressure calculation is described in Appendix V) by changing the salinity of the brine surrounding the sample to 35%.
6. An LVDT measures the axial displacement of the sample while it is being subjected to mechanical and osmotic loads throughout the experiment.

After completing each test, the apparatus is cleaned and dried to avoid salt scale forming in the bath. The oven remains at 32°C to dry the system ready for the next test.

2.6.3.1. MicroRX data analysis procedures

Bunger (2009) and Bunger et al. (2014) presented a model employing the Bayesian inverse problem method to calculate material parameters, and this yields the best match between the model and the experimental data. Figure 20 demonstrates the schematic of a cylindrical specimen in MicroRX.

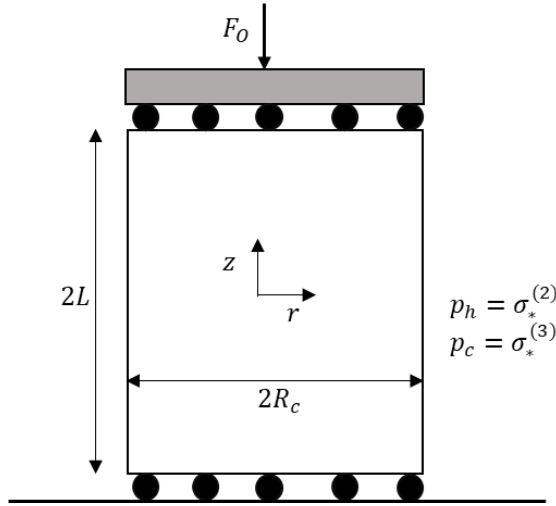


Figure 20: A cross-section of the cylindrical specimen subjected to three modes of loading (Yan et al., 2014)

At time $t = 0$, the three modes of loading are as follows (Bunger, 2010):

- the mechanical load, $\sigma_*^{(1)}$, due to the force F_0 applied to the top platen; $\sigma_*^{(1)} = \frac{F_0}{\pi R_c^2}$
- the hydraulic load, $\sigma_*^{(2)}$, from the sudden increase in pressure of the surrounding fluid bath
- the chemical load, $\sigma_*^{(3)}$, from the sudden increase in the salt concentration of the surrounding fluid bath; $\sigma_*^{(3)} = R_g T \Delta c_s$, where c_s is the molar concentration, R_g is the gas constant (8.31 J/mol K) and T is the absolute temperature.

The model delivers chemoporoelastic solutions for all three loading aspects of the experiment, including mechanical–hydraulic and osmotic (Bunger, 2010).

Axial mechanical loading

The state of the uniaxial stress immediately after applying load F_0 is :

$$\sigma_{zz} = \sigma_*^1 \quad (46)$$

$$\sigma = \sigma_*^1 / 3 \quad (47)$$

The same stress state returns when $t \rightarrow \infty$, after the pore and osmotic pressure fields have once more reached uniform values.

The early-time (undrained) case when $\xi = \theta = 0$ can be defined by equation (48) (by neglecting the osmotic terms into strain-displacement relation for via integration of equation (37)):

$$u_{zo}^{(1)} = \frac{-2LC_d\sigma_*^1}{3} \left(\frac{1}{1-2\nu} - \frac{bB}{3} \right) \quad (48)$$

At longer times, the transient pore and osmotic pressure fields have dissipated, and so $p_h = p_c = 0$. Equation (36) yields:

$$\varepsilon_\infty^1 = \frac{-C_d\sigma_*^1}{3}, \quad \xi_\infty^1 = \frac{-b C_d\sigma_*^1}{3}, \quad \theta_\infty^1 = \frac{bC_d\sigma_*^1\alpha}{3} \quad (49)$$

and the long-term (drained) displacement of the top platen, $u_{z\infty}^{(1)}$, follows directly from the integration of equation (37):

$$u_{z\infty}^{(1)} = \frac{-2LC_d\sigma_*^1}{3(1-2\nu)} \quad (50)$$

Stage 1 carries on for up to 6 h and provides an approximation of the mechanical properties of the shale, including its drained elastic compliance C_d , Poisson's ratio ν and hydraulic diffusivity D_h , assuming a shale Biot stress coefficient of $b = 0.98$ and Skempton pore pressure coefficient of $B = 0.98$. The poroelastic specific storage coefficient S is the increment of fluid content per unit change in pore pressure:

$$S = -\frac{\partial \zeta}{\partial \varepsilon} \quad (51)$$

Depending on the boundary conditions under which this parameter is measured, various specific storage coefficients can be defined: unconstrained specific storage under constant stress, constrained specific storage under zero strain, and uniaxial specific storage under uniaxial strain.

In the case of compliant shales, the specific storage coefficient S can be approximated as the mechanical compliance, on the assumption that the drained elastic compliance is in large part due to fluid draining from the material and that the compressibility of the released fluid is negligible compared with that of the solid constituents of the shale.

The specific storage coefficient S is related to the hydraulic diffusivity D_h and permeability k of the sample, as detailed in the following. Consequently, various diffusivity coefficients can be defined in relation to the corresponding specific storage coefficient.

Hydraulic diffusivity D_h

The hydraulic diffusivity D_h determines the diffusion rate of the pore fluid through the rock material. It is related to the permeability k of the rock and the dynamic viscosity μ of the pore fluid:

$$D_h = \frac{k}{\mu S} \quad (52)$$

Note that in the experimental configuration of the Micro-Rx, and in the corresponding chemoporoelastic model, diffusion of the pore fluid and ions occurs in the radial direction only, meaning that there is no flow through the end surfaces of a cylindrical specimen.

Ionic diffusivity D_c

The ionic diffusivity D_c determines the diffusion rate of the ions through the rock. For practical reasons, inversion of experimental data uses the ratio of the chemical to hydraulic diffusivities ω along with the hydraulic diffusivity D_h of the two diffusivities separately:

$$\omega = \frac{D_c}{D_h} \quad (53)$$

The diffusivity ratio is typically smaller than unity, as ionic diffusion is expected to proceed more slowly than hydraulic diffusion.

Osmotic loading (radial)

Osmotic loading (Bunger, 2010) is applied by changing the salinity of the solution. In the experimental configuration of the Micro-Rx, the chemomechanical coupling coefficient α is determined from the axial displacement of the shale specimen during chemical loading and defined by equation (54):

$$u_{z\infty}^{(3)} = \frac{-2LC_d b \alpha \sigma_*^3}{3} \quad (54)$$

The response of the sample to an increase in the NaCl brine concentration is used to estimate and refine the chemoporomechanical properties of the shale. α is the dimensionless chemomechanical coupling parameter coupling osmotic pressure and strain, and it relates the increment in osmotic pressure (salt content of the pore fluid) to the volumetric strain of the rock under drained conditions. α can be between 0 (no chemical activity) and 1 (perfect chemical activity; ion exclusion membrane).

It is also expected that during osmotic loading, the axial displacement of the specimen reaches an intermediate steady-state solution, as shown in equation (55):

$$u_{zint}^{(3)} = \frac{-2LC_d b R \sigma_*^3}{3} \quad (55)$$

where R (the reflection coefficient) is a dimensionless transport parameter characteristic of the shale–fluid system and corresponds to the resistance that the rock exhibits to ion transport (the rock efficiency).

The value of R can vary between 0 (mean ion flow is not hindered compared with water) and 1 (a perfect ion exclusion membrane).

To compute the shale reflection coefficient, the sample's shrinking/swelling response to chemical loading (from an increase in Na^+ and Cl^- ions concentration over approximately 12–16 h) is interpreted. The chemomechanical coupling parameter α , diffusivity ratio ω and reflection coefficient R are estimated using the asymptotic solutions for hydraulic and ionic diffusivity. In this study, the incorporation of salt concentration is defined such that the osmotic pressure is increased at the last stage to 3 MPa for all tests.

2.6.3.2. Measuring specific surface area

The SSA in fine-grained rocks can be determined via direct methods using gas adsorption, polar liquid retention, sedimentations and optical analyses.

There is a strong relationship between the mechanical properties of clay-bearing shales and their chemistry. The ion exchange that occurs during the shale's interactions with fluids leads to an

alteration in its behaviour such that the shale acts as a semi-permeable membrane. The ion exchange can impact hydraulic and osmotic flow and subsequently impact the stress and pore pressure conditions in the vicinity of a wellbore. For instance, ion exchange can cause shale shrinkage or swelling, depending on the chemistry of the fluid (Josh et al., 2014).

SSA and CEC are correlated with the reflection coefficient (R) and the chemomechanical coupling coefficient α (relating osmotic pressure to strain). CEC and SSA are strongly correlated to each other (Josh, 2014). Bungler et al. (2014) developed the following empirical equations that express the correlations between α and R with SSA:

$$\alpha \approx 0.0013 \times SSA + 0.115 \quad r^2 = 0.58 \quad (56)$$

$$R \approx 0.0012 \times SSA + 0.090 \quad r^2 = 0.56 \quad (57)$$

which are applicable when SSA is in the units of m^2/g .

SSA correlations with creep behaviour

The high magnitude of SSA in shales is attributed to the presence of a high amount of fine-grained clay minerals and/or organic matter containing a dense network of nanopores. The SSA and creep deformation magnitude are directly affected by the total clay mineral content (which depends on the clay type: illite, smectite, kaolinite or chlorite) and total organic carbon. Smectite and illite have the largest value of SSA, and therefore their volumetric fraction strongly controls the SSA value of shale (Mandal et al., 2021, 2022) Mandal et al., 2022).

SSA correlations with mineralogical constituents

As shown in Table 12, the range of values suggested for the SSA of smectite is 700–800 m^2/g , whereas the range for illite is 10–100 m^2/g (Josh, 2014; Ratner-Zohar et al., 1983).

2.6.3.3. Measuring cation exchange capacity

Bunger et al. (2014) developed the following empirical equations that state the correlations between α and R with CEC:

$$\alpha \approx 0.0075 \times CEC + 0.120 \quad r^2 = 0.64 \quad (58)$$

$$R \approx 0.0064 \times CEC + 0.109 \quad r^2 = 0.51 \quad (59)$$

which are applicable when CEC is in units of cmol/kg .

However, in this study, soluble cations and anions, CEC and exchangeable cations of the samples using NH_4 were determined using the methods detailed in Rayment and Higginson (1992).

The samples' exchangeable cations and CEC at pH 8.5 (oven-dried 60°C basis) are shown in Table 17 and discussed below:

- *Depth 2316.3 m – Velkerri*: This sample has a CEC of 24 $\text{cmol}(+)/\text{kg}$, which is the highest among the three samples. This high CEC indicates a high capacity for ion exchange, suggesting that the shale at this depth has a significant potential for chemical reactivity and swelling.
- *Depth 2511 m – Velkerri*: This sample has a slightly lower CEC of 20 $\text{cmol}(+)/\text{kg}$ compared with the 2316.3 m sample. It also shows a similar profile in exchangeable cations with a total of 3

cmol(+)/kg. The similarity in cation profile between the two Velkerri samples suggests comparable ion exchange properties, but this one may have slightly less chemical reactivity and swelling potential than the 2316.3 m sample.

- *Depth 1500 m – Kyalla*: This sample has the lowest CEC of 11 cmol(+)/kg, indicating the least chemical reactivity and swelling capacity among the three samples. The highest total exchangeable cations (5.7 cmol(+)/kg) with significantly higher exchangeable cations such as K and Na cations were observed. The low CEC could possibly be due to the presence of non-reactive (chemically stable) minerals, including chlorite (Tables 13 to 15).

Table 17: Exchangeable cations and CEC at pH 8.5 (oven-dried 60°C basis)

Sample	Exchangeable cations pH 8.5					CEC
	Ca	Mg	Na	K	Total	(NH ₄)
	cmol(+)/kg					
Shenandoah-1A, depth 2316.3 m – Velkerri	0.9	0.4	1.1	0.96	3	24
Shenandoah-1A, depth 2511 m – Velkerri	0.9	0.3	0.8	0.75	3	20
Shenandoah-1A, depth 1590 m – Kyalla	1.0	<0.2	1.7	2.86	5.7	11

The ‘total’ exchangeable cations reported in Table 17 represent the sum of the readily exchangeable cations (Ca, Mg, Na, K) at pH 8.5. However, it is important to note that the total may not always equal the simple sum of the individual cations due to potential rounding or experimental variations. Additionally, the total exchangeable cations might exclude minor cations that were not specifically measured or listed in Table 17.

In contrast, the CEC measured with NH₄⁺ reflects the total capacity of the sample to hold exchangeable cations when saturated with ammonium ions. This value includes the entire ion exchange potential of the sample, accounting for all types of exchangeable cations, not just those measured in the readily exchangeable cation test. As a result, the CEC values are often higher than the sum of the individual cations, indicating the shale’s overall ability to exchange ions, including those that may be less mobile or tightly bound.

CEC correlations with creep behaviour

Ozan et al. (2018) showed how smectite content, dielectric constant measurement, total TOC and clay content are the major material properties affecting creep behaviour. Chemical activity of the clays is also a factor controlling creep behaviour, as the most active clays (smectite > illite > kaolinite) usually show the highest time-dependent response.

2.7. Experimental results and discussion

The best-fit parameters were computed by fitting the full transient solution proposed by Bungler (2009) and Bungler et al. (2014) to the data via a Bayesian approach. The Bayesian inverse problem approach makes it possible to acquire material parameters in a way that delivers the best match between the model and experimental outcomes. In Bayesian inverse theory, the prior and posterior

data represent the probabilities of a model or hypothesis before and after observing data, respectively. The priors represent prior knowledge and assumptions, and then posterior information provides the fitted set of parameters.

First, C_d and v were obtained using equations (48) and (50) during the mechanical loading stage (incremental loading). In other words, during the mechanical loading stage equations (48) and (50) are simultaneously solved to obtain C_d and v . The values of C_d and v are subsequently integrated into the prior used while fitting the model to the transient data to find the best-fit values for C_d , v and D_h . The obtained best-fit values (C_d , v and D_h) from the mechanical loading stage are used to regularise the objective function for the osmotic loading stage. This is one of the advantages of the Bayesian approach, which allows the information to be carried from one loading step to the subsequent loading step. Searching for the minimum values for the objective function of the osmotic stage results in obtaining the best-fit values for C_d , v , D_h , $\omega = \frac{D_c}{D_h}$, R and α . The chemomechanical coupling parameter α relates the increment in osmotic pressure (salt content of the pore fluid) to the volumetric strain of the rock under drained conditions.

2.7.1. Measuring the chemoporoelastic properties of samples obtained from the Velkerri formation (depth 2316.3–2511 m)

Figures 21 and 22 illustrate displacement versus time throughout the whole experiment for Velkerri Formation samples acquired from the Shenandoah-1A well at depths of 2511 m and 2316 m, respectively.

Comparing the responses of the two samples as shown in Figures 21-22 highlights their different reactions to increasing osmotic pressure at the final stage of the experiments. As can be seen in Figure 21, after increasing the osmotic pressure, the sample undergoes shrinkage of 0.71 μm and then stabilises. In comparison, the sample shown in Figure 22 firstly experiences shrinkage of 0.423 μm , after which swelling starts and the displacement recovers. This contrast in behaviour can be attributed to the presence of interstratified illite–smectite in the sample obtained from a depth of 2316.3 m, as shown in Tables 13, 14 and 15.

In other words, Figure 22 shows that the sample's response to increased osmotic pressure is almost a flat response compared with the response of the sample in Figure 21. As shown in Figure 22, the sample experienced an instant shrinkage, after which the shrinkage partially recovered during the last 20 h of the test. The varying responses to increased osmotic pressure can be explained by differences in mineral content, particularly the significant variation in the amount of interstratified illite–smectite. Illite–smectite is one of the most common mixed-layer clay minerals (X. Wang & Wang, 2021) composed of alternating layers of two clay minerals – illite (a non-swelling clay) and smectite (a swelling clay) (Garg & Skibsted, 2016).

However, the degree of interstratification can vary: some interstratified illite–smectite clays are illite-dominant, while some can be smectite-dominant (Garg & Skibsted, 2016). Therefore, it is plausible

to assume that the interstratified illite–smectite clays in samples obtained from the depth of 2316 m are more smectite-dominant. Smectite has the highest CEC among clay minerals (Dewhurst et al., 2013), and Table 17 shows that Shenandoah-1A samples from a depth of 2316 m have higher CEC than the other samples.

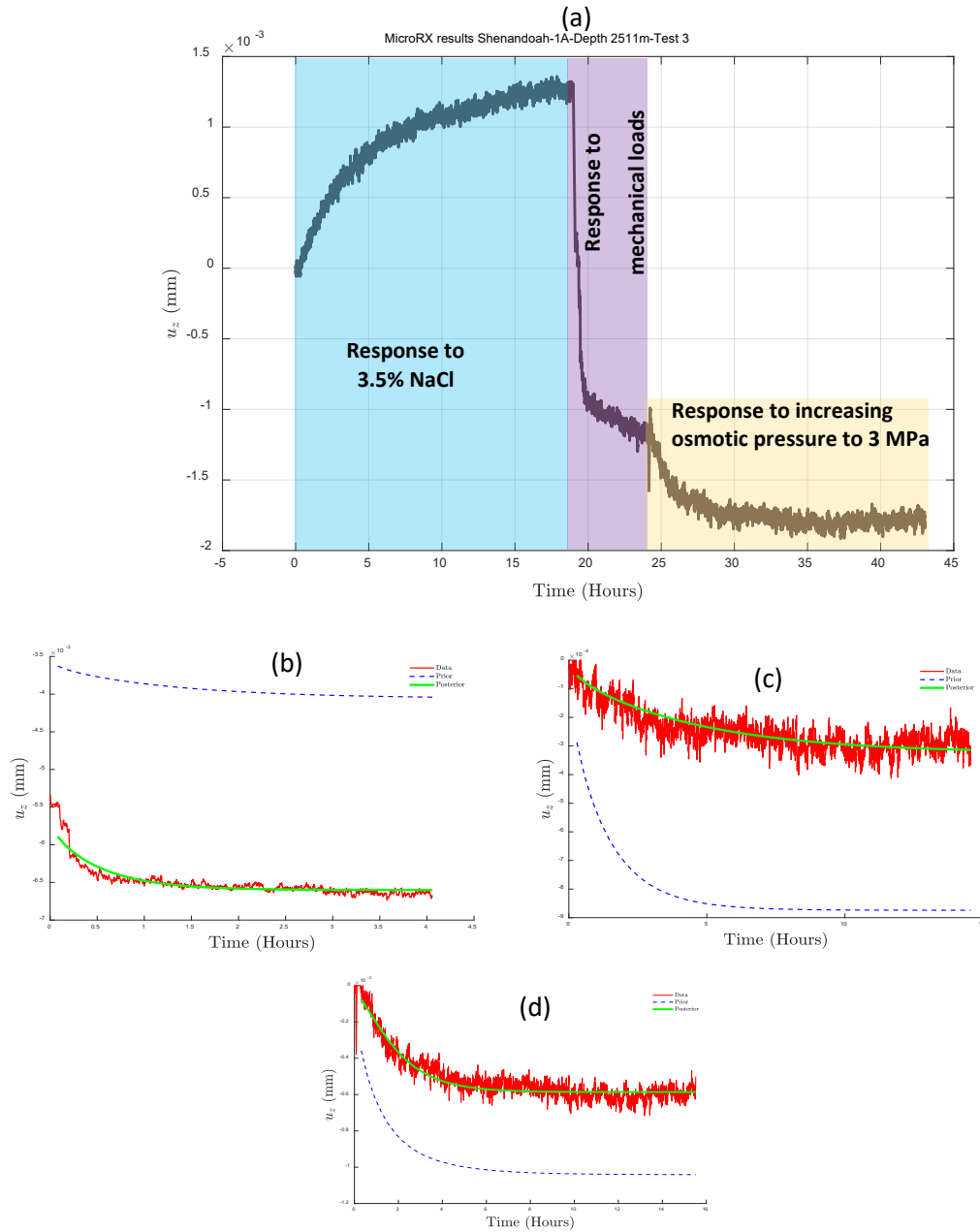


Figure 21: (a) Axial displacement vs time throughout the whole experiment at 32°C for a sample obtained from a depth of 2511 m; (b), (c) and (d) plots of axial displacements as a function of time throughout different stages of the mechanical and osmotic loading, along with the prior and posterior results

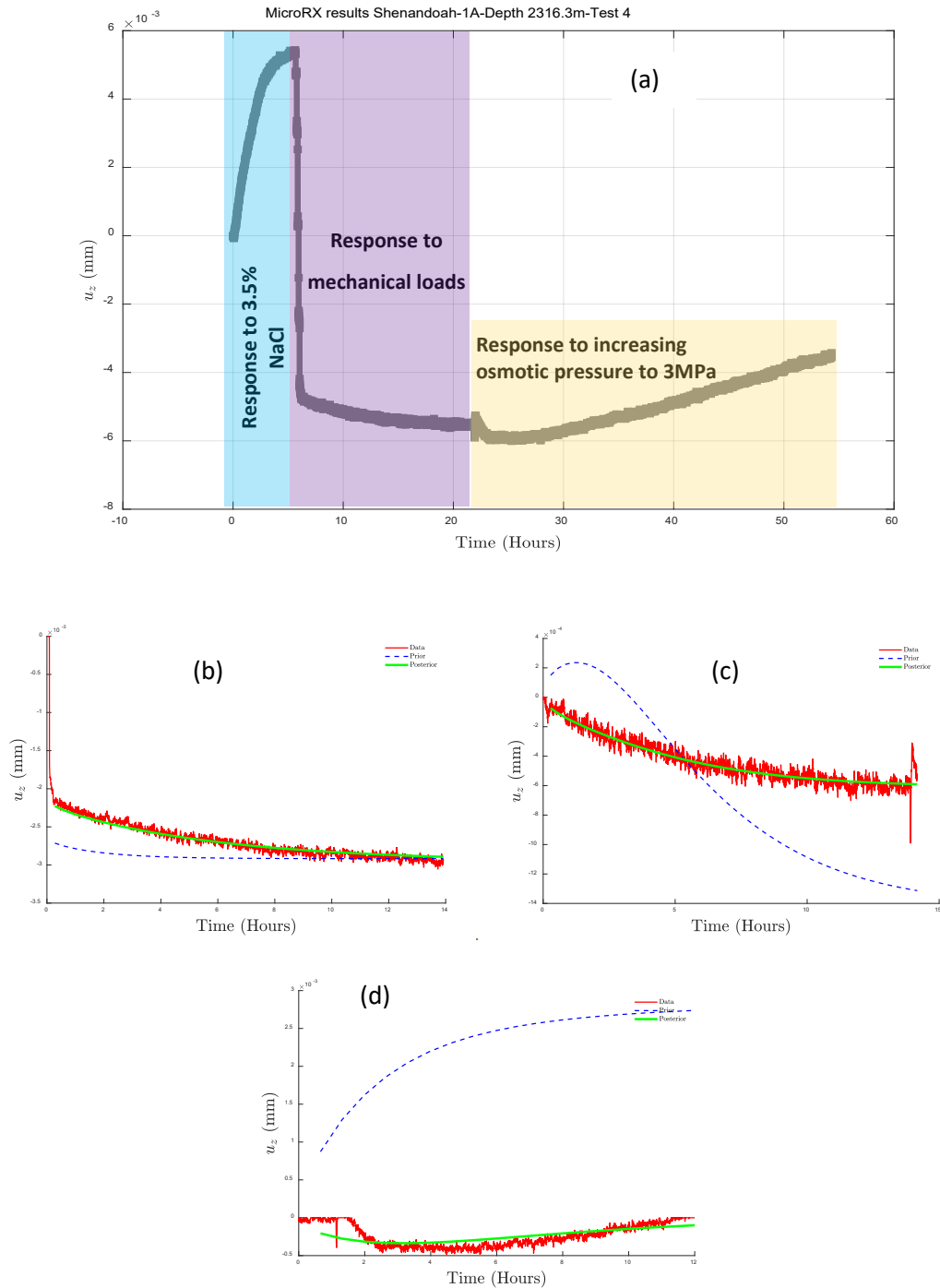


Figure 22: (a) Axial displacement vs time throughout the whole experiment at 32°C for a sample obtained from a depth of 2316 m; (b), (c) and (d) plots of axial displacements as a function of time throughout different stages of the mechanical and osmotic loading, along with the prior and posterior results

2.7.2. Measuring the chemoporoelastic properties of samples obtained from the Kyalla Formation (depth 1500 m)

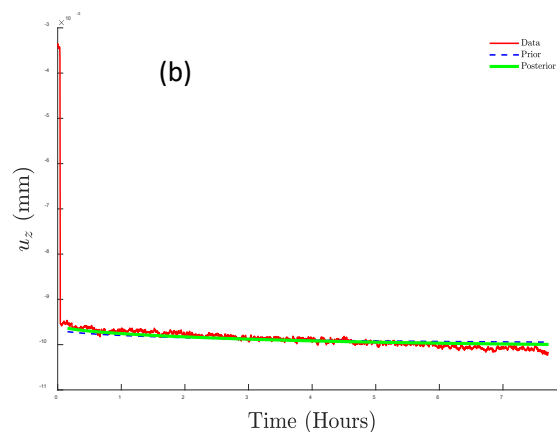
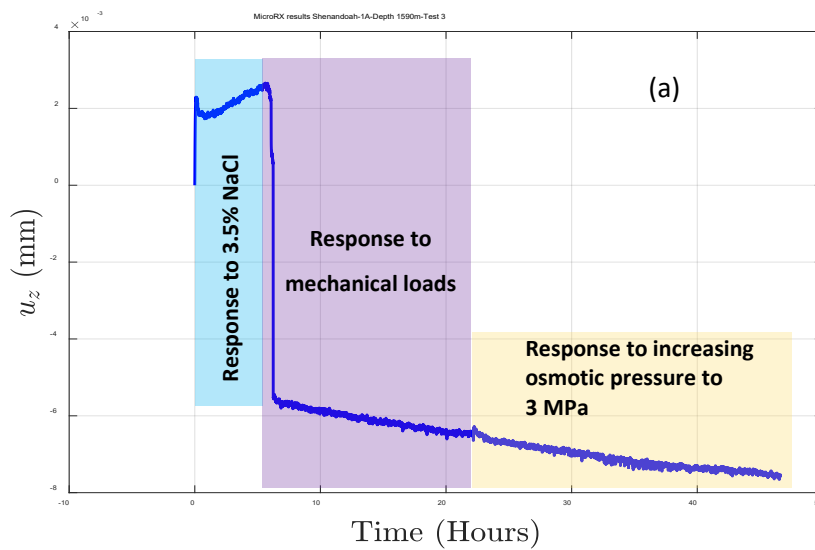
Figures 23a illustrates displacement versus time throughout the experiment for one of the Kyalla Formation samples acquired from the Shenandoah-1A well at a depth of 1590 m.

As shown in Figure 23b, the response of the Kyalla sample to increasing osmotic pressure is mostly monotonic shrinkage. Unfortunately, due to the existence of different kinds of clays, especially chlorite, equilibrium was not reached. Chlorite, with a high density (2.6–2.8 g/cm³) (Table 12), usually doesn't swell on exposure to water, and due to its positive surface charge, it may not assist water to penetrate the sample within the time period of the experiment (Kim et al., 2020).

Table 18 summarises the parameters measured by performing chemomechanical tests using MicroRX. The tests were repeated between three and five times, and the average of the most consistent tests in relation to each core are reported in the table.

Table 18: Results for tests on materials derived from each core

	α	\mathcal{R}	C (1/MPa)	ν	D_h	$\omega = D_c/D_h$
Shenandoah-1A, depth 2511 m – Velkerri						
Averaged	0.33	0.448	0.001371	0.31	2.30e-9	0.254
Shenandoah-1A, depth 2316.3 m – Velkerri						
Averaged	0.467	0.54	0.001738	0.045	3.81e-10	0.65
Shenandoah-1A, depth 1590 m – Kyalla						
Averaged	0.299	0.422	0.00194	0.229	3.48e-10	0.622



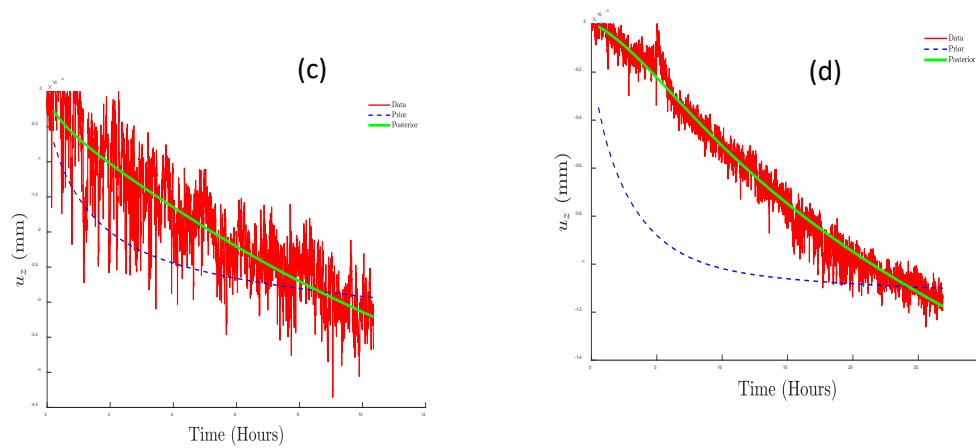


Figure 23: (a) Axial displacement vs time throughout the whole experiment at 32°C for a sample obtained from the depth of 1590 m; (b), (c) and (d) plots of axial displacements as a function of time throughout different stages of the mechanical and osmotic loading, along with the prior and posterior results

As shown in Table 18, shale samples obtained from different depths had different clay mineralogy (Tables 13, 14 and 15), and their responses differed when exposed to brine. Due to the presence of interstratified illite–smectite within the samples recovered from the Velkerri Formation at a depth of 231.3 m, it was found that, following instant shrinkage, they underwent a partial displacement recovery when osmotic pressure was increased (stage 3). However, samples acquired from the Velkerri Formation at a depth of 2511 m mostly showed a flat response (a minimal recovery) or monotonic shrinkage when osmotic pressure was increased.

The reflection coefficient R for samples acquired from 2316 m was greater than for samples from 2511 m, as shown in Table 18 (CEC is also greater for samples acquired from 2316 m). The reason is that the chemical reactivity/sensitivity or swelling capacity of shales is directly related to the magnitude of their CEC. In contrast, samples acquired from a depth of 1590 m had the lowest CEC of all three cores. During chemomechanical testing, the shale reactivity was also lower than the other samples. This can be attributed to the amount of chlorite and mica in these samples, since chlorite is a non-expanding mineral. The chemomechanical tests on the Kyalla samples were repeated five times; however, due to their low CEC, their responses to increased osmotic pressure were minimal. A possible explanation is the large amount of chlorite within the shale samples, and the high density of this material (2.6–2.8 g/cm³) (Table 17).

As described in section 2.1.1, the layered structure of clay minerals differs (1:1 or 2:1), and this directly affects their cation exchange capacity. As shown in Table 12, the exchange capacity depends on the magnitude of layer charge and the material’s ability to exchange cations in the interlayer space with external cations. The mineralogical composition of shales can impact and change CEC values significantly. However, as shown in Figure 17, substitution of cations occurs both in the interlayer space and in the tetrahedral or octahedral layers of a shale’s structure. Transformation of clay minerals therefore depends on their cation exchange capacity within the clay layers, and this change is evident on exposure to different downhole conditions, including pressure and temperature changes and the presence and concentrations of different chemicals.

The data presented in Tables 17 and 18 provide insights into the geochemical and chemomechanical properties of shale samples from different depths and formations. The exchangeable cations (Ca, Mg, Na and K) and CEC values (Table 17) indicate the ionic composition and reactivity of the shale samples. For instance, the sample from a depth of 2316.3 m in the Velkerri Formation shows relatively balanced cation content with a total of 3 mEq/100 g and a high CEC of 24 mEq/100 g, suggesting a higher capacity to hold and exchange cations. In contrast, the sample from 1500 m in the Kyalla Formation has a higher total cation content of 5.7 mEq/100 g but a significantly lower CEC of 11 mEq/100 g, indicating differences in potential reactivity.

Chemomechanical properties, detailed in Table 18, reveal variations in the mechanical behaviour and transport properties of the shale samples. The α parameter, which relates to chemomechanical coupling (relating osmotic pressure to strain), is highest for the Velkerri sample at a depth of 2316.3 m (0.467) and lowest for the Kyalla sample (0.299), implying differences in porosity and permeability. The \mathcal{R} parameter, indicating the rock's ability to deform, follows a similar trend, being highest for the Velkerri sample at a depth of 2316.3 m (0.54). The compliance (C) values, inversely proportional to stiffness, show that the Velkerri sample at a depth of 2316.3 m is the most compliant (0.0017381/MPa), while the Kyalla sample is the stiffest (0.001941/MPa).

The diffusivity (D_h) and the ratio ω (D_c/D_h), which indicate the ease of fluid transport through the shale, vary significantly among the samples. The Velkerri sample at a depth of 2316.3 m has the lowest D_h ($3.81e-10$ m²/s) but the highest ω (0.65), suggesting restricted fluid flow but higher selectivity in diffusion processes. These variations highlight the complex interplay between mineralogy, pore structure and mechanical properties that influence shale behaviour under different conditions.

2.8. Discussions

The data presented in Tables 17 and 18, along with the mineralogical information, provide a comprehensive understanding of the geochemical and chemomechanical properties of shale samples from different depths and formations in the Shenandoah-1A well.

2.8.1. Chemomechanical properties

The exchangeable cations and CEC values indicate the ionic composition and reactivity of the shale samples. For instance, the sample from the Velkerri Formation at a depth of 2316.3 m shows a balanced cation content (total 3 mEq/100g) and a high CEC (24 mEq/100g), suggesting a high capacity for ion exchange. This can be attributed to the presence of interstratified illite–smectite (13%), which is known for its high CEC.

Conversely, the sample from a depth of 2511 m in the Velkerri Formation, with a similar total cation content (3 mEq/100g), shows a lower CEC (20 mEq/100g), probably due to the lower content of interstratified illite–smectite (<1%) and a higher mica content (39%). Additionally, the higher quartz content in the fine fractions of this Velkerri sample might also contribute to the observed differences.

The sample from the Kyalla Formation at a depth of 1591.53 m exhibits the highest total cation content (5.7 mEq/100g) but a lower CEC (11 mEq/100g). This discrepancy might be related to the different mineralogical composition, with significant amounts of quartz (53%), chlorite (10%) and interstratified illite–smectite (13%). While the quartz content is comparable to that in the Velkerri samples, the high chlorite content in the Kyalla sample stands out. Chlorite typically has a lower CEC compared with other clay minerals, which could explain the lower overall CEC despite the higher total cation content. The differences in mica content between the samples also suggest varying influences on the CEC, with higher mica content in the Velkerri samples contributing to their distinctive properties.

It should be noted that these results are constrained by the number of samples tested, which may limit the generalisability of the findings. The variations in CEC among the samples can primarily be attributed to the differing contents of clay minerals, particularly interstratified illite–smectite and chlorite, as well as the presence of mica and quartz. These mineralogical differences highlight the complexity of the geochemical interactions within the formations and underscore the need for a detailed understanding of the mineral content to accurately assess the reactivity and hydrocarbon potential of the shales.

The sample from a depth of 2511 m in the Velkerri Formation shows a lower α value (0.33) and \mathcal{R} value (0.448), indicating less efficient ion exclusion and lower chemomechanical coupling. The Kyalla Formation sample, with the lowest α value (0.299) and an \mathcal{R} value of 0.422, demonstrates the least chemomechanical coupling and moderate resistance to ion transport. The mineralogical composition, particularly the quartz content, influences mechanical properties such as stiffness and compliance (0.00194 (1/MPa)).

The compliance (C) values indicate that the Kyalla sample is the stiffest (0.00194 1/MPa), while the Velkerri sample at a depth of 2316.3 m is the most compliant (0.001738 1/MPa). The diffusivity (D_h) and the ratio of effective to hydraulic diffusivity (ω) further emphasise the differences in fluid transport characteristics, with the Velkerri sample at a depth of 2316.3 m exhibiting the highest selectivity in diffusion processes ($\omega = 0.65$).

However, the differences in these parameters are not substantial, and additional factors must be considered. For instance, the quartz content in the finer fractions of the Velkerri Formation samples is higher than initially noted, which can influence the stiffness and compliance differently. The presence of chlorite and mica also plays a significant role. Chlorite content is higher in the Kyalla sample (10%), which typically has lower CEC and can contribute to the overall lower CEC observed. Mica content, higher in the Velkerri samples (39% at 2511 m), affects the rock's mechanical properties and ion exchange capacity.

Overall, these properties are crucial for understanding shale behaviour in response to mechanical and chemical stimuli, impacting its suitability for hydraulic fracturing and resource extraction. The slight variations in mineral content – particularly quartz, chlorite and mica – must be carefully considered to accurately interpret the mechanical and chemical properties of the shales.

2.9. Conclusion

This chapter sets out the outcomes of XRD and XRF testing performed on shale samples from the Velkerri and Kyalla formations in the Shenandoah-1A well located in the Beetaloo Sub-basin.

The mineralogy of a formation, specifically the amount of clay, plays a crucial role in determining whether the formation can act as a barrier to fluid flow or gas migration. The clay minerals identified in the Velkerri Formation at depths of 2316.3 m and 2511 m, across different fraction sizes, include kaolinite, mica (muscovite), and interstratified illite-smectite. Smectite was present in trace amounts (<1%) in some fractions. In contrast, the Kyalla Formation sample from 1591.53 m displayed significant amounts of chlorite, mica (muscovite), and interstratified illite-smectite across the fractions, particularly in the finer fractions, indicating a higher clay content and potentially greater suitability as a self-sealing barrier.

It is important to acknowledge that the samples examined were obtained from specific depths and may not fully capture the complete mineralogical variability of the Velkerri and Kyalla formations, which extend over several hundred meters. Mineral composition can vary significantly with depth, meaning the data from these samples might not represent the entire formations. Additionally, quartz-rich layers in shale tend to be more stable and less prone to degradation over time compared to clay-rich layers. Quartz, being a durable and chemically stable mineral, remains well-preserved in core samples, even after prolonged storage. In contrast, clay minerals, particularly smectites and other expandable clays, are more vulnerable to degradation, swelling, or alteration when exposed to environmental factors such as humidity, temperature changes, or variations in pore fluids. For the Shenandoah-1 cores, it is likely that the quartz-rich layers are better preserved than the clay-rich ones, which may have deteriorated over time. This should be considered when interpreting the mineralogical data, as the current condition of the cores may not fully reflect their original composition at the time of extraction.

The CEC of the samples was also measured using ammonium (NH_4^+); those obtained from the Velkerri shale (2316 m) had the greatest CEC (24), and those obtained from the Kyalla shale (1590 m) had the lowest (Table 17). These findings can be attributed to the positive charge of chlorite, which tends to hinder the penetration of water within the sample over the period of the experiments, as well as the relatively low CEC of chlorite minerals (Table 18).

The chemoporoelastic parameters describing the interaction of the shale samples with brine were measured. Because the samples were retrieved from different shale formations, their mineralogy was different and their response to increasing osmotic pressure also differed. The mineralogy of the Velkerri samples obtained from depths of 2316 m and 2511 m were similar except for the amount of interstratified illite–smectite, which was greater in the shallower sample (samples obtained from Kyalla Formation). For these samples, equilibrium was reached at the end of each loading stage (mechanical and osmotic), and the chemoporoelastic parameters could be measured using the model suggested by Bungler et al. (2010). The average of the measured parameters from the most consistent tests are reported in Table 18.

The Kyalla sample retrieved from a depth of 1590 m had a different mineral composition due to the substantial amount of chlorite within it. Although chlorite is classified as a non-expanding clay, its presence made a difference in the sample's response to increasing osmotic pressure. The chemical reactivity of the sample was found to be low. The variability is probably due to its low CEC (Table 17) as well as the presence of interstratified illite–smectite possessing negative charges and chlorite with positive ones. The chemomechanical tests on the Kyalla sample were repeated five times, and the average measured parameters are listed in Table 18.

In general, the absence of smectite (the clay mineral known for its significant swelling capacity) in both the Kyalla and Velkerri samples might explain the generally moderate to low swelling behaviour observed across the samples. However, the presence of chlorite in the Kyalla sample, which typically has a lower swelling capacity, and the substantial amount of mica in the Velkerri samples, which also has limited swelling potential, further influences the overall swelling behaviour.

This mineralogical analysis demonstrates that the specific types of clay and other minerals present in the samples play a critical role in determining their chemical reactivity and swelling potential. Despite the Kyalla sample's higher clay content, the types of clay minerals present (such as chlorite and illite–smectite) are less prone to swelling, which explains its lower swelling capacity compared with what might be expected from its clay content alone.

When seeking a suitable chemical solution to stimulate shale creep strains, an important first step is to understand the shale's chemoporomechanical parameters so that shale–fluid interactions can be predicted. The model employed predicts two types of behaviour depending on the ratio between the reflection coefficient and the chemomechanical coupling coefficient. The reflection coefficient and coupling coefficient have been determined and they directly correlate with CEC and SSA, again highlighting the importance of determining the mineral and chemical compositions of a shale prior to creep testing.

Chapter 3

Performing triaxial creep tests, investigating the effect of pore fluid chemistry on creep behaviour and interpreting the results

3.1. Introduction

Creep is defined as the inelastic, time-dependent deformation of rock. Figure 24a shows the three distinct stages of creep. The creep strain (Figure 24a) can be computed by subtracting the instantaneous deformation (ϵ_0) from the total strain.

- In the primary stage, the creep rate decreases quickly over time (also called transient creep).
- In the secondary stage, the creep rate stabilises (Figure 24b), exhibiting minimal changes over time (steady-state stage). A steady state is reached as an equilibrium between two conflicting influences: strain hardening, which diminishes the creep rate, and softening or recovery mechanisms, which cause the creep rate to increase. There is no increase in dislocation density, and if there is a sub-grain structure, it does not undergo further refinement as strain increases.
- In the tertiary stage, accelerated creep is observed. Throughout this stage, the creep rate is

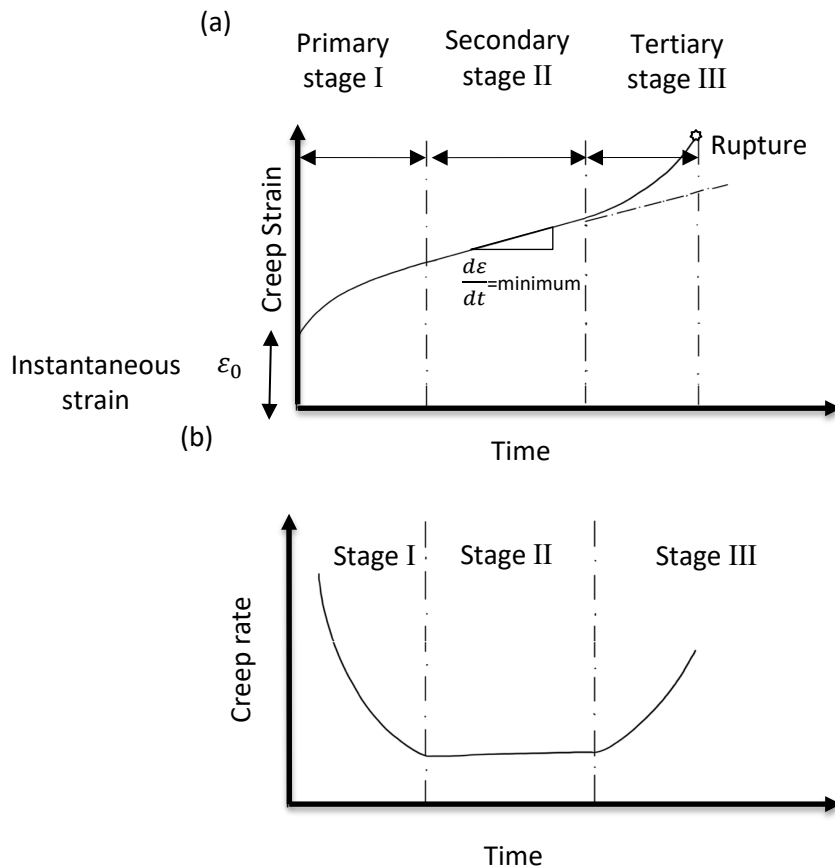


Figure 24: (a) Creep stages versus time; (b) creep rate variations as a function of time

greater than that in the steady-state stage and it constantly increases until the material fails (Bhaduri, 2018).

3.2. Downscaled laboratory experiments

Examining the mechanical properties of reservoir rocks in the laboratory often involves measuring elastic properties for applications such as interpreting seismic and sonic data or assessing rock strength for issues including wellbore stability. However, to accurately predict how reservoirs will behave over extended periods it is also crucial to investigate the time-dependent inelastic properties of rock samples. Laboratory studies have demonstrated that, over time, shales deform through a combination of elastic and visco-plastic behaviour (Sone & Zoback, 2014). This study focuses on the time-dependent behaviour and the constitutive relationships between stress, strain and time. The results are interpreted by linear viscoelastic theory to quantitatively assess the geomechanical effect of viscous time-dependent deformations over engineering and geological time scales.

3.2.1. Received core collection

Geomechanics testing as reported in this section starts with the availability of suitable material from which a set of companion samples representative of the formation of interest can be prepared. The test destroys material from a particular horizon/depth, so comparing data obtained under different saturated conditions requires that the samples be homogeneous and cohesive while they are extracted from a plug. Sample selection and preparation are therefore critical and often challenging for shale formations not properly preserved after retrieval.

For this study, CSIRO was supplied with material from the Northern Territory Geological Survey (NTGS) core library, involving five core sections from Jamison-1 and Shenandoah-1A wellbores, as reported in Table 19. The cores were old, unpreserved, and showed evidence of desiccation along the bedding planes, highlighted by sub-horizontal microfractures at the core surfaces (Figures 25–29).

Table 19: Core sections of Jamison-1 and Shenandoah-1A drill holes received from the NTGS library

Drill hole name	Diameter	Depth interval	Purpose	Status
Shenandoah 1A	100 mm	1591.42 – 1591.53 m	Mineralogy/geomechanics	Subsample prepared
Shenandoah 1A	100 mm	1592.23– 1592.37 m	Mineralogy/geomechanics	Untouched/ returned to NTGS
Shenandoah 1A	87 mm	2512.40– 2512.54 m	Mineralogy/geomechanics	Untouched/ returned to NTGS
Shenandoah 1A	87 mm	2513.25– 2513.42 m	Mineralogy/geomechanics	Untouched/ returned to NTGS

Jamison-1	62 mm	1025.75– 1025.85 m	Mineralogy/geomechanics	Untouched/ returned to NTGS
------------------	-------	-----------------------	-------------------------	-----------------------------------

The cores were systematically imaged using a Siemens SOMATOM, a well-known medical X-ray computed tomography (XRCT) scanner (helical image acquisition at 140 kV and 500 mAs with the smallest field of view of 4 cm). The reconstructed 3D XRCT image data have an optimal voxel size of ~ 100 x 100 x 100 µm.

Figures 25 to 29 demonstrate longitudinal and transversal XRCT 2D views centred in each of the core sections. Based on XRCT imaging, all sections exhibited various degrees of fracturing perpendicular to the core axes, which prevented further sampling. This issue is primarily caused by non-preservation of the cores, which lead to drying and desiccation along the weaker bedding planes and post-recovery stress relief. As testing required a minimum sample length of 50 mm, the Kyalla Formation (from a depth of 1591.42 m to 1591.53 m) appeared to be the only suitable core for further geomechanical testing. All the other cores were returned intact to NTGS.

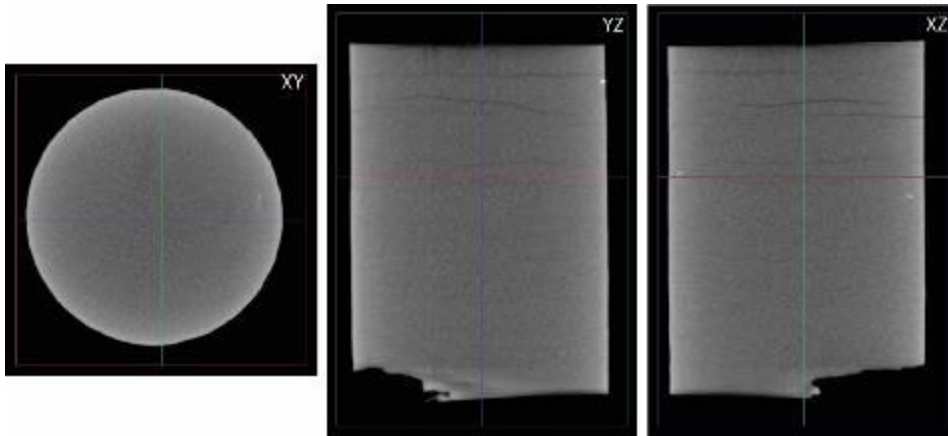


Figure 25: Axial and longitudinal XRCT 2D slices obtained on core section Shenandoah-1A (depth 1591.42–1591.53 m)

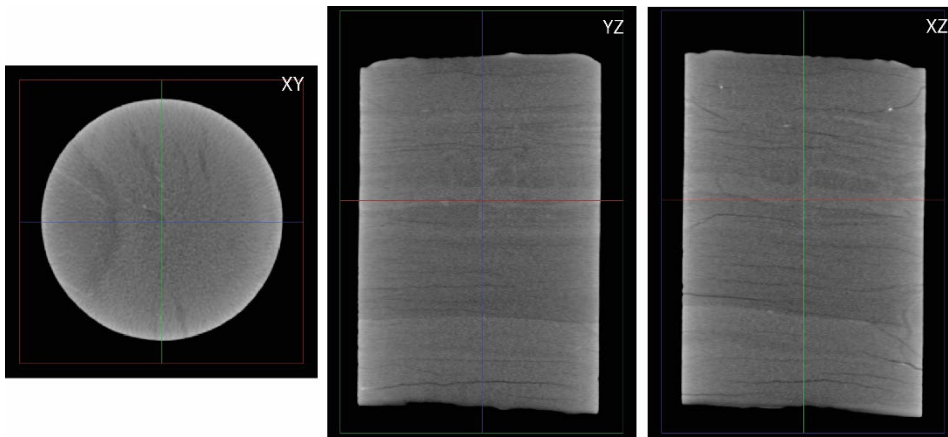


Figure 26: Axial and longitudinal XRCT 2D slices obtained on core section Shenandoah-1A (depth 1592.23–1592.37 m)

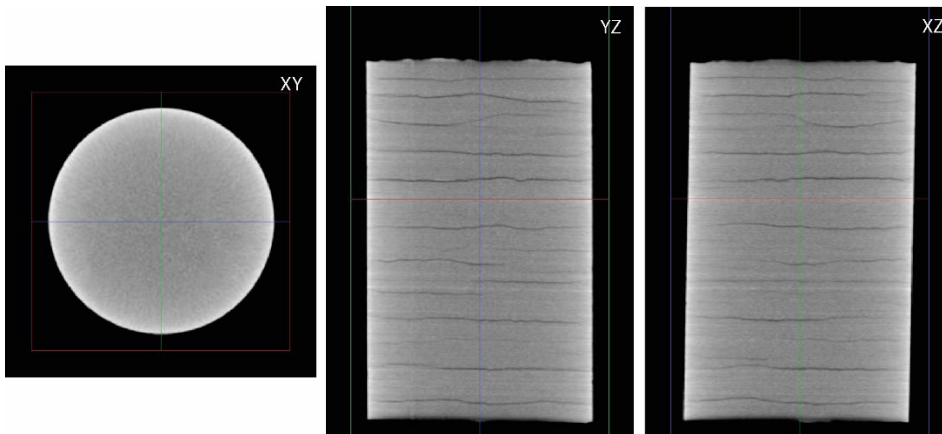


Figure 27: Axial and longitudinal XRCT 2D slices obtained on core section Shenandoah-1A (depth 2512.40–2512.54 m)

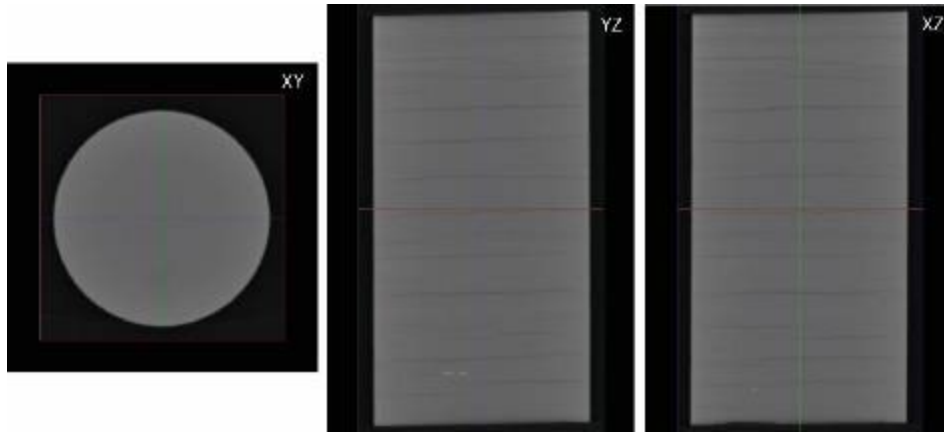


Figure 28: Axial and longitudinal XRCT 2D slices obtained on core section Shenandoah-1A (depth 2513.25–2513.42 m)

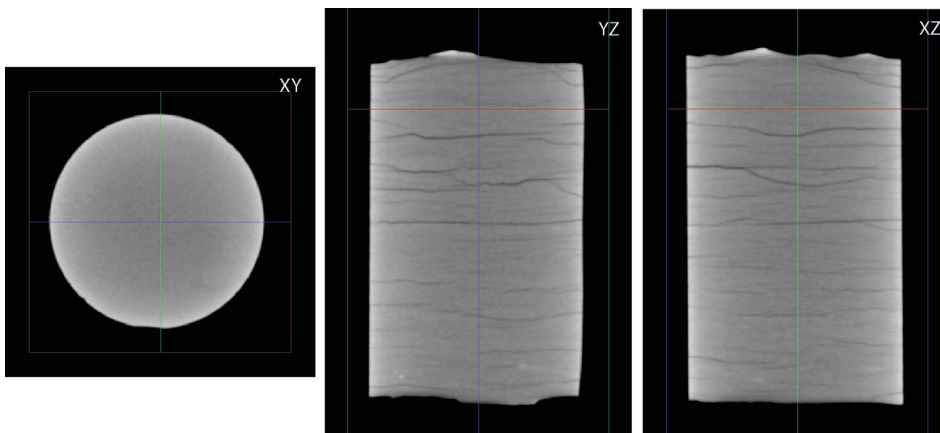


Figure 29: Axial and longitudinal XRCT 2D slices obtained on core section Jamison-1 (depth 1025.75–1025.85 m)

3.2.2. Sample preparation and collection

Four companion samples were extracted from Shenandoah-1 (depth 1591.42–1591.53 m). Since the core material was dry, samples were prepared under dry conditions to avoid exposure to non-equilibrated water. A Murg diamond-wire bandsaw was used to take core plugs, and these plugs were finished off with a cylindrical grinder. This method enabled significantly better core plugs to be recovered from these particularly difficult-to-prepare rocks. Shales are at their weakest in tension parallel to the bedding, and so rotary core plugs often lead to discing (due to closely spaced fractures developing parallel to the fabric anisotropy from induced torsional stresses). By using a diamond-wire bandsaw, however, no stress is induced by torque, so plugs can be taken from more difficult rocks – like shale – without imposing stresses on intrinsic planes of weakness, resulting in better plugs and improved recovery rates.

A section of the core was also cut and ground into 200 g of powder which, for re-saturation purposes, was chemically equilibrated with brine. Similar powder was also used to measure the grain density of the samples. The equilibrated brine was used to run the creep test, described in detail in

section 3.4.3. The brine was prepared by diluting 50 cc (i.e. roughly 140 g of powder) in 1.95 L of deionised water to make up a total of 2 L of solution. The powder was maintained in suspension with a magnetic stirrer, and the conductivity of the solution was monitored until equilibrium was reached. The chemical composition of the solution was measured for different salts (Table 20).

Table 20: Measured chemical composition of brine equilibrated with shale powder

Sample	Unit	Practical quantification limit (PQL)	Concentration
CATIONS			
Sodium	mg/L	0.5	140
Potassium	mg/L	0.5	21
Calcium	mg/L	0.5	22
Magnesium	mg/L	0.5	6.5
Hardness as CaCO ₃	mg/L	3	31
METALS			
Iron	mg/L	0.01	0.026
Strontium	mg/L	0.001	0.180
INORGANICS			
Bromide	mg/L	0.5	0.9
Chloride	mg/L	1	100
Fluoride	mg/L	0.1	<0.1
Nitrates as N	mg/L	0.005	0.018
Phosphate as P	mg/L	0.005	<0.005
Sulfate	mg/L	1	58

The dimensions of the collected plugs, their properties and the type of test conducted are reported in Table 21.

Table 21: Samples available for geomechanical and creep testing

Sample ID	Length (mm)	Diameter (mm)	Dry mass (g)	Sat. mass (g)	Dry bulk density (g/cc)	Wet bulk density (g/cc)	Grain density (g/cc)	Porosity (%)	Test
3991	54.89	25.45	73.06	N/A	2.616	N/A	2.768	N/A	STXL dry
3992	55.43	25.44	73.67	N/A	2.615	N/A	2.768	N/A	MSTXL creep dry

3993	54.01	25.40	71.62	72.57	2.617	2.651	2.768	5.53	MSTXL creep brine sat.
3994	53.40	25.40	70.77	71.61	2.615	2.646	2.768	5.48	MSTXL creep Na: SiO ₂ sat.

To reach full saturation, the plugs were placed in a dedicated saturation cell, which was vacuumed for 6 h before filling it with the saturating fluid. The fluid pressure was maintained at 2.5 MPa through a separator for 2 weeks. The wet mass of the sample was then measured, and the porosity evaluated and compared with that measured using the shale grain density. The results of the MSTXL creep test on samples 3993 and 3994 are discussed in sections 3.4.3 and 3.4.4, respectively. Figures 30 to 33 show the XRCT scans and photographs of the samples. As seen on the XRCT scans, the samples are not affected by internal heterogeneity or fractures and can thus be considered comparable.

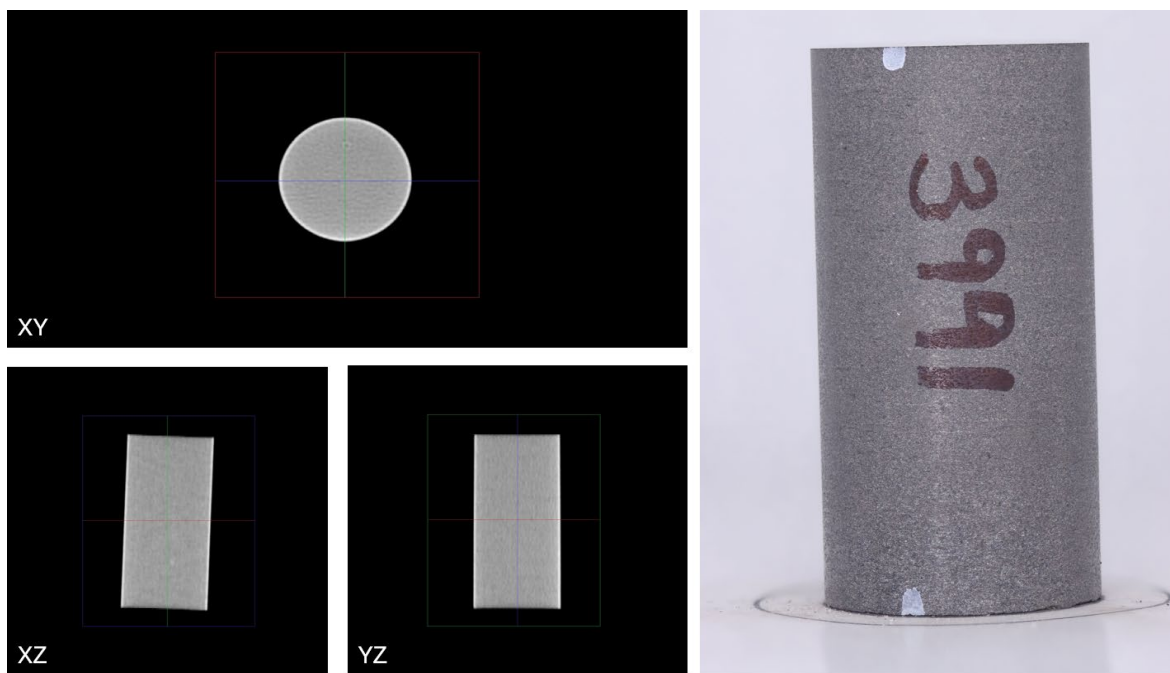


Figure 30: Axial and longitudinal XRCT 2D slices (a) and a picture of sample 3991 before STXL testing (b)

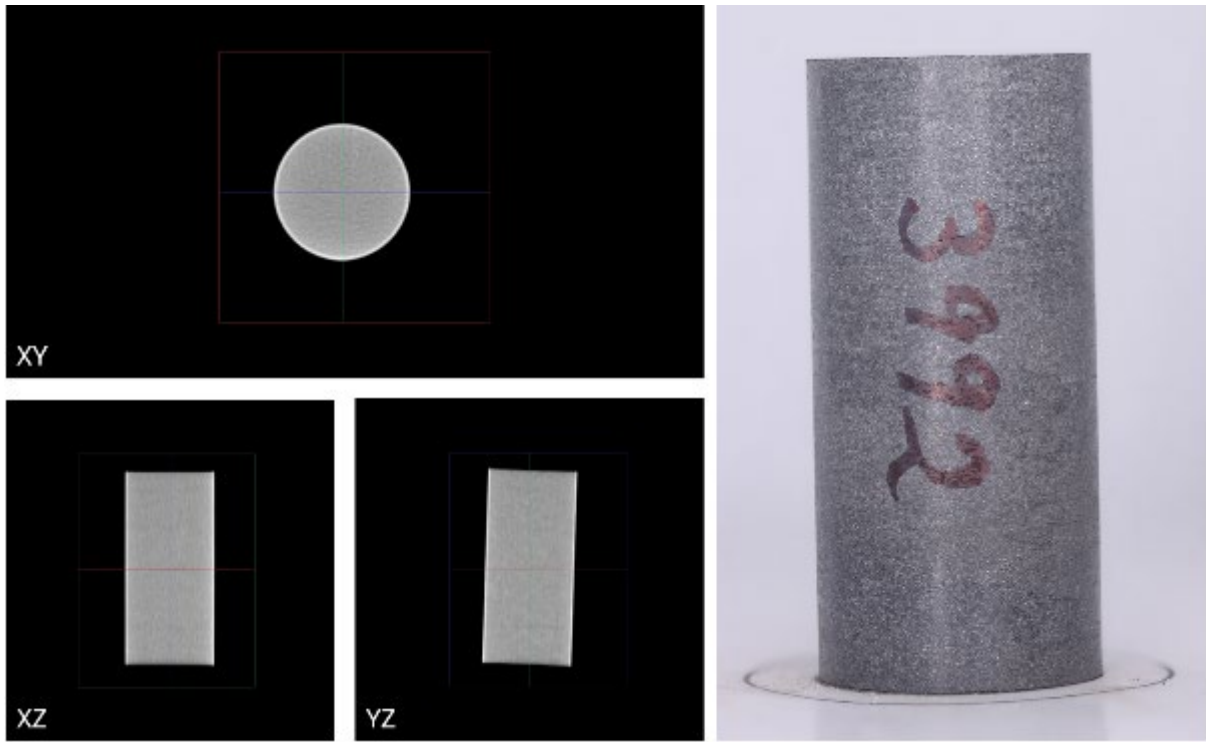


Figure 31: Axial and longitudinal XRCT 2D slices (a) and a picture of sample 3992 before dry creep MSTXL testing (b)

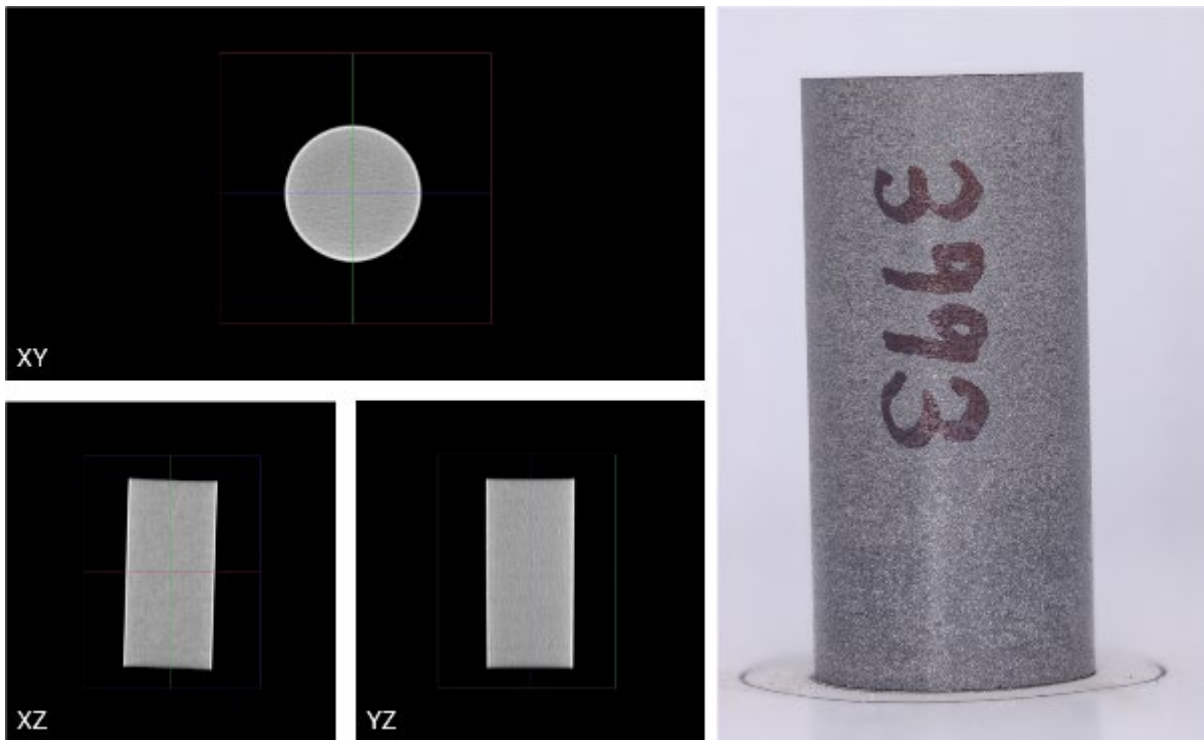


Figure 32: Axial and longitudinal XRCT 2D slices (a) and a picture of sample 3993 before brine saturation and creep MSTXL testing (b)



Figure 33: Axial and longitudinal XRCT 2D slices (a) and a picture of sample 3994 before sodium silicate solution saturation and creep MSTXL testing (b)

3.2.3. Geomechanical testing equipment

STXL and MSTXL tests were conducted using autonomous triaxial cells (ATCs) with a capacity of up to 65 MPa and operating at temperatures up to 100°C, with provision for measurement of sample axial and radial deformations, axial load (up to 400 kN), and cell and pore pressures (Figure 34).

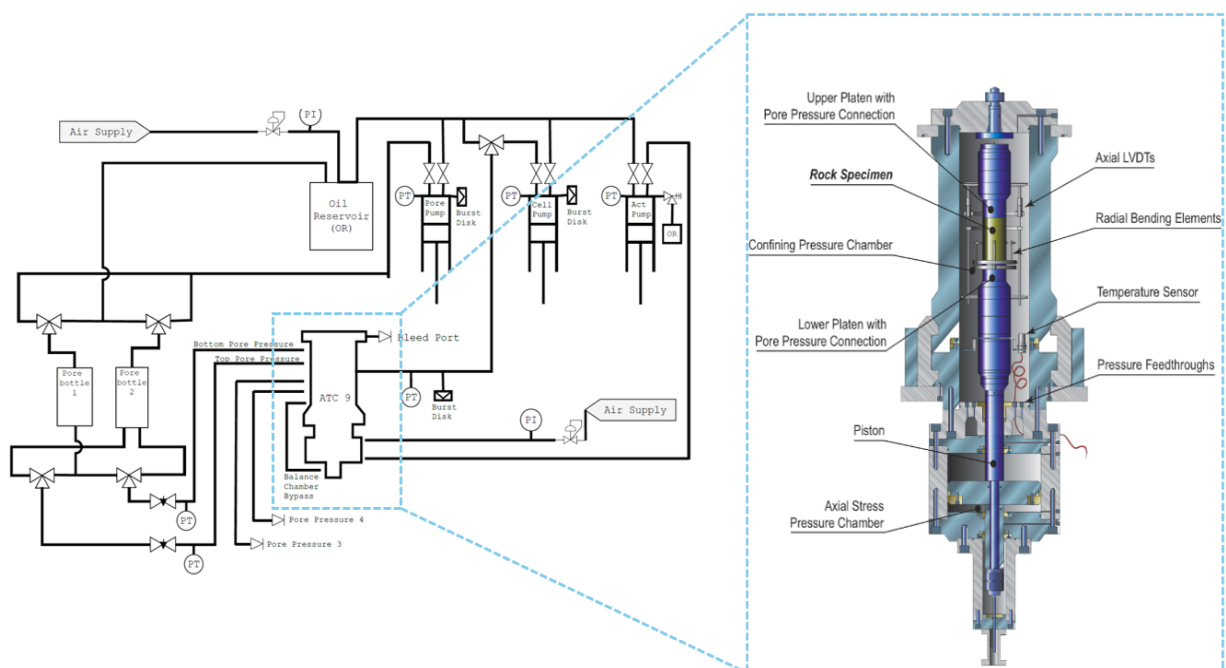


Figure 34: Schematic of ATC installation and its cross-section

The system is operated by three independent hydraulic pumps that use mineral oil to:

- apply and regulate the radial confining pressure
- apply a load via an actuator under the assembly
- apply a saturating fluid pressure through the sample.

The instruments used to measure the behaviour of the sample were:

- two diametrically opposed LVDTs mounted between the sample end platens to measure axial deformation of the sample
- four cantilever (orthogonal) radial gauges mounted at the mid-height of the sample to measure radial deformation
- a load cell beneath the base platen to measure axial load
- a pressure transducer to measure cell pressure
- a pressure transducer to measure the mean pore pressure connected to each end of the sample.

To avoid corrosion of the pump system, the prepared equilibrated brine was loaded into a separator/bottle connected to both ends of the sample.

3.2.4. Geomechanical testing procedures

All geomechanical testing was performed using the in-situ pressure and temperature conditions of the Kyalla Formation in Shenandoah-1A (i.e. a confining pressure of 20 MPa and a temperature of 82°C).

A standard triaxial test was conducted on sample 3991 under dry conditions. Section 3.4.1 elaborates on the findings of this test. The results, particularly regarding the strength of the Kyalla Formation, were then used to establish the parameters for the MSTXL creep tests.

We adopted the standard convention of rock mechanics for the strains (axial ε_a , radial ε_r and volumetric ε_v); that is, positive for compression and negative for extension.

Axial strains are inferred from the recorded displacement (ΔL) and the average of two independent LVDTs and the initial sample length (L), so that:

$$\varepsilon_a = \frac{1}{2} \left(\frac{\Delta L_{LVDT1}}{L} + \frac{\Delta L_{LVDT2}}{L} \right) \times 1000 \quad (60)$$

Radial strains, expressed in milli-strain, are inferred from the recorded displacement (Δd) averaged over two independent instrumented cantilevers and the initial sample diameter (d) so that:

$$\varepsilon_r = \frac{1}{2} \left(\frac{\Delta d_{radial1}}{d} + \frac{\Delta d_{radial2}}{d} \right) \times 1000 \quad (61)$$

Volumetric strains (ε_v), expressed in milli-strain, are calculated from both the axial (ε_a) and radial (ε_r) strains as:

$$\varepsilon_v = \varepsilon_a + 2\varepsilon_r \quad (62)$$

The geomechanical test results are reported by referring to the effective stress σ'_i and the differential stress q defined as:

$$\sigma'_i = \sigma_i - \alpha Pp \quad (63)$$

$$q = \sigma'_1 - \sigma'_3 \quad (64)$$

where α is the dimensionless Biot–Willis's coefficient (Biot, 1941). It is commonly assumed that α has a value close to 1 in water-saturated shales (Dewhurst and Siggins, 2006). The test results are hence reported using this assumption.

In conventional (axisymmetric) triaxial deformation experiments, σ_1 and σ_3 represent the axial stress and the confining pressure applied on the rock sample, respectively, and $\sigma_2 = \sigma_3$. The parameters σ'_1 and σ'_3 are the maximum and minimum effective stresses, respectively.

The results are illustrated referring to the effective mean stress (p') and differential stress (q). Differential stress is determined from the load applied on the sample (expressed in kN) and corrected for any potential offset of the load cell. Similarly, the sample surface is corrected for radial deformation (in milli-strain).

Finally, the mean effective stress reported here is simply:

$$p' = \frac{\sigma'_1 + 2\sigma'_3}{3} \quad (65)$$

where σ'_1 and σ'_3 are the effective axial stress and confining pressure during the loading of the specimens, respectively.

The Young's modulus and Poisson's ratio define the static elastic moduli inferred from the stress–strain curves within the elastic regime of deformation sustained by the sample under undrained axial loading. These parameters are usually 40–60% of the peak differential stress reached during an undrained test. In the selected domain, Young's modulus (E) and Poisson's ratio (ν) are simply defined as $E = \frac{q}{\varepsilon_a}$ and $\nu = \frac{\varepsilon_r}{\varepsilon_a}$.

3.2.4.1. STXL procedure on dry sample 3991

The procedure comprised the following steps:

2. *Sample installation.* Once installed in the triaxial cell, a cell pressure of 0.7 MPa was applied to allow the platens to contact the lapped end faces of the sample and maintain sample stability. Pore pressure was applied from one end of the sample until a fluid pressure was noted at the other end, indicating sample saturation.
3. *Temperature increase.* The temperature was increased at a rate of $\sim 18^\circ\text{C}/\text{h}$ until it reached 82°C ; the temperature remained constant for the rest of the experiment. Temperature stability was reached overnight.

4. *Sample pressurisation.* Once at temperature, cell pressure of 20 MPa was applied at a constant rate of approximately 2 MPa/min. A suitable sample stabilisation period was observed.
5. *Loading.* Once the sample had sufficiently stabilised, a differential axial load was applied at a constant average axial displacement rate equivalent to a strain rate of 5×10^{-7} per second. Loading was stopped once peak and residual strength were observed.

3.2.4.2. MSTXL procedure on dry sample labelled as 3992

The procedure comprised the following steps:

1. *Sample installation.* Once installed in the triaxial cell, a cell pressure of 0.7 MPa was applied to allow the platens to contact the lapped end faces of the sample and maintain sample stability. The sample was installed either dry or pre-saturated. In the case of installing pre-saturated samples, a nominal 0.3 MPa pore pressure was applied from both ends of the sample.
2. *Temperature increase.* The temperature was increased at a rate of $\sim 18^\circ\text{C}/\text{h}$ until it reached 82°C ; the temperature remained constant for the rest of the experiment. Temperature stability was reached overnight.
3. *Sample pressurisation:* Once the target temperature was reached, and for the saturated samples, both the pressure inside the triaxial cell (cell pressure) and the pressure of the fluid within the pores of the sample (pore pressure) were gradually increased at a constant rate of approximately 2 MPa/min until the desired test pressures were reached. The top and bottom pore pressure valves remained open during this process. The cell pressure was raised to 22 MPa, while the pore pressure was set to 2 MPa, resulting in an effective confining pressure of 20 MPa. This pressure condition is equivalent to that applied to the dry sample. Afterward, a suitable stabilization period for the sample was observed.
4. *Loading.* Once the sample had sufficiently stabilised (minimum of 6 h), an incremental axial load was applied at a constant loading rate (inferred from the dry STXL test) at predetermined values (also inferred from the dry STXL test). The applied stress was maintained at the targeted value until the creep strain did not increase, even over a relatively long time. Due to time constraints on the project, this period was set at 2 weeks for the saturated samples. The procedure was repeated until the specimens failed or the system became unstable.

3.2.4.3. MSTXL procedure on saturated samples 3993 and 3994

Sample 3993 was saturated with synthetic brine (Table 20), while sample 3994 was saturated with a sodium silicate solution formulated as 10% v/v 2.6 $\text{SiO}_2:\text{Na}_2\text{O}$ (silicate-to-alkali). This ratio was obtained by mixing commercially available 37% sodium silicate with the synthetic brine. The pH of the solution prior to saturating the sample was 10.5.

The details pertaining to preparing the synthetic brine and the analysed chemical composition (Table 20) of the brine are described in section 3.2.2.

3.3. Predicting creep behaviour using empirical and analytical models

Understanding the creep behaviour of formation rocks calls for a thorough examination of creep constitutive models. These models serve as fundamental tools for analysing rock failure processes, describing mechanical properties and creep deformation parameters, and assessing the relationship between rock stress, strain and time (Zhou et al., 2022). Although several models have been developed to understand how rocks deform under stress, many of them overlook factors like friction angle and time to failure. To determine model parameters, researchers typically resort to fitting curves to experimental data. However, the ability of these calibrated models to predict behaviour under untested stress conditions involves much uncertainty (R. Wang et al., 2019).

In this study, various creep models were used to predict the creep strain behavior of the specimens, including empirical laws (such as parabolic, logarithmic, hyperbolic, and crack-damage models) and analytical or rheological models (such as the Kelvin–Voigt, standard linear, and Burgers models). The constitutive components and principles of the analytical or rheological models, along with the theoretical framework, are thoroughly discussed in Section 1.4. The underlying constitutive parameters were derived from STXL and MSTXL creep experiments conducted over various time intervals. Short-term creep tests can produce the constitutive model parameters useful for predicting the long-term deformation of a shale under test conditions (Rassouli & Zoback, 2015). To do so, it is important to identify the model or models (and underlying constitutive parameters) that provide the best predictive capability and are specifically suited to the specimen under test.

In the following sections, empirical creep laws and analytical creep models are fitted to laboratory-derived creep curves, with the aim of estimating the most appropriate model(s) and the best constitutive parameters. It is worth mentioning here that none of the aforementioned models can simulate the third stage of creep (accelerated creep) caused by high stress levels.

3.3.1. Empirical creep models

Currently, common equations for empirical creep models include the following formulations (equations 66-69) (Y. Xie et al., 2023).

Parabolic (power-law):

$$\varepsilon = At^m \quad \text{and} \quad \dot{\varepsilon} = Amt^{m-1} \quad (66)$$

Logarithmic:

$$\varepsilon = A_1 + B_1 \log_{10} t \quad \text{and} \quad \dot{\varepsilon} = \frac{B_1}{t \ln t} \quad (67)$$

Hyperbolic:

$$\varepsilon = A_3 \sinh[(B_3 t)^s] \quad \text{and} \quad \dot{\varepsilon} = A_3 s B_3 \cosh[(B_3 t)^s] (B_3 t)^{s-1} \quad (68)$$

Crack-damage:

$$\varepsilon = A_4 e^{-B_4/\ln(kt)} \quad \text{and} \quad \dot{\varepsilon} = A_4 e^{-B_4/\ln(kt)} \frac{B_4}{t(\ln(kt))^2} \quad (69)$$

where ε and $\dot{\varepsilon}$ are strain and the strain rate, respectively; t is the creep time; and A_i , m , B_i , s , k and t_0 are constants (fitting parameters). A_i and B_i been labelled (numbered) to ensure clarity during curve-fitting and to prevent confusion.

Empirical creep models, while commonly used for shale, face numerous challenges due to their simplified representation of complex shale behaviour. The challenges include limited predictive capability for long-term deformation, difficulty in capturing the anisotropic properties of shale, and their inadequate representation of microstructural changes. Furthermore, empirical models rely heavily on available experimental data, making it difficult to select the most appropriate model for a particular stress condition. In other words, there is large uncertainty in our ability to accurately capture the diverse mechanical responses of shales.

Although they are simple and practical, empirical creep models can struggle to accurately predict long-term creep deformation, and there is a big question mark over whether they are reliable. In particular, there is considerable debate over whether these models adequately represent the intrinsic anisotropic properties of shales. Therefore, there is a pressing need to develop alternative modelling approaches specifically tailored to the unique characteristics of shale formations, particularly for predicting long-term behaviour under direct shear.

Given these challenges, researchers are now exploring alternative modelling approaches – such as the Kelvin–Voigt, standard linear or Burgers models – to better capture the intricate time-dependent mechanical behaviour of shales. By turning to these models, which offer more realistic representations of viscoelastic and visco-plastic behaviour, the objective is to overcome the limitations of empirical creep models in predicting the long-term deformation of shales under particular loading conditions. In this investigation, the aim is to enhance our understanding of shale mechanics and improve the accuracy of predictive models, thereby helping to make more informed decisions in engineering and geotechnical applications.

3.3.2. Analytical models

3.3.2.1. Kelvin–Voigt model

The two-element Kelvin–Voigt model is composed of a parallel arrangement of spring and dashpot, as shown in Figure 35 (Z. Zhang et al., 2022).

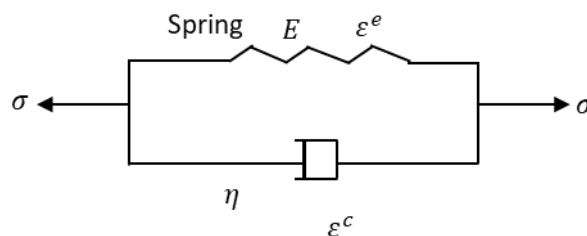


Figure 35: Schematic of the Kelvin–Voigt fractional-order derivative model

$$\begin{cases} \varepsilon^e = \frac{\sigma}{E} \\ \dot{\varepsilon}^c = \frac{\sigma}{\eta} \end{cases} \quad (70)$$

The elastic strain (ε^e) and creep strain rate ($\dot{\varepsilon}^c$) are defined as shown in equation (70).

$$\varepsilon = \frac{\sigma}{E} \left(1 - \exp\left(-\frac{E}{\eta}t\right) \right) \quad (71)$$

where is E the elastic modulus of the spring, and η is the viscosity of the dashpot.

In the conventional triaxial creep experiment on rock ($\sigma_1 \geq \sigma_2 = \sigma_3$), when a rock is subjected to three-dimensional stress, its internal stress can be separated into two components: a spherical stress tensor, denoted as σ_m ; and a differential stress tensor, represented by S_{ij} :

$$\begin{cases} \sigma_m = \frac{1}{3}(\sigma_1 + \sigma_2 + \sigma_3) = \frac{1}{3}\sigma_{kk} \\ S_{ij} = \sigma_{ij} - \delta_{ij}\sigma_m = \sigma_{ij} - \frac{1}{3}\delta_{ij}\sigma_{kk} \end{cases} \quad (72)$$

where δ_{ij} is the Kronecker delta function.

As a result, equation (72) can convey the total stress σ_{ij} as:

$$\sigma_{ij} = S_{ij} + \delta_{ij}\sigma_m \quad (73)$$

in which S_{ij} is the differential stress (which influences the shape of materials) and the $\delta_{ij}\sigma_m$ is the product of the Kronecker delta and the spherical stress, which influences the volume of materials.

The strain tensor can also be split into a spherical strain tensor ε_m and a differential strain tensor e_{ij} , so that:

$$\begin{cases} \varepsilon_m = \frac{1}{3}(\varepsilon_1 + \varepsilon_2 + \varepsilon_3) = \frac{1}{3}\varepsilon_{kk} \\ e_{ij} = \varepsilon_{ij} - \delta_{ij}\varepsilon_m = \varepsilon_{ij} - \frac{1}{3}\delta_{ij}\varepsilon_{kk} \end{cases} \quad (74)$$

Thus, the following equation can also be derived:

$$\varepsilon_{ij} = e_{ij} + \delta_{ij}\varepsilon_m \quad (75)$$

The bulk modulus of the rock (K) and its shear modulus (G) can be defined based on equation (77). According to the generalised Hooke's law, the three-dimensional constitutive relationship of elastic materials is:

$$\begin{cases} \sigma_m = 3K\varepsilon_m \\ S_{ij} = 2Ge_{ij} \end{cases} \quad (76)$$

The constitutive equation of the Kelvin–Voigt model under three-dimensional stress is governed by:

$$S_{ij} = 2Ge_{ij} + 2\eta \frac{de_{ij}}{dt} \quad (77)$$

where e_{ij} is the deviatoric strain tensor.

Combining equations (71–76) and (77), the three-dimensional Kelvin-Voigt creep equation turns out to be:

$$\varepsilon_{ij} = \frac{S_{ij}}{2G} \left(1 - \exp\left(-\frac{G}{\eta} t\right) \right) \text{ and } \varepsilon_k = \frac{\sigma_1 - \sigma_3}{3G} \left(1 - \exp\left(-\frac{G}{\eta} t\right) \right) \quad (78)$$

where ε_k is the axial creep strain.

3.3.2.2. Standard linear model

The standard linear model (Figure 36, equation (80)) expresses the stress–strain relationship of a rock by incorporating three elements: a spring and a Kelvin-Voigt unit (a spring and a dashpot connected in parallel) (Peng et al., 2020).

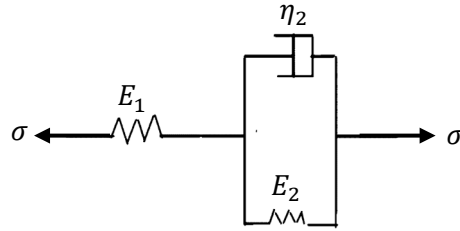


Figure 36: Schematic of the standard linear model

The one-dimensional standard linear model can describe the creep behaviour as:

$$\varepsilon = \sigma \left[\frac{1}{E_1} + \frac{1}{E_2} \left(1 - \exp\left(-\frac{E_2}{\eta_2} t\right) \right) \right] \quad (79)$$

In three-dimensions, with the stress state based on equations (74–78) and (80), the axial creep equation is:

$$\varepsilon_k = \frac{\sigma_1 + 2\sigma_3}{9K_1} + \frac{\sigma_1 - \sigma_3}{3G_2} \left[1 - \exp\left(-\frac{G_2}{\eta_2} t\right) \right] \quad (80)$$

3.3.2.3. Burgers model

The Burgers model (Figure 37) expresses the stress–strain relationship of a rock by incorporating four elements: a Maxwell unit (comprising a spring and a dashpot in series) and a Kelvin unit (comprising a spring and a dashpot connected in parallel) (Paraskevopoulou & Diederichs, 2013).

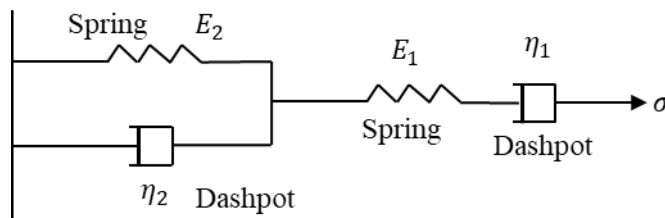


Figure 37: Schematic of the Burgers model

The one-dimensional Burgers model can describe creep behaviour during the primary and secondary stages (X. Li et al., 2023):

$$\varepsilon_{ij}^t = \varepsilon_{ij}^e + \varepsilon_{ij}^v + \varepsilon_{ij}^{ve} \quad (81)$$

so that the one-dimensional Burgers model is:

$$\varepsilon_{(Burgers)}^t = \frac{\sigma}{E_1} + \frac{\sigma}{\eta_1} t + \frac{\sigma}{E_2} \left(1 - \exp\left(-\frac{E_2}{\eta_2} t\right) \right) \quad (82)$$

As stated by the generalised Hooke's law, the three-dimensional constitutive relationship of elastic materials can be defined as:

$$\begin{cases} \sigma_m = 3K\varepsilon_m \\ S_{ij} = 2Ge_{ij} \end{cases} \quad (83)$$

In three-dimensions, the stress state derived by combining equations (74–78) and (82–84) is:

$$\varepsilon = \frac{\sigma_1 + 2\sigma_3}{9K_1} + \frac{\sigma_1 - \sigma_3}{3G_1} + \frac{\sigma_1 - \sigma_3}{3G_2} \left[1 - \exp\left(-\frac{G_2}{\eta_2} t\right) \right] + \frac{\sigma_1 - \sigma_3}{3\eta_2} t \quad (84)$$

3.3.3. Measuring goodness of fit

When evaluating the goodness of fit of mathematical models applied to experimental creep data, the standard error of the residuals (stderr) and the coefficient of determination (R^2) serve as key metrics. The value of stderr quantifies the average deviation of the residuals, representing the differences between the observed data and model predictions. Lower stderr values indicate better fit, implying that the model predictions closely align with the observed data.

In addition, in this study R^2 was used as a crucial metric for evaluating the goodness of fit of mathematical models to experimental creep data. Within the loop iterating over different models fitted to the dataset, the code computes R^2 by comparing observed data with model predictions. The calculation involves two key components: the sum of squared residuals (SSR) and the total sum of squares (SST). R^2 can be computed by dividing SSR by SST, which quantifies the proportion of variance in the dependent variable explained by the independent variable. This approach ensures accurate evaluation of model performance, making it easier to identify the model that most effectively captures the variability of the experimental data.

When R^2 is negative, it indicates that the model fits the data worse than a horizontal line (there is a poor fit of the model to the data). In other words, the model's predictions are so poor that it performs worse than just using the mean value of the dependent variable as the prediction for all observations. This can happen when the model is inappropriate for the data or when there are issues such as overfitting.

3.4. Results

3.4.1. STXL test on dry sample 3991

Figure 38 represents stress–strain curves inferred from a dry STXL test performed on a sample of the Kyalla Formation. The sample failed in the brittle regime, as shown on the stress–strain curve where the maximum differential stress is quickly followed by a stress drop indicative of macroscopic failure propagation.

XRCT images of the sample after testing, shown in Figure 39, depict the development of a discrete failure plane oblique to the axial load. The main mechanical properties of the dry Kyalla sample are reported in Table 22.

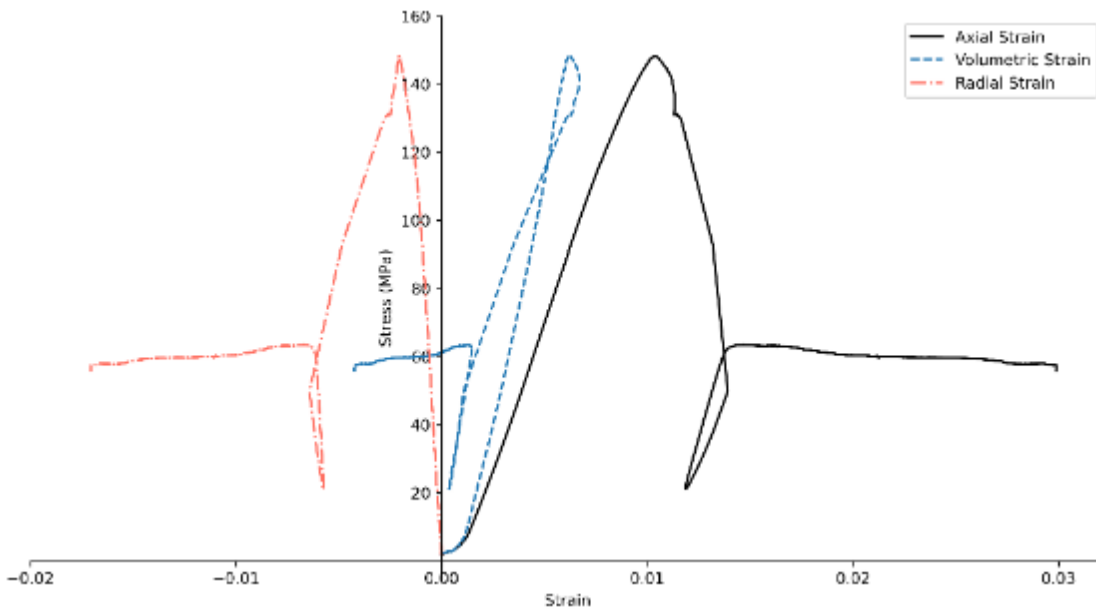


Figure 38: Stress–strain curves inferred from an STXL test on a dry sample (sample 3991).

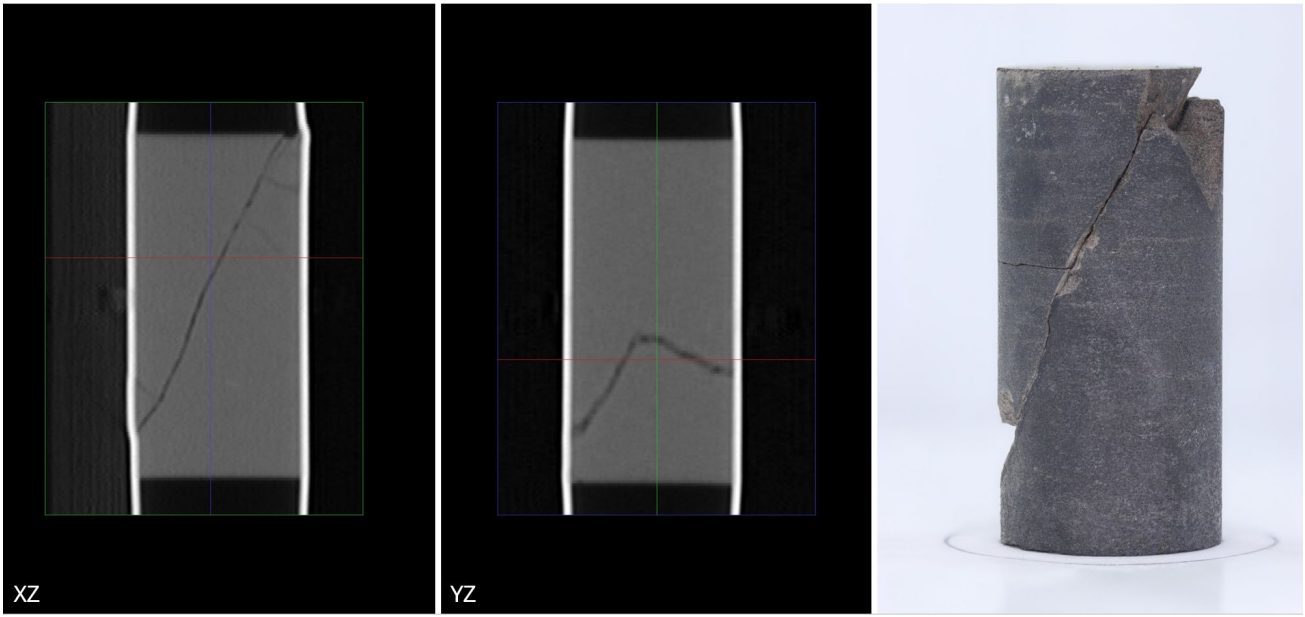


Figure 39: Longitudinal XRCT 2D slices (a) and a picture of sample 3991 after the dry STXL test (b)

Table 22: Mechanical properties of a sample of the Kyalla Formation as inferred from a dry STXL test at 82°C

Effective confining stress (MPa) σ'_3	Differential peak stress (MPa)	Residual stress (MPa)	Young's modulus (GPa) E	Poisson's ratio ν	Bulk modulus (GPa) K	Shear modulus (GPa) G
20	148.3	59.31	17.76	0.19	9.55	7.46

3.4.1.1. Determination of triaxial deformation parameters

$$K = \frac{E}{3(1-2\nu)} \quad \text{and} \quad K = \frac{\sigma_1 + 2\sigma_3}{3(\varepsilon_1 + 2\varepsilon_3)} \quad (85)$$

$$G = \frac{E}{2(1+\nu)} \quad \text{and} \quad G = \frac{\sigma_1 - \sigma_3}{2(\varepsilon_1 - \varepsilon_3)} \quad (86)$$

where K is the bulk modulus of the rock and G is the shear modulus of the rock.

Running an STXL compression test before performing an MSTXL triaxial test on shale samples is significant for several reasons. It provides baseline data on the mechanical behaviour of the shale, including its peak strength, elastic properties and failure characteristics, which are critical for designing more complex tests including MSTXL creep test with stress levels that are a fraction of the peak strength (e.g. 60%, 80%). This allows the shale to experience creep at stress levels below its failure point, simulating more realistic subsurface conditions over time. In other words, the stress limits for the MSTXL test can be selected based on the peak stress from the STXL test, allowing for the simulation of creep behaviour under realistic subsurface conditions. Mechanical properties like

Young's modulus and Poisson's ratio obtained from the STXL test also inform long-term creep behaviour modelling.

3.4.2. MSTXL creep test on dry sample 3992

Creep tests are used to characterise the creep rate, identify distinct creep stages (i.e. primary, steady-state and accelerated) and determine the threshold stress for creep behaviour (Zhou et al., 2022). Using a servo-controlled apparatus at ambient temperature, an MSTXL creep test was conducted on the specimen to assess its creep characteristics and identify its three-dimensional creep behaviour under different deviatoric stresses.

The MSTXL creep test (incremental loading method) entails applying pressure in gradual stages to the specimen, maintaining each stress level for a designated period. Once the creep reaches the predetermined time or deformation stabilises, stress is increased to the next level, and the process is repeated until failure occurs. This method is widely used in laboratories to study rock creep.

Considering that creep is the inclination of shale rock to deform under constant stress, in this study creep deformations were measured while applying constant stresses. Creep tests commenced with a relatively low differential stress (σ_d , the difference between axial and confining stresses) and then increased sequentially – 25 MPa, 50 MPa, 75 MPa, 100 MPa and eventually 125 MPa – while the confining pressure (P_c) remained at 20 MPa during the entire experiment. The stress path (trajectory) employed is illustrated in Figure 40. Axial deformation was measured using two sets of LVDTs and the radial deformation measured.

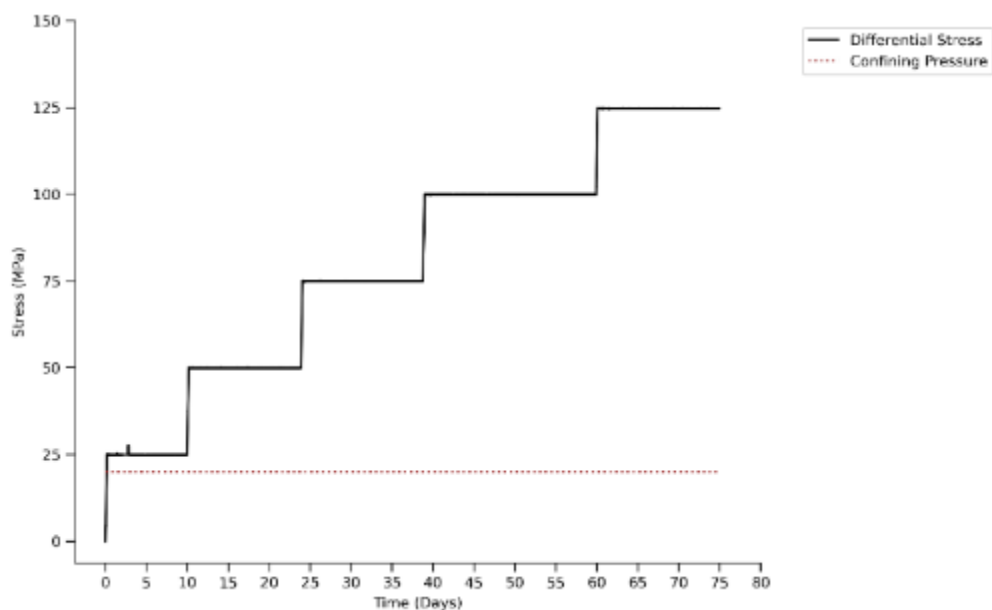


Figure 40: Stress path employed for MSTXL creep test

Figure 41a demonstrates the evolution of axial, radial and volumetric strains over time from the MSTXL creep test on dry sample 3922 and Figure 41b shows the stress–strain relationship obtained from the MSTXL test.

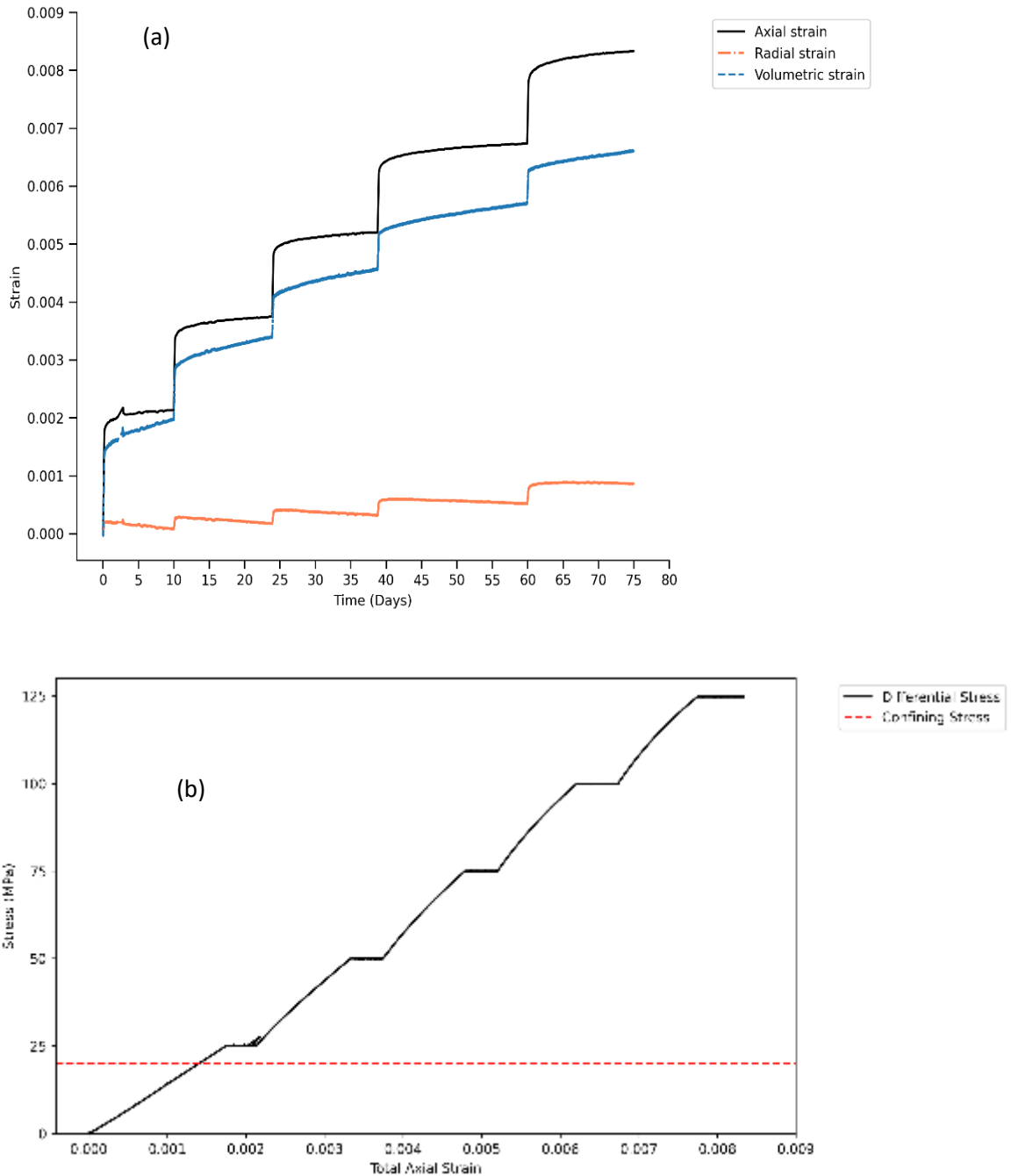


Figure 41: (a) Axial, radial and volumetric strains obtained from the MSTXL creep test;
 (b) stress–strain relationship for sample 3992

Figure 42a demonstrates the evolution of total axial, elastic and creep strain across each stage over time. Figure 42b depicts stress plotted against elastic and creep strain for each stage, aiming to further investigate the creep behaviour in more detail. As can be seen in Figure 43, the duration of the first stage when the differential stress is 25 MPa is about 10 days and the maximum total axial strain (ϵ_t), elastic strain (ϵ_e) and creep strain (ϵ_c) achieved are 0.00215, 0.00119 and 0.00095, respectively.

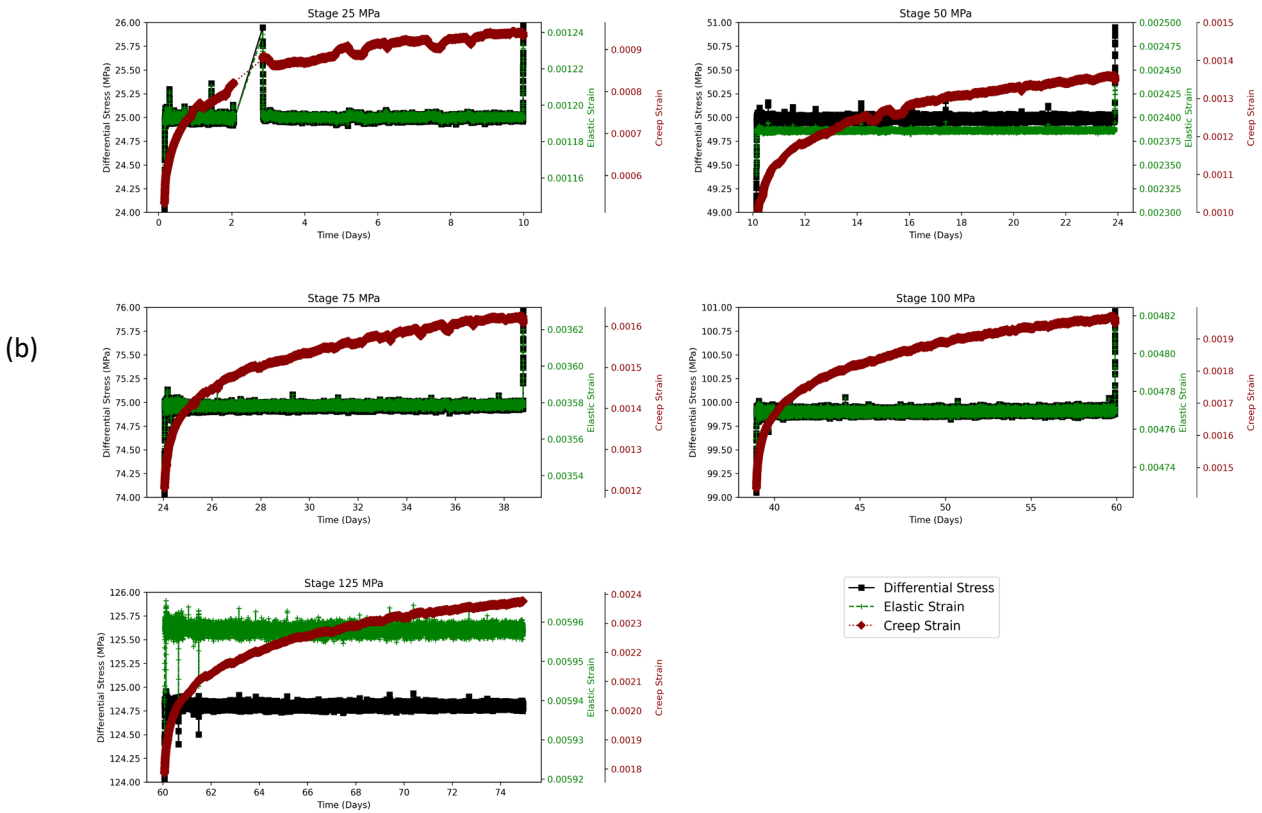
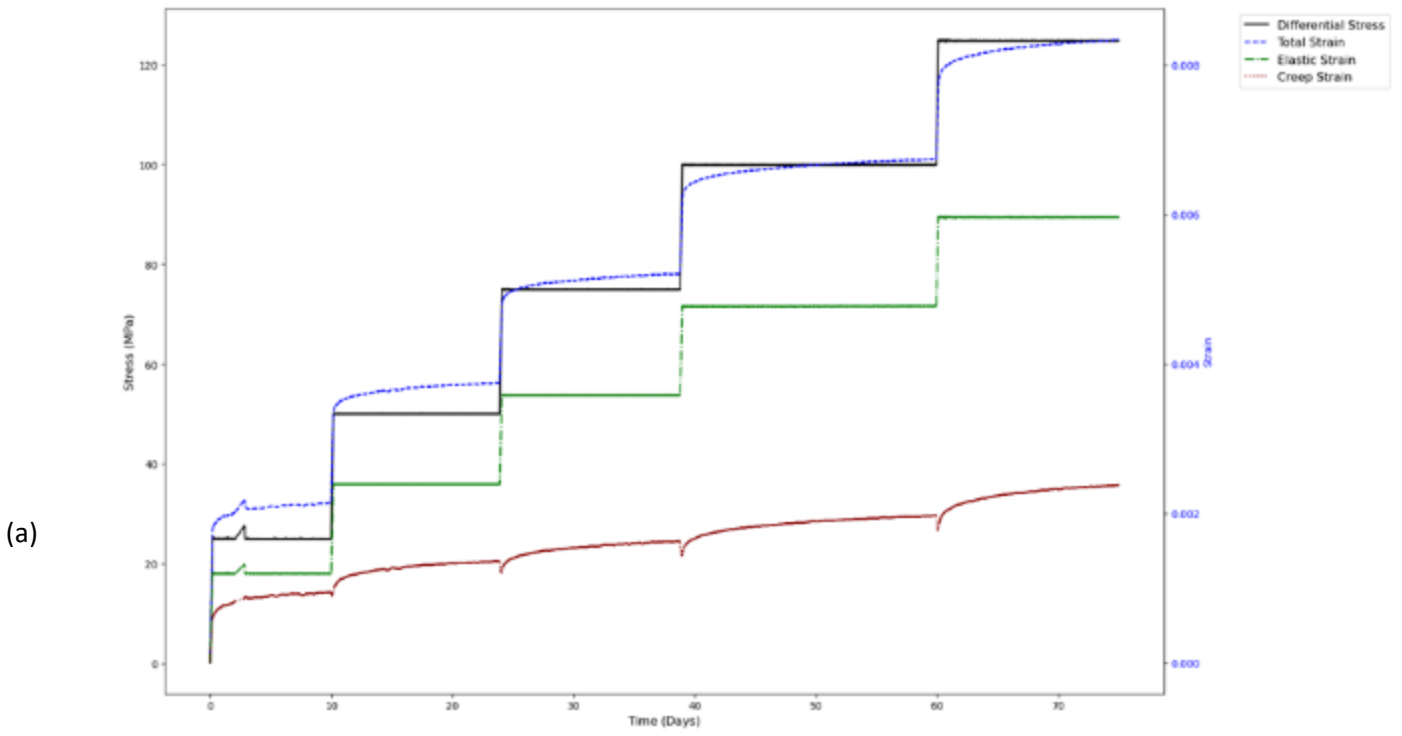


Figure 42: (a) Differential stress–strain behaviour over time obtained from performing MSTXL creep tests; (b) differential stress–strain (including elastic and creep strain) behaviour over time for each stage

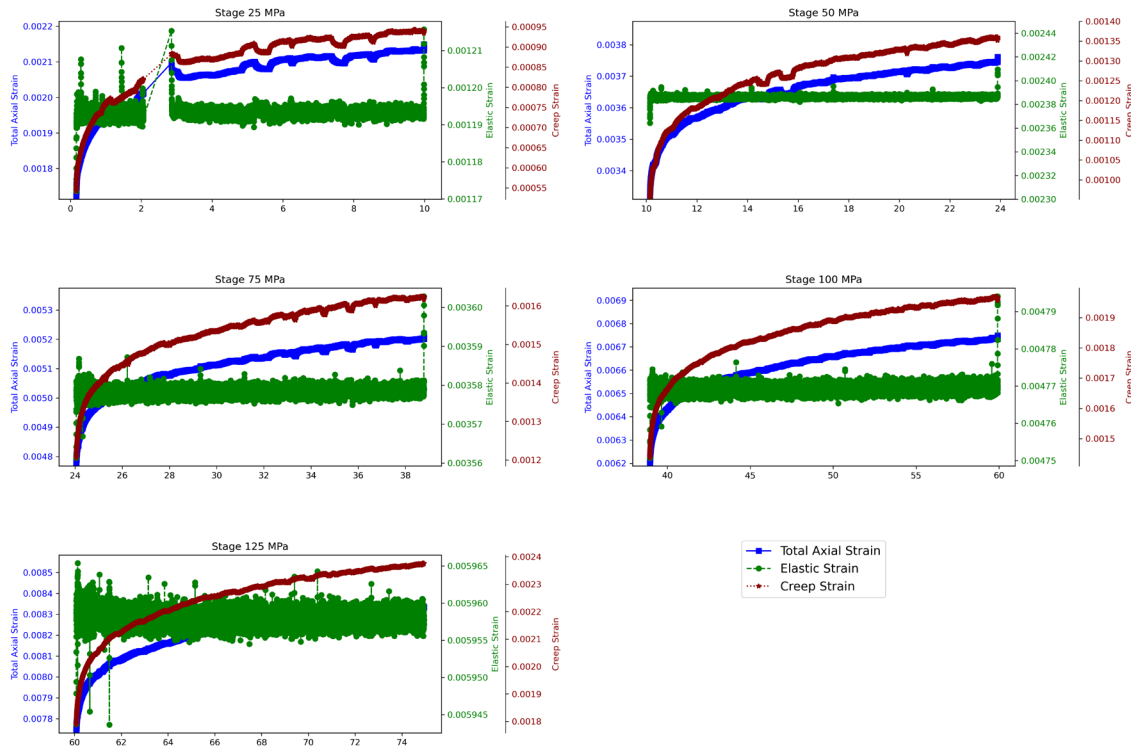


Figure 43: Evolution of total axial, elastic, and creep strain across each stage over time for sample 3992

Thus, the ratio of creep strain to total axial strain (ϵ_c/ϵ_t) for the first stage was 43%. At the end of stages 2 and 3 ($\sigma_d = 50$ and 75 MPa), each lasting approximately 14 days, the ratio of creep strain to total axial strain decreased to 38% and 30%, respectively. The creep strain increased to 0.000195 at the end of stage 4 ($\sigma_d = 100$ MPa), which spanned 20 days, resulting in a ratio of 29%. For the final stage ($\sigma_d = 125$ MPa), the ratio plateaued at 28% over a span of 14 days.

Figure 44 illustrates the creep strain magnitude in comparison to elastic strain and the creep strain rate for each stage. From Figures 40 and 44, it is evident that during each loading stage, the shale transitions from the primary creep stage to the secondary stage. In the primary stage, strain continually increases over time with a descending trend, then the trend stabilises at a certain value as it enters the secondary stage. In this stage, the creep rate remains constant, while strain linearly increases over time.

3.4.2.1. Predicting creep strain behaviour for dry sample 3992

Figure 45 demonstrates the results when creep data for sample 3992 (obtained from experiments) were fitted to all of the aforementioned creep models along with the stderr for each stage of the MSTLX test. The corresponding fitting parameters for each stage, and the values of R^2 and stderr, are given in Table 23.

It is worth noting that, to compare the capability of each model in predicting the long-term creep behaviour for each stage, only 20% of the experimental data (shown with a red dashed line and labelled as data1 in Figure 45) was used for the purpose of curve-fitting and obtaining the

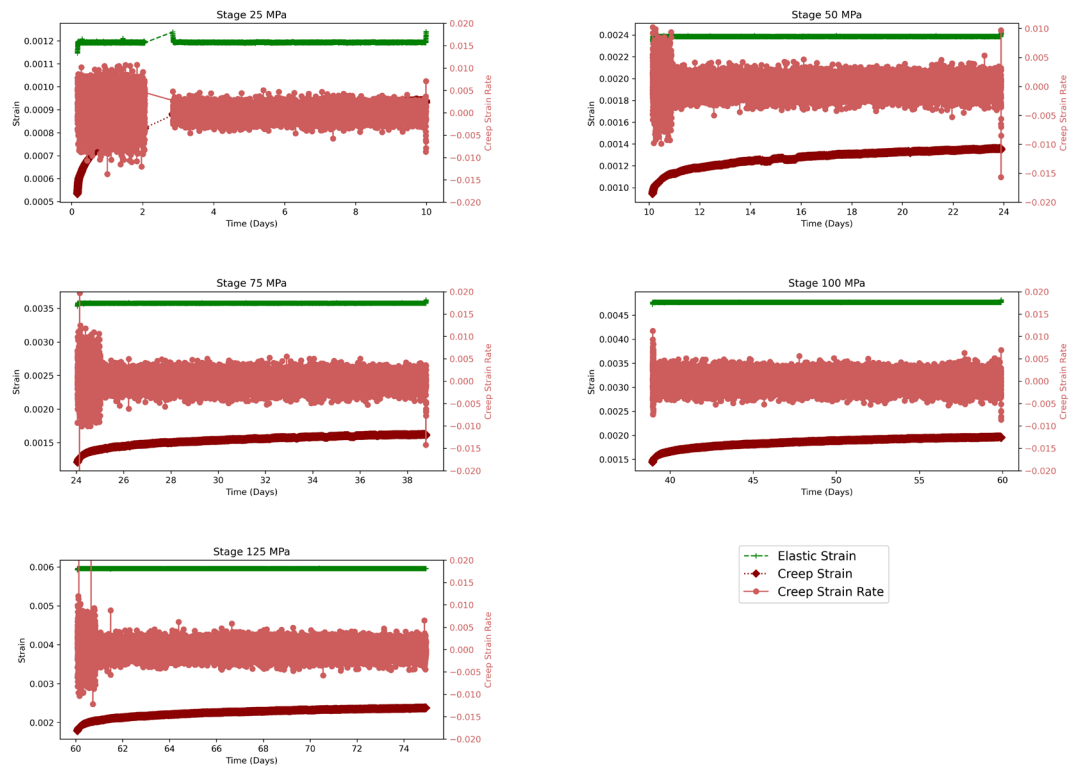


Figure 44: Magnitudes of creep strain vs elastic strain, as well as the creep strain rate over time, for each stage of testing sample 3992

corresponding parameters for each model. Subsequently, the model uses the acquired parameters to predict the remaining creep behaviour.

Considering the average values of R^2 and $stderr$ of the five stages for each model (Table 23), it appears that the parabolic model has the highest average R^2 at 0.972, indicating a strong correlation between the predicted and observed data points. Additionally, it has a relatively low average $stderr$ at 9.843. This suggests that the parabolic model provides a satisfactory fit to the data with minimal prediction error. Following closely behind is the hyperbolic model, which also demonstrates a respectable R^2 value of 0.825 and a relatively low $stderr$ of 23.782.

Conversely, the Kelvin–Voigt and standard linear models demonstrate poor performance, as evidenced by their negative R^2 values and relatively high $stderr$ values. Notably, the Burgers model stands out as one of the worst-performing models with a negative R^2 value (average R^2 for all stages of -3.946), indicating even poorer performance.

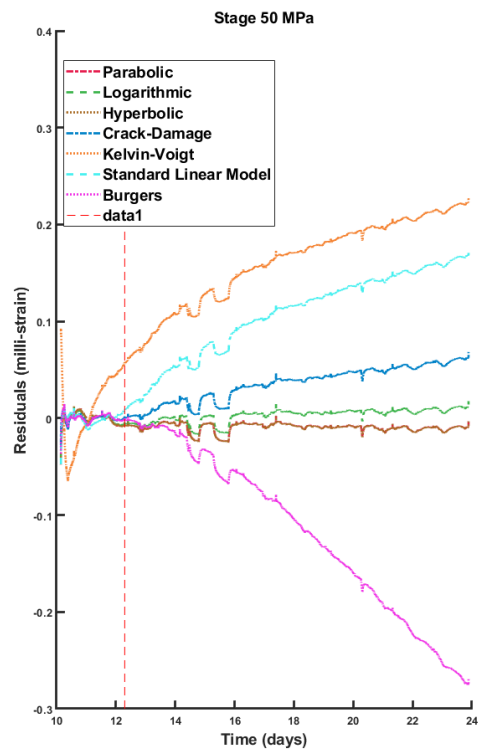
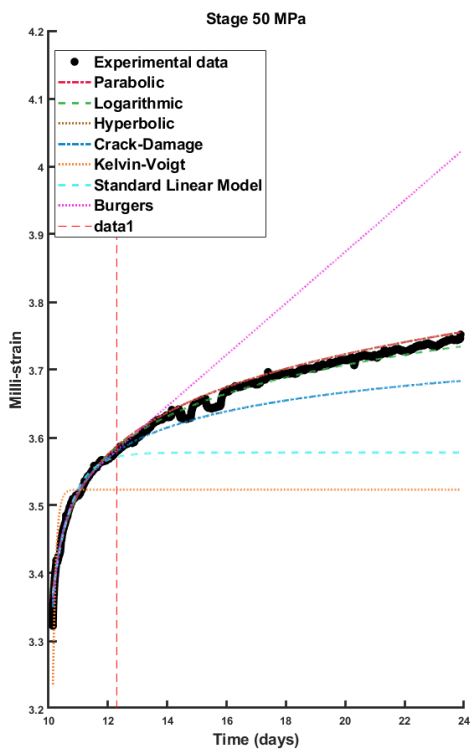
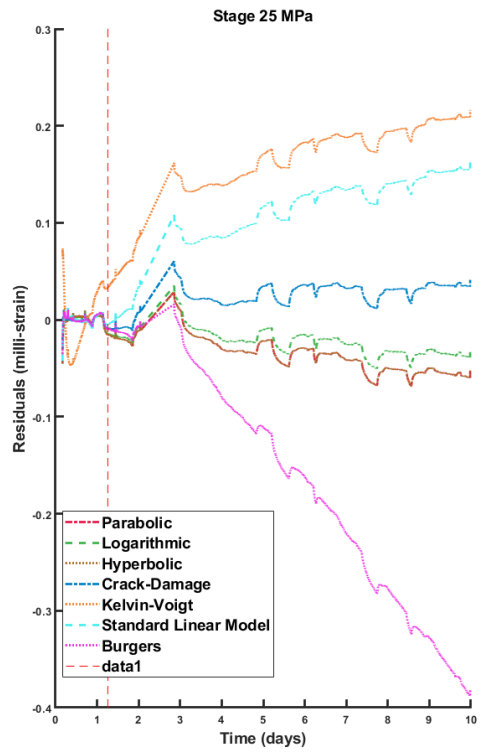
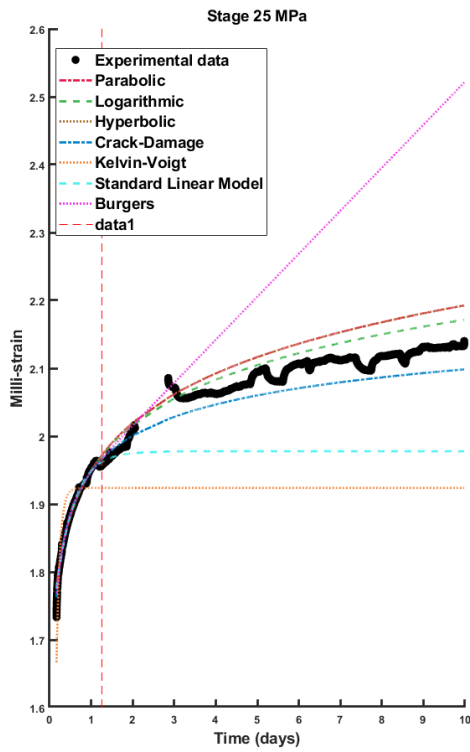
These findings underscore the importance of selecting appropriate models that accurately capture the underlying patterns within the data. The poor performance of Kelvin–Voigt, standard linear and Burgers models can be attributed to the fact that the creep behaviour of all viscoelastic models, which are composed of springs and dashpots, either exhibits a strain asymptote (long-term solid-like behaviour) or reaches a stable strain rate (long-term liquid-like behaviour) after a characteristic time constant that describes the duration of the transient behaviour (Sone & Zoback, 2014). Therefore, these types of viscoelastic models are unable to accurately represent creep behaviour across all timescales.

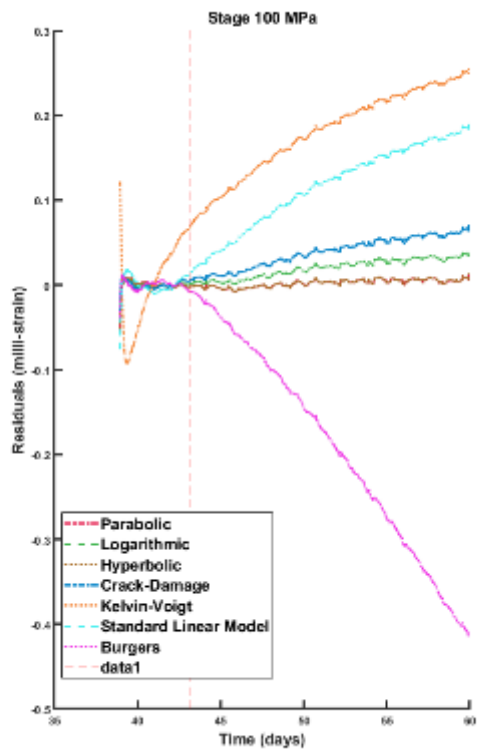
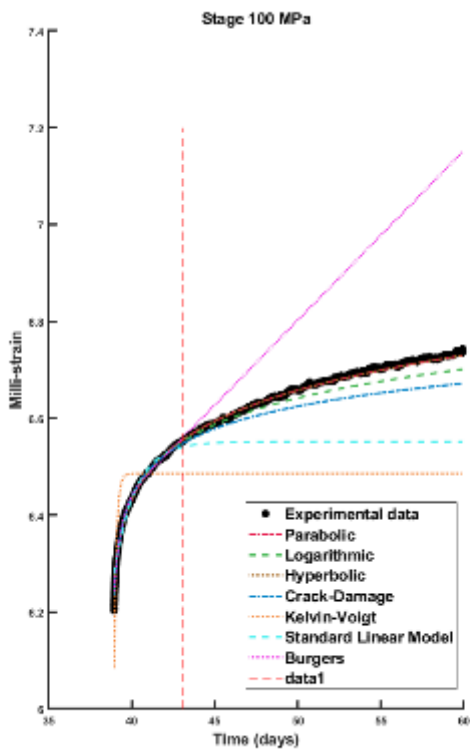
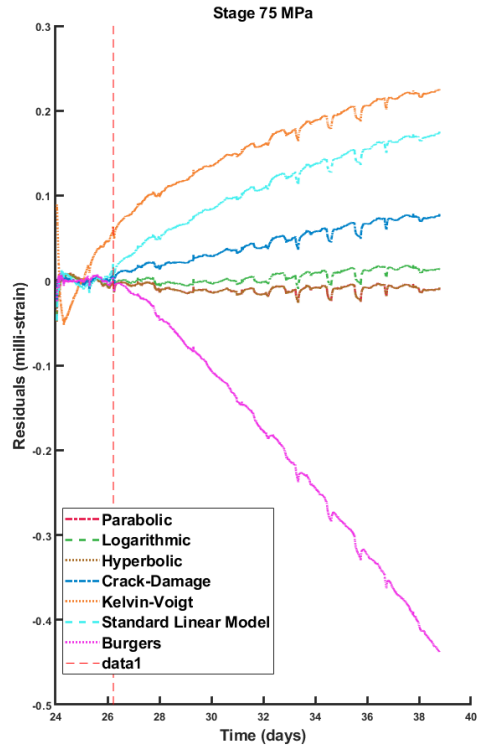
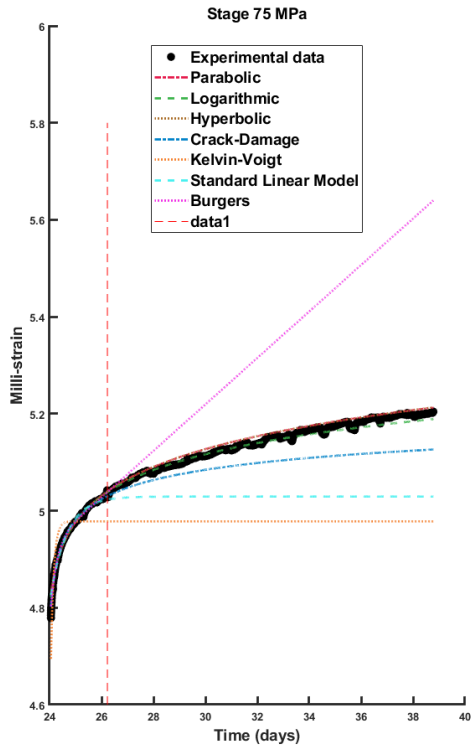
Table 23: Fitted parameters from empirical models of dry shale

Model	Stage	A_i	m	B_i	k	s	E	E_1	E_2	η_1	η_2	η	stderr	R^2
Parabolic	25	0.001949	0.05										20.8101	0.8354
	50	0.001375	0.06										6.1497	0.9874
	75	0.001216	0.069										6.2844	0.9863
	100	0.001209	0.076										4.5749	0.9975
	125	0.001261	0.091										9.3172	0.9803
Logarithmic	25	0.001949		9.668E-05									14.4288	0.927083
	50	0.001376		8.303E-05									6.55857	0.993526
	75	0.001217		8.157E-05									7.0076	0.991939
	100	0.001211		9.352E-05									12.6546	0.95673
	125	0.001263		1.133E-04									8.56739	0.991667
Hyperbolic	25	19.81858		4.41E-79		0.0511							20.794	0.836
	50	14.55286		2.08E-66		0.0613							6.181	0.987
	75	12.94876		7.03E-60		0.068							6.305	0.986
	100	13.62094		6.78E-54		0.076							4.583	0.997
	125	13.8265		5.02E-45		0.0912							9.282	0.981
Crack-damage	25	0.002673		2.365	1761.082								16.436	0.921
	50	0.00221		3.951	4314.917								21.568	0.832
	75	0.001857		2.870	932.7624								26.249	0.739
	100	0.003065		11.012	146749.3								22.268	0.847
	125	0.0023		4.209	1179.723								32.390	0.788
Kelvin-Voigt	25						12995.57					1077.248	77.7843	-1.85573
	50						18076.17					1873.665	77.7357	-1.99609
	75						20391.3					2296.021	78.0417	-2.01748
	100						19510.44					2780.127	87.8366	-2.03088
	125						19233.74					2700.385	104.833	-1.82889
Standard linear	25						14886.27	83788.53				36031.59	59.280	-0.354
	50						21401.5	92723.41				58308.94	58.269	-0.412
	75						24676.34	94639.35				59541.39	60.132	-0.517
	100						24119.54	80571.98				102813	64.003	-0.339
	125						25070.12	67325.43				45902	80.867	-0.430
Burgers	25						14886.27	83788.53	26307.52	1627.15			125.913	-3.42925
	50						21401.5	92723.41	263582.5	2476.77			88.4676	-1.20852
	75						24676.34	94639.35	382531.3	1485.03			140.264	-4.94292
	100						24119.54	80571.98	760671.6	2597.33			131.813	-3.34096
	125						25070.12	67325.43	541938.4	1123.2			188.106	-4.56819

A_i , m , B_i , k and s are the constitutive parameters associated with the parabolic, logarithmic, hyperbolic and crack-damage for empirical creep models, respectively.

E , E_1 , E_2 , η_1 , η_2 and η are the constitutive parameters associated with the Kelvin-Voigt, standard linear and Burgers analytical models, respectively. Each E and η is representative of the modulus of elasticity in the corresponding springs and the viscosity coefficient in the corresponding dashpots.





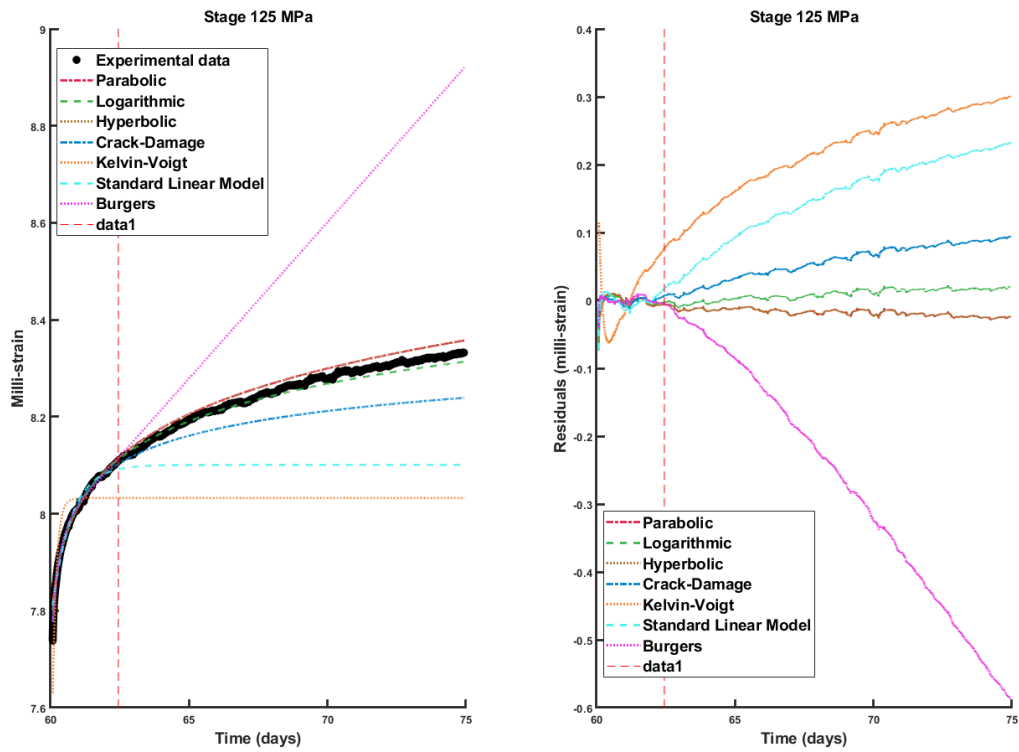


Figure 45: Comparative analysis of the fitted creep models and corresponding standard errors across multiple stages of the MSTXL creep test on sample 3992

3.4.3. MSTXL creep tests on synthetic-brine saturated sample 3933

The saturation process and the chemical composition of the synthetic brine were explained in section 3.2.2 and Table 20, respectively. The creep tests commenced with a relatively low differential stress level (σ_d , difference between axial and confining stresses) and then increased in sequential stages of 25 MPa, 50 MPa and 80 MPa, and eventually the sample failed at 104.8 MPa, while the confining pressure (P_c) remained at 20 MPa throughout the experiment. The stress trajectory employed is demonstrated in Figure 46.

Figure 47 illustrates the stress versus total axial strain measured during the MSTXL creep test on sample 3993. The test was performed in four stages. The duration of the test on the saturated sample was approximately 60 days.

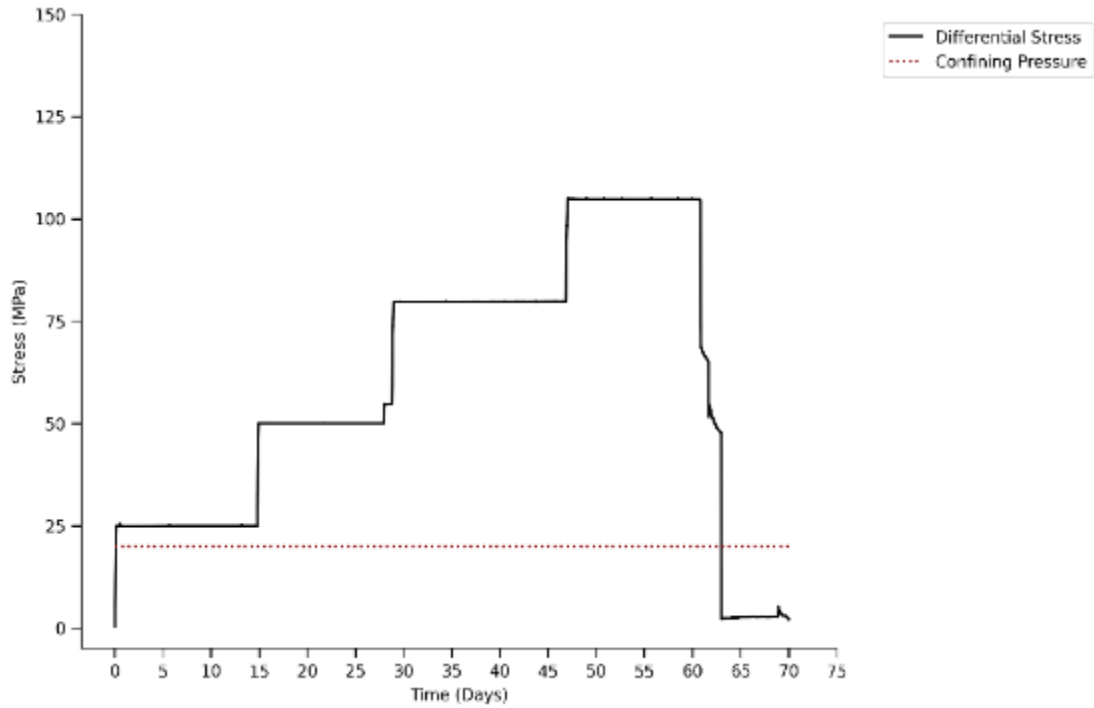


Figure 46: Stress path employed for the MSTXL creep test on sample 3993

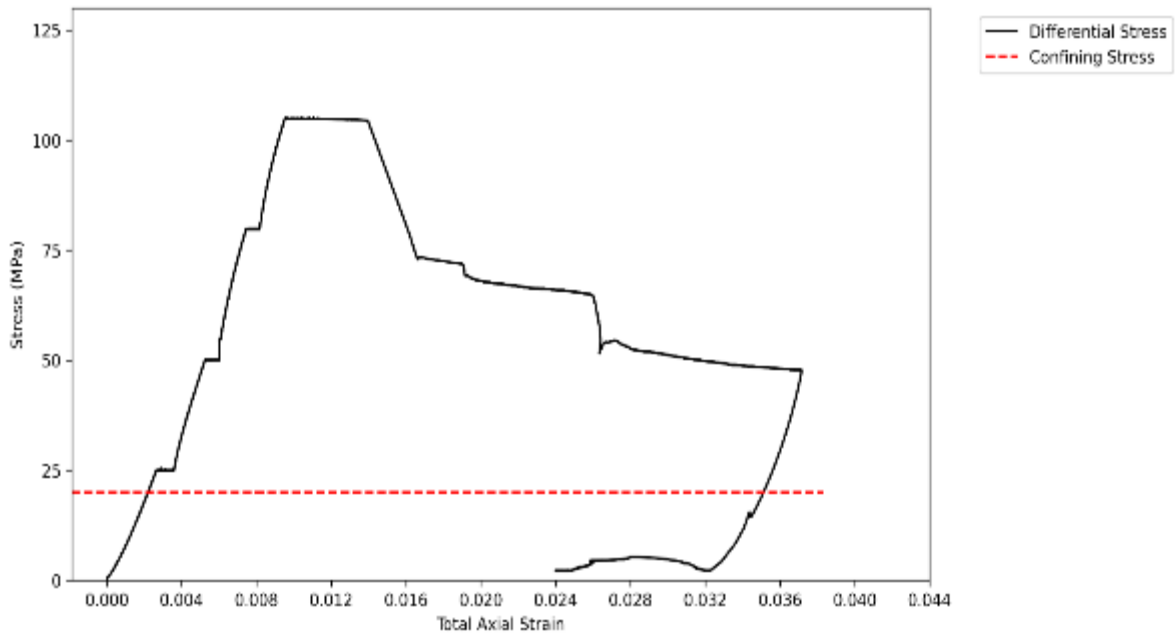


Figure 47: Stress vs axial total strain measured during the MSTXL creep test on sample 3993

Figure 48a shows the differential stress and the corresponding total strain, elastic strain and creep strain. Figure 48b shows, for the saturated sample, the elastic and creep strain in each stage versus time during constant differential stress.

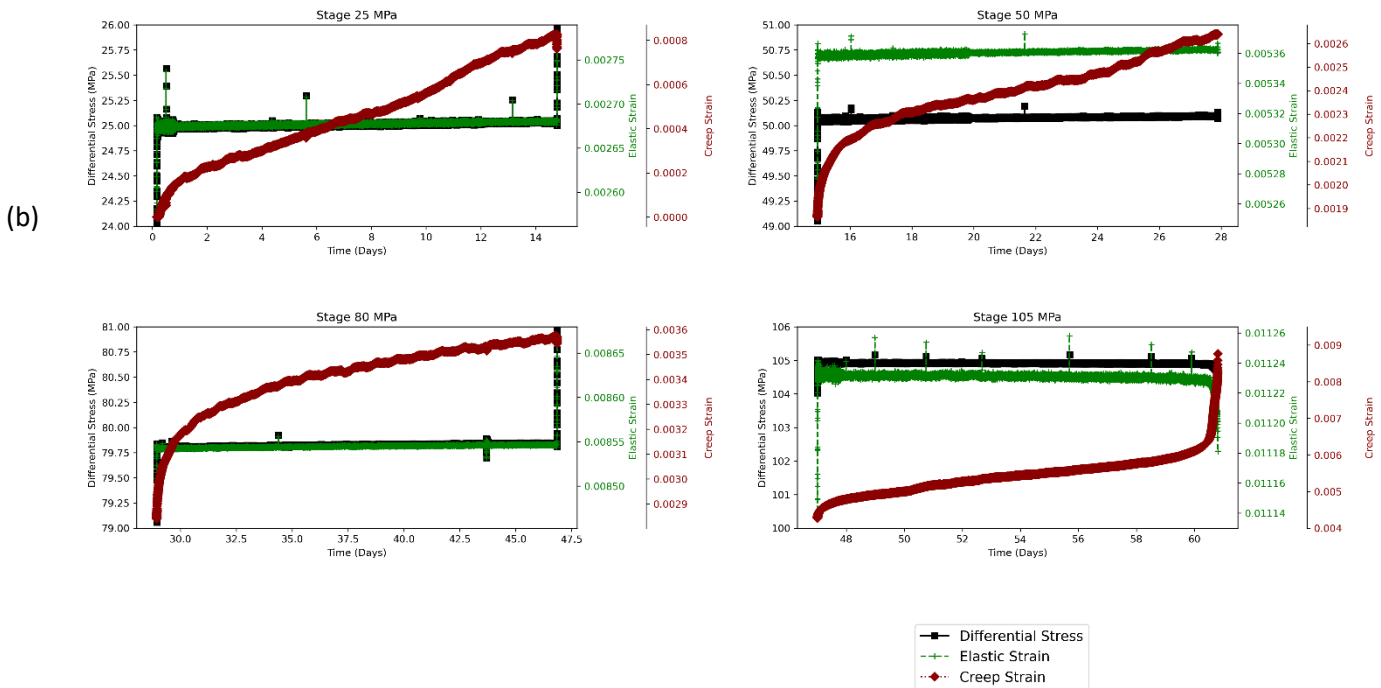
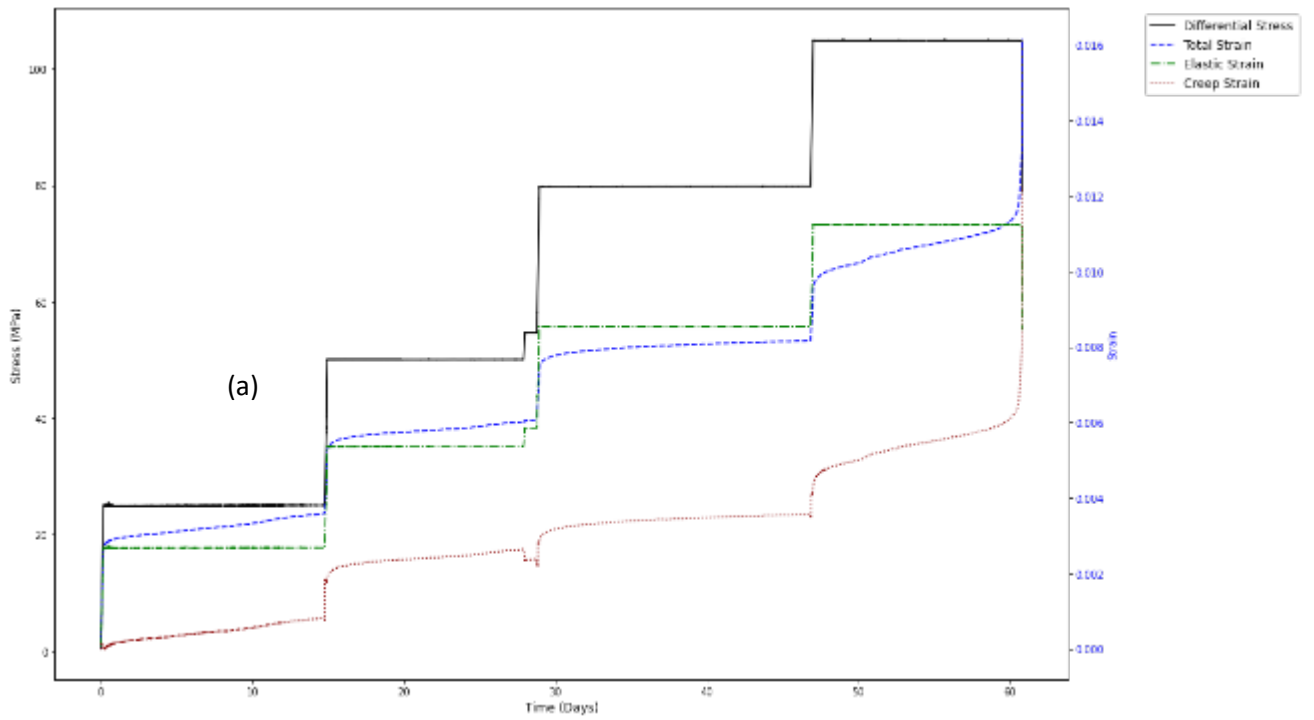


Figure 48: (a) Differential stress–strain behaviour over time obtained from performing a MSTXL creep test on sample 3993 saturated with synthetic brine; (b) analysing differential stress–strain behaviour (including elastic and creep strain) over time for each stage

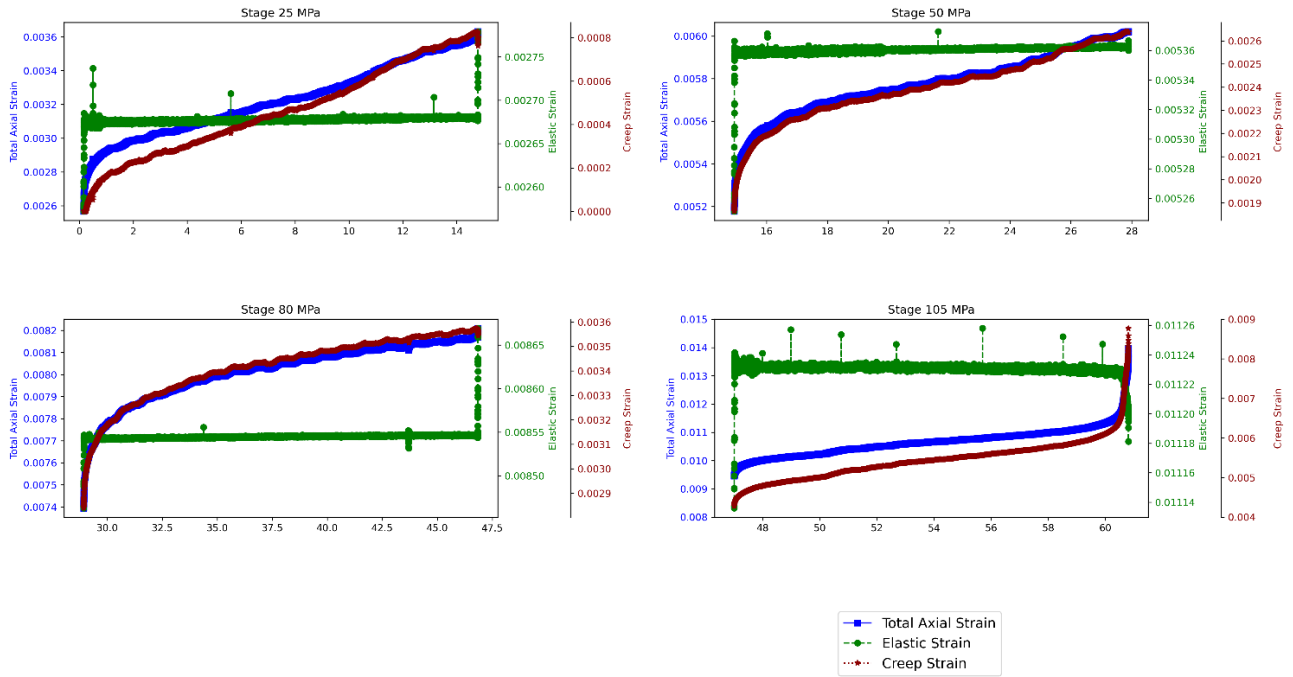


Figure 49: The evolution of total axial, elastic and creep strain over time during each of the four stages for sample 3993

As can be seen in Figure 49, at the first stage, the differential stress was kept constant at 25 MPa for 14 days; and the total strain and creep strain reached 0.0036 and 0.0008, respectively. Thus, the creep strain (ϵ_c) was 22% of the total strain ($\epsilon^c/\epsilon_t = 22\%$). In the second stage, during which the differential stress was kept constant at 50 MPa for 13 days, the ratio of creep strain to total strain reached 43% ($\epsilon^c/\epsilon_t = 0.0026/0.006$). In the third stage, when the differential stress was kept constant at 100 MPa for 18 days, this ratio increased slightly to 44%. During the last stage, in which differential

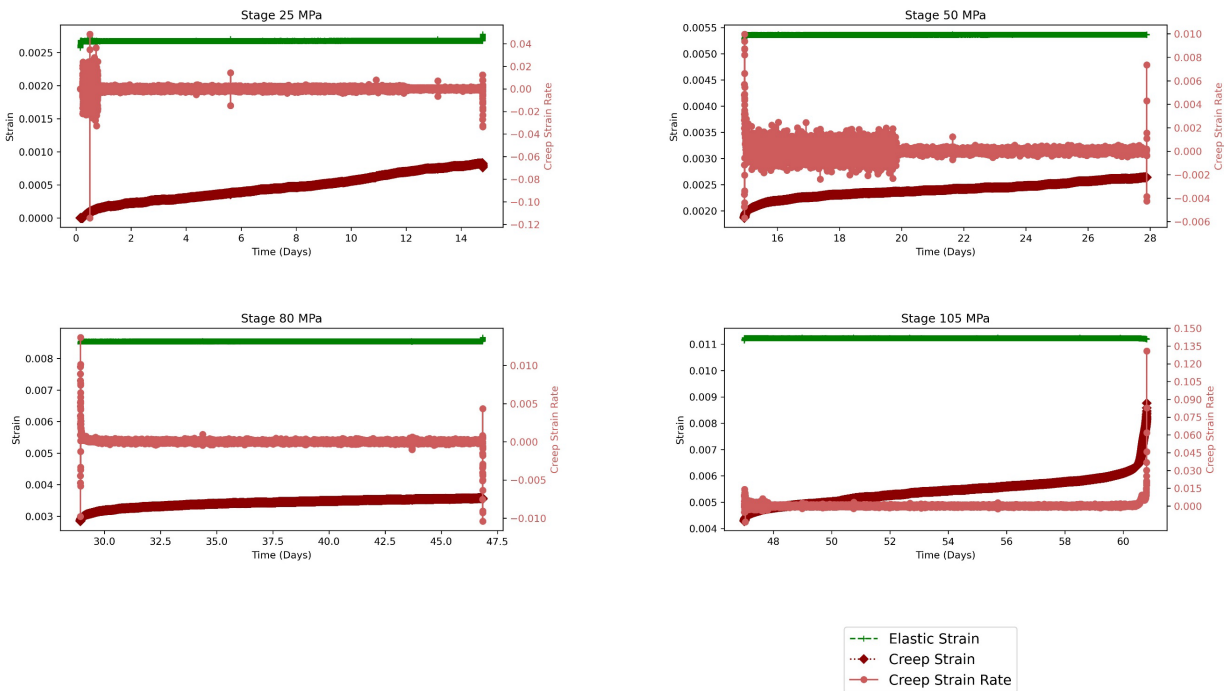


Figure 50: The magnitudes of creep strain (dark red), elastic strain (green) and creep strain rate (red) over time during each stage for sample 3993

stress was kept constant at 105 MPa for 13 days, the ratio increased to 60% and sample failure occurred.

Figure 50 depicts the magnitudes of creep strain, elastic strain and creep strain rate over time for each stage for sample 3993. It shows that creep strain enters the secondary stage more quickly at higher differential stress stages (i.e. the strain rate stabilises more quickly). The three stages of creep can be observed in the 104 MPa stage: the primary stage is very short, the secondary stage lasts approximately 12 days and the accelerated stage leads to sample failure. As can be seen in Figure 50, the duration of the primary stage, which is characterised by a decelerating strain rate, is very short for all stages except for the 50 hold MPa stage. This can be attributed to shale heterogeneity and anisotropic behaviour, which leads to it exhibiting nonlinear behaviour at different stress levels. At the 50 MPa hold stage, shale might be undergoing microstructural adjustments that prolong the primary creep phase, whereas at lower and higher stress levels, these adjustments occur more rapidly. This stage might involve more significant microcrack closure or grain boundary sliding, processes that typically exhibit a decelerating strain rate over an extended period.

3.4.3.1. Predicting creep strain behaviour for synthetic-brine saturated sample 3993

Figure 51 demonstrates that the creep data (obtained from the experiments) were fitted to all of the aforementioned creep models along with the *stderr* for each stage of the MSTLX test on sample 3993. The corresponding fitting parameters for each stage and the values of R^2 and *stderr* are given in Table 24.

Based on Table 24 and considering the average values of R^2 and the *stderr* of the four stages for each model, the parabolic and hyperbolic models appear to perform relatively better compared to the other models. The parabolic and hyperbolic models exhibit similar R^2 values (average R^2 for four stages of approximately 0.595 and 0.595, respectively), suggesting moderate correlations between the predicted and observed data points. It is worth noting that due to the inability of the models to predict the tertiary stage of creep, R^2 is lower than the corresponding values for sample 3992. In addition, it appears that, compared with the dry sample, saturating the sample using synthetic brine prolongs the duration of strain stabilisation, particularly at lower differential stress levels of 25 MPa and 50 MPa (as can be seen in Figure 48b).

Additionally, both models have a relatively low *stderr* of 119.237 and 119.283, respectively, indicating that the prediction errors were reasonably small.

Conversely, the Kelvin–Voigt and standard linear models showed the poorest performance among the models considered. The Kelvin–Voigt model displays a notably high *stderr* of 227.751 and a negative R^2 value of -1.320 , indicating poor predictive ability and potential overfitting or model misspecification. Similarly, the standard linear model also exhibited a high *stderr* of 209.121 and a negative R^2 value of -0.669 , again suggesting inadequate model fitting and poor predictive accuracy.

The Burgers and crack-damage models fall somewhere between the best- and worst-performing models. While the crack-damage model demonstrates a moderate R^2 value of 0.224, its *stderr* is relatively high at 159.618, indicating substantial prediction errors. Similarly, the Burgers model

displays a negative R^2 value of -0.966 and a high $stderr$ of 171.074 , indicating poor fit and predictive accuracy.

Overall, based on the combination of R^2 values and $stderr$, the parabolic and hyperbolic models appear to be the best-fitting models, while the Kelvin–Voigt and standard linear models perform the worst. The crack-damage and Burgers models exhibit intermediate performance but are still outperformed by the parabolic and hyperbolic models in accurately representing the relationship between the variables in the experimental data.

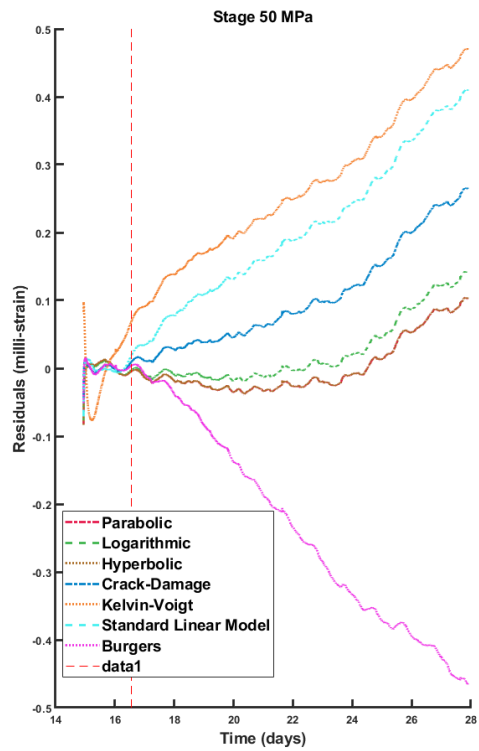
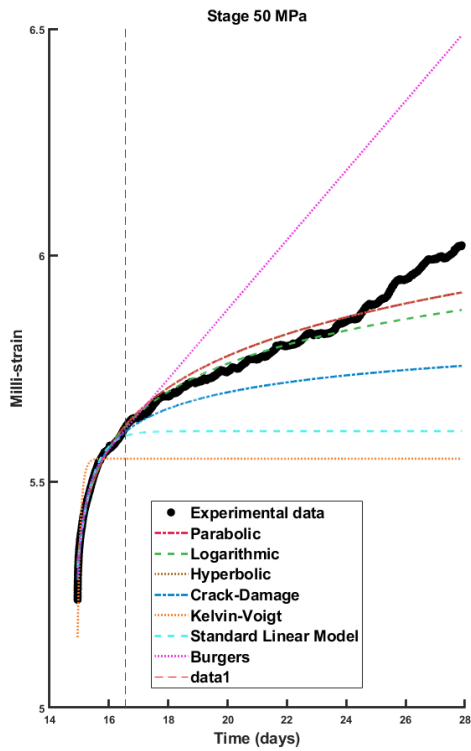
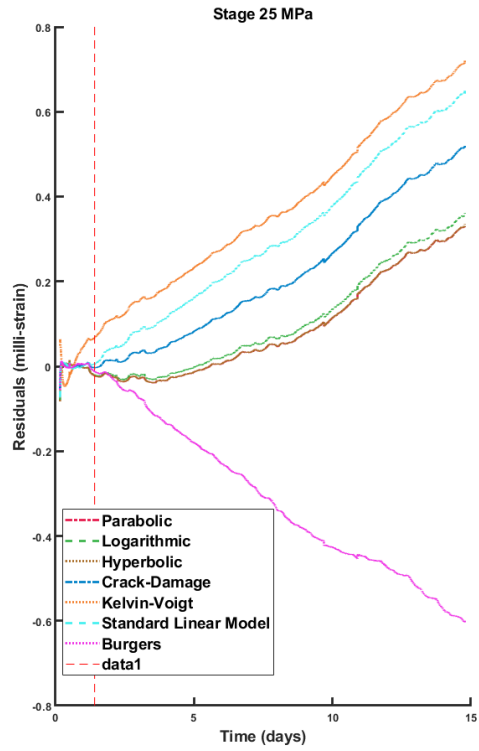
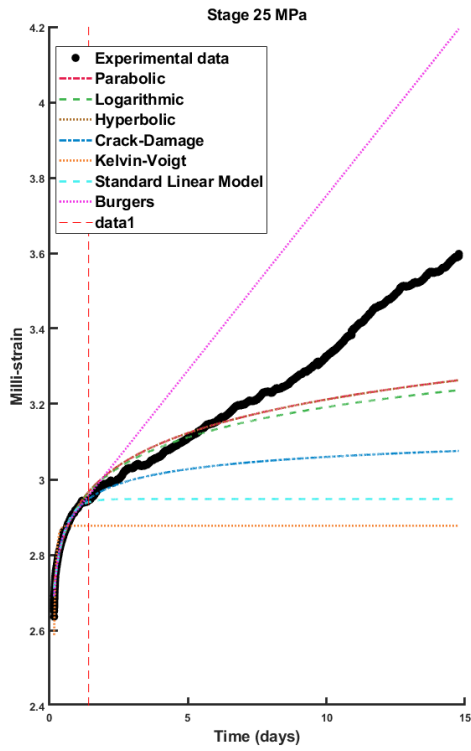
Table 24: Fitted parameters of empirical laws models for the shale sample saturated with the synthetic brine

Model	Stage	A_i	m	B_i	k	s	E	E_1	E_2	η_1	η_2	η	$stderr$	R^2
Parabolic	25	0.00293	0.04										103.008	0.708328
	50	0.00195	0.067										32.2873	0.950412
	80	0.00156	0.135										61.586	0.295645
	104	0.00180	0.119										280.068	0.426944
Logarithmic	25	0.00293		0.00012									110.225	0.642748
	50	0.00195		0.00013									39.6716	0.919381
	80	0.00155		0.00024									40.2205	0.679703
	104	0.00181		0.00021									311.332	0.227787
Hyperbolic	25	29.72607		0.00		0.040							103.081	0.707542
	50	20.38082		0.00		0.067							32.3055	0.950385
	80	19.49066		0.00		0.134							61.6179	0.294865
	104	20.04327		0.00		0.118							280.129	0.426497
Crack-damage	25	0.00339		0.766	166.0895								156.553	-0.0025
	50	0.00268		1.787	284.5523								72.2406	0.550534
	80	0.00213		0.273	2.022068								58.3969	0.431426
	104	0.00369		4.77	845.0594								351.28	-0.0830261
Kelvin–Voigt	25						8.69E + 03					614.4	215.36	-1.60194
	50						1.28E + 04					1313.3	134.77	-1.41976
	80						1.61E + 04					10776.55	98.2515	-0.83414
	104						1.37E + 04					2055.919	462.623	-1.42437
Standard linear	25						9.69E + 03	6.79E + 04				25278.83	196.664	-0.859201
	50						1.57E + 04	5.89E + 04				28408.51	117.524	-0.498331
	80						3.98E + 04	2.64E + 04				24949.85	90.7688	-0.459646
	104						1.94E + 04	3.76E + 04				23272.08	431.526	-0.860544
	25						9.69E + 03	6.79E + 04	18002.72	679.2071		192.264	-0.9018	

Burgers	50						1.57E + 04	5.89E + 04	130251.9	969.85		151.852	-1.057
	80						3.98E + 04	2.64E + 04	372826.2	188.861		167.648	-2.68
	104						1.94E + 04	3.76E + 04	209447.3	581.8317		172.533	0.780

A_i , m , B_i , k and s are the constitutive parameters associated with the parabolic, logarithmic, hyperbolic and crack-damage empirical models, respectively.

E , E_1 , E_2 , η_1 , η_2 and η are the constitutive parameters associated with the Kelvin–Voigt, standard linear and Burgers analytical models, respectively. Each E and η is representative of the modulus of elasticity in the corresponding springs and the viscosity coefficient in the corresponding dashpots.



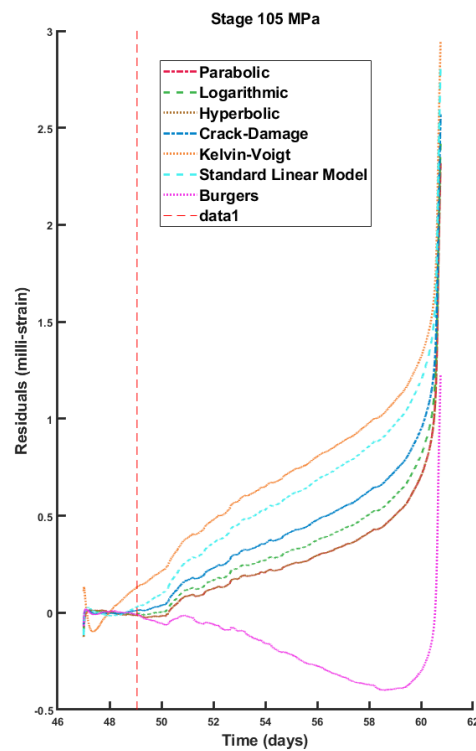
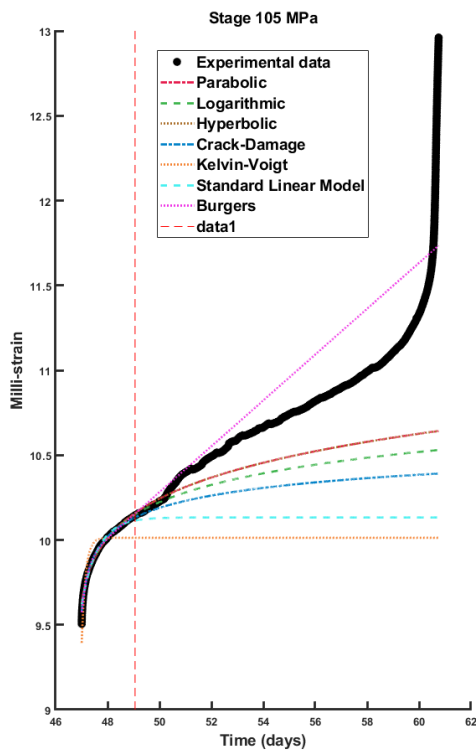
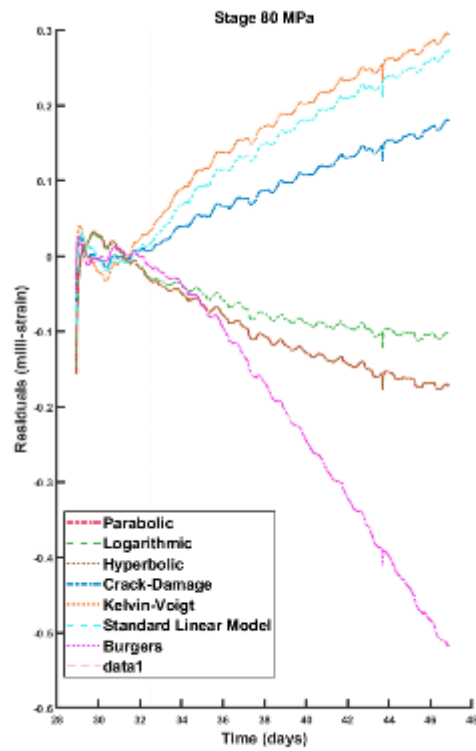
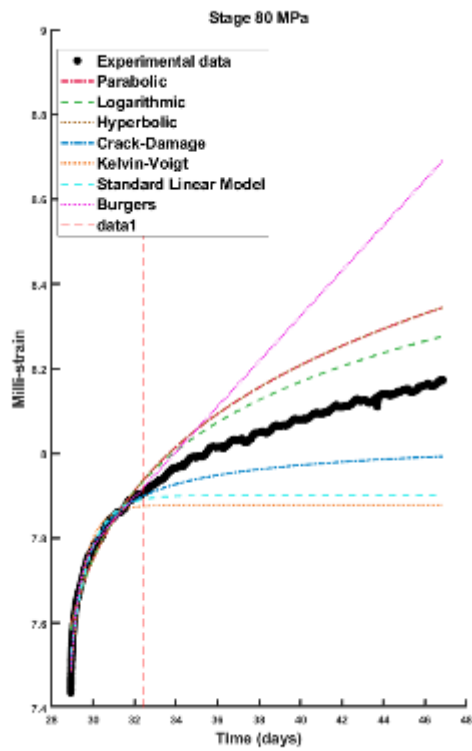


Figure 51: Comparative analysis of fitted creep models and corresponding standard errors across multiple stages of the triaxial creep test on sample 3993

3.4.4. MSTXL creep test on Na₂SiO₃-saturated sample 3994

The mechanical properties of shale rocks, including Young's modulus and hardness, may undergo alterations when subjected to certain solutions. Observations of shale behaviour in the field have also revealed that when subjected to water-based fracturing fluids, shale tends to experience creep over time, transitioning from its initial brittle state to a more viscous material (Du et al., 2018). This reduction in stiffness leads to acceleration of creep deformation. That is, chemical solutions can weaken shale by reducing its stiffness, which is beneficial in terms of accelerating creep deformation and activation of shale barriers.

However, the selection of chemical solutions needs to be carefully engineered. Different chemical solutions have been used near wellbores for a range of purposes, including use of inhibitor solutions to improve wellbore stability. Research has shown that sodium silicate solutions perform poorly in terms of wellbore stability, and therefore they might be suitable candidates for stimulating shale to form a barrier (van Oort et al., 2020). The reason for this behaviour can be attributed to the high alkalinity (pH ~11) of silicate solutions, which leads to weakening of shale and its dispersion.

Additionally, clay swelling can be induced by unfavourable cation exchange at clay sites, such as the replacement of potassium ions by sodium or lithium ions. This process results in heightened intermolecular hydration forces and double-layer repulsion in the clay fabric. The inhibition potential of smectic clays by cations follows, in descending order, Cs⁺ > K⁺ > Na⁺ > Li⁺. Thus, sodium silicate seems well suited for shale barrier activation (van Oort et al., 2020).

Figure 52 illustrates the stress path employed to examine the response of sample 3994, which was tested post-saturation with Na₂SiO₃ solution, to the MSTXL creep test. As can be seen, the test began with a relatively low differential stress level (σ_d , difference between axial and confining stresses) and then, for each stage, the differential stress was held constant until the strain stabilised and then the next stage began. The differential stress was increased in sequential stages: 25 MPa, 50 MPa, 75 MPa,

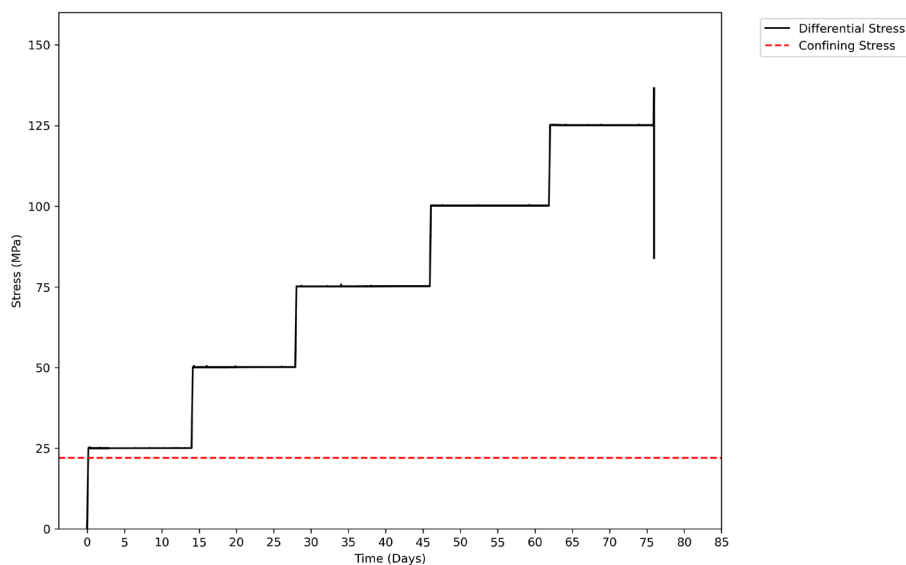


Figure 52: Stress path employed to investigate the response of sample 3994 saturated with Na₂SiO₃ to the MSTXL creep test

100 MPa and 125 MPa, and eventually the sample failed at $\sigma_d = 136.66$ MPa after 75.95 days, while the confining pressure (P_c) remained at 22 MPa throughout the experiment.

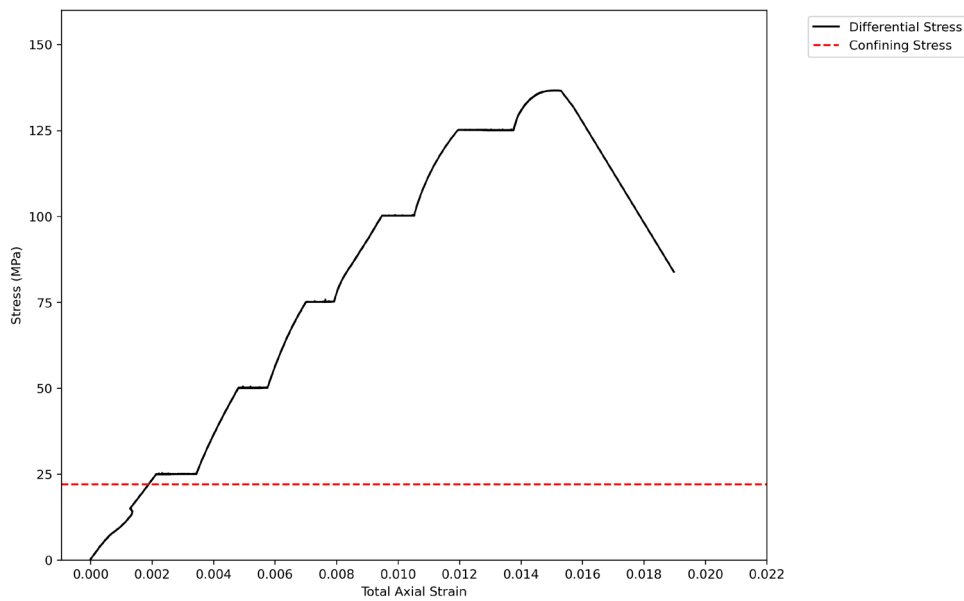
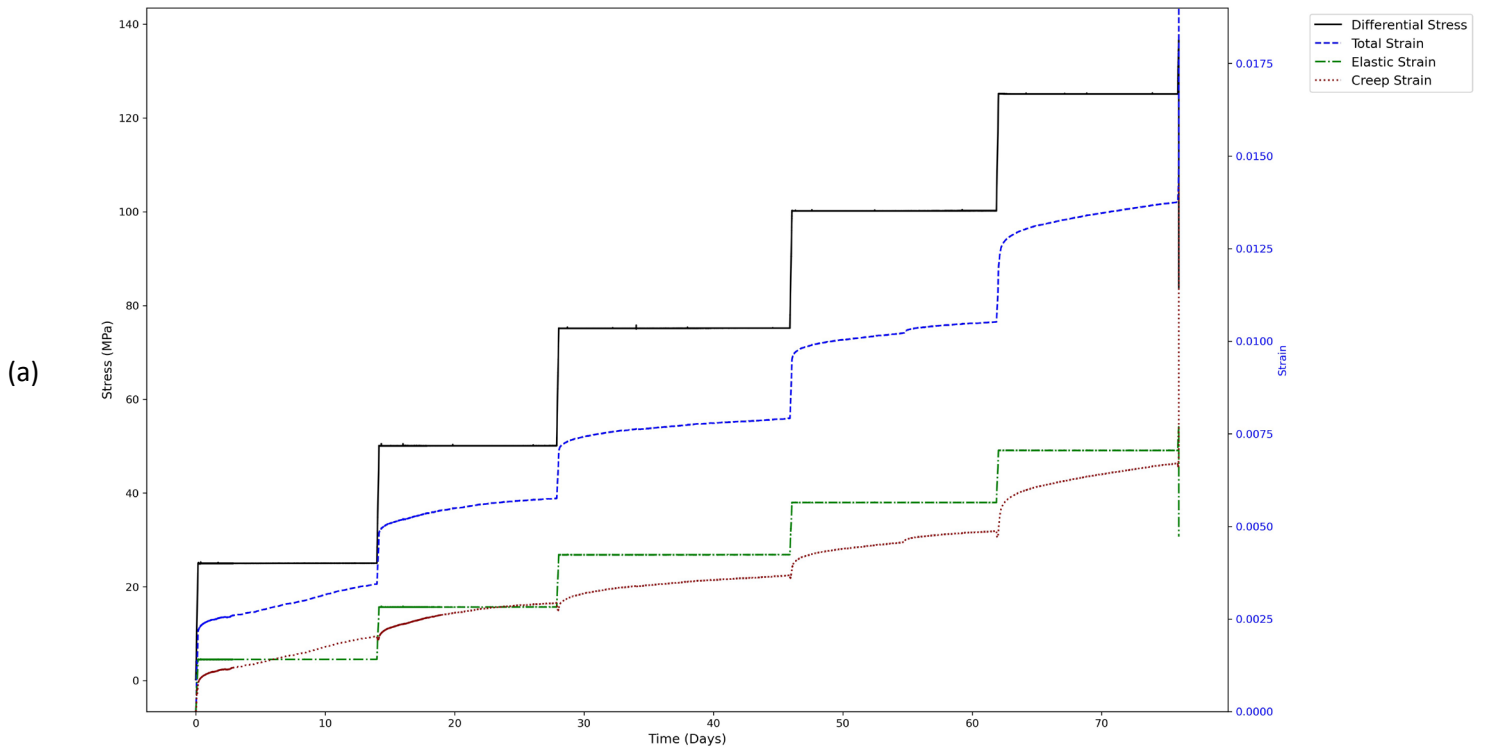


Figure 53: Stress–strain response of sample 3994, saturated with Na_2SiO_3 solution, to the MSTXL creep test

Figure 53 depicts the stress–strain response of sample 3994 saturated with Na_2SiO_3 solution prior to undergoing the MSTXL creep test. The sample withstood five stages of increased differential stress and their respective hold stages and eventually failed at a strain of 0.01497.



(b)

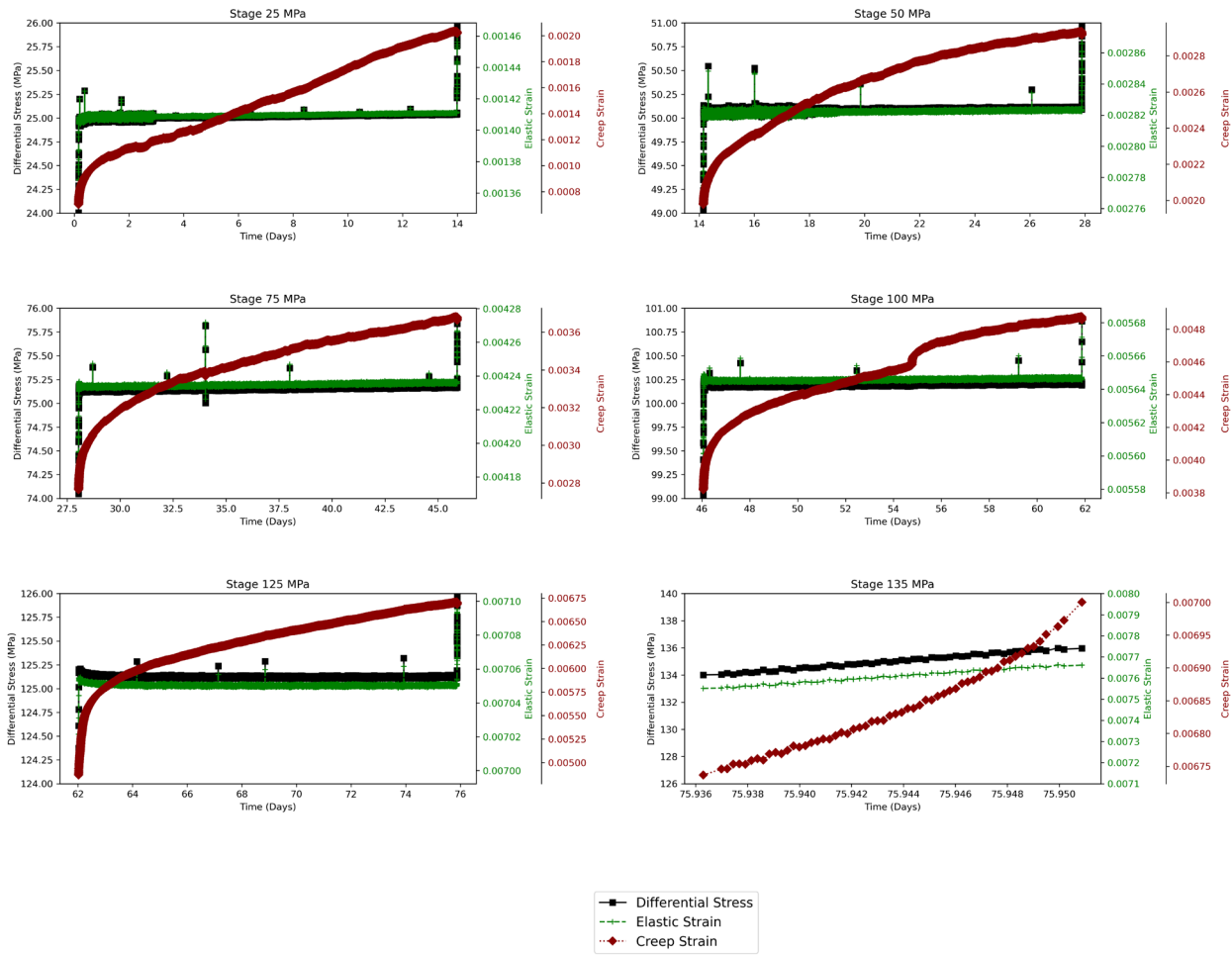


Figure 54: (a) Differential stress–strain behaviour over time in the MSTXL creep test on sample 3944; (b) analysing the differential stress–strain (including elastic and creep strain) behaviour over time for each stage

Figure 54a shows the differential stress and the corresponding total strain, elastic strain and creep strain. Figure 54b demonstrates elastic and time-dependent creep strain in each stage versus time during constant differential stress for the saturated sample. The test was performed in five complete stages (increasing the differential stress and holding it for at least 14 days). The primary and secondary stages of creep can be observed in all stages, except for the 135 MPa stage. In this last stage the strain failed to stabilise and the sample failed at 136.66 MPa after 75.955 days.

Figure 55 depicts the evolution of total axial, elastic and creep strain over time for each stage. In the first stage, the differential stress was kept constant at 25 MPa for 14 days, and the total axial strain and creep strain reached 0.0035 and 0.002, respectively. The creep strain (ϵ_c) reached 57% of the total strain ($\epsilon_c/\epsilon_t = 57\%$), which is significantly different behaviour compared with sample 3993 (where the ratio was 22%). In the second stage, in which the differential stress was kept constant at 50 MPa for 13 days, the ratio of creep strain to total strain decreased to 51% ($\epsilon_c/\epsilon_t = 0.0028/0.0055$). This ratio slightly reduced to 49% in the third stage (differential stress constant at 100 MPa, for 18 days). In the fifth stage, when the differential stress was kept constant at 125 MPa 13 days, the creep

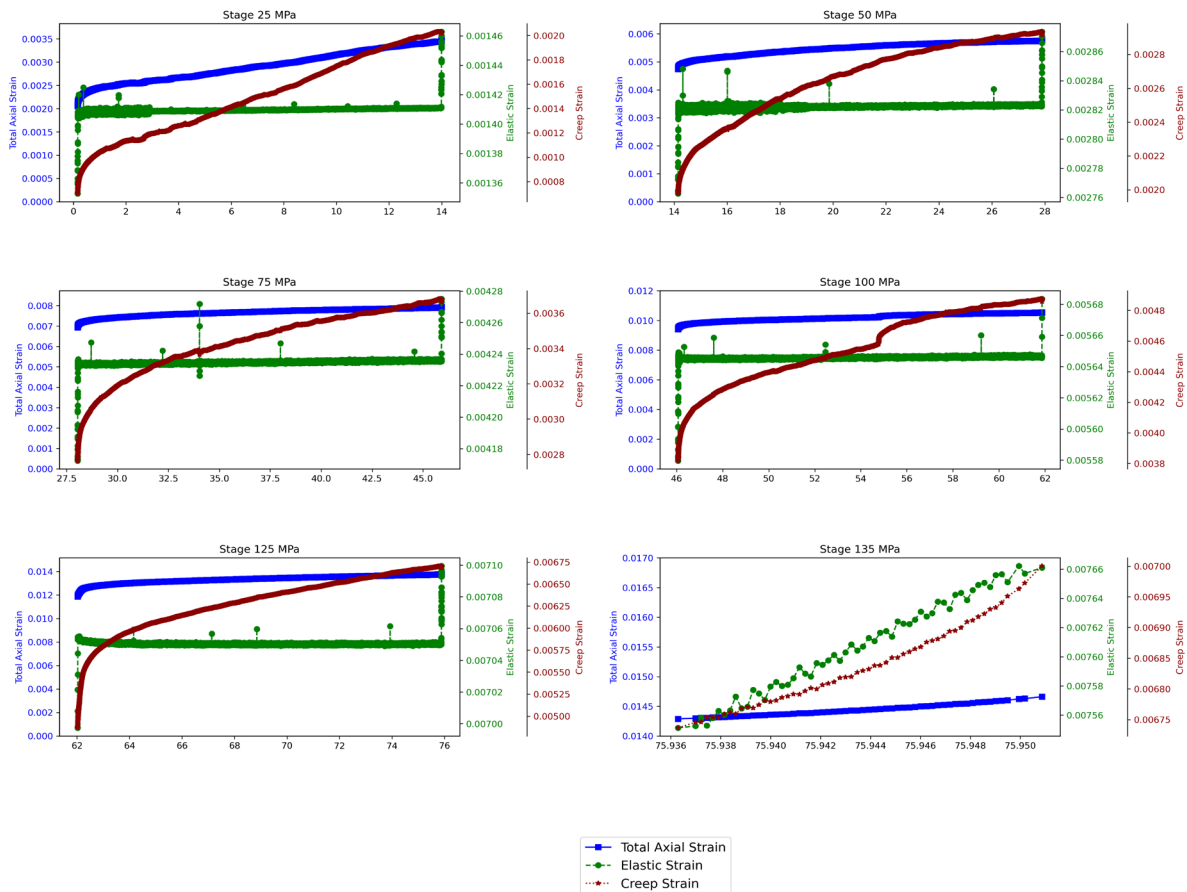


Figure 55: The evolution of total axial, elastic, and creep strain over time for each stage of testing sample 3994

strain reached 0.0066, resulting in a ratio of 48%. It is worth noting that in the last stage when stress reached

136.66 MPa the sample failed and therefore it wasn't possible to keep the stress constant to measure creep strain; what is shown as creep strain is, in fact, the inelastic strain that occurred prior to failure.

Figure 56 illustrates the evolution of creep strain rate during the holding stages for sample 3994. Both the primary and secondary stages of creep are observable in all stages, except for the 130 MPa stage. Comparison of these figures reveals that as the sample is subjected to higher differential stress, the transition time from primary creep stage to secondary creep stage shortens. In other words, the microstructural variations in the shale sample – including mineral composition, grain size and pre-existing microcracks – could influence its response to different stress levels. At lower stress levels (25 MPa and 50 MPa; the durations of primary creep stage for stage 25 MPa and 50 MPa are 3 and 4 days, respectively) the material exhibited a more significant time-dependent response due to the slower closure of microcracks and the redistribution of stress within the matrix. Additionally, at lower stresses, the primary creep stage is induced by time-dependent processes such as microcrack healing, slow grain boundary sliding and the viscoelastic behaviour of the shale. As the stress increases, these processes occur more rapidly or are overtaken by faster deformation mechanisms, such as dislocation movement and plastic flow, resulting in a shorter primary stage.

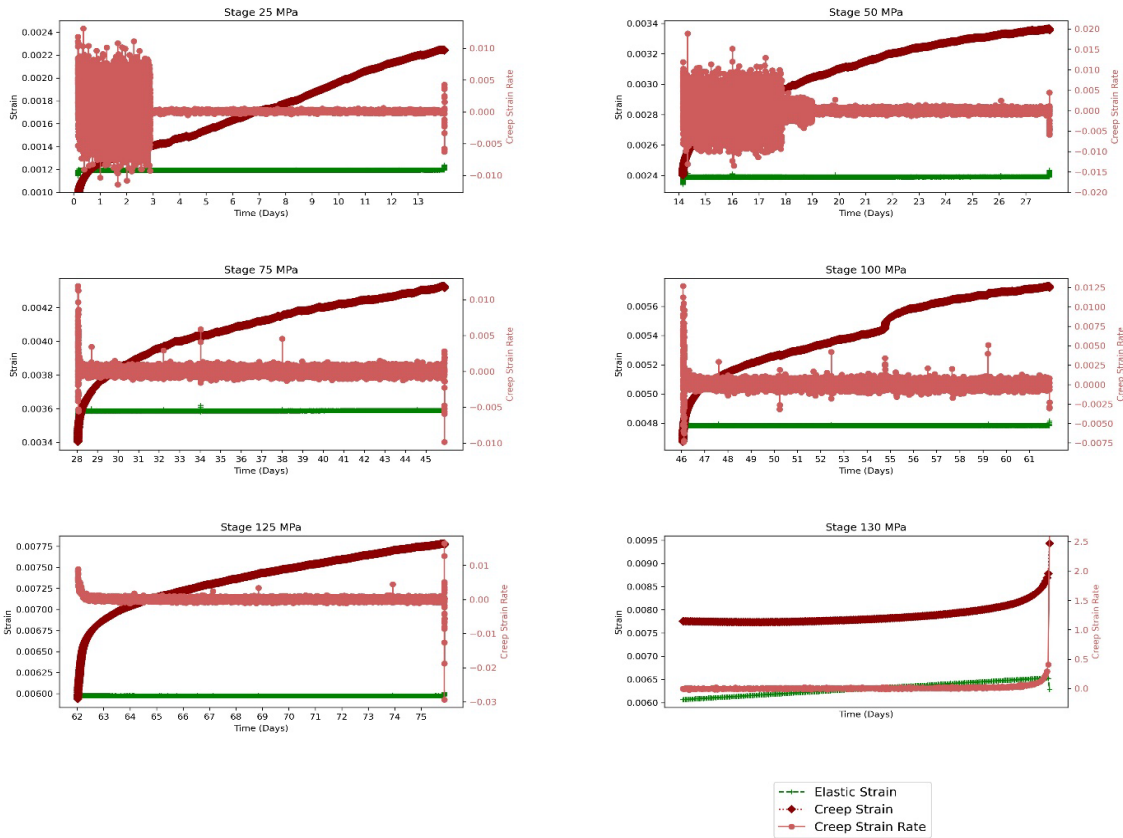


Figure 56: The magnitudes of creep strain, elastic strain and creep strain rate over time for each stage of testing sample 3994

3.4.4.1. Predicting creep strain behaviour for Na₂SiO₃-saturated sample 3994

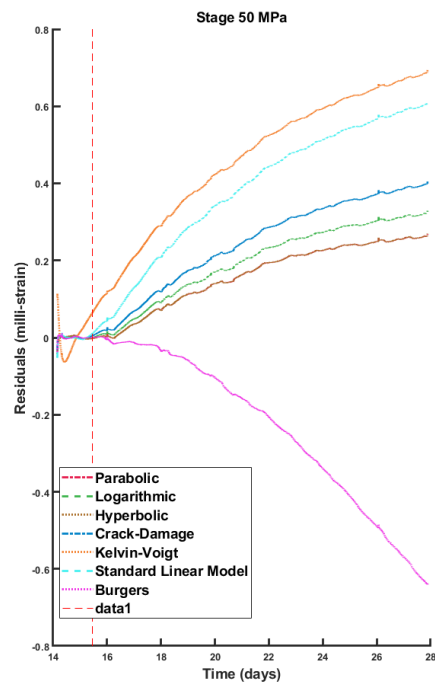
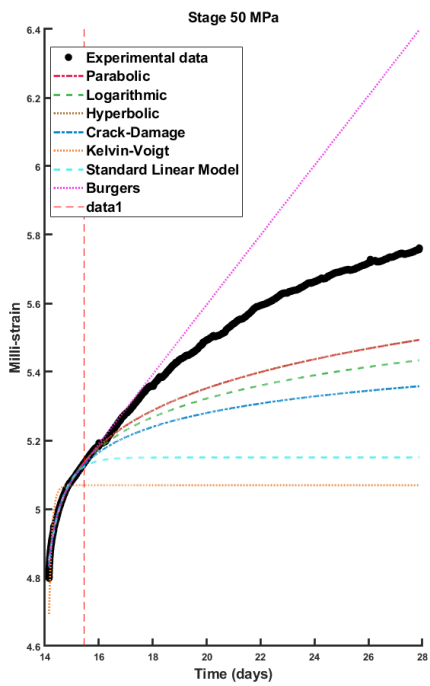
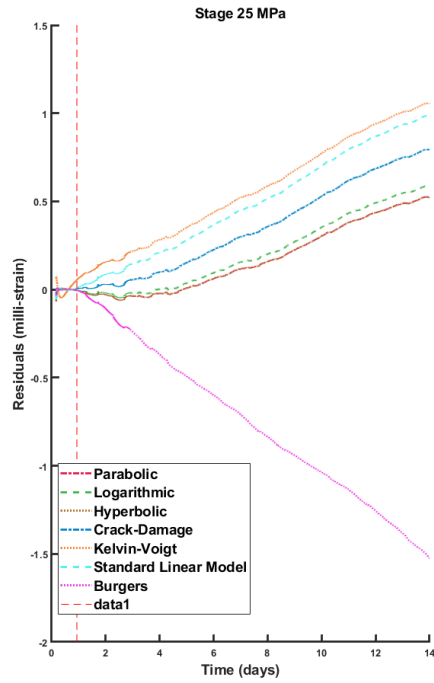
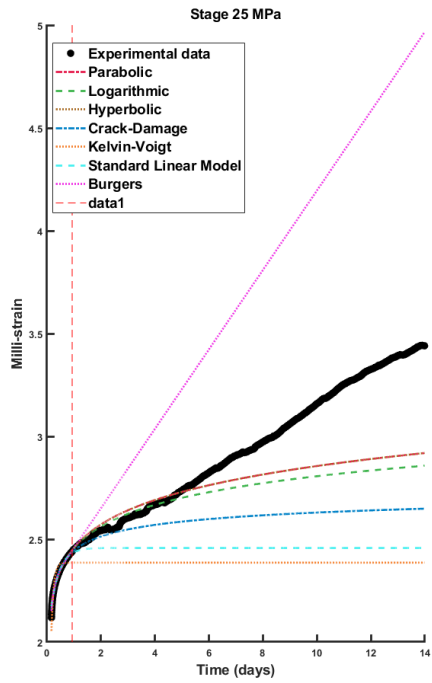
In this section, the strain responses obtained from each stage are used to perform curve-fitting procedures using the various models introduced in section 3.2. In this way, we obtain the corresponding parameters from which we predict the long-term viscoelastic behaviour of the shale post-saturation with Na₂SiO₃ solution.

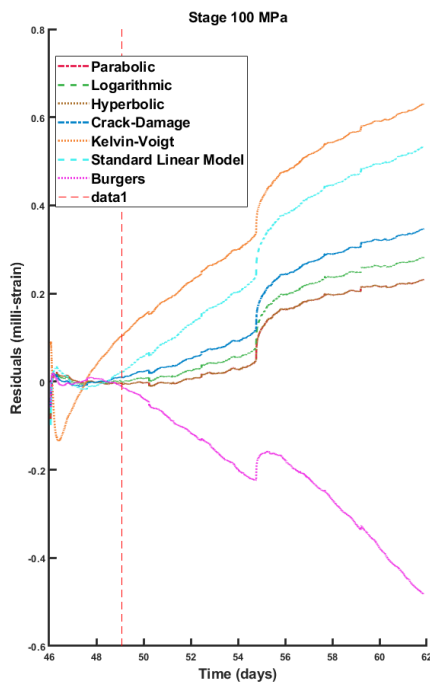
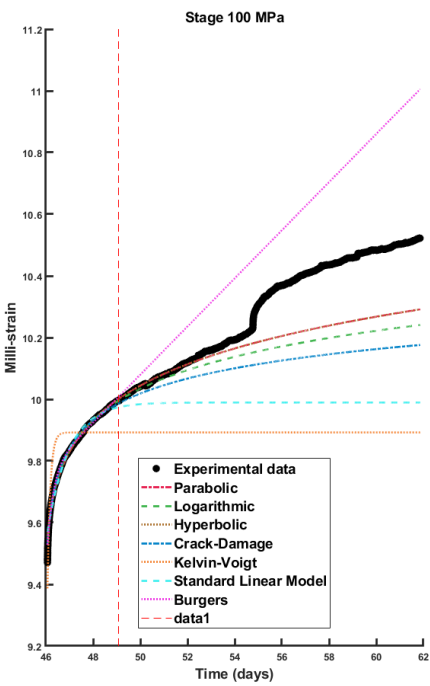
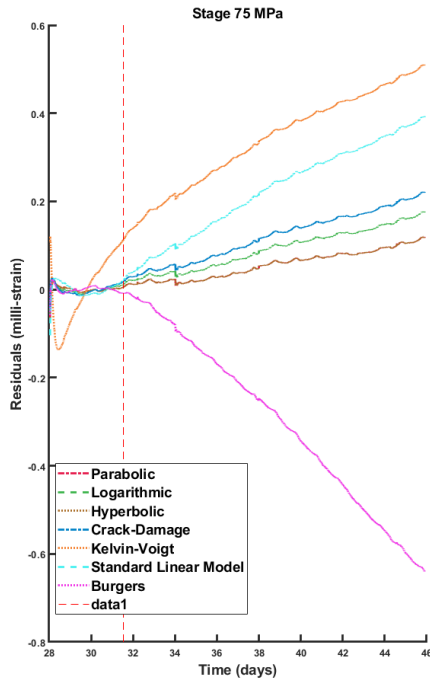
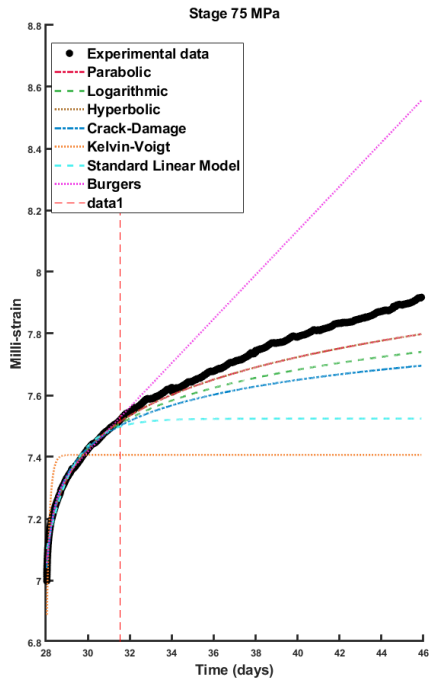
Figure 57 illustrates the creep data acquired from experiments, highlighting the fitting of various creep models together with the stderr for each phase of the MSTLX test on sample 3994. Table 25 provides the respective fitting parameters for each phase, along with the values of R^2 and stderr. Note that, to assess the capacity of each model to predict the long-term creep behaviour in each phase, only 20% of the experimental data (marked by the red dashed line and denoted as 'data1' in Figures 45, 51 and 57) was employed for curve-fitting and parameter derivation. Subsequently, these parameters were used by the model to forecast the remaining creep behaviour.

From examining Table 25, it is evident that certain models perform better than others in terms of their ability to predict long-term creep behaviour. Note here that the parameters obtained for the 135 MPa stage were discarded, since all shales experienced failure and stress did not stabilise in this stage.

The hyperbolic and parabolic models exhibited the highest average R^2 values (0.804), indicating a strong correlation between the model predictions and experimental data across all stages, a figure

much higher than the other models investigated. Additionally, the hyperbolic and parabolic models also showed the lowest average stderr further validating their accuracy in describing the observed creep behaviour. Conversely, the Kelvin–Voigt model performed the poorest, with an average R^2 value of -1.432 , signifying a very poor relationship between the model predictions and the experimental data. Overall, the hyperbolic and parabolic models emerged as the top performers, while the Kelvin–Voigt model falls short due to its inherent limitations in capturing the intricacies of creep deformation.





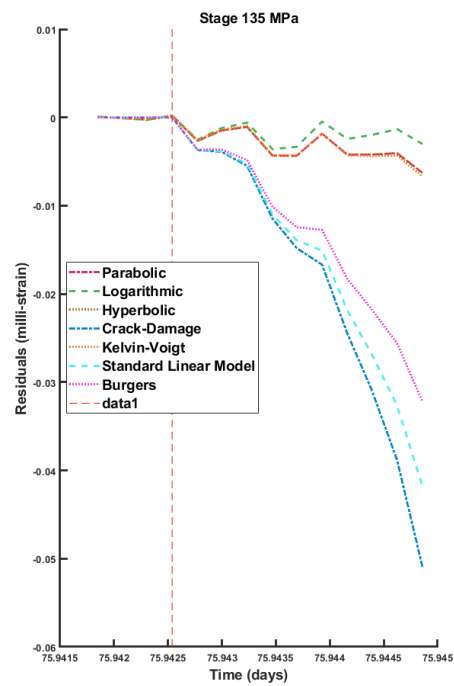
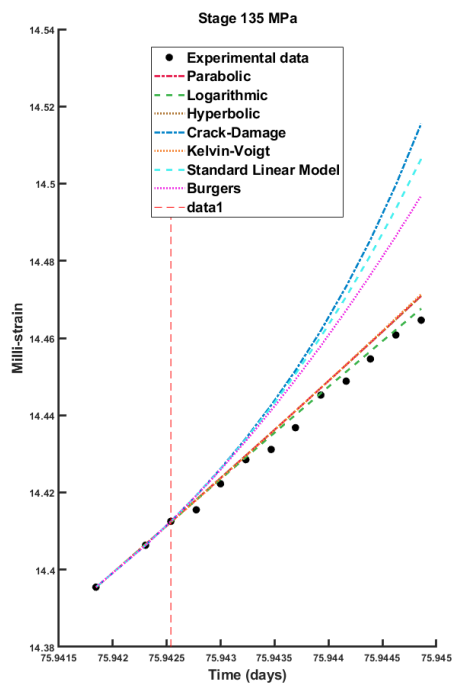
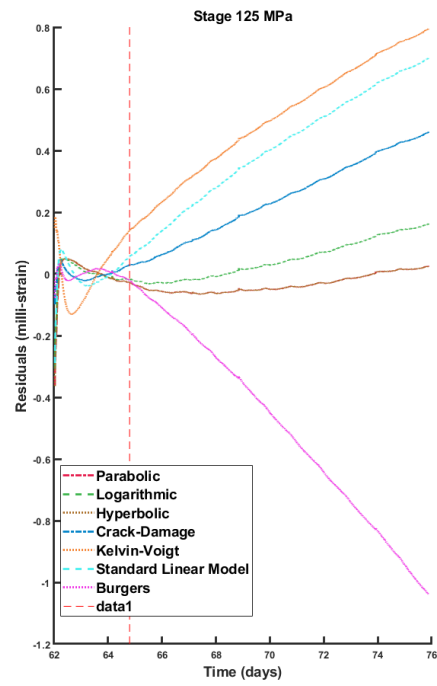
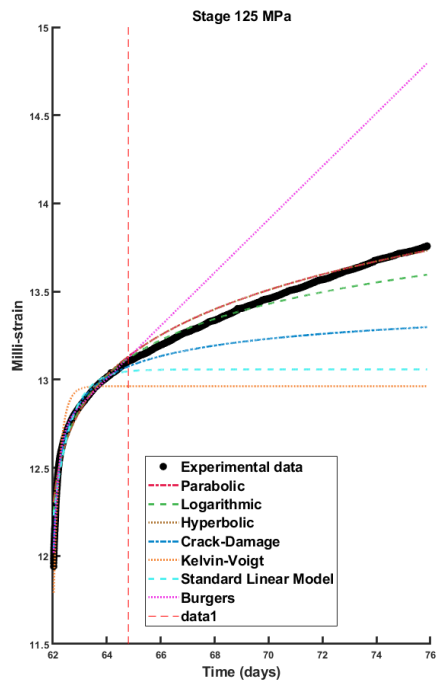


Figure 57: Comparisons of fitted creep models and their corresponding standard errors across multiple stages of the triaxial creep test on sample 3994

Table 25: Fitted parameters of empirical law models for shale saturated with Na₂SiO₃ solution

Model	Stage	A_i	m	B_i	k	s	E	E_1	E_2	η_1	η_2	η	$stderr$	R^2	
Parabolic	25	0.0024	0.0651										147.423	0.73	
	50	0.0016	0.0851										93.3156	0.71	
	75	0.0015	0.0942										36.1581	0.90	
	100	0.0019	0.0809										95.0797	0.70	
	125	0.0022	0.1325										34.9649	0.98	
	135												2.07017	0.97	
Logarithmic	25	0.0024	0.0002			0.0650							163.468		
	50	0.0016	0.0001			0.085							111.763	0.56	
	75	0.0015	0.0001			0.094							54.9315	0.76	
	100	0.0019	0.0002			0.080							110.614	0.56	
	125	0.0022	0.0003			0.133							60.106	0.95	
	135														
Hyperbolic	25	24.51	3.34E-62										147.43	0.73	
	50	17.145	5.40E-48										93.35	0.71	
	75	17.60	9.04E-44										36.16	0.90	
	100	20.84	1.11E-50										95.12	0.70	
	125	26.31	2.15E-31										34.96	0.98	
	135														
Crack-damage	25	0.0031	1.2932		207.2								219.57	0.26	
	50	0.0033	6.8052		1351								135.54	0.33	
	75	0.0044	11.756		7600								69.70	0.59	
	100	0.0041	7.7894		2277								130.87	0.33	
	125	0.0035	1.6051		39.22								151.02	0.36	
	135				14.03										
Kelvin–Voigt	25						10477.6					871.8764	222.88	-1.65	
	50						15420					1738.34	263.60	-1.46	
	75						15206.2					2159.353	2.18	0.97	
	100						12709.88					1538.292	288.06	-0.69	
	125						19233.74					2297.945	226.20	-1.37	
	135														
Standard linear	25							12588.18	53036.6				16993.09	274.91	-0.32
	50							19266.47	61788.93				33485.59	204.58	-0.63
	75							19530.35	51921.2				65152.98	129.56	-0.42
	100							16001.05	49865.99				45438.28	193.67	-0.68
	125							17032.77	23187.05				14798.48	233.52	-0.71
	135														
Burgers	25							12588.1	53036.6	5179.385	161.6361		413.51	-2.04	
	50							19266.47	61788.93	92115.85	776.9498		176.78	0.19	
	75							19530.35	51921.2	247434.3	867.4992		207.12	-1.93	
	100							16001.05	49865.99	333976.8	605.1905		140.78	0.14	
	125							17032.77	23187.05	227937.5	108.2283		331.16	-1.86	
	135														

A_i , m , B_i , k and s are the constitutive parameters associated with the parabolic, logarithmic, hyperbolic and crack-damage empirical models, respectively.

E , E_1 , E_2 , η_1 , η_2 and η are the constitutive parameters associated with the Kelvin–Voigt, standard linear and Burgers analytical models, respectively. Each E and η is representative of the modulus of elasticity in the corresponding springs and the viscosity coefficient in the corresponding dashpots.

3.5. Discussion

Figure 58 compares the time-dependent stress–strain responses of the three samples – denoted as 3992 (dry sample), 3993 (sample saturated with the synthetic brine) and 3994 (sample saturated with the Na_2SiO_3 solution) – when subjected to MSTXL creep tests. The corresponding total axial strain and creep strain are compared in Figure 59a and 59b, respectively. All samples demonstrated time-dependent deformation over time but to different extents. The general observation was that strain responses increased as the applied axial differential stresses were increased from one stage to the next.

The MSTXL creep tests on sample 3992 were conducted under dry conditions at an in-situ temperature of 82°C (temperature retrieved from the Shenandoah-1A General Information Report, available on the Northern Territory Government website) and a confining stress of 20 MPa. This sample underwent five sequential increases in differential stress, and the corresponding hold stages, and eventually failed at a stress point of 125 MPa and a corresponding strain of 0.0083 after 74.87 days.

Prior to conducting the MSTXL creep test, sample 3993 was saturated with synthetic brine (the composition of which is detailed in Table 20). The sample experienced failure after 60.76 days during the fourth stage, at an axial differential stress of 104 MPa and corresponding strain of 0.013. Again, the confining pressure and temperature were maintained constant at 20 MPa and 82°C , respectively.

To investigate the effect of chemical solutions on the time-dependent behaviour, sample 3994 was saturated with a sodium silicate solution (Na_2SiO_3) before being subjected to the MSTXL creep test, under similar confining conditions. The sample failed at the fifth stage (differential stress of 125 MPa and a hold stage of 2 weeks) at an axial differential stress of 136.66 MPa and a corresponding strain of 0.015.

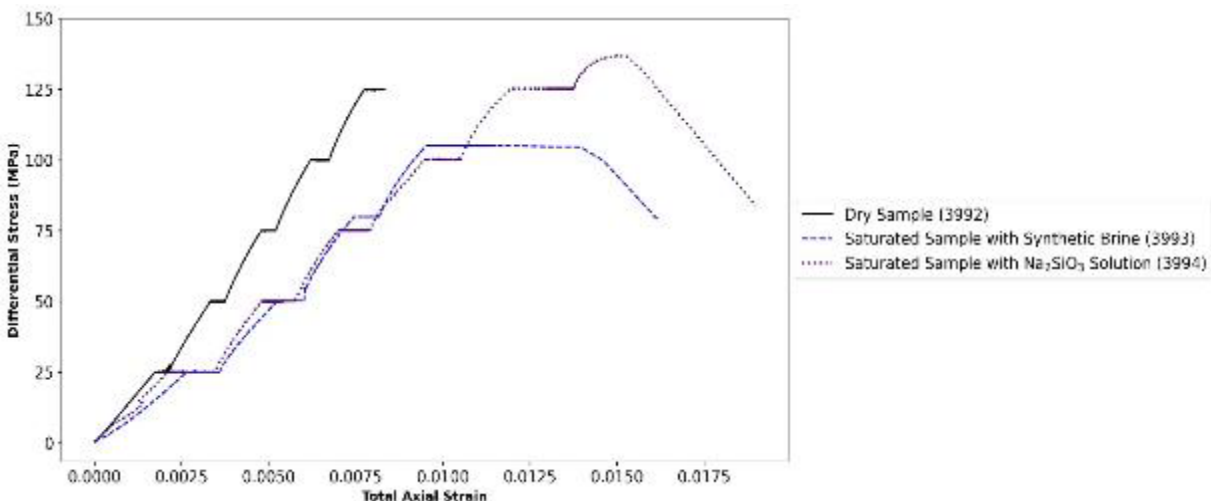


Figure 58: Comparing the stress–strain response of the shale samples to MSTXL creep tests under three conditions: dry and after saturation with the synthetic brine or Na_2SiO_3 solution

The stress–strain responses of samples 3992 and 3994 under the MSTXL creep tests reveal their distinctive behaviours and failure mechanisms. For sample 3992, when subjected to sequential stress stages of 25 MPa, 50 MPa, 75 MPa, 100 MPa and 125 MPa, the observed maximum strain reached approximately 0.008. Notably, sample 3992 experienced failure during the holding stage of 125 MPa. On the other hand, sample 3994, when undergoing the same stages of stress, withstood the final stress stage of 125 MPa for 15 days and finally failed at a stress of 136.66 MPa (each stress stage typically lasted ~15 days). Looking at the stress–strain responses of the three samples, the curve corresponding to sample 3992 (dry) exhibited the steepest slope.

This indicates that the dry sample exhibited higher stiffness or resistance to deformation (brittleness). The average Young’s modulus of the dry sample was calculated as 20.95 GPa. This

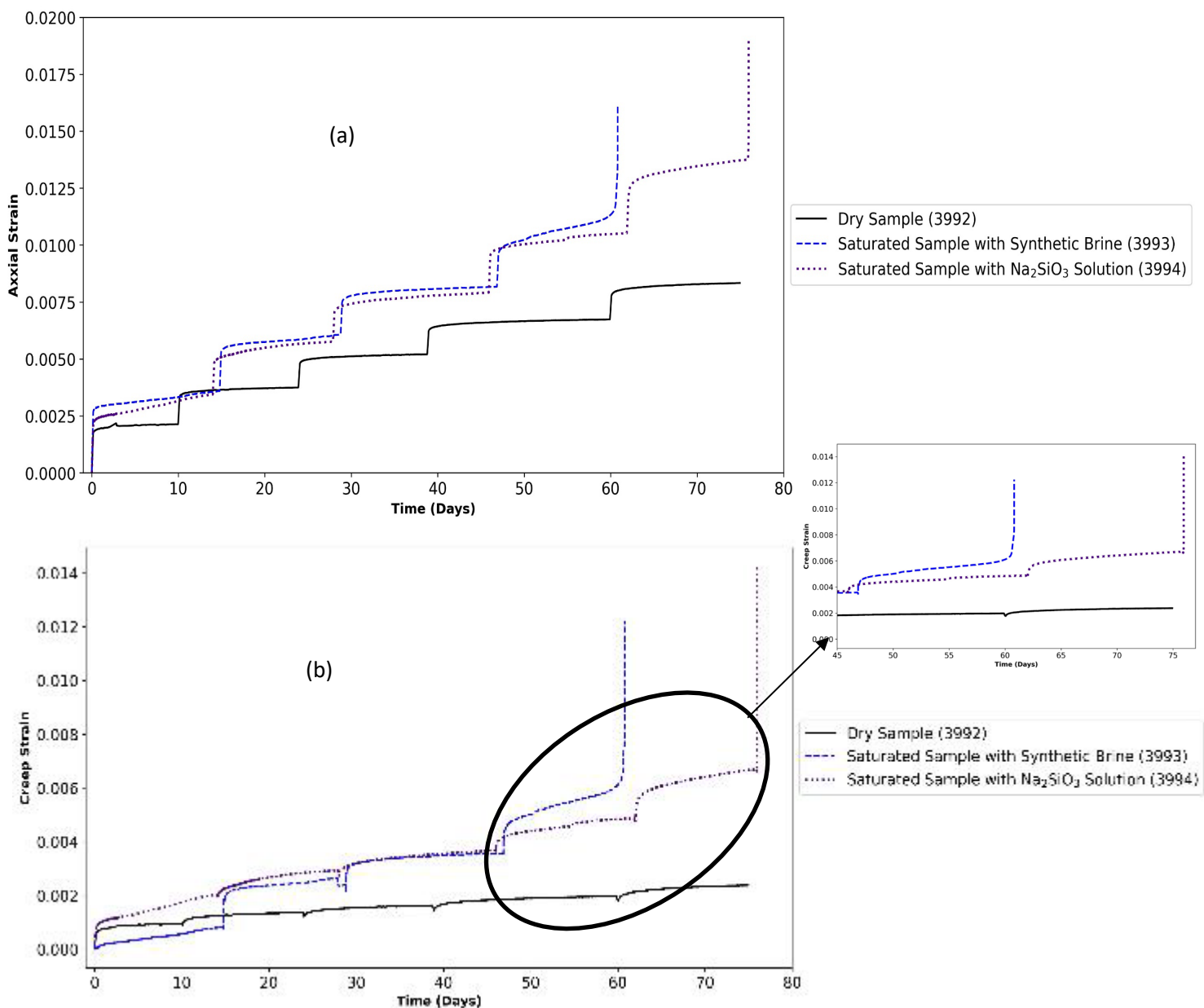


Figure 59: (a) Comparison of the axial strain and creep strain magnitudes of the three shale samples under MSTXL creep tests; the conditions are dry and after saturation with synthetic brine or Na₂SiO₃ solution

contrasts with samples 3993 and 3994, which showed more ductile behaviour, with an average Young's modulus of 15.33 and 16.37 GPa, respectively.

Comparing the responses of the dry sample (3992) with the sample saturated with Na_2SiO_3 (3994) also reveals how incorporating the chemical solution might play a significant role in stimulating creep deformation and creating barriers during decommissioning. In stage 25 MPa, the dry sample took 10 days to stabilise, while for sample 3994 the strain increased linearly for 15 days. The magnitude of the total axial strain for sample 3994 at stage 50 MPa stabilised at 0.0052, while the corresponding magnitude for the dry sample (3992) was 0.00375. Assessing the magnitude of strain at the holding stage of 125 MPa indicates that it reached 0.01375, whereas the corresponding strain for the dry sample was 0.0075. These results are in consistent agreement with results obtained from studies carried out by Du et al. (2018) and Lui et al. (2018).

An increase in shale softening leads to greater creep deformation, as observed in studies correlating creep with decreased Young's modulus and hardness. This means that as shale becomes more compliant, its viscous deformation becomes more pronounced, especially when exposed to water-based solutions, resulting in a decrease in shale strength. In addition, chemical solutions can function as lubricants by reducing friction between shale grains, facilitating smoother sliding. The concentration of salts is critical in this process: lower concentrations may promote dispersion and weaken the shale. Moreover, ion exchange processes occur where cations in saline solutions induce osmotic effects, influencing the behaviour of the shale.

In other words, increased shale softening leads to greater creep deformation, as evidenced by studies correlating creep with decreased Young's modulus and hardness. The major mechanisms contributing to shale softening while incorporating chemical solutions are the physical-chemical interactions during shale interaction with the chemical solutions. These involve clay-fluid interactions and shale hydration (Y. Liu et al., 2022), double-layer repulsion, mineral dissolution and distortion, as well as a mechanism related to the breaking and reforming of molecular bonds within the grains or rearrangement at both the grain and molecular levels in shales and viscous adjustment of clay structure.

Studies have indicated that stiff constituent within shale – such as quartz, feldspar and carbonate – generally considered resistant to fluid interactions may experience to some extent weakening when subjected to chemical solutions and hydration processes (Y. Liu et al., 2022). It is worth noting that the sensitivities of creep strain rates to these mechanisms vary significantly depending on how shale-fluid interactions affect the mechanisms of creep, which involve dislocation activities (including shifts in crystal structure) and diffusion processes (such as grain boundary diffusion and grain boundary sliding).

Our experiments demonstrate that the softening of shales from the Kyalla Formation (at a depth of 1590 m) in the Beetaloo Sub-basin causes a transition from brittle behaviour to a more viscous state. This transformation results in significant creep deformation over time. The softened shales exhibit increased plasticity and a propensity for gradual deformation under constant stress conditions. This phenomenon highlights their altered mechanical response, illustrating how shale softening in this geological context leads to pronounced creep behaviour.

3.6. Conclusion

This chapter has explored the complicated relationship between the time-dependent behaviour exhibited by shales and the effect of applied stress. It has also examined the effects of incorporating chemical solutions to induce creep and establish barriers, with potential applications in the decommissioning of wells. The response of shales during creep tests follows distinct stages: an initial elastic strain, primary (transient) creep, secondary (steady-state) creep, and tertiary (accelerating) creep, ultimately resulting in material failure. The occurrence of secondary and tertiary creep depends on several factors, including but not limited to the stress magnitude, the duration of the applied stress, the chemistry of the surrounding environment and the geomechanical properties of the sample.

This study has specifically focused on examining the primary and secondary creep stages of samples obtained from the Kyalla Formation (Shenandoah-1A well), both experimentally and in subsequent curve-fitting.

It is worth mentioning that these samples may not be fully representative of the entire Kyalla shale reservoir, which spans hundreds of metres and is known to be more clay-rich.

In addition, a segment of core was processed to extract powder for synthesising chemically equilibrated brine, which was used for re-saturation and producing the synthetic brine.

The samples – numbered 3991, 3992, 3993 and 3994 – underwent geomechanical testing including STXL compression and MSTXL creep tests. STXL was performed on sample 3991 and MSTXL on sample 3922 under dry conditions. MSTXL testing was also conducted on samples 3933 and 3994 after saturation with synthetic brine and Na_2SiO_3 solution, respectively. All geomechanical assessments were conducted while maintaining a confining pressure of 20–22 MPa and a temperature of 82°C (in-situ temperature).

When comparing the stress–strain responses of the three samples, the curve of sample 3992 (dry conditions) displayed the steepest slope, indicating that the dry sample demonstrated greater stiffness and brittleness. The average Young's modulus of the dry sample was calculated as 20.95 GPa. In contrast, samples 3993 and 3994 exhibited more ductile behaviour, with average Young's moduli of 15.33 and 16.37 GPa, respectively.

Looking in more detail at the behaviours of the dry sample (3992) and the sample saturated with Na_2SiO_3 (3994) highlights the significant effect of chemical solutions in inducing creep deformation and establishing a barrier during decommissioning. Incorporating specific chemical solutions softens the shale (decreasing Young's modulus and brittleness) and enhances creep deformation. In other words, the shale becomes more flexible and deformable.

In order to predict the long-term viscoelastic behavior of shale gas reservoirs, fitting the experimental data to various empirical creep models (such as parabolic, logarithmic, hyperbolic, and crack-damage) and analytical or rheological models (including Kelvin–Voigt, standard linear, and Burgers) proved to be an effective approach. The constitutive model parameters could then be derived through curve-fitting to the STXL and MSTXL creep data. Notably, short-term creep tests can provide

constitutive model parameters capable of predicting long-term deformation in shales under test. The primary task is to select a model(s) capable of reliably predicting the behavior of the specimen under in-situ conditions, using the constitutive parameters derived from the model.

R^2 and $stderr$ are appropriate measures to evaluate the goodness of fit. R^2 values range from 0 to 1, with higher R^2 values indicating a better fit, as they show how well the model explains the variance in the data. An R^2 value of 1 represents a perfect fit, while values closer to 0 indicate that the model does not explain much of the variance. On the other hand, $stderr$ measures the accuracy of predictions by indicating the discrepancy between observed and predicted values. A lower $stderr$ suggests that the data points are closer to the regression line, meaning the model's predictions are more accurate. Collectively, a higher R^2 and a lower $stderr$ together indicate a strong model fit. Our analysis of R^2 and $stderr$ revealed that the parabolic and hyperbolic models demonstrated best performance, especially for samples 3992 and 3993, successfully capturing the creep deformation behaviours of these samples.

It is important to acknowledge that these results are constrained by the limited number of samples tested, which may impact the generalisability of these findings. The limited sample set used in this study may not fully represent the behaviour of all shale reservoirs in the Beetaloo Sub-basin. To address this limitation, it is recommended that similar experiments be conducted on a greater number of core samples to thoroughly examine the variability in shale properties and their impact on creep behaviour across the extensive thicknesses of the Velkerri and Kyalla shales, which span several hundred metres.

It is also worth mentioning that, in the Northern Territory, incorporating natural shale barriers in decommissioned wells could serve as an extra measure for preventing fugitive emissions and enhancing overall well integrity, complementing existing regulations in the code of practice regarding cement plugging and decommissioning procedures.

Chapter 4

Developing a leakage simulator

Nomenclature

R_c	casing radius
h_c	casing thickness
k	cement permeability
R_{cem}	cement radius
A	cross-section of the cement plug or cemented annulus
k_1	Darcian (viscous) permeability
ρ_g	density of gas
ρ_l	density of pore liquid
ρ	density of reservoir fluid
Q	flow rate
h	fracture aperture
α	fracture orientation
W	fracture width
g	gravitational constant
L	length of the cement plug or annular cement
δR	micro-annuli gap
R	micro-annuli radius
k_2	non-Darcian (inertia) permeability
ΔP	pressure difference between the top and bottom of the cement
P_T	pressure inside the tubing
Re	Reynolds number
β	slope of the Forchheimer graph
TOC	top of cement
TVD	true vertical depth
R_T	tubing radius
μ_g	viscosity of gas
μ_l	viscosity of pore liquid
μ	viscosity of reservoir fluid
θ	well inclination at the depth of the plug or annular cement
E_{cem}	Young's modulus of cement
E_{st}	Young's modulus of steel

4.1 Introduction

Leaks from petroleum wells pose a significant environmental risk, potentially allowing the release of pore fluids, including gases, into various geological strata or even reaching the surface. Throughout the lifecycle of a well, several leakage pathways might be created, increasing the likelihood of such events.

This chapter presents the development of a leakage rate simulator aimed at assessing the risks associated with compromised wellbore integrity, including plugged and decommissioned wells. The simulator estimates the rate at which hydrocarbon fluids may migrate through potential leakage pathways, such as the micro-annulus between the cement and surrounding rock.

4.2 Developing a leakage rate simulator

The simulator offers valuable insights into the likelihood and magnitude of fluid migration, facilitating informed decision-making in well integrity management. The simulator enables users to estimate the flow rate (flux) of liquids or gases through these potential pathways, predicting their movement toward various formation layers or the surface.

4.2.1 Potential leakage pathways

Leakage incidents occur provided that three criteria are present simultaneously: a source of fluid, failure of one or two barriers with a wellbore, and driving forces for fluid movement, such as fluid

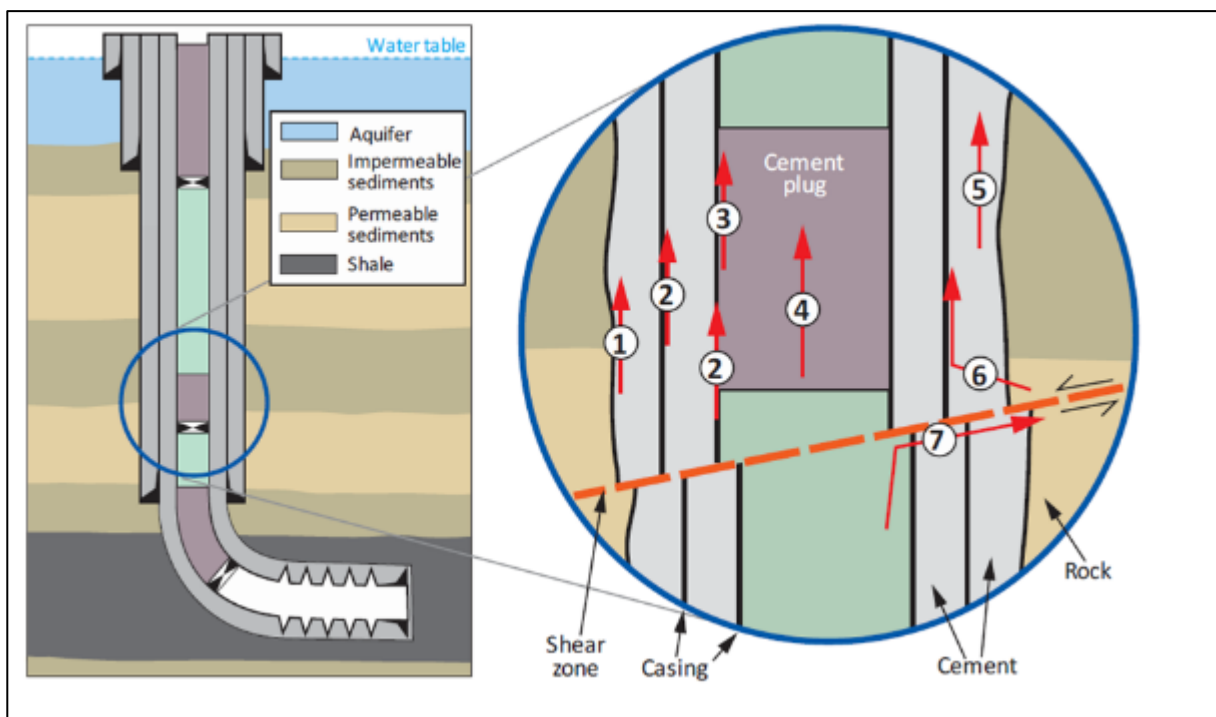


Figure 60: Conceptual leakage pathways (numbered 1–7) through degraded well barriers

buoyancy or excessive pore pressure (Davies et al., 2014). Figure 60 demonstrates the potential leakage pathways that may be created within a plugged and decommissioned well.

The leakage pathways can be categorised into two different groups: primary and secondary (Weideman & Nygaard, 2014).

The primary pathways are more related to the time of primary cementing, and the secondary pathways are associated with the events and conditions after cementing is complete (Weideman & Nygaard, 2014). The primary leakage pathways can be created due to mechanical failure of the casing (casing burst/collapse) or corrosion (Figure 60, pathways 6 and 7) (Crow et al., 2010; Weideman & Nygaard, 2014). For instance, casing strings undergo internal pressure increases and temperature decreases during wellbore operations. The driving forces may lead to piston force, buckling effect, ballooning effect and temperature effect (King et al., 2013).

The secondary pathways include the leakage pathways created along micro-annuli at the cement sheath interfaces with the casing and the formation (Figure 60, pathways 1, 2 and 3) (Crow et al., 2010; Weideman & Nygaard, 2014) and within the cement sheath due to cement degradation and cement mechanical failures (Figure 60, pathways 4 and 5). It is worth noting that pathways 1, 2 and 3 might be created for many reasons, including but not limited to deterioration of cement bond strength and cement shrinkage. It may also happen due to an unsatisfactory annular cementing job when the cement does not fill the annulus entirely, poor bonding due to the existence of mud cake and the development of channels (Figure 60, pathway 1) in the cement.

Shear failure mechanisms may happen in specific geological conditions due to reservoir compaction in the production period, which can lead to the creation of a shear failure zone in the formation and casing above the reservoir (Figure 60, pathway 7).

It is worth noting that the cement used in the oil and gas industry has very low permeability, usually less than 0.2 mD (Lecampion et al., 2011; Maharidge et al., 2016), which indicates that hydraulic isolation is accomplished straightforwardly, and any possible leakage can only occur through mechanical failures of the cement sheath (Lecampion et al., 2011). Therefore, the integrity of the cement sheath may be compromised mostly because of the creation of cracks and micro-annulus within the cement sheath (Saidin et al., 2008).

4.2.2 Methodology

The main emphasis is placed on the potential leakage pathways that might be created at the interface of the casing and the rock formation (micro-annulus). Certain characteristics of the well design, wellbore-formation system and underground formations must be known or estimated to calculate flow through the conceptual leakage pathways along a well. This includes the cement sheath outer diameter (where the micro-annuli occur), the well trajectory, the cement plug depth and length, the fracture aperture and orientation, cement permeability, the depth of the source formation, the temperature in the source formation, the pressure in the source formation, and reservoir fluid characterisation (Ford et al., 2017).

4.2.2.1 Methods to simulate fluid flow along leakage pathways

Ford et al. (2017) described the governing equations for calculating the fluid and gas flow in an arbitrary well as follows.

Leakage through the bulk of the cement

Leakage through the cement can be computed using equation (87):

$$Q = \left(\frac{kA}{\mu L} \right) (\Delta P - \rho g L \cos \theta) \quad (87)$$

In equation (88), based on Darcy's law, k represents cement permeability, an uncertain parameter, and g represents the acceleration due to gravity (9.81 m/s^2), The pressure difference (ΔP) at the bottom of the cement can be computed by reducing the hydrostatic pressure of the fluid column from the reservoir pressure. Q represents the volumetric flow rate of the fluid. A and L represent the cross-sectional area through which the fluid flows and the length of the flow path, respectively. μ and ρ correspond to the dynamic viscosity of the fluid and the density of the fluid, respectively. Pressure at the top of the cement is estimated by the hydrostatic pressure of the fluid (mud) column above the cement.

Darcy's law is valid to describe flow in porous media and fractures at low flow rates (Reynolds number <1), at which the flow rate and the pressure gradient have a linear relationship.

Leakage through cracks

The flow rate of fugitive gas leakage through fractures and cracks within the cement plug can be computed using equation (88):

$$Q = \left(\frac{h^3 \cos \alpha}{12\mu} \right) \left(\frac{\Delta P}{L} \right) W \quad (88)$$

where α and h represent fracture orientation and fracture aperture, respectively; and W corresponds to fracture width.

The fracture aperture, orientation and width are other sources of uncertainty. The fracture orientation is defined as the angle between the fracture and the axis of the pressure gradient.

Leakage through micro-annuli gaps

Leakage through micro-annuli is featured in the simulator using the model developed by Aas et al. (2017) as described in equations (82) to (85). For example, one scenario that leads to the creation of a micro-annulus is pressure testing operations. During pressure tests at high pressures, the casing expands while the cement contracts due to pressurisation. This results in the creation of an induced micro-annulus between the cement and the steel casing wall. These induced micro-annuli also affect the measured flow.

The casing expansion, while subjected to internal pressure, can be estimated via equation (89):

$$\delta R_c = \left(\frac{R_c^2 P_{internal}}{E_{st} h_c} \right) \quad (89)$$

where R_c and h_c correspond to the casing radius and casing wall thickness, respectively; and E_{st} is Yong's modulus of steel.

As a result, the cement sheath within the casing annulus will contract (equation (90)):

$$\delta R_{cem,A} = \left(\frac{\Delta R_{cem} P}{E_{cem}} \right) \quad (90)$$

The radius of a cement cylinder within the tubing of the radius R_T will shrink according to the subjected pressure, as equation (91) indicates.

$$\delta R_{cem,T} = \left(\frac{R_T P_T}{E_{cem}} \right) \quad (91)$$

which yields the fluid flow rate as explained via equation (92):

$$Q = \left(\frac{\pi R_c \Delta P}{6 \mu L} \right) \delta R^3 \quad (92)$$

where Q represents fluid flow rate, μ is the fluid viscosity and ΔP is the pressure drop along the assembly length L .

However, the influence of inertial effects on the flow of fluids through fractured media has not been considered. The 'cubic law' estimates a straightforward correlation between the hydraulic aperture of a fracture and its permeability for the Darcian flow of a given fluid. While at higher flow velocities, fracture flow becomes non-Darcian, the velocity–permeability relationship converts to a nonlinear relationship and the cubic law becomes inapplicable (Ranjith & Viète, 2011).

Darcian flow

Fracture flow is usually considered as flow through a volume bounded by two parallel plates. Therefore, the total free-flow area is calculated by $A = hW$, where h is hydraulic aperture and W is the width of the fracture joint. For Darcian flow of a compressible fluid within a fracture, equation (93) is valid:

$$\frac{P_i^2 - P_0^2}{2PL} = Q \frac{12\mu}{h^3 W \rho g} \quad (93)$$

In isothermal flow of an ideal gas, gas density is directly proportional to gas pressure and volumetric gas flow is inversely proportional to gas pressure. Consequently, ρ and Q for a gas at pressure P can be estimated from the known density (ρ_0) and measured flow rate (Q_0) at (P_0), by $\rho = \frac{\rho_0 P}{P_0}$ and $Q = \frac{Q_0 P_0}{P}$, respectively.

Non-Darcian flow

As fluid velocity increases, flow within the porous media or fracture media becomes non-Darcian and the correlation between the pressure gradient and the velocity becomes nonlinear. As the flow rate (Reynolds number) increases further, the pressure loss transforms from a weak inertia regime to a Forchheimer (strong inertia) regime (Takhanov, 2011). In other words, permeability varies based on the variations of flow velocity. This relationship is attributed to the impact of inertial effects. The

Reynolds number (Re) provides insights into the flow regime type; that is, laminar or non-laminar (Ranjith & Viète, 2011). According to the Forchheimer equation (equation (94)):

$$-\Delta p = \frac{\mu}{k} V + \beta \rho V^2 \quad (94)$$

where β is an empirical constant that accounts for the dependency of k on V .

For a compressible fluid (assumed an ideal gas) in isothermal condition, equation (95) is valid:

$$\frac{P_i^2 - P_0^2}{2PL} = \frac{\mu}{k_1} V + \frac{\rho}{k_2} V^2 \quad (95)$$

Both k_1 and k_2 can be considered as properties only of the porous medium.

Java script documentation

The leakage simulator presumes that users are aware of the range within which uncertain input parameters should fall, which can be defined in terms of a mean and variance. The following derives the leakage mean and variance due uncertain input parameters. The Taylor series expansion is used due to convenience, as it results in a polynomial of central moments.

In the following, μ with a subscript refers to the mean of the subscript, and σ^2 with a subscript refers to the subscript's variance (second central moment).

Leakage through bulk cement

The equation for the leakage through the bulk of the cement (equation (96)) with uncertain input parameter k , can be expressed using a Taylor series expansion as follows:

$$Q = \left(\frac{(\Delta P - \rho g L \cos[\theta]) A}{\mu L} \right) k \quad (96)$$

$$\begin{aligned} \mu_Q &= E[Q] \\ &= \left(\frac{(\Delta P - \rho g L \cos[\theta]) A}{\mu L} \right) E[k] \end{aligned} \quad (97)$$

$$\sigma_Q^2 = Var[Q] = \left(\frac{(\Delta P - \rho g L \cos[\theta]) A}{\mu L} \right)^2 Var[k] \quad (98)$$

As a Taylor series expansion, k is:

$$k = \mu_k + (k - \mu_k) \quad (99)$$

$$E[k] = \mu_k \quad (100)$$

$$Var[k] = E[(k - \mu_k)^2] = \sigma_k^2 \quad (101)$$

Note that it might be more convenient to express the leakage in terms of well vertical depth h , to make the expression more general, thereby allowing for wells that do not follow a linear path:

$$L \cos[\theta] = h \quad (102)$$

Leakage through micro-annuli

The leakage through micro-annuli gap equation (equation (89)) with an uncertain input parameter of δR can be expressed as:

$$Q = \left(\frac{\pi R_c \Delta P}{6\mu L} \right) \delta R^3 \quad (103)$$

$$\mu_Q = E[Q] = \left(\frac{\pi R_c \Delta P}{6\mu L} \right) E[\delta R^3] \quad (104)$$

$$\sigma_Q^2 = Var[Q] = \left(\frac{\pi R_c \Delta P}{6\mu L} \right)^2 Var[\delta R^3] \quad (105)$$

As a Taylor series expansion, δR^3 is:

$$\delta R^3 = \mu_{\delta R}^3 + 3\mu_{\delta R}^2(\delta R - \mu_{\delta R}) + 3\mu_{\delta R}(\delta R - \mu_{\delta R})^2 + (\delta R - \mu_{\delta R})^3 \quad (106)$$

Assuming a symmetrical distribution so that all odd central moments are zero:

$$E[\delta R^3] = \mu_{\delta R}^3 + 3\mu_{\delta R}\sigma_{\delta R}^2 \quad (107)$$

Further assuming that the symmetrical distribution is a normal distribution:

$$Var[\delta R^3] = 9\mu_{\delta R}^4\sigma_{\delta R}^2 + 36\mu_{\delta R}^2\sigma_{\delta R}^4 + 15\sigma_{\delta R}^6 \quad (108)$$

where it has been used that for a normal distribution the n th central moment is:

$$E[(X - E[X])^n] = \begin{cases} 0, & n \text{ is odd} \\ \sigma_X^n \prod_{k=1}^{n/2} (2k-1), & n \text{ is even} \end{cases} \quad (109)$$

Leakage through cracks

The equation pertaining to leakage through cracks (equation (88)) with uncertain fracture input parameters h , α and W can be expressed as:

$$Q = \left(\frac{\Delta P}{12\mu L} \right) h^3 W \cos(\alpha) \quad (110)$$

$$\mu_Q = E[Q] = \left(\frac{\Delta P}{12\mu L} \right) E[h^3 W \cos(\alpha)] \quad (111)$$

$$\sigma_Q^2 = Var[Q] = \left(\frac{\Delta P}{12\mu L} \right)^2 Var[h^3 W \cos(\alpha)] \quad (112)$$

Assuming that the uncertain input parameters are random independent variables, the following may be used:

$$E[AB] = E[A]E[B] \quad (113)$$

From which it follows that:

$$\begin{aligned} Var[AB] &= E[(AB - E[AB])^2] = E[(AB)^2] - (E[AB])^2 = E[A^2]E[B^2] - (E[A]E[B])^2 \\ &= (E[A]^2 + Var[A])(E[B]^2 + Var[B]) \\ &\quad - E[A]^2 E[B]^2 \end{aligned} \quad (114)$$

Therefore:

$$E[h^3 W \cos(\alpha)] = E[h^3]E[W]E[\cos(\alpha)] \quad (115)$$

$$\begin{aligned} & Var[h^3 W \cos(\alpha)] \\ &= (E[h^3]^2 + Var[h^3])(E[W]^2 + Var[W])(E[\cos(\alpha)]^2 + Var[\cos(\alpha)]) \\ &- E[h^3]^2 E[W]^2 E[\cos(\alpha)]^2 \end{aligned} \quad (116)$$

The form of the expectation values and variances for h^3 and W have already been derived in previous sections, whereas that of a cosine function has not. The Taylor series of a cosine is an infinite series, thus in practice only the first n terms necessary to achieve convergence to within the desired non-zero tolerance are included (the first bracketed term contains the even powers of the central moment, while the second contains the odd powers):

$$\begin{aligned} \cos(\alpha) = & \left(\sum_{k=0}^{\lfloor (n+1)/2 \rfloor} \frac{(-1)^{2k} \cos(\mu_\alpha)}{(2k)!} (\alpha - \mu_\alpha)^{2k} \right) \\ & + \left(\sum_{k=0}^{\lfloor n/2 \rfloor} \frac{(-1)^{2k+1} \sin(\mu_\alpha)}{(2k+1)!} (\alpha - \mu_\alpha)^{2k+1} \right) \end{aligned} \quad (117)$$

Assuming a symmetrical distribution so that all odd central moments are zero:

$$E[\cos(\alpha)] = \sum_{k=0}^{\lfloor (n+1)/2 \rfloor} \frac{(-1)^{2k} \cos(\mu_\alpha)}{(2k)!} E[(\alpha - \mu_\alpha)^{2k}] \quad (118)$$

$$Var[\cos(\alpha)] = E[\cos^2(\alpha)] - E[\cos(\alpha)]^2 \quad (119)$$

$$\begin{aligned} E[\cos^2(\alpha)] = & E \left[\left(\sum_{k=0}^{\lfloor (n+1)/2 \rfloor} \frac{(-1)^{2k} \cos(\mu_\alpha)}{(2k)!} (\alpha - \mu_\alpha)^{2k} \right)^2 \right] \\ & + E \left[\left(\sum_{k=0}^{\lfloor n/2 \rfloor} \frac{(-1)^{2k+1} \sin(\mu_\alpha)}{(2k+1)!} (\alpha - \mu_\alpha)^{2k+1} \right)^2 \right] \end{aligned} \quad (120)$$

4.2.2.2 Case study of the estimated flow rate in the Beetaloo Sub-basin

Figure 61 depicts the schematic of an arbitrarily plugged and decommissioned well. The area in the vicinity of the intermediate casing shoe is marked, and a hypothetical scenario is defined for further analyses in the following section.

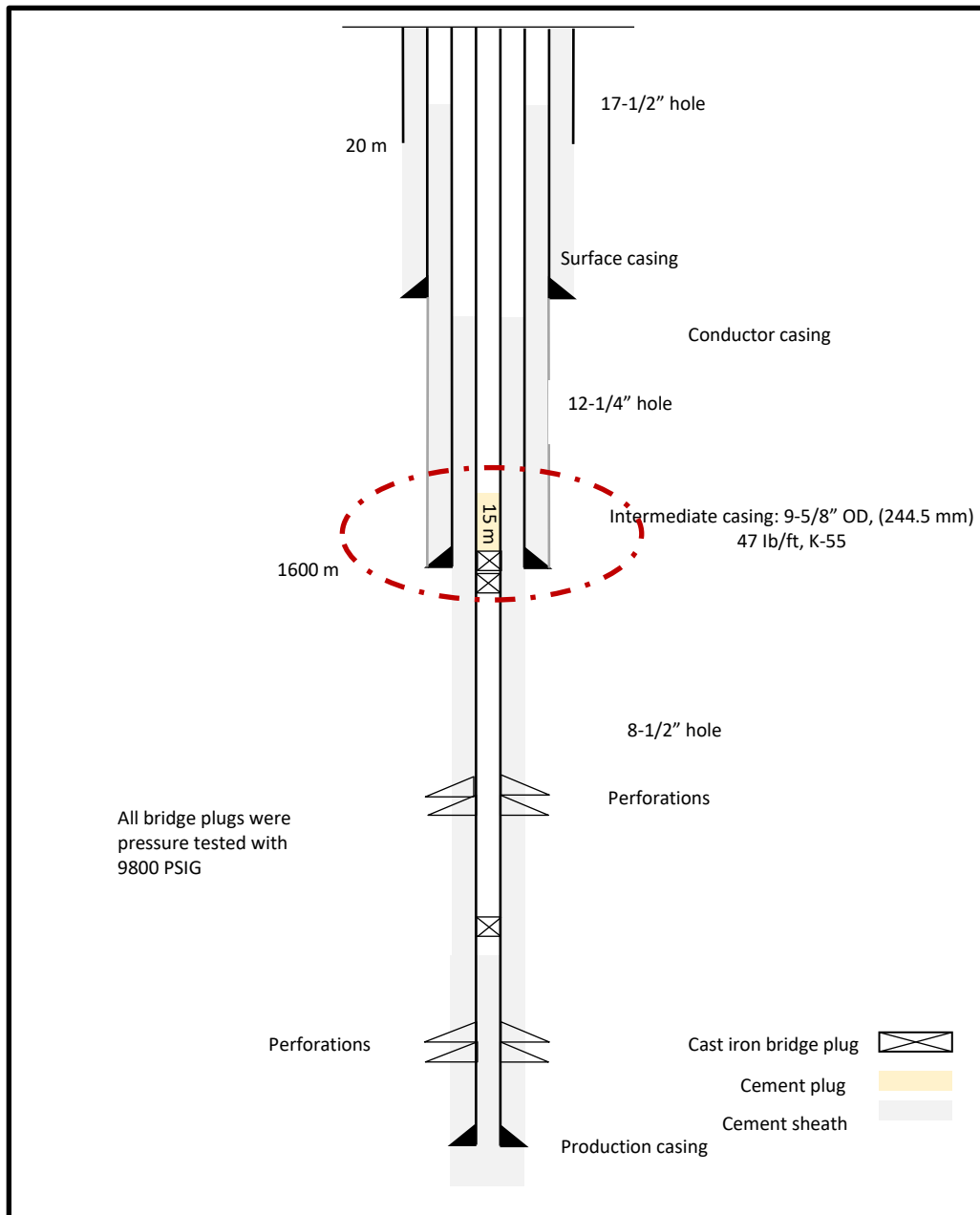


Figure 61: An arbitrary well schematics used in the case study

Input parameters for leakage calculator

Figure 62 demonstrates the potential leakage pathways in the marked portion of Figure 61 for formation fluids that might be created after installing the cement plug. The red pathway in Figure 62 shows the potential leakage pathway through the cement bulk.

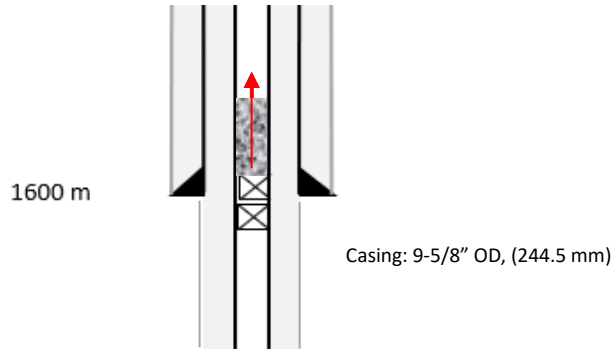


Figure 62: Potential leakage pathways at the marked portion of a plugged and decommissioned well

To compute the potential leakage rate within the cement plug, users must input the pressure difference between the top and the bottom of the cement, the cement length, the viscosity and density of the reservoir fluid, the cross-sectional area of the cement, the well inclination, and the average and standard deviation of cement permeability (Figure 63).

Please select leakage pathways

Permeating through cement
 Micro-annuli
 Fractures

General parameters

Pressure difference between top and bottom of cement [MPa]

Cement length [m]

Reservoir fluid viscosity [$\mu\text{Pa}\cdot\text{s}$]

Cement permeation parameters

Reservoir fluid density [kg/m^3]

Cement cross-sectional area [m^2]

Cement inclination [degrees]

Cement permeability average [nm^2]

Cement permeability standard deviation [nm^2]

Calculate

Calculator results

Leakage pathway	Leakage average [m^3/s]	Leakage uncertainty (standard deviation) [m^3/s]
Cement	2.51e-10	2.79e-9
Combined	2.51e-10	2.79e-9

Figure 63: The input parameters required for calculating leakage rate through the cement bulk, and the associated results 40

By factoring in both the average permeability and its standard deviation, the calculator accounts for the inherent uncertainty in permeability values, ensuring a comprehensive assessment of potential leakage rates. This approach acknowledges the range of possible permeability values rather than relying solely on a single average value, thereby providing a more realistic estimation of leakage behaviour. Consequently, the results obtained from the calculator provide a clearer understanding of the potential leakage rates and associated uncertainty in the system.

4.3 Incorporating the creep behaviour of Beetaloo Sub-basin shale properties into the leakage simulator

In sections 3.4.2-3.4.4, the empirical and rheological models were fitted to the experimental outcomes to predict the shale’s long-term creep strain behaviour. By applying these empirical models (equations (65)–(70)) – parabolic, logarithmic, hyperbolic and crack-damage – and analytical models ((equations (72), (81) and (85)) – Kelvin-Voigt, standard linear and Burgers models – the study aimed to derive constitutive parameters from STXL and MSTXL creep experiments. These parameters, obtained from short-term creep tests, help predict long-term shale deformations under specific tested conditions. It is crucial to identify models and their respective constitutive parameters that offer superior predictive abilities adapted to the tested specimens’ characteristics and consider the in-situ conditions. The goodness of fit was assessed using R^2 and the stderr , which indicated that the parabolic and hyperbolic models performed best, particularly for samples 3992 and 3993.

Therefore, in this part, the parabolic model (equation (65); $\varepsilon = At^m$) was integrated into the leakage simulator to assess the state of the annulus gap between the casing and the shale formation. This incorporation aimed to provide insights into whether the annulus would gradually fill and close over time due to shale creep or remain open. By using the predictive capabilities of the parabolic model, the simulator could simulate the long-term behaviour of the shale and its interaction with the casing, offering valuable information for decision-making in well integrity studies. The integration of the parabolic creep model can be found under the micro-annulus section within the simulator.



Figure 64: Potential leakage pathways at the interface of the casing and the rock formation (annulus)

Figure 64 demonstrates a schematic of a micro-annular gap between the casing and the rock formation. Users are required to input parameters including the casing diameter, mean and standard deviation of the micro-annulus gap, the parabolic constitutive parameters represented by A and m , the time duration and the formation width (outer radius minus inner radius). The simulator will produce graphs showing the evolution of formation strain caused by creep (based on the parabolic model) and the corresponding leakage rate from the micro-annulus (m^3/s) versus time (Figure 65b).

(a)

Please select leakage pathways

Permeating through cement

Micro-annuli

Fractures

General parameters

Pressure difference between top and bottom of cement [MPa]

Cement length [m]

Reservoir fluid viscosity [$\mu Pa \cdot s$]

Micro-annuli leakage parameters

Casing diameter [cm]

Micro-annuli gap average [μm]

Micro-annuli gap standard deviation [μm]

Creep modelling

$\epsilon[\dot{\epsilon}] = At^m$ (Power Law) Use the append thingy

A [micro-strain/year^m]

m

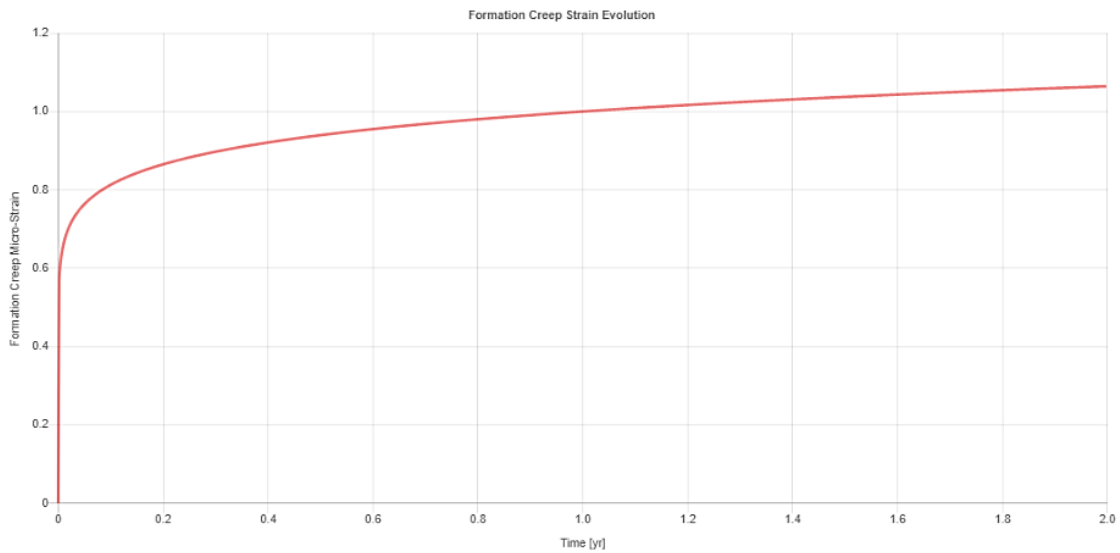
Time [years]

Formation width [m]

Calculate

Calculator results

Leakage pathway	Leakage average [m ³ /s]	Leakage uncertainty (standard deviation) [m ³ /s]
Micro-annuli	1.33e-7	3.15e-7
Combined	1.33e-7	3.15e-7



(b)

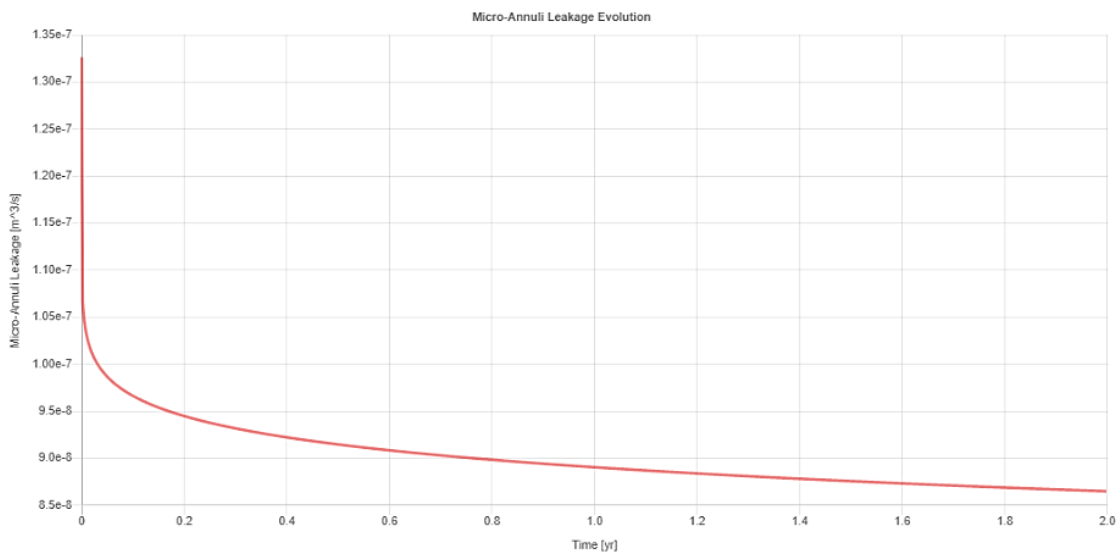


Figure 65: (a) The input parameters and (b) the associated results to calculate the formation creep strain and the corresponding leakage rate evolution

The integration of the parabolic creep model is placed under the micro-annulus section within the simulator.

By considering both the average micro-annulus gap and its standard deviation, users gain valuable insights into variability and uncertainty when it comes to calculating the leakage rate and gap closure. Additionally, users can better account for the range of potential scenarios and outcomes.

4.4 Summary and conclusion

This chapter presents the development of a leakage rate simulator aimed at assessing potential risks associated with the integrity of plugged and decommissioned wells. The simulator enables users to estimate the rate at which hydrocarbon fluids, including gases and liquids, may escape through potential leakage pathways. By integrating critical parameters such as well design features, formation properties, cement sheath dimensions, fracture characteristics, and reservoir conditions, and other relevant factors. The simulator provides a means to predict fluid migration into different geological strata or to the surface.

The chapter also incorporates the parabolic model into the leakage rate simulator to assess the evolution of the annulus gap between the casing and the shale formation. This integration helps predict whether the gap will close over time as a result of shale creep or remain open, which is vital for evaluating well integrity. By utilizing the model's predictive strengths, the simulator provides a long-term forecast of how the shale interacts with the casing, offering important data to guide decisions in well integrity evaluations.

In conclusion, the leakage rate simulator and the use of predictive models for shale behavior enhance the ability of decision makers to assess wellbore integrity and environmental risks. These tools offer valuable insights into the conditions that may lead to fluid migration and provide more accurate predictions of long-term deformation in wellbore systems, contributing to improved well management and mitigation strategies.

Chapter 5

Defining the key concepts in the long-term integrity of decommissioned wells

5.1 Introduction

Surface and groundwater assets can be contaminated due to operational procedures in a decommissioned well where fluids or chemicals injected deep into a geological formation subsequently escape to water-bearing layers, overlying aquifers or nearby water bores.

Huddlestone-Holmes et al.(2017) provides an overview of the well lifecycle and well integrity, including decommissioning. Huddlestone-Holmes et al.(2022) looked at monitoring of decommissioned wells and included an assessment of failure mechanisms. This section summarises and extends on that work.

Figure 66 shows the potential leakage pathways from a decommissioned well (Nichol & Kariyawasam, 2000). The leakage path through the reservoir zone isolation plug (P1) can be created if there is a build-up of fluid pressure or injection from a nearby production well. The performance of the surface casing and the creation of a leakage path through the surface casing shoe (P4) relies on the proper operation of the reservoir zone isolation plug and the production casing plug. If the surface casing shoe fails, gas migration occurs through pathway leakage P5 and P6, unrestrained by the hanger, seal or conductor casing. Another potential leakage pathway is P7 within the annulus of the conductor and surface casing. The creation of P4 might also compromise the integrity of the surface plug P3 (Babaleye et al., 2019).

5.2 Integrity failures of plugged and decommissioned wells

A study conducted by the Energy Resource Conservation Board (ERCB) in Alberta, Canada, gathered industry information in relation to well size, production method, abandonment method, stimulation, geological formations and geographic relationship and compared this data with outcomes of surface casing vent flow and gas migration tests. It also looked at casing failure to determine those factors leading to no evident impact, minor impacts or major impacts after leakage from wells (Watson & Bachu, 2009).

The factors with major impacts are as follows (Watson & Bachu, 2009):

- *Wellbore deviation*: gas migration and surface casing vent flow occurred more often in deviated wells, wells with different degrees of eccentricity and those with cement slumping issues compared with wells that are vertical.
- *Abandonment method*: the data showed that in abandoned wells with bridge plugs, leakage

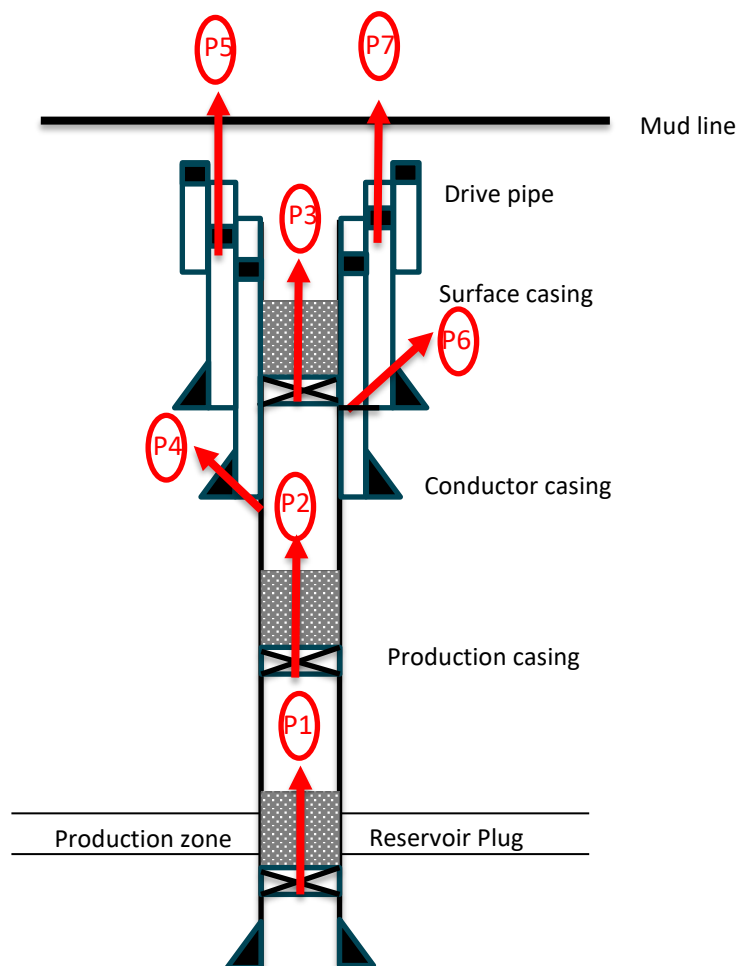


Figure 66: Schematic of a plugged well and its leakage pathways (P1–P7) (Nichol & Kariyawasam, 2000)

rates were higher than in decommissioned wells that relied on other methods (e.g. using a balanced plug, setting cement with a retainer and squeezing cement through perforated

intervals). The data showed that approximately 10% of bridge plugs tend to fail after a number of years (the service life of a bridge plug is about 5–30 years).

- *Welded cap failure*: the failure of the welded cap, which is the final barrier to the escape of gas from the reservoir, needs to be considered. The data showed that such caps can be very unreliable. However, cap failure can reduce the risk of over-pressurising the casing shoe in the event of a gas leakage.
- *Uncemented casing*: the majority of casing failures are related to cases with poor or no cement in the annulus. Therefore, the location of the cement top for each well should be considered regarding the hydrocarbon-bearing formation and casing depths.

5.2.1 Methane emission measurements

Leakage of fluids from a geological formation into the surrounding environment can appear in the form of saline water; hydrocarbons such as methane (CH₄), ethane (C₂H₆), and propane (C₃H₈) (in liquid or gas form); radionuclides; and other anthropogenic and naturally occurring contaminants (Kang et al., 2021; Huddleston-Holmes et al., 2022).

According to an Intergovernmental Panel on Climate Change (IPCC) report, methane is significantly more powerful than CO₂ in retaining heat in the atmosphere (86 times more effective over 20 years and 34 times more over 100 years) (Alboiu & Walker, 2019).

According to the American Petroleum Institute (API)-RP14B, the maximum allowable annulus leak is as follows (Calosa et al., 2018):

- *liquid hydrocarbon*: 6.3 gallons/hour, equivalent to 3.6 barrels per day (BPD) or 7 cubic centimetres per second (cc/sec)
- *gas*: 15 standard cubic feet per minute (SCF/min), equivalent to 21,600 standard cubic feet per day (mscf/d) or 0.25 standard cubic feet per second (SCF/sec)
- *water*: 400 gallons per hour, equivalent to 229 barrels per day (BPD) or 416 cubic centimetres per second (cc/sec).

Riddick et al. (2020) measured CH₄ emissions from 18 decommissioned oil and gas wells in the USA and the UK continuously for 24 hours (hr) using a dynamic flux chamber. Subsequently, they repeated their 24-hr measurements at one specific site for 12 months. The chamber was comprised of a semiconductor gas sensor to monitor CH₄ concentrations continuously. They observed that CH₄ emissions at all wells fluctuated over 24 hours (range 0.2–81,000 mg CH₄ hr⁻¹), with average emissions fluctuating by a factor of 18 and varying from factors of 1.1 to 142. The alkane ratios for 17 out of 18 wells showed that the CH₄ emitted was from a thermogenic source. Due to the lack of available historical documentation for these wells, they couldn't identify the primary leakage pathways. Note that these wells were very old, and there were no regulatory statutes at the time of their abandonment, so it is possible that the wells were never sealed at the end of their life cycle. One of their key observations is that CH₄ emissions obtained by computing the short-term CH₄ concentration measurements (~1 hr) can be considerably different from the daily average CH₄ emissions, since large fluctuations in emissions can occur over minutes to hours.

Kang et al. (2014) also directly measured CH₄ emissions from 19 of Pennsylvania’s decommissioned oil and gas wells. The mean methane flow rates of the 19 wells were estimated at 11,000 mg/hr/well (0.27 kg/d/well), and the mean methane flow rate at the control locations was 4.5×10^{-6} kg/d/location. Three of the 19 wells were high emitters, with methane flow rates three orders of magnitude larger than the median flow rate of 1.3×10^{-3} kg/d/well. Table 26 lists the average published methane emission rates released from unplugged and plugged wells in the USA.

Table 26: Summary of average published methane emission rates released from unplugged and plugged wells in the USA (Kang et al., 2014)

Average CH ₄ emissions (tonne/year/well)		Number of measurements		Study region	Reference
Unplugged	Plugged	Unplugged	Plugged		
0.19	0.13	53	35	Pennsylvania, USA	Kang et al. (2016)
0.03	8.8×10^{-4}	147	112	West Virginia, USA	Riddick et al. (2019)
0.36	0.015	1	102	UK	Boothroyd et al. (2016)
0.09	1.8×10^{-5}	19	119	Colorado, Wyoming, Utah, Ohio, USA	Townsend-Small et al. (2016)
15	NA	1	0	Pennsylvania, USA	Etiopie et al. (2913)

Saint-Vincent et al. (2020) analysed 179 wells in Oklahoma, of which 89% were unplugged and 11% were plugged, to look for a link between a well’s characteristics and the release of CH₄. The emission rates were examined in terms of well characteristics, including plugging status, location, depth, age and duration of inactivity. The wells were inspected for leaks by using a handheld laser detector at a distance of roughly 1 meter from the wellhead. All fittings, openings and connections, as well as the external casing connection to the ground, were checked.

To make the results comparable with published data, the measurements were converted from litres per minute (L/min) to grams per day (g/day) using the density of CH₄ (0.683 g/L) under conditions of 99.97 kPa and 10°C, the average conditions recorded during the field studies. The emission factor was determined by taking the average of individual emission factors for a specific subset of wells, and the standard deviation of this mean was calculated for the entire group.

The study showed that shallower wells tend to emit CH₄ more frequently than deeper ones. It is plausible that the integrity of deeper wells might have been compromised just as frequently, but perhaps their leaks occurred at a shallower depth or in a way that caused gas to migrate away from the wellhead. It is important to note that the monitoring focused solely on the wellhead and did not

cover a wider surface area because some research indicates that liquid and gas tends to migrate away from the wellhead. While ground disturbances could potentially challenge well integrity, leading to higher CH₄ emissions, the findings did not reveal a significant correlation between observed CH₄ emissions and the proximity to earthquake epicentres or active unconventional wells.

A study by McMahan et al. (2018) revealed contamination of shallow groundwater with thermogenic methane in the vicinity of a decommissioned gas well in Colorado, USA. Examination of drilling and decommissioned records for Sulphur Creek #1, located 27 m away from the contaminated shallow monitoring well, revealed the presence of approximately 1000 meters of uncemented annular space behind the production casing, connecting to gas-bearing formations. This uncemented annular space extended through the confining layer and was the probable pathway through which deep-seated gas migrated into the shallow aquifer. Alongside the geochemical data, these records implicated the gas well as the source of thermogenic methane contamination in the shallow aquifer.

5.3 Environmental contamination and adverse impacts

The release of greenhouse gases such as CO₂, CH₄, nitrous oxide (N₂O), hydrofluorocarbons, perfluorocarbons and sulfur hexafluoride (SF₆) has an impact on the atmosphere's radiative balance, commonly referred to as radiative forcing. Due to the effect of radiative forcing, the Earth's atmospheric temperature is rising, leading to alterations in climate (Oves et al., 2017).

5.3.1 Air contamination

CO₂ is an effective heat-trapping gas. When comparing CH₄, also known as natural gas, with CO₂ in the atmosphere, the abundance of CO₂ exceeds that of CH₄ by a significant margin. Nevertheless, the issue with CH₄ lies in its prolonged atmospheric lifespan. Due to its enhanced heat-trapping efficiency, CH₄ is more effective at elevating atmospheric temperatures than CO₂. One CH₄ molecule is nearly 30 times more efficient at capturing infrared radiation emitted from the Earth's surface than one CO₂ molecule (Oves et al., 2017). Rising levels of harmful substances in the atmosphere, together known as air pollution, have detrimental impacts on human health, the environment and overall quality of life. In particular, air contaminants significantly affect human health, leading to major issues such as cancer and respiratory problems.

Moreover, all living organisms, and the ecosystem more generally, bear the brunt of these harmful pollutants. Certain air pollutants, such as oxides, combine with water vapour and fall to the Earth as acid rain or snow, corroding statues and buildings, harming crops and forests, and rendering lakes and streams inhospitable for fish and other plant and animal life (Oves et al., 2017).

5.3.2 Soil contamination

Soil contamination can arise from the accidental release of fluids during a well's operational life, and even from decommissioning activities. It can also occur during transportation via trucks or wastewater pipelines. Additionally, the failure of well casings, equipment malfunctions and the corrosion of pipes and tanks can contribute to soil contamination (Pichtel, 2016). The leakage of

stored CO₂ or associated compounds can impact plant and animal life. Effects may also be observed on microorganisms in the deep subsurface, as well as on plants and animals in shallow surface soils (Pichtel, 2016).

5.3.3 Water contamination

Leakage of CO₂ can potentially impair groundwater quality, harm certain hydrocarbon or mineral reserves, and cause harmful effects on plants and subsoil fauna. Elevations in the concentration of dissolved CO₂ have the potential to alter the chemistry of groundwater. This alteration may impact the quality of shallow groundwater used for drinking water, industrial purposes or agriculture. Dissolved CO₂ forms carbonic acid, lowering the pH and potentially resulting in secondary effects such as the release of (harmful) metals, sulfates or chlorides. It may also cause the water to exhibit unusual odours, colour or taste. In the most severe cases, contamination levels can become hazardous, rendering the groundwater unsuitable for drinking or irrigation (Solomon, 2007).

Leakage of CH₄ can also be a hazard to shallow groundwater (Steelman et al., 2017). Interaction of CH₄ with near-surface groundwater may result in the following chemical changes, as predicted by both thermodynamics and equilibrium simulations:

- compromise the quality of the groundwater if natural gas is dissolved in drinkable groundwater under specific conditions (e.g. microbial communities)
- pose explosion risks due to the combustibility of natural gas, which might reach surface infrastructure like homes and water wells (Cahill et al., 2020)
- cause an increase in pH
- cause a decrease in eH (the electrochemical potential relative to the standard H electrode, which characterises the oxidation-reduction (redox) chemistry of natural waters (Auqué et al., 2008))
- generate alkalinity through CH₄ oxidation
- almost completely reduce SO₄²⁻ (sulfate) to HS⁻ (hydrogen sulfide)
- completely to almost completely reduce NO₃⁻ to NH₄⁺
- reduce Fe and Mn oxides, leading to increased aqueous concentrations and the precipitation of Fe and Mn carbonates and/or sulfides (Kelly et al., 1985).

5.4 Time-dependent barrier material retrogression and deterioration

In the context of oil and gas wells, the progressive ageing and degradation of critical components – including casings, cementitious materials and cement bonding(s)– are fundamental issues when considering wellbore management. The extended exposure of these materials to harsh downhole conditions speeds up ageing and deterioration involving complicated physicochemical reactions. The decline in structural integrity over time poses a challenge to the overall wellbore integrity. A good understanding of how wellbore elements deteriorate provides an important basis for developing

strategic approaches to mitigate risks and preserve the long-term integrity of the wellbore (OEUK, 2022).

5.4.1 Cement deterioration

Portland cement has a long history with the oil and gas industry as a material of choice for ensuring well integrity and zonal isolation. It stands out as the most widely employed material for permanently plugging abandoned oil and gas wells. The primary constituents of Portland cement are CaO, SiO₂, Al₂O₃ and Fe₂O₃. Clinker, comprising over 90% of the cement, is formed through the high-temperature processing (exceeding 1300°C) of hydrated lime. This results in the combination of Ca₂SiO₄, belite and calcium oxide (CaO) to produce Ca₃SiO₅. The clinker consists of four major mineral phases: 50–70% tricalcium silicate (3CaO·SiO₂ or 'C₃S'), 15–30% dicalcium silicate (2CaO·SiO₂ or 'C₂S'), 5–15% tricalcium aluminate (3CaO·Al₂O₃ or 'C₃A') and 5–10% tetracalcium aluminoferrite (4CaO·Al₂O₃Fe₂O₃ or 'C₄AF') (Chukwuemeka et al., 2023a).

Cement undergoes chemical degradation on exposure to aggressive fluids such as carbonic acid, sulfuric acid, hydrochloric acid and hydrogen sulfide. When subjected to these acidic substances, chemical reactions such as carbonation, leaching and sulfidation occur, contributing to the deterioration of the cement structure (Noik et al., 1999). The cement sheath is in contact with fluid-bearing layers containing aqueous species (ions such as calcium (Ca²⁺), magnesium (Mg²⁺), sulfates (SO₄²⁻), and chlorides (Cl⁻), etc.). These species can transfer from the porous rock into the pore space of the cement via advection–diffusion and dissolution, which cause chemical degradation of the cement. Calcium dissolution mostly affects the calcium silicate hydrate (C-S-H) phases (C-S-H is a gel-like substance that forms during the hydration of cement), and this material is responsible for the macroscopic cohesion and strength of cement (S. Y. Xie et al., 2008; Zuo & Bennett, 2019).

The chemical reactions between the cement and the rock formation fluid are generally acid–base reactions, mineral dissolution and precipitation, surface complexation, and ion exchange. These chemical reactions increase the cement's porosity and permeability, which facilitates the penetration of harmful species and adversely affects the elastic–plastic behaviour of the cement (S. Y. Xie et al., 2008; Zuo & Bennett, 2019).

In general, cement degradation is speeded up by exposure to sour gases, including hydrogen sulfide (H₂S) and CO₂. The alteration mechanisms are different, however: exposure to CO₂ dissolves calcium-bearing minerals and precipitates carbonates within the cement pores, and this gradually reduces permeability and increases porosity. Exposure to H₂S, on the other hand, leads to a sharp increase in cement porosity and mechanically weakens the underlying matrix (Lécolier et al., 2008).

Vrålstad et al. (2016) investigated the integrity of cement following exposure to different fluids by exposing Portland cement samples, with and without silica flour as an additive, to crude oil, brine and H₂S (in brine) at a temperature of 100°C and a pressure of 50 MPa (500 bar) for 1, 3, 6 and 12 months. The long-term integrity of the samples was assessed by measuring alterations in weight, volume, mechanical strength, permeability and physical appearance.

The results showed that cement is mostly nonreactive to crude oil, moderately affected by brine and significantly degraded by H₂S in brine. Krilov et al. (2000) studied cement carbonation and leaching under downhole conditions and found that there was an irreversible decline in compressive strength. In high-pressure, high-temperature wells, the elevated temperature would result in debonding of the cement from the casing and the surrounding rock and the creation of cracks due to thermally induced stresses (Chukwuemeka et al., 2023b).

Micro-annuli tend to form in wells because of debonding at the inner side (between the cement and the casing) or at the outer side of the cement sheath (between the cement and the rock formation). These interfaces are the weakest link in ensuring zonal isolation (Lecampion et al., 2013). Micro-annuli form for many reasons, including deterioration of cement bond strength, poor removal of the mud cake created during drilling, wellbore de-pressurisation, injection of cold water (to lower the temperature of a well), mechanical failure of the casing, perforations, cement shrinkage and mechanical failure of the cement itself (Yan et al., 2014; Chen et al., 2003). The strength of a bond also depends on the surface properties of the surrounding rock formation (Van Der Tuuk Opedal et al., 2013).

5.4.2 Casing deterioration

Corrosion inevitably occurs because metals tend to return to their original form (which is more stable), the form in which they exist in nature (e.g. oxides, sulfates or carbonates). Corrosion is defined as the slow loss of electrons from the surface of a metal, activating that metal and changing it to its ionic form. The rate of corrosion can be quantified in terms of weight loss and penetration rate (Al-Shehri, 2019). Casing corrosion and wear can both lead to loss of strength and deformation of the casing. The rate of casing wear depends on the grade of the casing steel, rotary speed, and the contact force and friction between drill rods and the casing, all of which result in thinning and pitting of the casing (Guen et al., 2011; Q. Zhang et al., 2016).

Corrosion of a casing leads to pits at both its inner and outer walls, which in turn lead to a localised concentration of stresses around cavities within the casing. Loads applied to the casing can then result in loss of strength and eventually its mechanical failure (T. Lin et al., 2016).

5.5 Formation as barrier deterioration

The effectiveness of shale as a barrier has been observed over a long period of time by Fjær et al. (2023) under constant boundary conditions. They found that the ultimate sealing efficiency hinges mostly on the effective stress (defined as the in-situ stress minus the in-situ pore pressure). The contact pressure, the rock–casing gap and rock properties also affect the ultimate sealing efficiency. Hence, changes in sealing effectiveness over time depend on variations in the effective in-situ stress (Fjær et al., 2023). Theoretical analyses indicate that seal enhancement can be markedly accelerated at moderately higher temperatures, pointing to a strong effect of formation temperature on the overall outcome (Fjær et al., 2023).

5.6 Defining ‘long-term’

The integrity requirements for decommissioned wells are generally stated qualitatively in terms of leakage rates and time frames. There are general requirements that wells must not leak or allow fluids (such as gas, hydrocarbons or water) to move between formations or to the surface. However, there is evidence suggesting that achieving zero leakage may not be achievable in all cases. Any intervention post-decommissioning will have potential environmental impacts, and these may cause more harm than a small leak. For these reasons, quantifying an acceptable leak rate is a challenge. A possible approach is to consider that the rate of potential fluid movement through a decommissioned well should be similar to the natural rate of fluid movement within the Earth’s crust.

The time frame for decommissioned well integrity is often described as ‘in perpetuity’ (Huddleston-Holmes et al., 2022). This is problematic for any engineered system (such as the steel casing and cement used in decommissioning) as it is unquantified. In common practice, engineers use the concept of design life, or life expectancy, to design materials or components to last for a specific number of years. It is impractical to extend this concept to indefinite or geological time periods. Nevertheless, it may be possible to evaluate over long time periods the behaviour of a geological formation through which a well is being drilled.

Long-term well integrity (multiple decades to centuries) is a topic of interest in the geological storage of CO₂ (Feitz et al., 2014; Jenkins, 2020) and nuclear waste (Kuppler & Hocke, 2019). There are challenging questions around the timescales required for well integrity and long-term implications. Over centuries, many generations will have passed, institutions will have changed, and technologies will have evolved. Storing nuclear waste and CO₂ both involve the disposal of waste material in the subsurface; a key difference for decommissioned petroleum wells is how they interact with a natural system.

5.7 Summary and conclusion

The potential leakage of formation fluids into the surrounding environment imposes a substantial environmental risk, involving possible release of saline water, liquid hydrocarbons or gases such as methane, propane and ethane. This means that monitoring, measuring and analysing these emissions is of prime importance, not only to quantify the extent of the release but also to trace their origin. Being able to identify the source of an emission is crucial for putting in place effective remediation measures and for implementing preventive strategies. Understanding the properties and concentrations of the materials involved will aid in developing appropriate solutions for mitigating environmental impacts.

References

- Aas, B., Sørbrø, J., Stokka, S., Saasen, A., Godøy, R., Lunde, Ø., & Vrålstad, T. (2017). Cement placement with tubing left in hole during plug-and-abandonment operations. *JPT, Journal of Petroleum Technology*, 69(5), 85–86. <https://doi.org/10.2118/0517-0085-jpt>
- Abel, J. F., & Donald Gentry, J. W. (1975). *EVALUATION OF EXCAVATION EXPERIENCE: PIERRE SHALE mmm OF-FICE OF WASTE ISOLATION*.
- Ahmed, H. M., Kamal, M. S., & Al-Harathi, M. (2019a). Polymeric and low molecular weight shale inhibitors: A review. *Fuel*, 251(March), 187–217. <https://doi.org/10.1016/j.fuel.2019.04.038>
- Ahmed, H. M., Kamal, M. S., & Al-Harathi, M. (2019b). Polymeric and low molecular weight shale inhibitors: A review. *Fuel*, 251(March), 187–217. <https://doi.org/10.1016/j.fuel.2019.04.038>
- Al-Arfaj, M. K., Amanullah, M., Sultan, A. S., Hossain, E., & Abdulraheem, A. (2014). Chemical and mechanical aspects of wellbore stability in shale formations: A literature review. *Society of Petroleum Engineers - 30th Abu Dhabi International Petroleum Exhibition and Conference, ADIPEC 2014: Challenges and Opportunities for the Next 30 Years*, 1, 1–11. <https://doi.org/10.2118/171682-ms>
- Al-Shehri, D. A. (2019). Oil and gas wells: Enhanced wellbore casing integrity management through corrosion rate prediction using an augmented intelligent approach. *Sustainability (Switzerland)*, 11(3), 1–17. <https://doi.org/10.3390/su11030818>
- Alboiu, V., & Walker, T. R. (2019). Pollution, management, and mitigation of idle and orphaned oil and gas wells in Alberta, Canada. *Environmental Monitoring and Assessment*, 191(10). <https://doi.org/10.1007/s10661-019-7780-x>
- Altmann, C., Baruch, E., Close, D., Faiz, M., Richards, B., & Cote, A. (2018). Could the Mesoproterozoic Kyalla Formation Emerge as a Viable Gas Condensate Source Rock Reservoir Play in the Beetaloo Sub-Basin? *ASEG Extended Abstracts*, 2018(1), 1–8. https://doi.org/10.1071/aseg2018abw9_2c
- Augustesen, A., Lade, P. V., & Liingaard, M. (2004). Characterization of Models for Time-Dependent Behavior of Soils. *International Journal of Geomechanics*, 4(3), 157–177. [https://doi.org/10.1061/\(asce\)1532-3641\(2004\)4:3\(157\)](https://doi.org/10.1061/(asce)1532-3641(2004)4:3(157))
- Auqué, L., Gimeno, M. J., Gómez, J., & Nilsson, A. C. (2008). Potentiometrically measured Eh in groundwaters from the Scandinavian Shield. *Applied Geochemistry*, 23(7), 1820–1833. <https://doi.org/10.1016/j.apgeochem.2008.02.016>
- Austbø, L. E. (2016). Laboratory testing to study initiation and evolution of shale barriers. *Master Thesis Dissertation, June*. <http://hdl.handle.net/11250/2405966>
- Babaleye, A. O., Kurt, R. E., & Khan, F. (2019). Safety analysis of plugging and abandonment of oil and gas wells in uncertain conditions with limited data. *Reliability Engineering and System Safety*, 188(March), 133–141. <https://doi.org/10.1016/j.ress.2019.03.027>
- Barker, J. W., Feland, K. W., & Tsao, Y. H. (1994). Drilling long salt sections along the US Gulf Coast. *SPE Drilling & Completion*, 9(3), 185–188. <https://doi.org/10.2118/24605-pa>
- Baruch, E. T., Altmann, C. M., Close, D. I., Mohinudeen, F. M., Richards, B. A., & Côté, A. J. (2018). The Kyalla Formation prospectivity from a mineralogical and sedimentological perspective. *Annual Geoscience Exploration Seminar (AGES) 2018*, 40–48.

- Bauer, A., Stenebråten, J. F., Li, L., & Fjær, E. (2017). Can heating-induced creep result in shale barriers for P&A applications? *51st US Rock Mechanics / Geomechanics Symposium 2017*, 4, 2947–2951.
- Bhaduri, A. (2018). Creep and stress rupture. In *Springer Series in Materials Science* (Vol. 264). https://doi.org/10.1007/978-981-10-7209-3_7
- Boul, P. J., Reddy, B. R., Zhang, J., & Thaemlitz, C. (2017). Functionalized nanosilicas as shale inhibitors in water-based drilling fluids. *SPE Drilling and Completion*, 32(2), 121–130. <https://doi.org/10.2118/185950-pa>
- Bunger, A. P. (2010). The Mandel–Cryer effect in chemoporoelasticity. *International Journal for Numerical and Analytical Methods in Geomechanics, November 2009*, 1479–1511. <https://doi.org/10.1002/nag>
- Bunger, A. P., Sarout, J., Kear, J., Delle Piane, C., Detournay, E., Josh, M., & Dewhurst, D. N. (2014). Experimental chemoporoelastic characterization of shale using millimeter-scale specimens. *Journal of Petroleum Science and Engineering*, 118, 40–51. <https://doi.org/10.1016/j.petrol.2014.04.004>
- Cahill, A. G., Ladd, B., Chao, J., Soares, J., Cary, T., Finke, N., Manning, C., Popp, A. L., Chopra, C., Mayer, K. U., Black, A., Lauer, R., van Geloven, C., Welch, L., Crowe, S., Mayer, B., & Beckie, R. D. (2020). Controlled Natural Gas Release Experiment in a Confined Aquifer, Northeastern British Columbia (NTS 094A / 04): Activity Report 2018 – 2019. *Geoscience BC Report*, 145–160.
- Calosa, W. J., Rahman, H., & Dewanto, C. W. (2018). Exceeding well life design in mature field using well integrity management system. *Society of Petroleum Engineers - SPE/DGS Saudi Arabia Section Technical Symposium and Exhibition 2011*, 388–405. <https://doi.org/10.2118/149087-ms>
- Cao, T. T., Song, Z. G., Wang, S. B., & Xia, J. (2015). A comparative study of the specific surface area and pore structure of different shales and their kerogens. *Science China Earth Sciences*, 58(4), 510–522. <https://doi.org/10.1007/s11430-014-5021-2>
- Carney, L. L. (1986). The basic “K” mud system: A nontoxic mud system field proven to be superior to lignosulfonate muds. *Society of Petroleum Engineers - SPE California Regional Meeting, CRM 1986*, 159–168. <https://doi.org/10.2118/151110-ms>
- Carpenter, C. (2021). Using Shale as a Barrier Simplifies Well Abandonment. *Journal of Petroleum Technology*, 73(01), 62–63. <https://doi.org/10.2118/0121-0062-jpt>
- Cerasi, P., Lund, E., Kleiven, M. L., Stroisz, A., Pradhan, S., Kjøller, C., Frykman, P., & Fjær, E. (2017). Shale Creep as Leakage Healing Mechanism in CO₂ Sequestration. *Energy Procedia*, 114(1876), 3096–3112. <https://doi.org/10.1016/j.egypro.2017.03.1439>
- Chen, G., Chenevert, M. E., Sharma, M. M., & Yu, M. (2003). A study of wellbore stability in shales including poroelastic, chemical, and thermal effects. *Journal of Petroleum Science and Engineering*, 38(3–4), 167–176. [https://doi.org/10.1016/S0920-4105\(03\)00030-5](https://doi.org/10.1016/S0920-4105(03)00030-5)
- Chu, M.-S., & Chang, N.-Y. (1980). Uniaxial Creep of Oil Shale Under Elevated Temperatures. In *The 21st U.S. Symposium on Rock Mechanics (USRMS)* (p. ARMA-80-0207).
- Chukwuemeka, A. O., Oluyemi, G., Mohammed, A. I., & Njuguna, J. (2023a). Plug and abandonment of oil and gas wells – A comprehensive review of regulations, practices, and related impact of materials selection. *Geoenergy Science and Engineering*, 226(September 2022), 211718. <https://doi.org/10.1016/j.geoen.2023.211718>
- Chukwuemeka, A. O., Oluyemi, G., Mohammed, A. I., & Njuguna, J. (2023b). Plug and abandonment of oil

and gas wells – A comprehensive review of regulations, practices, and related impact of materials selection. *Geoenergy Science and Engineering*, 226(February), 211718.
<https://doi.org/10.1016/j.geoen.2023.211718>

- Côté, A., Richards, B., Altmann, C., Baruch, E., & Close, D. (2018). Australia's premier shale basin: five plays, 1 000 000 000 years in the making. *The APPEA Journal*, 58(2), 799. <https://doi.org/10.1071/aj17040>
- Crow, W., Carey, J. W., Gasda, S., Brian Williams, D., & Celia, M. (2010). Wellbore integrity analysis of a natural CO₂ producer. *International Journal of Greenhouse Gas Control*, 4(2), 186–197.
<https://doi.org/10.1016/j.ijggc.2009.10.010>
- Dahi Taleghani, A., & Santos, L. (2023). Wellbore Integrity. In *Wellbore Integrity*.
<https://doi.org/10.1007/978-3-031-19024-7>
- Davies, R. J., Almond, S., Ward, R. S., Jackson, R. B., Adams, C., Worrall, F., Herringshaw, L. G., Gluyas, J. G., & Whitehead, M. A. (2014). Oil and gas wells and their integrity: Implications for shale and unconventional resource exploitation. *Marine and Petroleum Geology*, 56, 239–254.
<https://doi.org/10.1016/j.marpetgeo.2014.03.001>
- Derkowski, A., Marynowski, L., Kazak, E. S., Kazak, A. V., Josh, M., Esteban, L., Delle Piane, C., Sarout, J. J., Dewhurst, D. N., Clennell, M. B., Sarout, J. J., Delle Piane, C., Siggins, A. F., Raven, M. D., Aderibigbe, A. A., Lane, R. H., Das, P., Achalpurkar, M., Pal, O., ... Clennell, B. (2015). Experimental features of cation exchange capacity determination in organic-rich mudstones. *Journal of Petroleum Science and Engineering*, 2(May), 1003–1012. <https://doi.org/10.1016/j.jngse.2020.103456>
- Dewhurst, D. N., Bungler, A., Josh, M., Sarout, J., Delle Piane, C., Esteban, L., & Clennell, M. B. (2013). Mechanics, physics, chemistry and shale rock properties. *47th US Rock Mechanics / Geomechanics Symposium 2013*, 2, 1255–1265.
- Du, J., Hu, L., Meegoda, J. N., & Zhang, G. (2018). Shale softening: Observations, phenomenological behavior, and mechanisms. *Applied Clay Science*, 161(April), 290–300. <https://doi.org/10.1016/j.clay.2018.04.033>
- Dusseault, M. B., Gray, M. N., & Nawrocki, P. A. (2000). Why oilwells leak: Cement behavior and long-term consequences. *Society of Petroleum Engineers - International Oil and Gas Conference and Exhibition in China 2000, IOGCEC 2000*. <https://doi.org/10.2523/64733-ms>
- Enayatpour, S., Thombare, A., Aldin, M., & van Oort, E. (2019). Exploiting shale creep deformation to create annular barriers for well plugging and abandonment: Experimental investigation and numerical simulation. *Proceedings - SPE Annual Technical Conference and Exhibition, 2019-Septe*.
<https://doi.org/10.2118/195966-ms>
- Ewy, R. T. (2014). Shale swelling/shrinkage and water content change due to imposed suction and due to direct brine contact. *Acta Geotechnica*, 9(5), 869–886. <https://doi.org/10.1007/s11440-013-0297-5>
- Ewy, R. T. (2015). Shale/claystone response to air and liquid exposure, and implications for handling, sampling and testing. *International Journal of Rock Mechanics and Mining Sciences*, 80, 388–401.
<https://doi.org/10.1016/j.ijrmms.2015.10.009>
- Ewy, R. T., Bovberg, C. A., & Stankovich, R. J. (2008). Shale Triaxial strength alteration due to brine exposure. *42nd U.S. Rock Mechanics - 2nd U.S.-Canada Rock Mechanics Symposium*.
- Faiz, M., Crombez, V., Delle Piane, C., Langhi, L., Lupton, N., & Hidalgo, J. C. (2024). Beetaloo gas, hydrogen and geothermal resources – insights from 3D basin modelling. *Australian Energy Producers Journal*, 64(2), S371–S375. <https://doi.org/10.1071/ep23032>

- Feitz, A. J., Leamon, G., Jenkins, C., Jones, D. G., Moreira, A., Bressan, L., Melo, C., Dobeck, L. M., Repasky, K., Spangler, L. H., Lee, H., Moreira, A., Bressan, L., Melo, C., Dobeck, L. M., Repasky, K., & Spangler, L. H. (2014). Looking for leakage or monitoring for public assurance? *Energy Procedia*, *63*, 3881–3890. <https://doi.org/10.1016/j.egypro.2014.11.418>
- Feng, W. Q., Lalit, B., Yin, Z. Y., & Yin, J. H. (2017). Long-term Non-linear creep and swelling behavior of Hong Kong marine deposits in oedometer condition. *Computers and Geotechnics*, *84*, 1–15. <https://doi.org/10.1016/j.compgeo.2016.11.009>
- Fjær, E., Bakheim, S., & Stenebråten, J. F. (2023). *Long-Term Development of Shale Barrier Efficiency: Laboratory Tests on an Outcrop Shale*. 23–26. <https://doi.org/10.56952/arma-2023-0612>
- Fjær, E., Folstad, J. S., & Li, L. (2016). How creeping shale may form a sealing barrier around a well. *50th US Rock Mechanics / Geomechanics Symposium 2016*, *4*(1), 3036–3043.
- Ford, E. P., Moeinikia, F., Lohne, H. P., Arild, O., Majoumerd, M. M., & Fjelde, K. K. (2017). Leakage calculator for plugged and abandoned wells. *Society of Petroleum Engineers - SPE Bergen One Day Seminar 2017, 010*(2013). <https://doi.org/10.2118/185890-ms>
- Garg, N., & Skibsted, J. (2016). Pozzolanic reactivity of a calcined interstratified illite/smectite (70/30) clay. *Cement and Concrete Research*, *79*, 101–111. <https://doi.org/10.1016/j.cemconres.2015.08.006>
- Gawel, K., Lozovyi, M., Bhuiyan, M. H., Bjørge, R., & Fjær, E. (2021). Acid treatment as a way to reduce shale rock mechanical strength and to create a material prone to the formation of permanent well barrier. In *Energies* (Vol. 14, Issue 9). <https://doi.org/10.3390/en14092342>
- Geological, I., & Report, W. (n.d.). Beetaloo basin, northern territory, australia location map. *Shenandoah-1a Interim Geological Well Report*.
- Ghassemi, A., & Suarez-Rivera, R. (2012). Sustaining fracture area and conductivity of shale gas reservoirs for enhancing long-term production and recovery. *College Station, TX*.
- Gholami, R., Elochukwu, H., Fakhari, N., & Sarmadivaleh, M. (2018). A review on borehole instability in active shale formations: Interactions, mechanisms and inhibitors. *Earth-Science Reviews*, *177*(April 2017), 2–13. <https://doi.org/10.1016/j.earscirev.2017.11.002>
- Gorter, J., & Grey, K. (2012). Velkerri Formation Depositional Model - Beetaloo Sub-basin, Northern Territory, Australia: Biostratigraphy and Organic Enrichment. *Central Australian Basins Symposium III*, *6*.
- Gray, K. E., Podnos, E., & Becker, E. (2009). Finite-element studies of near-wellbore region during cementing operations: Part I. *SPE Drilling & Completion*, *24*(01), 127–136.
- Guen, Y. Le, Huot, M., Loizzo, M., & Poupard, O. (2011). Well integrity risk assessment of Ketzin injection well (Ktzi-201) over a prolonged sequestration period. *Energy Procedia*, *4*, 4076–4083. <https://doi.org/10.1016/j.egypro.2011.02.350>
- Holder, C. F., & Schaak, R. E. (2019). Tutorial on Powder X-ray Diffraction for Characterizing Nanoscale Materials. *ACS Nano*, *13*(7), 7359–7365. <https://doi.org/10.1021/acs.nano.9b05157>
- Holt, R. M., Fjær, E., Larsen, I., Stenebråten, J. F., & Raaen, A. M. (2019). On the border between brittle and ductile behavior of shale. *53rd U.S. Rock Mechanics/Geomechanics Symposium*.
- Holt, R. M., & Kolstø, M. I. (2017). How does water near clay mineral surfaces influence the rock physics of shales? *Geophysical Prospecting*, *65*(6), 1615–1629. <https://doi.org/10.1111/1365-2478.12503>

- Horsrud, P., Sønsteb Ø, E. F., & Bøe, R. (1998). Mechanical and petrophysical properties of North Sea shales. *International Journal of Rock Mechanics and Mining Sciences*, 35(8), 1009–1020. [https://doi.org/10.1016/S0148-9062\(98\)00162-4](https://doi.org/10.1016/S0148-9062(98)00162-4)
- Huddleston-Holmes, C., Arjomand, E., & Kear, J. (2022). *Long-term monitoring of decommissioned onshore gas wells*. May. <https://gisera.csiro.au/wp-content/uploads/2022/05/Final-Report-GISERA-W20-Monitoring-of-Decommissioned-Wells.pdf>
- Huddleston-Holmes, C. R., Wu, B., Kear, J., & Pandurangan, R. (2017). Report into the shale gas well life cycle and well integrity. *Prepared for the Northern Territory Hydraulic Fracturing Inquiry, December*, 1–92. <https://publications.csiro.au/rpr/pub?pid=csiro:EP179028>
- Hunziker, J. C., Frey, M., Clauer, N., Dallmeyer, R. D., Friedrichsen, H., Flehmig, W., Hochstrasser, K., Roggwiler, P., & Schwander, H. (1986). The evolution of illite to muscovite: mineralogical and isotopic data from the Glarus Alps, Switzerland. *Contributions to Mineralogy and Petrology*, 92(2), 157–180. <https://doi.org/10.1007/BF00375291>
- Ilgen, A. G., Heath, J. E., Akkutlu, I. Y., Bryndzia, L. T., Cole, D. R., Kharaka, Y. K., Kneafsey, T. J., Milliken, K. L., Pyrak-Nolte, L. J., & Suarez-Rivera, R. (2017). Shales at all scales: Exploring coupled processes in mudrocks. *Earth-Science Reviews*, 166, 132–152. <https://doi.org/10.1016/j.earscirev.2016.12.013>
- Jenkins, C. (2020). The State of the Art in Monitoring and Verification: an update five years on. *International Journal of Greenhouse Gas Control*, 100(August), 103118. <https://doi.org/10.1016/j.ijggc.2020.103118>
- Josh, M. (2014). Dielectric Permittivity: A Petrophysical Parameter for Shales. *Petrophysics*, 55(04), 319–332.
- Josh, M., Bungler, A., Kear, J., Sarout, J., Dewhurst, D., Raven, M. D., Delle Piane, C., Esteban, L., & Clennell, M. B. (2014). The role of specific surface area and cation exchange capacity in determining shale rock properties. *4th EAGE Shale Workshop 2014 - Shales: What Do They Have in Common?, April 2015*, 6–10. <https://doi.org/10.3997/2214-4609.20140014>
- Kang, M., Brandt, A. R., Zheng, Z., Boutot, J., Yung, C., Peltz, A. S., & Jackson, R. B. (2021). Orphaned oil and gas well stimulus-maximizing economic and environmental benefits. *Elementa*, 9(1), 1–13. <https://doi.org/10.1525/elementa.2020.20.00161>
- Karpiński, B., & Szkodo, M. (2015). Clay Minerals – Mineralogy and Phenomenon of Clay Swelling in Oil & Gas Industry. *Advances in Materials Science*, 15(1), 37–55. <https://doi.org/10.1515/adms-2015-0006>
- Kelly, W. R., Matisoff, G., & Fisher, J. B. (1985). The effects of a gas well blow out on groundwater chemistry. *Environmental Geology and Water Sciences*, 7(4), 205–213. <https://doi.org/10.1007/BF02509921>
- Kim, Y., Kim, C., Kim, J., Kim, Y., & Lee, J. (2020). Experimental investigation on the complex chemical reactions between clay minerals and brine in low salinity water-flooding. *Journal of Industrial and Engineering Chemistry*, 89, 316–333. <https://doi.org/10.1016/j.jiec.2020.05.027>
- King, G. E., Corporation, A., King, D. E., & Consulting, W. G. (2013). *SPE 166142 Environmental Risk Arising From Well Construction Failure : Difference Between Barrier and Well Failure , and Estimates of Failure Frequency Across Common Well Types , Locations and Well Age*. September, 166142.
- Kristiansen, T. G., Delabroy, L., Obando Palacio, G. A., Winther, T., Aarseth, N. A., Bauer, A., Hagenes, K., Lindal, A., & Tyberø, P. (2021). Implementing a strategy for shale as well barrier in new wells. *SPE/IADC Drilling Conference, Proceedings, 2021-March*. <https://doi.org/10.2118/204075-MS>
- Kristiansen, T. G., Dyngeland, T., Kinn, S., Flatebø, R., & Aarseth, N. A. (2018). Activating shale to form well

barriers: Theory and field examples. *Proceedings - SPE Annual Technical Conference and Exhibition, 2018-Sept*(September), 24–26. <https://doi.org/10.2118/191607-ms>

- Kuppler, S., & Hocke, P. (2019). The role of long-term planning in nuclear waste governance. *Journal of Risk Research*, 22(11), 1343–1356. <https://doi.org/10.1080/13669877.2018.1459791>
- Lal, M. (1999). Shale stability: Drilling fluid interaction and shale strength. *Society of Petroleum Engineers - SPE Asia Pacific Oil and Gas Conference and Exhibition 1999, APOGCE 1999*. <https://doi.org/10.2523/54356-ms>
- Landon, S., Mather, T., Berg, E., & Colorado, U. S. A. (2005). Hydrocarbon Potential of the Beetaloo Basin Northern Territory, Australia Prepared for SweetPea Corporation Pty Ltd. *SweetPea Corporation Pty Ltd, January*.
- Lavery, D., Jambunathan, V., & Shafikova, G. M. (2019). Turning a negative into a positive: Shale annular barrier identification for plug and abandonment. *SPWLA 60th Annual Logging Symposium 2019*. https://doi.org/10.30632/T60ALS-2019_LL
- Lecampion, B., Bungler, A., Kear, J., & Quesada, D. (2013). Interface debonding driven by fluid injection in a cased and cemented wellbore: Modeling and experiments. *International Journal of Greenhouse Gas Control*, 18, 208–223. <https://doi.org/10.1016/j.ijggc.2013.07.012>
- Lecampion, B., Quesada, D., Loizzo, M., Bungler, A., Kear, J., Deremble, L., & Desroches, J. (2011). Interface debonding as a controlling mechanism for loss of well integrity: Importance for CO₂ injector wells. *Energy Procedia*, 4, 5219–5226. <https://doi.org/10.1016/j.egypro.2011.02.500>
- Lécolier, E., Rivereau, A., Ferrer, N., Audibert, A., & Longaygue, X. (2008). Study of new solutions for acid-resistant cements. *Proceedings - SPE Annual Technical Conference and Exhibition*, 5(September), 2991–3001.
- Li, H., Kalinin, D., Bruce, A., & Bukovac, T. (2023). Pioneering Beetaloo Shale Appraisal: Case Study of Australia's Largest Multistage Fracturing Operation. *Society of Petroleum Engineers - Asia Pacific Unconventional Resources Symposium, APUR 2023*. <https://doi.org/10.2118/217282-MS>
- Li, X., Wang, M., & Shen, F. (2023). A three-dimensional nonlinear rock damage creep model with double damage factors and residual strength. *Natural Hazards*, 115(3), 2205–2222. <https://doi.org/10.1007/s11069-022-05634-y>
- Li, Y., & Ghassemi, A. (2012). Creep behavior of Barnett, Haynesville, and Marcellus shale. *46th US Rock Mechanics / Geomechanics Symposium 2012*, 1, 641–647.
- Li, Y., Wang, M., An, Y., Li, K., Wei, Z., Bo, K., Cao, P., & Guo, M. (2022). In Situ Shale Wettability Regulation Using Sophisticated Nanoemulsion to Maintain Wellbore Stability in Deep Well Drilling. *Langmuir*, 38(41), 12539–12550. <https://doi.org/10.1021/acs.langmuir.2c01989>
- Li, Y., Wang, M., Tan, X., An, Y., Liu, H., Gao, K., & Guo, M. (2021). Application of Hybrid Silicate as a Film-Forming Agent in High-Temperature Water-Based Drilling Fluids. *ACS Omega*, 6(31), 20577–20589. <https://doi.org/10.1021/acsomega.1c02725>
- Lin, J. (2022). *Proceedings of the International Field Exploration and Development*.
- Lin, T., Zhang, Q., Lian, Z., Chang, X., Zhu, K., & Liu, Y. (2016). Evaluation of casing integrity defects considering wear and corrosion – Application to casing design. *Journal of Natural Gas Science and Engineering*, 29, 440–452. <https://doi.org/10.1016/j.jngse.2016.01.029>

- Liu, X., Birchwood, R., & Hooyman, P. J. (2011). A new analytical solution for wellbore creep in soft sediments and salt. *45th US Rock Mechanics / Geomechanics Symposium*, 1–13.
- Liu, Y., Yang, C., Wang, J., Xiong, Y., & Peng, P. (2022). New insights into hydration-induced creep behavior of shale: A comparison study of brittle black shale and clayey oil shale at micro-scale. *Marine and Petroleum Geology*, 138(September 2021), 105554. <https://doi.org/10.1016/j.marpetgeo.2022.105554>
- Lucas, A., Stokkeland, T. A., Jackson, D., & Ingram, S. (2018). Improving the understanding, application and reliability of the perforate, wash and cement technique through the use of cement bond logs, tool enhancements and barrier verification via annular pressure monitoring. *Proceedings - SPE Annual Technical Conference and Exhibition, 2018-Septe*. <https://doi.org/10.2118/191528-ms>
- Maharidge, R., Bottiglieri, A., Dighe, S. S., Holley, A., Zhang, H., & Koch, A. (2016). Development of permeability and mechanical properties of class G cement from slurry to set. *Proceedings - SPE Annual Technical Conference and Exhibition, 2016-Janua*.
- Mandal, P. P., Sarout, J., & Rezaee, R. (2021). Specific surface area: A reliable predictor of creep and stress relaxation in gas shales. *Leading Edge*, 40(11), 815–822. <https://doi.org/10.1190/tle40110815.1>
- Mandal, P. P., Sarout, J., Rezaee, R., & Hossain, M. (2022). Can We Predict Primary Creep and Least Principal Stress Shmin at Depth Either from Specific Surface Area or Weak Phase of Gas Shales? *International Petroleum Technology Conference*. <https://doi.org/10.2523/iptc-22212-ms>
- Martín, D., Aparicio, P., García, S., & Maroto-Valer, M. M. (2022). Mixed-Layer Illite-Smectite Illitization under Supercritical CO₂ Conditions. *Applied Sciences (Switzerland)*, 12(22). <https://doi.org/10.3390/app122211477>
- Mazon, A. L. (2022). Numerical modelling of evaporites as a natural barrier for the abandonment of oil wells. In *Master Thesis Dissertation* (Issue April).
- Mu, Y., Hu, Z., Shen, R., Chang, J., Duan, X., Li, Y., & Guo, Q. (2022). Water Occurrence Characteristics of Gas Shale Based on 2D NMR Technology. *Energy and Fuels*, 36(2), 910–921. <https://doi.org/10.1021/acs.energyfuels.1c03870>
- Munson, T. J. (2016). Sedimentary characterisation and correlation of the Wilton package , greater McArthur Basin : in , Alice Spri ... *Annual Geoscience Exploration Seminar (AGES) Proceedings, March*.
- Nayak, P. S., & Singh, B. K. (2007). Instrumental characterization of clay by XRF, XRD and FTIR. *Bulletin of Materials Science*, 30(3), 235–238. <https://doi.org/10.1007/s12034-007-0042-5>
- Nichol, J. ., & Kariyawasam, S. . (2000). *Risk Assessment of Temporarily Abandoned or Shut-in Wells* (Issue 1435, p. 72). United States Department of the Interior, Minerals Management Service.
- Noik, C., Rivereau, A., & Français, I. (1999). *SPE 56538 Oilwell Cement Durability*.
- NORSOK D-10. (2021). D-010 Well integrity in drilling and well operations. *NORSOK Standard D-010: Standards Norway*.
- Northern Territory Government. (2019). *Code of Practice : Onshore Petroleum Activities in the Northern Territory. April*, 1–120.
- Odom, I. E. (1984). Smectite clay minerals: properties and uses. *Philosophical Transactions of the Royal Society of London*, 409(A311), 391–409. <https://doi.org/10.1098/rsta.1984.0036>

- OEUK. (2022). *Use of Barrier Materials in Well Decommissioning: Guidelines* (Issue 3). www.OEUK.org.uk
- Osman, M. A., & Suter, U. W. (2000). Determination of the cation-exchange capacity of muscovite mica. *Journal of Colloid and Interface Science*, 224(1), 112–115. <https://doi.org/10.1006/jcis.1999.6677>
- Oves, M., Khan, M. Z., & Ismail, I. M. I. (2017). Modern age environmental problems and their remediation. In *Modern Age Environmental Problems and their Remediation*. <https://doi.org/10.1007/978-3-319-64501-8>
- Paraskevopoulou, C., & Diederichs, M. (2013). Long term behaviour in tunnelling : limitations in using creep parameters. *Canadian Geotechnical Symposium GeoMontreal on Geoscience for Sustainability, February*.
- Peng, Y., Zhao, J., Sepehrnoori, K., & Li, Z. (2020). Fractional model for simulating the viscoelastic behavior of artificial fracture in shale gas. *Engineering Fracture Mechanics*, 228(January), 106892. <https://doi.org/10.1016/j.engfracmech.2020.106892>
- Pichtel, J. (2016). Oil and gas production wastewater: Soil contamination and pollution prevention. *Applied and Environmental Soil Science*, 2016. <https://doi.org/10.1155/2016/2707989>
- Poole, D. A. (2021). NORSOK Standard D-010. In *Norwegian Standard Organization (NORSOK Standard D-010)* (Issue August). <https://doi.org/10.1016/B978-0-12-821956-0.00005-5>
- Qin, X., Han, D. H., & Zhao, L. (2019). Elastic characteristics of overpressure due to smectite-to-illite transition based on micromechanism analysis. *Geophysics*, 84(4), WA23–WA42. <https://doi.org/10.1190/GEO2018-0338.1>
- Ranjith, P. G., & Viete, D. R. (2011). Applicability of the “cubic law” for non-Darcian fracture flow. *Journal of Petroleum Science and Engineering*, 78(2), 321–327. <https://doi.org/10.1016/j.petrol.2011.07.015>
- Rassouli, F. S., & Zoback, M. D. (2015). Long-term creep experiments on Haynesville shale rocks. *49th US Rock Mechanics / Geomechanics Symposium 2015*, 1, 511–516.
- Ratner-Zohar, Y., Banin, A., & Chen, Y. (1983). Oven Drying as a Pretreatment for Surface-Area Determinations of Soils and Clays. *Soil Science Society of America Journal*, 47(5), 1056–1058. <https://doi.org/10.2136/sssaj1983.03615995004700050048x>
- Ruble, T., Revie, D., Roberts, E., Barcelona, E., Gupta, N., Hankins, B., Smith, C., & Edgoose, C. (2019). Assessing Unconventional Resource Potential of the Mesoproterozoic Roper Group, Beetaloo Sub-Basin Region, Australia. *AAPG 2018 AAPG Annual Convention and Exhibition*. <https://doi.org/10.1306/80671Ruble2019>
- Rybacki, E., Reinicke, A., Meier, T., Makasi, M., & Dresen, G. (2015). What controls the mechanical properties of shale rocks? - Part I: Strength and Young’s modulus. *Journal of Petroleum Science and Engineering*, 135, 702–722. <https://doi.org/10.1016/j.petrol.2015.10.028>
- Saidin, S., Sonny, I., & Nuruddin, M. F. (2008). A new approach for optimizing cement design to eliminate microannulus in steam injection wells. *International Petroleum Technology Conference, IPTC 2008*, 3, 1527–1541.
- Santos, H. (1997). *A new conceptual approach to shale stability*. the university of Oklahoma.
- Sarout, J., & Detournay, E. (2011). Chemoporoelastic analysis and experimental validation of the pore pressure transmission test for reactive shales. *International Journal of Rock Mechanics and Mining*

Sciences, 48(5), 759–772. <https://doi.org/10.1016/j.ijrmms.2011.04.009>

- Shi, X. (2022). Experimental investigation on the creep behaviors of shale using nanoindentation technique and fractional constitutive models. *Rock Mechanics and Rock Engineering*, 55(11), 6643–6661. <https://doi.org/10.1007/s00603-022-02976-8>
- Silverman, M., & Ahlbrandt, T. (2011). Mesoproterozoic Unconventional Plays in the Beetaloo Basin, Australia: The World's Oldest Petroleum Systems. *Aapg Ice 2011*, 10295.
- Solomon, S. (2007). Carbon Dioxide Storage: Geological Security and Environmental Issues-Case Study on the Sleipner Gas field in Norway. *Bellona Report*, May, 128.
- Sone, H., & Zoback, M. D. (2014). Time-dependent deformation of shale gas reservoir rocks and its long-term effect on the in situ state of stress. *International Journal of Rock Mechanics and Mining Sciences*, 69, 120–132. <https://doi.org/10.1016/j.ijrmms.2014.04.002>
- Stanjek, P. H., & Aachen, R. (2009). *Modification of Mechanical Behaviour of Clays for Improving*. June 2014.
- Steelman, C. M., Klazinga, D. R., Cahill, A. G., Endres, A. L., & Parker, B. L. (2017). Monitoring the evolution and migration of a methane gas plume in an unconfined sandy aquifer using time-lapse GPR and ERT. *Journal of Contaminant Hydrology*, 205(August), 12–24. <https://doi.org/10.1016/j.jconhyd.2017.08.011>
- Stixrude, L., & Peacor, D. R. (2002). First-principles study of illite-smectite and implications for clay mineral systems. *Nature*, 420(6912), 165–168. <https://doi.org/10.1038/nature01155>
- Takhanov, D. (2011). Forchheimer Model for Non-Darcy Flow in Porous Media and Fractures. *Centre for Petroleum Studies, Department*(September), 1–31.
- Thombare, A., Aldin, M., & van Oort, E. (2020). Experimental technique to investigate shale creep for annular barrier formation in oil and gas wells. *54th U.S. Rock Mechanics/Geomechanics Symposium*.
- Torsæter, M., Vullum, P. E., Nes, O. M., & Rinna, J. (2012). Nanostructure vs macroscopic properties of Mancos shale. *Society of Petroleum Engineers - SPE Canadian Unconventional Resources Conference 2012, CURC 2012*, 2, 1086–1098. <https://doi.org/10.2118/162737-ms>
- UK-OG. (2015). Guidelines on Qualification of Materials for the Abandonment of Wells-Issue 2. *OIL & GAS UK, London*.
- Van Der Tuuk Opedal, N., Torsæter, M., Vralstad, T., & Cerasi, P. (2013). Potential leakage paths along cement-formation interfaces in wellbores; Implications for CO2 storage. *Energy Procedia*, 51, 56–64. <https://doi.org/10.1016/j.egypro.2014.07.007>
- van Oort, E. (2003). On the physical and chemical stability of shales. *Journal of Petroleum Science and Engineering*, 38(3–4), 213–235. [https://doi.org/10.1016/S0920-4105\(03\)00034-2](https://doi.org/10.1016/S0920-4105(03)00034-2)
- van Oort, E., Juenger, M., Aldin, M., Thombare, A., & McDonald, M. (2020). Simplifying well abandonments using shale as a barrier. *SPE/IADC Drilling Conference, Proceedings, 2020-March*. <https://doi.org/10.2118/199654-ms>
- van Oort, E., Thombare, A., Aldin, M., & Lucas, A. (2022a). Annular Creep Barrier Evaluation and Qualification Using Ultrasonic Measurements. *SPE - International Association of Drilling Contractors Drilling Conference Proceedings, 2022-March*. <https://doi.org/10.2118/208782-MS>
- van Oort, E., Thombare, A., Aldin, M., & Lucas, A. (2022b). Annular Creep Barrier Evaluation and Qualification

- Using Ultrasonic Measurements. *SPE - International Association of Drilling Contractors Drilling Conference Proceedings, 2022-March*(December), 8–10. <https://doi.org/10.2118/208782-MS>
- van Oort, E., Thombare, A., Aldin, M., & Lucas, A. (2022c). Annular Creep Barrier Evaluation and Qualification Using Ultrasonic Measurements. *SPE - International Association of Drilling Contractors Drilling Conference Proceedings, 2022-March*(February), 8–10. <https://doi.org/10.2118/208782-MS>
- Vergara, M. R., & Triantafyllidis, T. (2016). *Influence of Water Content on the Mechanical Properties of an Argillaceous Swelling Rock*. 2555–2568. <https://doi.org/10.1007/s00603-016-0938-8>
- Voltolini, M. (2021). In-situ 4D visualization and analysis of temperature-driven creep in an oil shale propped fracture. *Journal of Petroleum Science and Engineering, 200*(September 2020), 108375. <https://doi.org/10.1016/j.petrol.2021.108375>
- Wang, H., Qian, H., Gao, Y., & Li, Y. (2020). Classification and physical characteristics of bound water in loess and its main clay minerals. *Engineering Geology, 265*(December 2019), 105394. <https://doi.org/10.1016/j.enggeo.2019.105394>
- Wang, R., Li, L., & Simon, R. (2019). A model for describing and predicting the creep strain of rocks from the primary to the tertiary stage. *International Journal of Rock Mechanics and Mining Sciences, 123*(October 2018). <https://doi.org/10.1016/j.ijrmmms.2019.104087>
- Wang, X., & Wang, H. (2021). Structural analysis of interstratified illite-smectite by the rietveld method. *Crystals, 11*(3), 1–15. <https://doi.org/10.3390/cryst11030244>
- Watson, T. L., & Bachu, S. (2009). Evaluation of the potential for gas and CO₂ leakage along wellbores. *SPE Drilling and Completion, 24*(1), 115–126. <https://doi.org/10.2118/106817-PA>
- Weideman, B., & Nygaard, R. (2014). *AADE-14-FTCE-20 How Cement Operations affect your Cement Sheath Short and Long Term Integrity*. 1–14.
- Xie, S. Y., Shao, J. F., & Burlion, N. (2008). Experimental study of mechanical behaviour of cement paste under compressive stress and chemical degradation. *Cement and Concrete Research, 38*(12), 1416–1423. <https://doi.org/10.1016/j.cemconres.2008.06.011>
- Xie, Y., Hou, M. Z., Liu, H., & Li, C. (2023). Anisotropic time-dependent behaviors of shale under direct shearing and associated empirical creep models. *Journal of Rock Mechanics and Geotechnical Engineering, xxxx*, 1–18. <https://doi.org/10.1016/j.jrmge.2023.05.001>
- Yan, C., Deng, J., Yu, B., Li, W., Chen, Z., Hu, L., & Li, Y. (2014). Borehole Stability in High-Temperature Formations. *Rock Mechanics and Rock Engineering, 47*(6), 2199–2209. <https://doi.org/10.1007/s00603-013-0496-2>
- Yang, B., Smith, T. M., Collins, A. S., Munson, T. J., Schoemaker, B., Nicholls, D., Cox, G., Farkas, J., & Glorie, S. (2018). Spatial and temporal variation in detrital zircon age provenance of the hydrocarbon-bearing upper Roper Group, Beetaloo Sub-basin, Northern Territory, Australia. *Precambrian Research, 304*(October 2017), 140–155. <https://doi.org/10.1016/j.precamres.2017.10.025>
- Yasin, Q., Du, Q., Sohail, G. M., & Ismail, A. (2017). *Impact of organic contents and brittleness indices to differentiate the brittle-ductile transitional zone in shale gas reservoir*. 21(5), 779–789.
- Zhang, D., Ranjith, P. G., & Perera, M. S. A. (2016). The brittleness indices used in rock mechanics and their application in shale hydraulic fracturing : A review. *Journal of Petroleum Science and Engineering, 143*, 158–170. <https://doi.org/10.1016/j.petrol.2016.02.011>

- Zhang, J., Mahbod, P., Shafer, R., Mueller, D., & Anderson, C. (2019). Multi-string isolation logging - A cost effective solution for P&A. *Society of Petroleum Engineers - SPE Norway One Day Seminar 2019, May*. <https://doi.org/10.2118/195607-ms>
- Zhang, Q., Lian, Z., Lin, T., Deng, Z., Xu, D., & Gan, Q. (2016). Casing wear analysis helps verify the feasibility of gas drilling in directional wells. *Journal of Natural Gas Science and Engineering*, 35, 291–298. <https://doi.org/10.1016/j.jngse.2016.08.066>
- Zhang, Z., Huang, C., Jin, H., Feng, W., Jin, D., & Zhang, G. (2022). A creep model for frozen soil based on the fractional Kelvin–Voigt’s model. *Acta Geotechnica*, 17(10), 4377–4393. <https://doi.org/10.1007/s11440-021-01390-8>
- Zhao, Z., Liu, Z., Lu, C., He, T., & Chen, M. (2022). Brittleness evaluation based on shale fracture morphology. *Journal of Natural Gas Science and Engineering*, 104(8). <https://doi.org/10.1016/j.jngse.2022.104679>
- Zhou, X., Liu, D., Bu, H., Deng, L., Liu, H., Yuan, P., Du, P., & Song, H. (2018). XRD-based quantitative analysis of clay minerals using reference intensity ratios, mineral intensity factors, Rietveld, and full pattern summation methods: A critical review. *Solid Earth Sciences*, 3(1), 16–29. <https://doi.org/10.1016/j.sesci.2017.12.002>
- Zhou, X., Pan, X., & Berto, F. (2022). A state-of-the-art review on creep damage mechanics of rocks. *Fatigue and Fracture of Engineering Materials and Structures*, 45(3), 627–652. <https://doi.org/10.1111/ffe.13625>
- Zuo, Z., & Bennett, T. (2019). Simulation of the degradation of oilwell cement for the prediction of long-term performance. *Construction and Building Materials*, 202, 669–680. <https://doi.org/10.1016/j.conbuildmat.2019.01.062>

Appendix I: Map of petroleum wells in the Northern Territory



Figure 67: A visual representation of petroleum well sites in the Northern Territory

Appendix II: Creeping formation criteria

Table 27: Creeping formation criteria retrieved from NORSOK-D10*

Features	Acceptance criteria	Reference
A. Description	The element consists of creeping formation (formation that plastically has been extruded into the wellbore) located in the annulus between the casing/liner and the borehole wall.	
B. Function	The purpose of the element is to provide a continuous, permanent seal along the casing annulus to prevent flow of formation fluids and to resist pressures from above and below.	
C. Design, construction, and selection	<ol style="list-style-type: none"> 1. Consideration of a formation as well barrier elements (WBE) applies where the formation is known to have plastic properties and can be expected to form a seal with acceptable integrity towards axial leakage. 2. The element shall be capable of providing an eternal pressure seal. <ol style="list-style-type: none"> (a) The formation interval shall be geologically homogeneous and laterally continuous. (b) Creeping formations include any low-permeability formations which are sufficiently mobile to allow rapid closure of cracks, such as claystone, shale and salt. Typical formation characteristics include low permeability, ductile, high smectite and clay content or salt, low content of cementing materials (quartz, carbonates, etc.), low friction angle, low cohesion and low unconfined compressive strength (UCS). (c) Permeable and non-mobile formations such as silts, sandstones, basalt and granite are excluded. 3. The minimum formation interval shall be 30 m MD for a qualified well barrier element and 2 × 30 m MD if it is part of the primary and secondary well barrier. 4. The minimum formation integrity at the base of the element shall be sufficient to withstand the maximum pressure that could be applied. 	UK Oil and Gas, Guidelines on qualification of Materials for the Abandonment of Wells (UK-OG, 2015).
D. Initial test and verification	<ol style="list-style-type: none"> 1. Position and length of the element shall be verified by bond logs: <ol style="list-style-type: none"> (a) Two independent logging measurements/tools shall be applied. Logging measurements shall provide azimuthal data. (b) Logging data shall be interpreted and verified by qualified personnel and documented. (c) The log response criteria shall be established prior to the logging operation. (d) The minimum contact length shall be 30 m MD for a single well barrier element or 2 × 30 m MD when the same formation will be a part of the primary and secondary well barrier, with azimuthal qualified bonding. 2. Pressure integrity shall be verified by application of a pressure differential across the interval. The interval should be no more than 30 m MD long. 3. Formation integrity at the base of the interval shall be verified according to Table 3, in order to qualify as a WBE. The results should be in accordance with the expected formation stress from the field model. 4. If the specific formation is previously qualified by logging and FIT, logging is considered adequate for subsequent wells. Differential pressure testing is required if the log response is not conclusive or if there is uncertainty regarding geological similarity. 	
E. Use	The element is primarily used in a permanently abandoned well.	
F. Monitoring	None	
G. Common well barrier	None	

*NORSOK D-010:2021+AC2:2021 (NORSOK D-10, 2021)

Appendix III: Report on diffraction, mineralogy and geochemistry characterisation



CSIRO Mineral Resources

Diffraction, Mineralogy and Geochemistry Characterisation Report

CLIENT	Elaheh Arjomand (Job No. 6018)
BU	Energy
DATE	07/02/2023
WBS/O2D	R-18431
ANALYST(S)	Rong Fan and Rodrigo Gomez-Camacho
SUBJECT	XRF and XRD analysis of drill cores and cuttings of Velkerri samples

Procedure

Two drill core samples were received for bulk and clay mineralogy by X-ray powder diffraction (XRPD) analysis. The samples were crushed by a jar crusher and representative sub-samples were further pulverised briefly using a ring mill for following XRD and XRF sample preparations.

For bulk quantitative XRD phase analysis of the samples, approximately 1.5 g of the pulverised powder sample was ground in ethanol in a McCrone micronising mill. The resulting slurry was oven-dried at 60°C then thoroughly mixed in an agate mortar and pestle before being lightly back-pressed into a stainless-steel sample holder for presentation to the X-ray beam. The samples were then Ca-exchanged in CaCl₂ solution to ensure that the phases with exchangeable cations (e.g. smectite) were in a divalent monoionic form. The Ca-exchanged samples were lightly back-pressed into a stainless-steel sample holder for presentation to the X-ray beam.

For fine clay analysis, approximately 15 g of the crushed samples were dispersed in NaCl solution. From this dispersion the size fractions (<0.2 µm, 0.2 to 2 µm, and >2 µm) were collected by repeated washing with high-purity water, ultrasonication and centrifugation. The recovered material (i.e. <0.2 µm and 0.2 to 2 µm fractions) was treated twice with 0.2 M acetic acid solution to remove carbonate mineral calcite and dolomite, and Ca-exchanged by washing twice with CaCl₂ solution and then removing excess Ca by washing firstly with high-purity water and secondly with ethanol. After the ethanol wash the samples were dried in an oven set to 60°C. The dried material was thoroughly mixed in an agate mortar and pestle before being lightly back-pressed into stainless steel sample holders for presentation to the X-ray beam. The remaining material after the fine clay separation (i.e. >0.2 µm fraction) was dried at 60°C and then weighed for mass balance calculation.

XRD patterns of the bulk and size fraction samples were recorded with a PANalytical X'Pert Pro Multi-purpose Diffractometer using Fe-filtered Co K α radiation, automatic divergence slit, 2° anti-scatter slit and fast X'Celerator Si strip detector. The diffraction patterns were recorded in steps of 0.017° 2 theta with a 0.5 second counting time per step for an overall counting time of approximately 30 minutes.

Phase identification was performed using PANalytical Highscore Plus[®] software (V4.8), which interfaces with the International Centre for Diffraction Data (ICDD) PDF 4+ 2021 database. Quantitative phase analysis (QPA) was carried out via the Rietveld method using the TOPAS V6 software. The QPA results obtained are the relative wt% of crystalline phases.

For XRF analysis, approximately 1 g of each oven-dried (105°C) bulk-pulverised sample was accurately weighed with 4 g of lithium tetraborate flux. The mixtures were heated to 1050°C in a Pt/Au crucible for 20 minutes to completely dissolve the sample then poured into a 32 mm Pt/Au mould heated to a similar temperature. The melt was cooled rapidly over a compressed air stream and the resulting glass disks were analysed under vacuum using a Spectro XEPOS He energy dispersive X-ray fluorescence spectrometer.

Soluble cations and anions, CEC and exchangeable cations of the bulk as received samples using NH₄⁺ were determined using the methods detailed in Rayment and Higginson (1992).

Results

Quantitative XRD analysis results (wt.%) of the bulk, micronised and calcium-saturated samples and their <0.2 and 0.2 to 2 µm fractions (relative concentrations) and the percentage of these size fractions (wt.%) are given in Tables 28 to 31, respectively.

The results of XRF analysis of the bulk samples are given in Table 32. Exchangeable cations and CEC at pH 8.5 (oven-dried 60°C basis) of the samples are shown in Table 33.

Phases identified in the sample are smectite (montmorillonite), kaolinite, interstratified illite–smectite, mica (muscovite), quartz, pyrite, plagioclase feldspar (albite), hematite, anatase, marcasite, fluorapatite, siderite, calcite and dolomite. XRD patterns of the micronised calcium-saturated, <0.2 µm and 0.2 to 2 µm size fractions of the samples are shown in Figures 68 to 73. Clay minerals identified in the sample are smectite, kaolinite, interstratified illite–smectite and mica.

Table 28: Quantitative XRD analysis results (wt.%) of the bulk, micronised and Ca-saturated samples (relative concentrations)

CSIRO ID	63935	63936
Client ID	Shenandoah-1A depth 2316.3 m	Shenandoah-1A depth 2511 m
Smectite	<1	<1
Kaolinite	1	1
Interstratified illite–smectite	13	<1
Mica	26	39
Quartz	47	46
Pyrite	2	3
Plagioclase feldspar	9	7
Hematite	<1	<1
Anatase	1	<1
Marcasite	1	
Fluorapatite	1	
Siderite		<1
Calcite		1
Dolomite		3

Table 29: Quantitative XRD analysis results (wt.%) of <0.2 µm fractions of the samples (relative concentrations)

CSIRO ID	63935	63936
Client ID	Shenandoah-1A depth 2316.3 m	Shenandoah-1A depth 2511 m
Kaolinite	<1	<1
Interstratified illite–smectite	48	23
Mica	42	71
Quartz	10	5

Table 30: Quantitative XRD analysis results (wt.%) of 0.2 to 2 µm fractions of the samples (relative concentrations)

CSIRO ID	63935	63936
Client ID	Shenandoah-1A depth 2316.3 m	Shenandoah-1A depth 2511 m
Smectite	<1	<1
Kaolinite	1	1
Interstratified illite–smectite	18	7
Mica	26	35
Quartz	48	51
Pyrite	<1	1
Plagioclase feldspar	5	4
Hematite	<1	<1
Anatase	<1	<1
Siderite		<1

Table 31: <0.2 µm and 0.2–2 µm particle size fractions (wt.%) of the samples

CSIRO ID	Client ID	<0.2 µm	0.2 to 2 µm	>2 µm	Loss
63935	Shenandoah-1A depth 2316.3 m	6.1	18.0	74.2	1.7
63936	Shenandoah-1A depth 2511 m	6.2	18.7	73.3	1.9

Table 32: XRF results of bulk samples

CSIRO ID	Client ID	SiO ₂ (%)	TiO ₂ (%)	Al ₂ O ₃ (%)	Fe ₂ O ₃ (%)	MnO (%)	MgO (%)	CaO (%)	Na ₂ O (%)	K ₂ O (%)	P ₂ O ₅ (%)	SO ₃ (%)	SUM (%)
63935	Shenandoah-1A depth 2316.3 m	69.7	0.54	12.4	3.9	0.01	1.0	0.8	1.1	2.7	0.5	0.2	92.80
63936	Shenandoah-1A depth 2511 m	65.6	0.49	12.0	4.3	0.05	1.4	1.7	0.8	2.8	0.4	0.2	89.62

Table 33: Exchangeable cations and CEC at pH 8.5 (oven-dried 60°C basis)

CSIRO ID	Client ID	Exchangeable cations pH 8.5					CEC
		Ca	Mg	Na	K	Total	(NH ₄)
		cmol(+)/kg					
63935	Shenandoah-1A depth 2316.3 m	0.9	0.4	1.1	0.96	3	24
63936	Shenandoah-1A depth 2511 m	0.9	0.3	0.8	0.75	3	20

Figure 68: XRD pattern of micronised bulk, Ca-saturated Shenandoah-1A depth 2316.3 m sample (Co K α radiation)

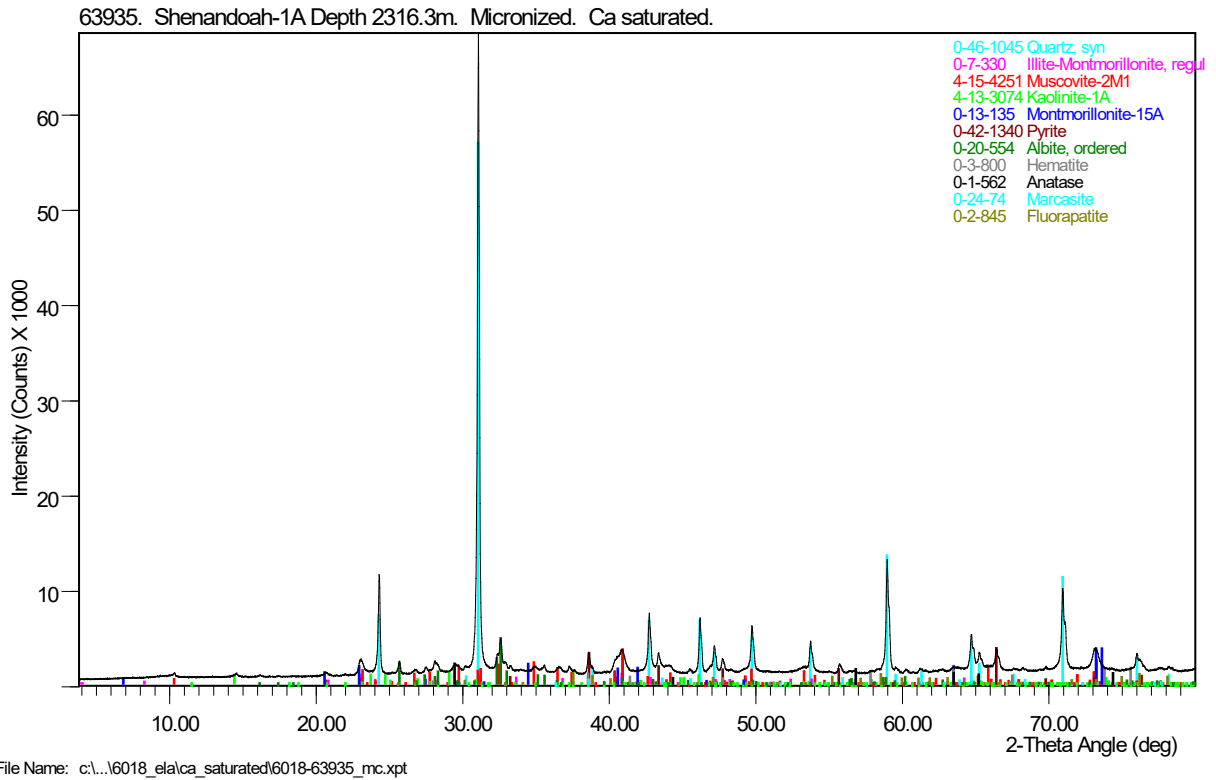


Figure 69: XRD pattern of the <0.2 μ m Ca-saturated fraction of Shenandoah-1A depth 2316.3 m sample (Co K α radiation)

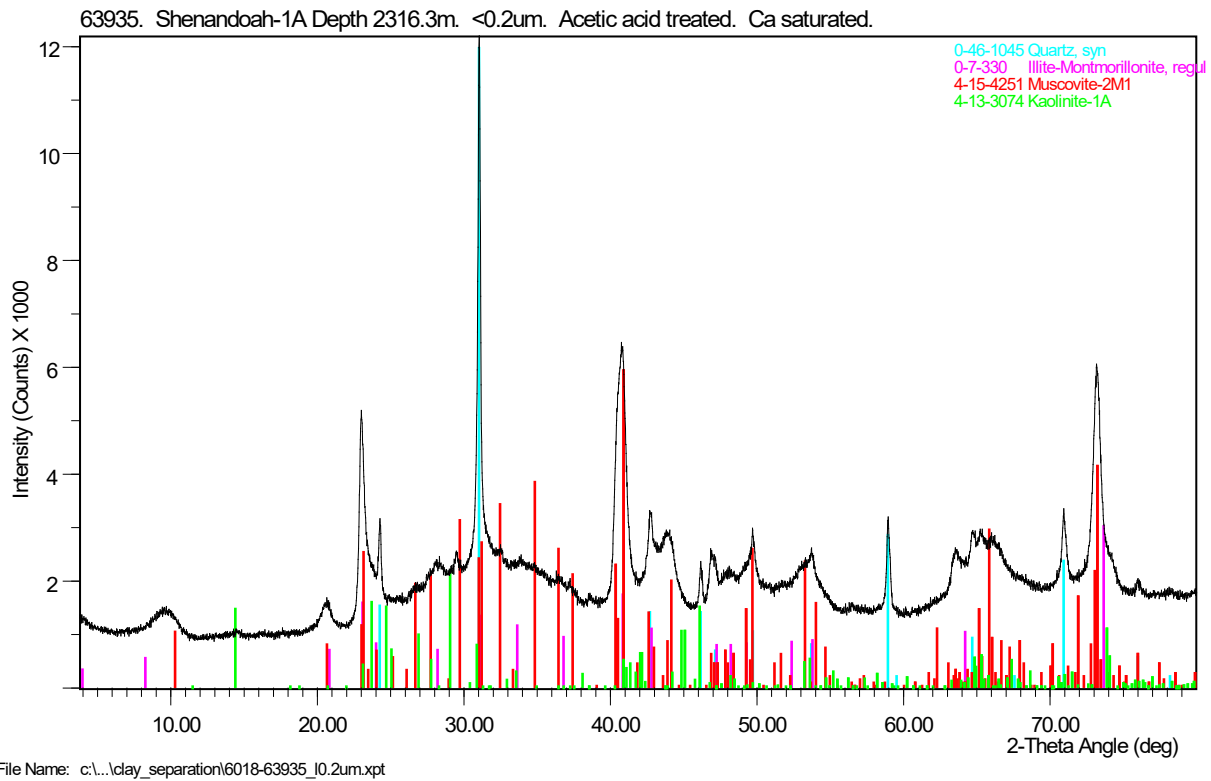


Figure 70: XRD pattern of the 0.2 to 2 μm Ca-saturated fraction of Shenandoah-1A depth 2316.3 m sample (Co Kα radiation)

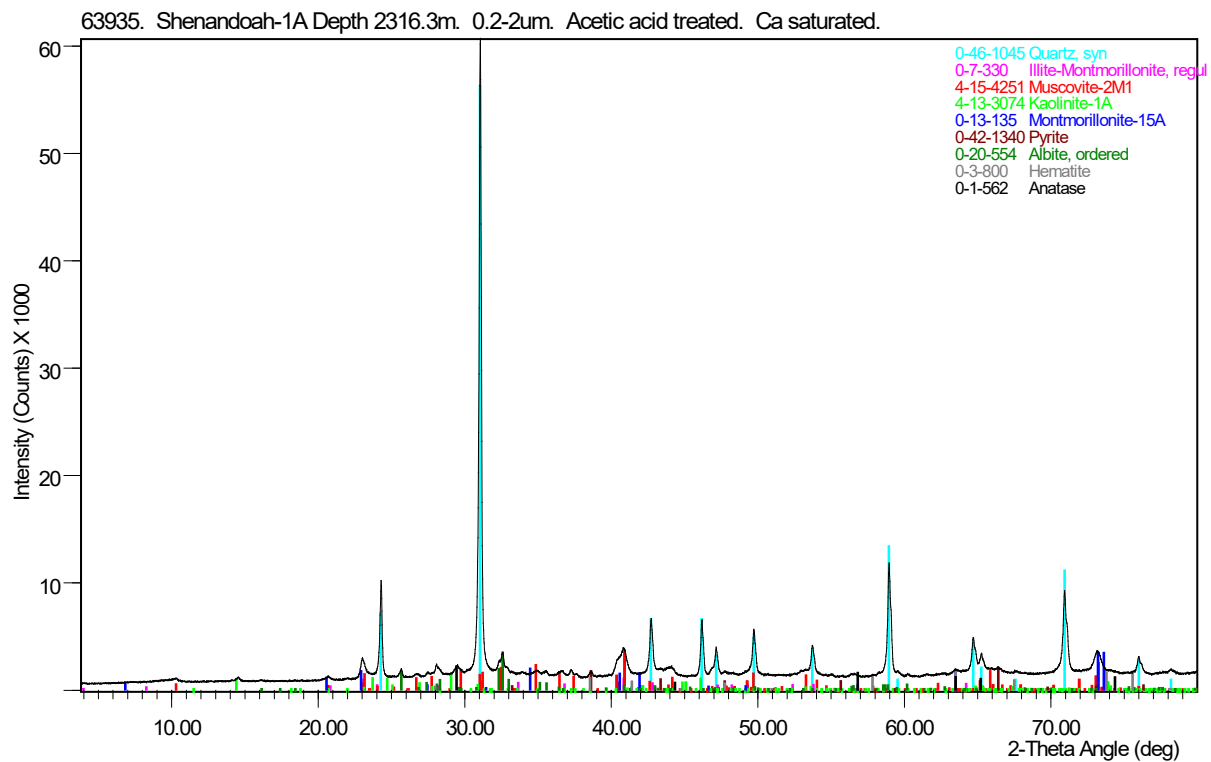


Figure 71: XRD pattern of micronised bulk, Ca-saturated Shenandoah-1A depth 2511 m sample (Co K α radiation)

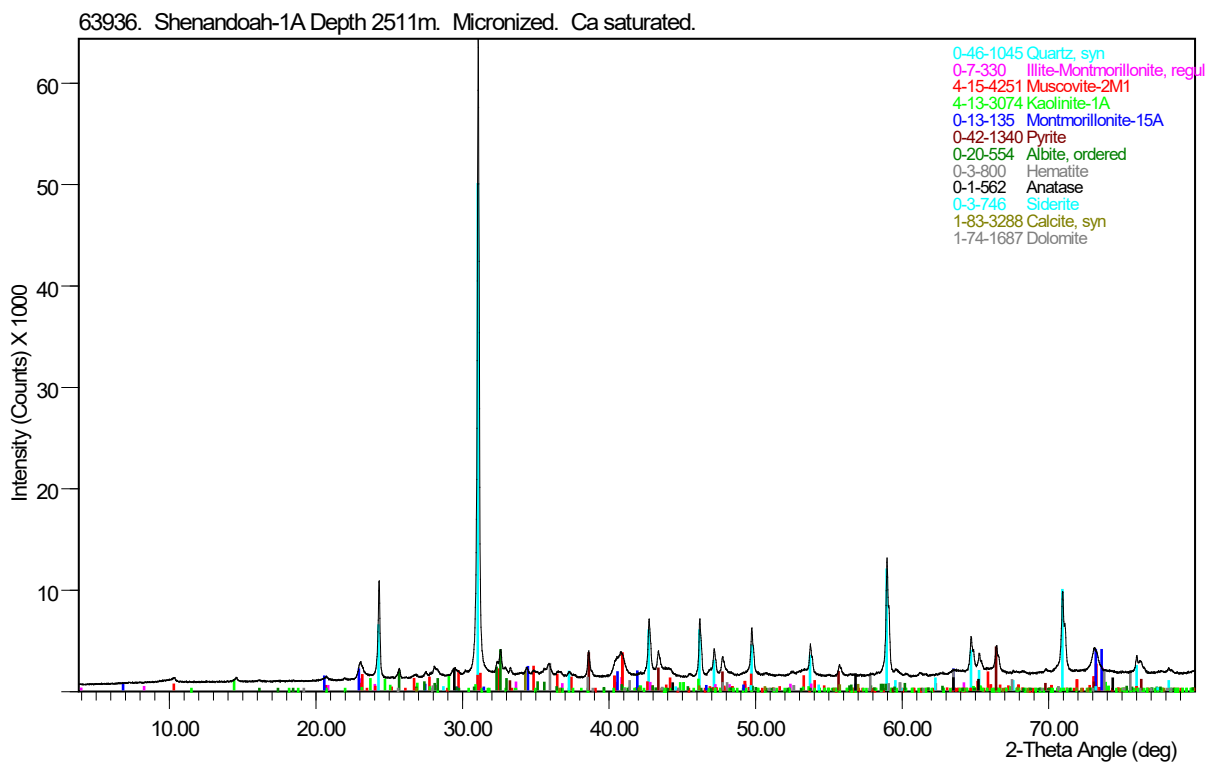
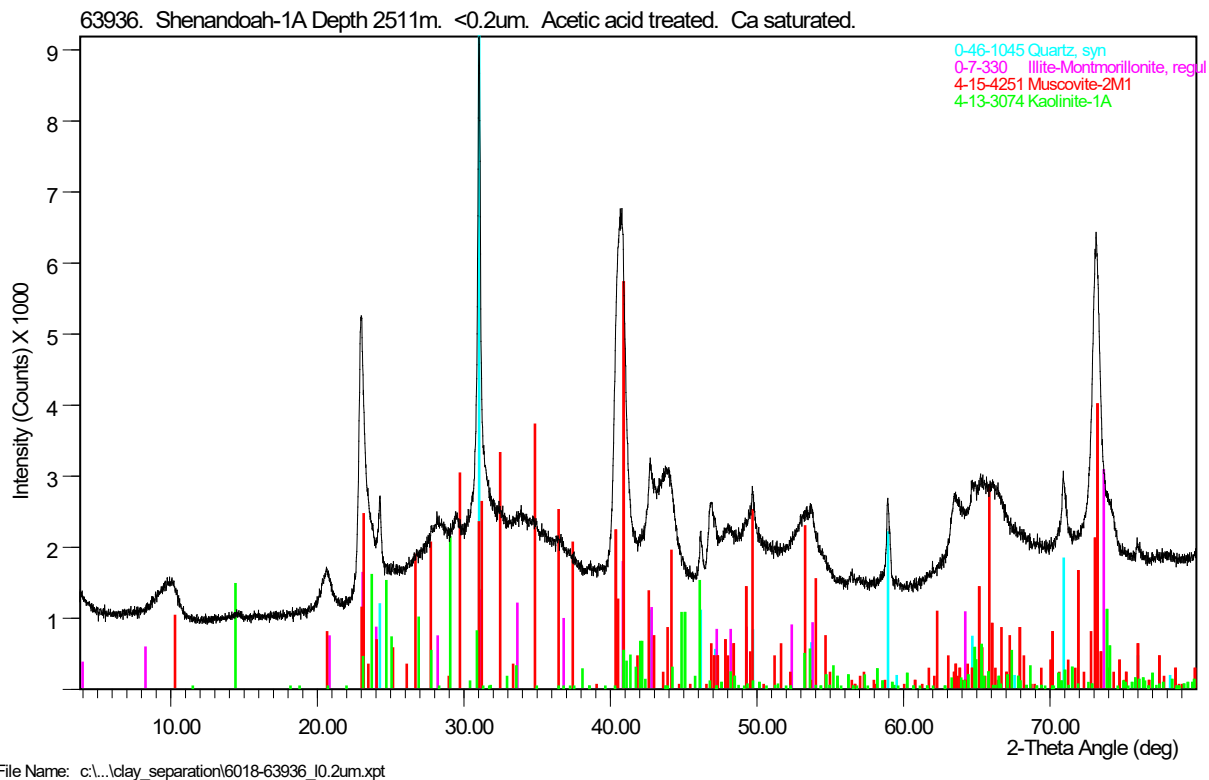


Figure 72: XRD pattern of the <0.2 μ m Ca-saturated fraction of Shenandoah-1A depth 2511 m sample (Co K α radiation)



63936. Shenandoah-1A Depth 2511m. 0.2-2um. Acetic acid treated. Ca saturated.

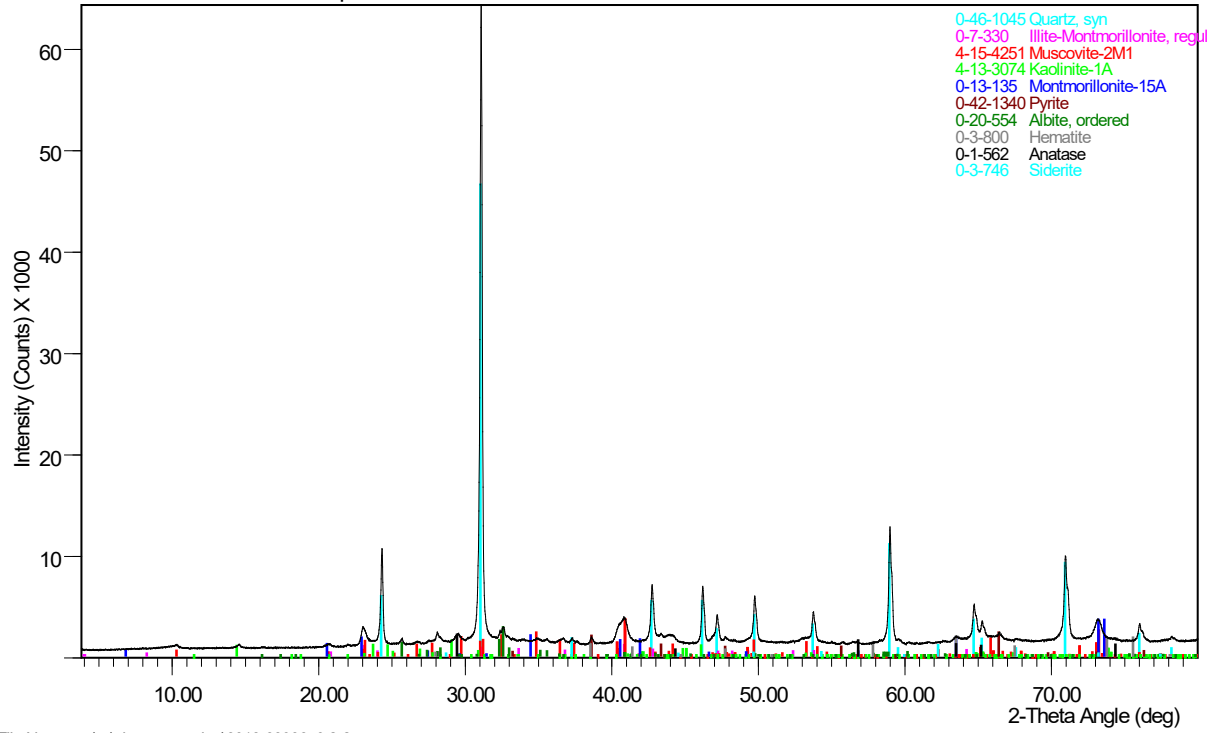


Figure 73: XRD pattern of the 0.2 to 2 μm Ca-saturated fraction of Shenandoah-1A depth 2511 m sample (Co K α radiation)



CSIRO Mineral Resources

Diffraction, Mineralogy and Geochemistry Characterisation Report

CLIENT	Elaheh Arjomand (Job No. 6107)
BU	Energy
DATE	22/05/2023
WBS/O2D	R-18431
ANALYST(S)	Rong Fan and Rodrigo Gomez-Camacho
SUBJECT	XRF and XRD analysis of a drill core sample of Kyalla samples

Procedure

A drill core sample was received for bulk and clay mineralogy by X-ray powder diffraction (XRPD) analysis. The sample was crushed by a jar crusher and a representative sub-sample was further pulverised briefly using a ring mill for following XRD and XRF sample preparation.

For bulk quantitative XRD phase analysis, approximately 1.5 g of the pulverised powder sample was ground in ethanol in a McCrone micronising mill. The resulting slurry was oven-dried at 60°C then thoroughly mixed in an agate mortar and pestle before being lightly back-pressed into a stainless-steel sample holder for presentation to the X-ray beam. The sample was then Ca-exchanged in CaCl₂ solution to ensure that the phases with exchangeable cations (e.g. smectite) were in a divalent monoionic form. The Ca-exchanged sample was lightly back-pressed into a stainless-steel sample holder for presentation to the X-ray beam.

For fine clay analysis, approximately 15 g of the crushed sample was dispersed in NaCl solution. From this dispersion the size fractions (<0.2 µm, 0.2 to 2 µm and >2 µm) were collected by repeated washing with high-purity water, ultrasonication and centrifugation. The recovered material (i.e. <0.2 µm and 0.2 to 2 µm fractions) was treated twice with 0.2 M acetic acid solution to remove carbonate mineral calcite and dolomite, and Ca-exchanged by washing twice with CaCl₂ solution and then removing excess Ca by washing firstly with high-purity water and secondly with ethanol. After the ethanol wash the samples were dried in an oven set to 60°C. The dried material was thoroughly mixed in an agate mortar and pestle before being lightly back-pressed into stainless steel sample holders for presentation to the X-ray beam. The remaining material after the fine clay separation (i.e. >0.2 µm fraction) was dried at 60°C and then weighed for mass balance calculation.

XRD patterns of the bulk and size fraction samples were recorded with a PANalytical X'Pert Pro Multi-purpose Diffractometer using Fe-filtered Co K α radiation, automatic divergence slit, 2° anti-scatter slit and fast X'Celerator Si strip detector. The diffraction patterns were recorded in steps of 0.017° 2 theta with a 0.5 second counting time per step for an overall counting time of approximately 30 minutes.

Phase identification was performed using PANalytical Highscore Plus© software (V4.8), which interfaces with the International Centre for Diffraction Data (ICDD) PDF 4+ 2021 database. Quantitative phase analysis (QPA) was carried out via the Rietveld method using the TOPAS V6 software. The QPA results obtained are the relative wt% of crystalline phases.

For XRF analysis, approximately 1 g of each oven-dried (105°C) bulk-pulverised sample was accurately weighed with 4 g of lithium tetraborate flux. The mixture was heated to 1050°C in a Pt/Au crucible for 20 minutes for

complete dissolution then poured into a 32 mm Pt/Au mould heated to a similar temperature. The melt was cooled rapidly over a compressed air stream and the resulting glass disk was analysed under vacuum using a Spectro XEPOS He energy dispersive X-ray fluorescence spectrometer.

Soluble cations and anions, CEC and exchangeable cations of the bulk as received sample using NH_4^+ were determined using the methods detailed in Rayment and Higginson (1992).

Results

Quantitative XRD analysis results (wt.%) of the bulk, micronised and calcium-saturated sample and its <0.2 and 0.2 to 2 μm fractions (relative concentrations) and the percentage of these size fractions (wt.%) are given in Tables 34 and 35, respectively.

The results of XRF analysis of the bulk sample are given in Table 36. Exchangeable cations and CEC at pH 8.5 (oven-dried 60°C basis) of the sample are shown in Table 37.

Phases identified in the sample are plagioclase feldspar (albite), chlorite (clinochlore), dolomite, mica (muscovite), interstratified illite–smectite, and quartz. XRD patterns of the micronised calcium-saturated, <0.2 μm and 0.2 to 2 μm size fractions of the sample are shown in Figures 74 to 76. Clay minerals identified in the sample are chlorite, mica and interstratified illite–smectite.

Table 34: Quantitative XRD analysis results (wt.%) of the bulk, micronised and Ca-saturated, <0.2 μm and 0.2 to 2 μm fractions of the sample (relative concentrations)

CSIRO ID	64565	64565	64565
Bulk/size fractions	Bulk, micronised and Ca-saturated sample	<0.2 μm fraction	0.2 to 2 μm fraction
Plagioclase feldspar	4		1
Chlorite	10	8	19
Dolomite	1		
Mica	19	34	27
Interstratified illite–smectite	13	55	30
Quartz	53	3	23

Table 35: <0.2 μm and 0.2 to 2 μm particle size fractions (wt.%) of the sample

CSIRO ID	Client ID	<0.2 μm	0.2 to 2 μm	>2 μm	Loss
64565	Kyalla 1591.5 m	4.1	13.1	81.4	1.4

Table 36: XRF results of the bulk sample

CSIRO ID	Client ID	SiO ₂ (%)	TiO ₂ (%)	Al ₂ O ₃ (%)	Fe ₂ O ₃ (%)	MnO (%)	MgO (%)	CaO (%)	Na ₂ O (%)	K ₂ O (%)	P ₂ O ₅ (%)	SO ₃ (%)	SUM (%)
64565	Kyalla 1591.5 m	69.0	0.7	14.0	6.0	0.1	1.9	0.4	0.2	2.8	0.1	0.1	95.3

Table 37: Exchangeable cations and CEC at pH 8.5 (oven-dried 60°C basis)

CSIRO ID	Client ID	Exchangeable cations pH 8.5					CEC
		Ca	Mg	Na	K	Total	(NH ₄)
		cmol(+)/kg					
64565	Kyalla 1591.5 m	1.0	<0.2	1.7	2.86	5.7	11

Figure 74: XRD pattern of micronised bulk, Ca-saturated Kyalla 1591.5 m sample (Co K α radiation)

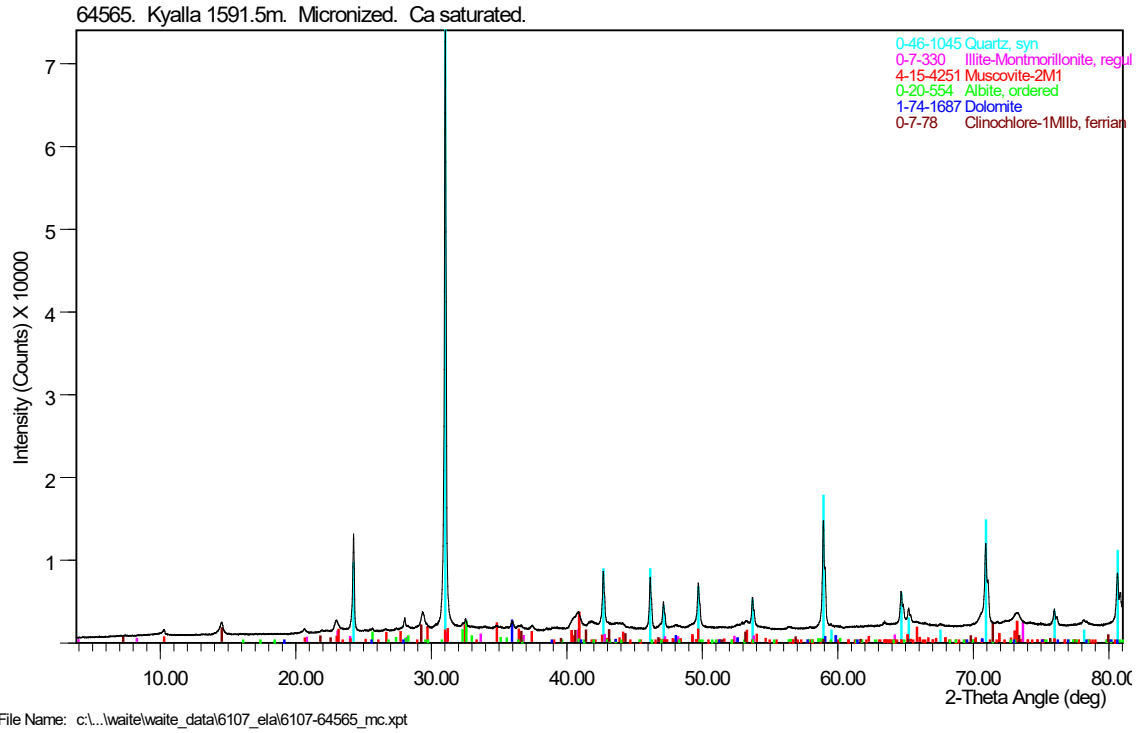


Figure 75: XRD pattern of the <0.2 μ m Ca-saturated fraction of Kyalla 1591.5 m sample (Co K α radiation)

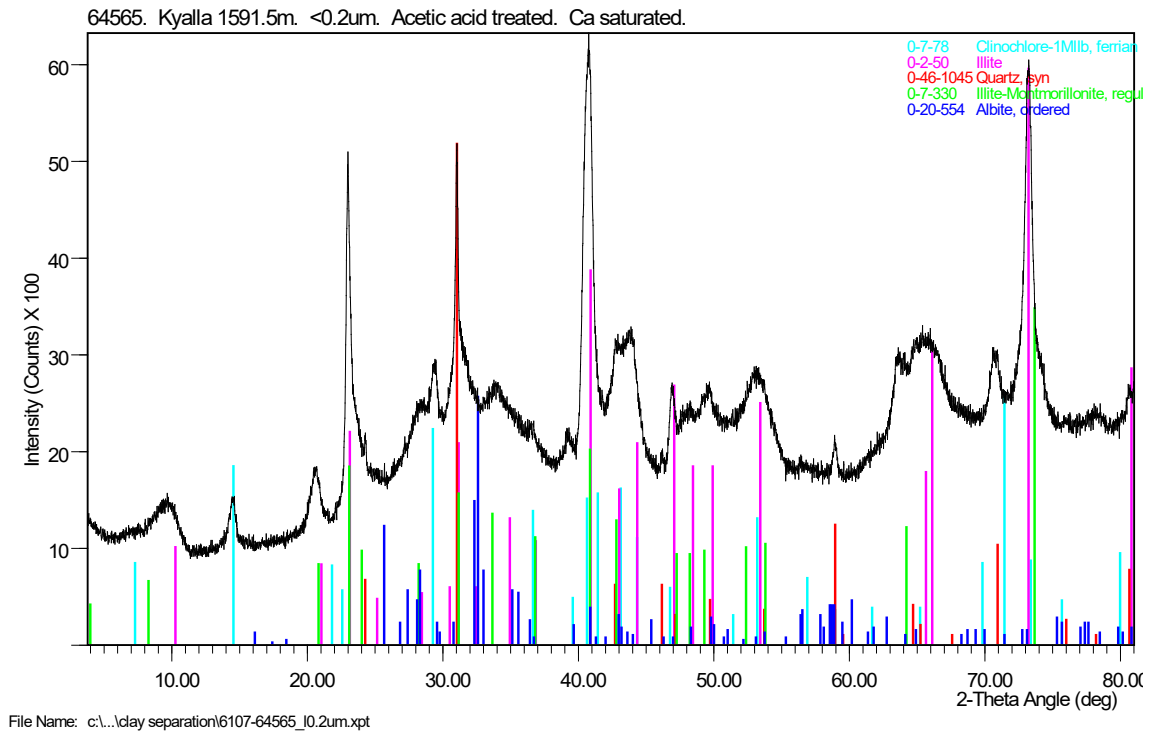
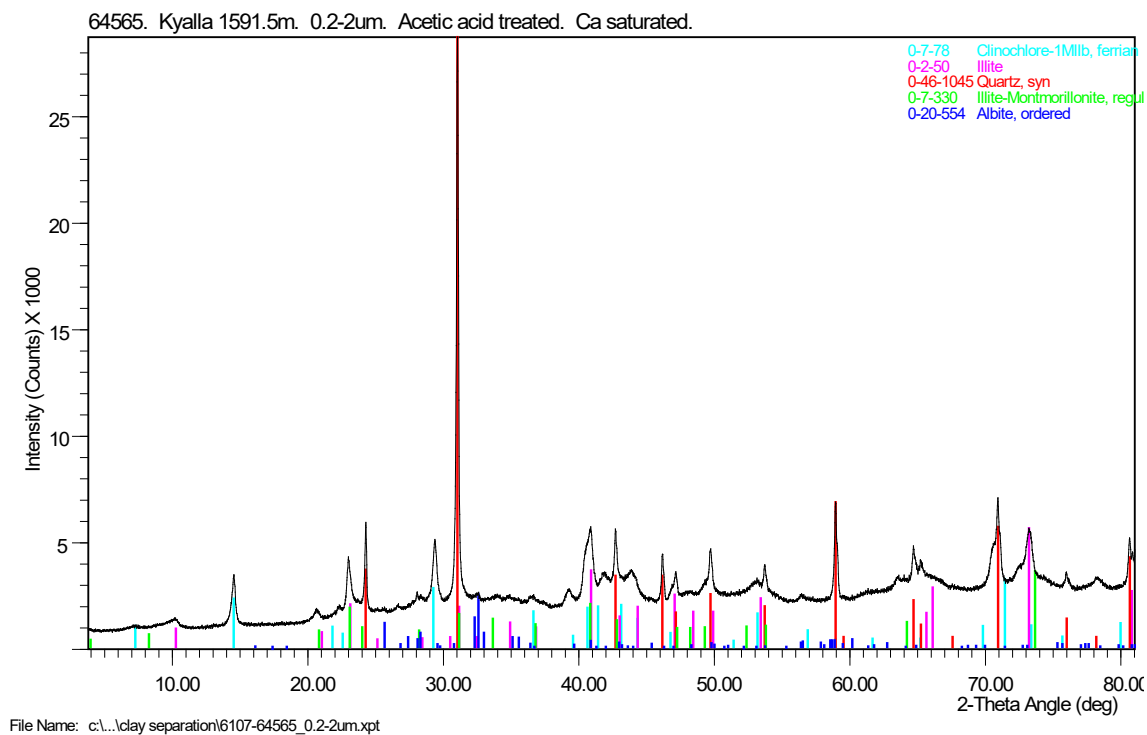


Figure 76: XRD pattern of the 0.2 to 2 μm Ca-saturated fraction of Kyalla 1591.5 m sample (Co Kα radiation)



Appendix IV: Measuring exchangeable cations using NH_4^+ guidelines

Measuring exchangeable cations using NH_4^+ as detailed in Rayment and Higginson (1992) involves the following steps:

1. Collect soil sample and air-dry it.
2. Crush the soil sample to pass through a 2 mm sieve.
3. Weigh 10 g of the air-dried soil and transfer it to a 50 mL centrifuge tube.
4. Add 20 mL of 1 M NH_4OAc (pH 7) to the soil in the tube.
5. Shake the tube vigorously for 1 hour.
6. Centrifuge the tube at 3000 rpm for 10 minutes.
7. Decant the supernatant into a clean centrifuge tube.
8. Add 20 mL of 1 M NH_4OAc to the residue in the original tube and shake vigorously for 15 minutes.
9. Centrifuge the tube at 3000 rpm for 10 minutes.
10. Decant the supernatant into the same tube as the first supernatant.
11. Filter the combined supernatants through a 0.45 μm filter into a clean 50 mL volumetric flask.
12. Rinse the residue on the filter with deionised water and add the rinse to the volumetric flask.
13. Make up the volume to 50 mL with deionised water and mix well.
14. Analyse the solution for exchangeable cations (K^+ , Mg^{2+} , Ca^{2+} , Na^+) using an appropriate analytical technique, such as atomic absorption spectroscopy or inductively coupled plasma-optical emission spectroscopy.

Note that the concentration of exchangeable cations is expressed as milliequivalents per 100 g of soil (mEq/100 g).

Appendix V: Calculating osmotic pressure

To calculate the osmotic pressure when 36 g of salt is added to 525.6 mL of water at 32°C:

1. Volume of solution = 525.6 mL = 0.5256 L
2. The molar mass of NaCl is 58.44 g/mol, so the number of moles of NaCl in 36 g can be calculated as: moles of NaCl = 36 g/58.44 g/mol = 0.616 mol
3. The molar concentration of the solution can be calculated as: molar concentration = 0.616 mol/0.5256 L = 1.172 M
4. Converting 32°C to Kelvin gives: $T = 32^{\circ}\text{C} + 273.15 = 305.15 \text{ K}$
5. The osmotic pressure is computed using the gas constant R ($R = 8.314 \text{ J/mol.K}$):
 $P_c = 1.172 \text{ M} \times 8.314 \text{ J/mol.K} \times 305.15 \text{ K} = 3.008 \text{ MPa}$.